



<https://theses.gla.ac.uk/>

Theses Digitisation:

<https://www.gla.ac.uk/myglasgow/research/enlighten/theses/digitisation/>

This is a digitised version of the original print thesis.

Copyright and moral rights for this work are retained by the author

A copy can be downloaded for personal non-commercial research or study, without prior permission or charge

This work cannot be reproduced or quoted extensively from without first obtaining permission in writing from the author

The content must not be changed in any way or sold commercially in any format or medium without the formal permission of the author

When referring to this work, full bibliographic details including the author, title, awarding institution and date of the thesis must be given

Enlighten: Theses

<https://theses.gla.ac.uk/>  
[research-enlighten@glasgow.ac.uk](mailto:research-enlighten@glasgow.ac.uk)

# Quantitative Magnetic Imaging of Thin Films with Reduced Dimensions

by Margit Herrmann

submitted for the degree of Doctor of Philosophy at the University of Glasgow



This work was conducted at

Solid State Physics Group  
Department of Physics and Astronomy  
University of Glasgow  
UK

© July 2000 Margit Herrmann

ProQuest Number: 10390817

All rights reserved

INFORMATION TO ALL USERS

The quality of this reproduction is dependent upon the quality of the copy submitted.

In the unlikely event that the author did not send a complete manuscript and there are missing pages, these will be noted. Also, if material had to be removed, a note will indicate the deletion.



ProQuest 10390817

Published by ProQuest LLC (2017). Copyright of the Dissertation is held by the Author.

All rights reserved.

This work is protected against unauthorized copying under Title 17, United States Code  
Microform Edition © ProQuest LLC.

ProQuest LLC.  
789 East Eisenhower Parkway  
P.O. Box 1346  
Ann Arbor, MI 48106 – 1346

GLASGOW  
UNIVERSITY  
LIBRARY

11958-COPY 2

With love and gratitude to my parents



## ACKNOWLEDGEMENTS

This thesis was enabled by a Marie Curie grant of the European Commission (contract no. ERBFMBICT 960815). I am also indebted to many people in Glasgow, Leeds and Regensburg for contributions and support. Especially I would like to thank

- ◆ my supervisors Dr S McVitie and Professor JN Chapman for giving me the chance to do this work, their continuous guidance, help, support and invaluable discussions. I also want to thank them for providing electron microscopy facilities in the Solid State Physics Group at the University of Glasgow and the freedom in realising own ideas;
- ◆ the entire SSP group – members and staff – for lots of different reasons e.g. guidance and teaching, general support; maintenance of the electron microscopes and evaporation facilities, management of the computers... – many of them even for their friendship. Special thanks to Dr KJ Kirk, Dr PR Aitchison, Dr S McFadzean, Dr M MacKenzie, Dr M Rahman, Dr. D Vlachos, Mr I Selkirk, Ms B Lynn, Mr A Howie, Mr S Connor, Mr CR How, Mr WA Smith, Ms S Murdoch, Ms F Docherty, Mr B Milton and last but not least Mr TS Munro;
- ◆ Professor RP Ferrier, Professor AJ Craven and Dr WAP Nicholson for their superb hospitality and friendliness;
- ◆ Professor CDW Wilkinson for provision of the electron beam lithography facilities in the Department of Electronics and Electrical Engineering and also his academic and technical staff for maintenance of the equipment, help and advice;
- ◆ Professor BJ Hickey and Dr CH Marrows from the University of Leeds for provision of the GMR samples and useful discussions;
- ◆ Professor MR Scheinfein from the Arizona State University for advice and custom made additions to his program 'LLG Micromagnetics Simulator™' which was used exclusively for the simulations in this work;

- ◆ Professor H Hoffmann and all members of his Lehrstuhl at the University of Regensburg for putting up with me, especially PD Dr J Zweck, Mr M Schneider, Mr W Brunner, Ms R Fischer, Ms C Mayer and the entire EM group - not only for access to different departmental resources and set-up of 'my' computer account, but also for useful discussions and personal support during the lengthy final stages of this thesis...
- ◆ Ms A Teichmann, Mr D Deigl, Ms M and Mr C Koch, Ms M and Mr G Riederer, Mr W Ernst, Ms N Daly, Ms G Penny and Mr D Bakewell for their friendship;
- ◆ last but by far not least my family for their continuous support and encouragement during my study years.

## DECLARATION

This thesis is a record of the work carried out by me in the Solid State Physics Group of the Department of Physics and Astronomy at the University of Glasgow. The work discussed herein is my own with the exception of the fabrication of the Co/Cu multilayers. These were produced at the University of Leeds by Dr CH Marrows who also carried out the MOKE and GMR experiments.

Some of the work given in this thesis can be found in the following papers:

'Effects of gas damage on coupling and anisotropy in sputtered Co/Cu multilayers'

Marrows CH, Hickey BJ, Herrmann M, McVitie S, Chapman JN, Proceedings of the MML'98 Conference; J. Magn. Magn. Mat.;198-199, p408 (1999)

'Damage caused to interlayer coupling of magnetic multilayers by residual gases'

Marrows CH, Hickey BJ, Herrmann M, McVitie S, Chapman JN, Ormston M and Petford-Long AK, Hase TPA, Tanner BK, Phys. Rev. B **61**, p4131 (2000)

'Investigation of the influence of edge structure on the micromagnetic behaviour of small magnetic elements'

Herrmann M, McVitie S and Chapman JN, J. Appl. Phys. **87**, p2994 (2000)

This thesis has not previously been submitted for a higher degree.

Margit Herrmann

July 2000

## SUMMARY

The work described in this thesis is based on the high spatial resolution magnetic imaging, which can be realised at the University of Glasgow on two transmission electron microscopes (TEMs). Both machines are highly modified to optimise magnetic imaging conditions. One is based on a JEOL 2000 FX and the other one on a Philips CM20 FEG microscope. Central to the thesis is the option to investigate samples in zero external field as well as to carry out in-situ magnetising experiments.

The aim was to study the magnetisation reversal behaviour of two groups of magnetic thin films with reduced dimensions which are not only interesting in terms of fundamental micromagnetic studies but also for applications (field sensors, MRAM). The first group were so-called small magnetic elements (patterned thin films of permalloy) and the second group were Co/Cu multilayers. The main focus of investigation for the former group lay on the effects of structuring the edges of acicular elements whilst in the case of the Co/Cu multilayers the influence of different degrees of gas-damage was evaluated. Furthermore experimental data of the small magnetic elements was compared with simulation results of a commercially available software package (LLG Micromagnetics Simulator™).

The first chapter gives an overview of basic ferromagnetism and discusses the energy considerations governing domain configurations in ferromagnetic thin films. Subsequently special emphasis was paid to the energy considerations with respect to the two groups of samples, which were investigated in this work, i.e. small magnetic elements and Co/Cu multilayers.

The second chapter deals with the instrumental requirements of a TEM in order to image the magnetic microstructure of thin film samples. The main focus hereby lies on the modified Philips CM20 FEG microscope. Different magnetic imaging modes, which were applied in this work are described and the magneto-optical Kerr and Faraday effects are also briefly discussed.

In chapter 3 the fabrication processes for small magnetic elements and electron transparent substrates ( $\text{Si}_3\text{N}_4$  membranes) are described. The in-plane dimensions of the small magnetic elements studied here lie in the micron to sub-micron range and are similar in size to state-of-the-art magnetic sensors. As the aim of this work is to assess the influence of structuring the edges of such elements, three types of periodic repeat structures were designed and are introduced in this chapter. No magnetising experiments

were carried out with the test patterns, only the as-grown and ac-demagnetised states have been investigated.

Chapter 4 focuses on the physical and magnetic microstructure of acicular elements and their magnetisation reversal behaviour. The length of the elements was in the micron-range and their width was mainly in the sub-micron range. Standard elements with nominally straight edges were compared with elements with structured edges. Two different lengths as well as two widths of elements were investigated in the first pattern. Three different types of periodic repeat structures were designed and the period of the structure features was varied over a wide range. The magnetic microstructure of the elements in their as-grown and ac-demagnetised state was investigated and in-situ magnetising experiments were carried out.

Results are presented in chapter 5 of a second and third pattern which were also designed with the intention to investigate the influence of structured edges on the micromagnetic states and reversal behaviour of acicular elements. The effects of two different tips ratios of the double pointed elements were evaluated and the height of the structure features was varied. A description of the second and third patterns is given and the physical microstructure of the elements is dealt with. The magnetic microstructure in the as-grown and ac-demagnetised state is discussed and the results of the magnetising experiments are presented.

The aim of chapter 6 is to determine the effects of variation of overall width of the elements with structured edges which was present in the former patterns. Therefore small magnetic elements were designed with structured edges but nominally constant width in the fourth and fifth patterns. All other parameters were the same as in the previous chapter. A description of the two patterns is given before the physical microstructure of the elements is evaluated. The magnetic microstructure of the elements in their as-grown and ac-demagnetised states is dealt with and the development of the domain configurations under the influence of external fields is described.

The magnetic microstructure during magnetising cycles was also modelled for a number of elements which were investigated experimentally using commercially available software (LLG Micromagnetics Simulator™) and the results are presented in chapter 7. A brief description of the theory underlying LLG is given and the set up of problems is discussed. A selection of simulation results is presented and compared with experimental findings.

Chapter 8 deals with another group of magnetic materials with reduced dimensions which are multilayer systems of alternate layers of magnetic and non-magnetic materials with layer thicknesses in the nanometer range. The effects of so-called gas-damage on the GMR performance of different multilayer systems are discussed and the preparation of three Co/Cu multilayers samples with different degrees of gas-damage which were investigated in this work is described. In the results sections GMR measurements and MOKE hysteresis loops are presented before the investigation of the samples with several applied TEM investigation techniques is discussed. By these means the so-called biquadratic coupling was verified and quantified.

In the final chapter this thesis concludes with the discussion of possible future experiments following on from this work.

<b>ACKNOWLEDGEMENTS</b>	iii
<b>DECLARATION</b>	v
<b>SUMMARY</b>	vi
<b>INDEX</b>	ix

## **CHAPTER 1:**

### **Magnetism of Thin Films of Magnetic Material**

1.1 Introduction	1
1.2 Basic Ferromagnetism	1
1.3 Energy Considerations	2
1.3.1 Exchange Energy	2
1.3.2 Magnetostatic Self-Energy	3
1.3.3 Anisotropy Energy	4
1.3.4 Zeeman Energy	7
1.3.5 Magnetic Domains and Wall Energy	7
1.3.6 Total Energy	10
1.4 Hysteresis	10
1.5 Small Magnetic Elements	11
1.6 Multilayer Structures - GMR	13

## **CHAPTER 2:**

### **Investigation of Magnetic Microstructure**

2.1 Introduction	17
2.2 Transmission Electron Microscopy - TEM	18
2.2.1 Electron Gun	19
2.2.2 Microscope Column	20
2.2.3 Aberrations in a CTEM	22
2.2.4 Image Recording	24
2.2.5 Magnetising Experiments	25
2.3 Observation of Magnetic Domains by Means of Electron Microscopy	26
2.3.1 Electron Beam and Specimen Interaction	26
2.3.2 Conventional Transmission Electron Microscopy Modes - CTEM	31
2.3.3 Scanning Transmission Electron Microscopy Modes - STEM	35

2.4 Observation of Magnetic Domains Utilising the Magneto-optical Kerr Effect (MOKE)	39
<b>Chapter 3:</b>	
<b>Preparation of Patterned Thin Films - Small Magnetic Elements</b>	
3.1 Introduction	42
3.2 Fabrication of Si <sub>3</sub> N <sub>4</sub> Membranes	42
3.3 Small Magnetic Elements	47
3.4 Fabrication of Patterned Thin Films	48
3.4.1 Electron Beam Lithography	48
3.4.2 Metal Deposition and Lift Off	50
3.5 Structured Edges of Small Magnetic Elements	52
3.6 Test Patterns - Physical and Magnetic Microstructure	53
3.6.1 Description of Patterns	54
3.6.2 Physical Microstructure	55
3.6.3 As-grown and ac-demagnetised State	57
3.7 Summary	64
<b>Chapter 4:</b>	
<b>1<sup>st</sup> Pattern: Acicular Elements with Structured Edges of Types A, B, C</b>	
4.1 Introduction	65
4.2 Description of Pattern	66
4.3 Physical Microstructure	68
4.4 As-grown and ac-demagnetised State	69
4.5 Magnetising Experiments	75
4.6 Summary	82
<b>Chapter 5:</b>	
<b>Acicular Elements with Structured Edges of Types A and C</b>	
<b>- 2<sup>nd</sup> and 3<sup>rd</sup> Pattern</b>	
5.1 Introduction	83
5.2 Description of Patterns	84
5.3 Physical Microstructure	86

5.4 As-grown and ac-demagnetised State	88
5.5 Magnetising Experiments	91
5.5.1 Standard Elements	92
5.5.2 Elements with Edge Structure Type A	98
5.5.3 Elements with Edge Structure Type C	110
5.6 Summary	118

## **Chapter 6:**

### **Acicular Elements with Structured Edges of Types A and C**

#### **- 4<sup>th</sup> and 5<sup>th</sup> Pattern**

6.1 Introduction	121
6.2 Description of Patterns	121
6.3 Physical Microstructure	124
6.4 As-grown and ac-demagnetised State	125
6.5 Magnetising Experiments	128
6.5.1 Elements with Edge Structure Type A	129
6.5.2 Elements with Edge Structure Type C	136
6.6 Summary	143

## **CHAPTER 7:**

### **Simulation of Micromagnetic States Using**

#### **LLG Micromagnetics Simulator™**

7.1 Introduction	146
7.2 Theory of Operation of LLG Micromagnetics Simulator	147
7.3 Set up of Problems	149
7.4 Modelling of Magnetising Experiments with and without Vertical Field: Magnetic Microstructure and Hysteresis Loops	157
7.4.1 Elements of 2 <sup>nd</sup> and 3 <sup>rd</sup> Patterns	158
7.4.1.1 Standard Elements	158
7.4.1.2 Elements with Edge Structure Type A	166
7.4.1.3 Elements with Edge Structure Type C	175
7.4.2 Elements of 4 <sup>th</sup> and 5 <sup>th</sup> Patterns	181
7.4.2.1 Elements with Edge Structure Type A	181

7.4.2.2 Elements with Edge Structure Type C	187
7.5 Summary	191
<b>CHAPTER 8:</b>	
<b>Co/Cu Multilayers - Giant Magneto Resistance (GMR)</b>	
8.1 Introduction	195
8.2 Effect of Gas-damage on GMR of Co/Cu Multilayers	196
8.3 Preparation of Samples with Different Degrees of Gas-damage	197
8.4 GMR Measurements and Hysteresis Loops	198
8.5 TEM Investigations	202
8.5.1 Physical Microstructure	202
8.5.2 Magnetic Microstructure - As-grown and ac-demagnetised State	203
8.5.3 Magnetising Experiments	204
8.5.3.1 Fresnel Mode	205
8.5.3.2 Low Angle Diffraction	215
8.6 Summary	232
<b>CHAPTER 9:</b>	
<b>Summary, Conclusions and Future Work</b>	234
9.1 Small Magnetic Elements	234
9.2 Micromagnetic Simulations	242
9.3 Co/Cu Multilayers	246
<b>CONVERSION TABLE</b>	247
<b>SYMBOLS AND ACRONYMS</b>	248
<b>REFERENCES</b>	252

**CHAPTER 1:****MAGNETISM OF THIN FILMS OF MAGNETIC MATERIAL****1.1 INTRODUCTION**

In this chapter the basic concepts of ferromagnetism are summarised in section 1.2 and the energy considerations which determine the properties and characteristics of ferromagnetic materials are discussed in section 1.3. The concept of domains and domain walls is then introduced in section 1.4. The last two sections deal with the characteristic effects and considerations for structured thin films firstly for so-called small magnetic elements in section 1.5 and secondly for multilayers in section 1.6.

**1.2 BASIC FERROMAGNETISM**

A type of material, which possesses a spontaneous non-zero net magnetic moment in the absence of an applied field is known as a ferromagnet. Examples of ferromagnets are transition metals, rare earth elements and certain alloys and oxides. All these materials display ferromagnetism below a critical temperature which is known as the Curie temperature ( $T_C$ ). When a material has a temperature above  $T_C$ , the atoms act as paramagnets resulting in a random distribution of the atomic dipole moments due to thermal agitation.

Elemental ferromagnetic materials possess a magnetic dipole moment associated with each atom. This is caused by the angular momentum which due to the quenching of orbital angular momentum, arises predominantly from the spin of unpaired electrons in the 3d or 4f shells. Unlike in a paramagnet, where the magnetic dipoles are randomly oriented the dipoles in a ferromagnet are aligned parallel to each other below the Curie temperature. Weiss (1907) proposed an internal molecular field in order to account for this co-operative phenomenon. This internal field  $\vec{H}_m$  is proportional to the magnetisation  $\vec{M}$  and causes the parallel alignment of the atomic dipole moments.

The molecular field was accounted for by Heisenberg (1928), who proposed a quantum mechanical interaction known as the exchange force between each atom and its nearest neighbours. Due to the Pauli exclusion principle the total wavefunction for a quantum mechanical system comprising electrons must be antisymmetric. The

wavefunction can be thought of as the product of spatial and spin wavefunctions and for a two electron system the electrostatic energy is dependent on the relative angle between the two spins. A minimum in electrostatic energy is obtained for parallel alignment of the spins when the spatial part of the wavefunction is antisymmetric. The exchange force tends to align the atomic magnetic dipoles parallel to each other in order to reduce electrostatic energy. Thus the exchange force is the phenomenon responsible for ferromagnetism.

### 1.3 ENERGY CONSIDERATIONS

In certain cases it is possible to predict the micromagnetic state of a system by minimising the total energy which comprises various macroscopic energy terms. For many systems, however, the energies of different states are finely balanced and micromagnetic calculations are required. The main contributing energy terms for the ferromagnetic systems dealt with in this work are exchange, magnetostatic, anisotropy and Zeeman energy.

#### 1.3.1 EXCHANGE ENERGY

As introduced in section 1.2 the exchange energy depends on the relative orientation of two spins  $\vec{s}_i$  and  $\vec{s}_j$  of the atomic moments and is given by

$$E_{ex} = -2J(r_{ij})\vec{s}_i \cdot \vec{s}_j \quad (1.1)$$

where  $J(r_{ij})$  is the exchange integral for the two interacting electrons separated by a distance  $r_{ij}$ . As the exchange integral is found to be positive in ferromagnetic materials eqn. (1.1) implies that the minimum energy state occurs for parallel alignment of the magnetic moments  $\vec{s}_i$  and  $\vec{s}_j$ .

In terms of a finite volume of magnetic material the exchange energy is more completely described by

$$E_{ex} = A \int_V \left[ (\nabla\alpha)^2 + (\nabla\beta)^2 + (\nabla\gamma)^2 \right] dV \quad (1.2)$$

where  $\alpha$ ,  $\beta$ , and  $\gamma$  are the directional cosines of the magnetic vector and  $A$  is the exchange constant of the material as defined below:

$$A = \frac{kJs^2}{a} \quad (1.3)$$

$k$  is a constant depending on the crystalline structure (1 simple cubic, 2 body centred cubic (bcc), 4 face centred cubic (fcc)),  $J$  is the exchange interaction constant (positive for ferromagnetic materials),  $s$  is the magnitude of the magnetic moment of the atom and  $a$  is the lattice constant. For permalloy the exchange constant was determined to be  $1 \times 10^{-6}$  erg/cm (Prutton, 1964) and this value did not need to be corrected very much since. According to Scheinfein (1998) it is  $1.05 \times 10^{-6}$  erg/cm .

### 1.3.2 MAGNETOSTATIC SELF-ENERGY

The magnetostatic contribution to the energy of a magnetic system  $E_s$  arises from the interaction between magnetic "free poles" (discontinuities of magnetisation) which are either generated within the volume of the magnetic material or at its surface where there is a divergent component of magnetisation. The energy contribution from the interaction of free poles takes the form

$$E_s = -\frac{1}{2} \mu_0 \int_V \vec{M} \cdot \vec{H}_d \, dV . \quad (1.4)$$

$\mu_0$  is the permeability of vacuum and  $H_d$  is the so-called demagnetising field (eqn. 1.5). The free poles give rise to both an external stray field and an internal field, which is antiparallel to the magnetisation. These fields can be described in terms of an integral over the volume  $V$  and surface  $S$  of the source. The resulting field is often termed the demagnetising field  $H_d$  and is given by

$$H_d = \frac{1}{4\pi} \int_V \frac{-\nabla \cdot \vec{M}}{r^2} \, dV + \frac{1}{4\pi} \int_S \frac{\vec{M} \cdot \vec{n}}{r^2} \, dS \quad (1.5)$$

where  $\vec{r}$  is the direction vector between the source and the considered field points and  $\vec{n}$  the outward pointing unit vector normal to the surface. The term  $\nabla \cdot \vec{M}$  is equivalent to the magnetic volume charge and  $\vec{M} \cdot \vec{n}$  is the magnetic surface energy. It should be noted that the second term in eqn. (1.5) is often termed surface anisotropy. The integrals in eqn. (1.5) are easily evaluated for an ellipsoid but for other common shapes, such as rectangles for example, the integral has no simple analytical form.

$E_s$  is highly dependent on the sample geometry and is at a minimum when the magnetisation forms a flux closure structure without free poles. This is in direct opposition/competition with the exchange energy  $E_{ex}$  and gives rise to the so-called shape anisotropy which is discussed in the next section.

### 1.3.3 ANISOTROPY ENERGY

A material possesses magnetic anisotropy if the magnetisation vector has a preferred direction and the energy necessary to magnetise/saturate the sample is dependent on the sample orientation. The preferred direction with minimal energy consumption for magnetising processes is referred to as the easy axis and deviation of the magnetisation vector from the easy axis results in an increase of the anisotropy energy. In the case of magnetocrystalline anisotropy the anisotropy energy is related to crystal lattice directions.

#### Magnetocrystalline Anisotropy

For a single cubic crystal the anisotropy energy is well described by the first two terms of a series expansion

$$E_K = \int_V \left[ K_1 (\alpha^2 \beta^2 + \beta^2 \gamma^2 + \gamma^2 \alpha^2) + K_2 \alpha^2 \beta^2 \gamma^2 \right] dV \quad (1.6)$$

where  $\alpha$ ,  $\beta$ , and  $\gamma$  are the direction cosines and  $K_1$  and  $K_2$  are the first two anisotropy constants of the material. For transition metals  $K_1 \gg K_2$  and the anisotropy energy can be approximated to just a single term.

For hexagonal or uniaxial crystals the anisotropy energy is described by

$$E_K = \int_V \left[ K_1 (1 - \gamma^2) + K_2 (1 - \gamma^2)^2 \right] dV \quad (1.7)$$

with the  $c$  axis being coincident with the symmetry axis.

When the magnetic material is micro-polycrystalline then the direction of magnetocrystalline anisotropy varies locally from crystallite to crystallite. This results in a random contribution to the local easy axis direction and causes fluctuations in the direction of the magnetisation vector. This phenomenon is often referred to as magnetisation ripple (Fuller et al, 1960), (Hoffmann, 1968).

### Shape Anisotropy

Magnetic anisotropy can also occur as a result of the shape of the sample. This shape anisotropy is based on the demagnetising field introduced in section 1.3.2 (eqn. 1.5). For an ellipsoidal sample it can be shown that

$$\vec{H}_d = -N \vec{M} \quad (1.8)$$

where  $N$  is the demagnetising tensor. Using the diagonal form of this tensor

$$N = \begin{pmatrix} N_x & & \\ & N_y & \\ & & N_z \end{pmatrix} \quad (1.9)$$

it can be shown that in the case of thin magnetic plates and continuous thin films the demagnetising factors for the three cartesian axes are  $N_x = N_y = 0$  and  $N_z = 1$  (in CGS units:  $4\pi$ ) (Chikazumi, 1964) which is the reason for the confinement of magnetisation in the film plane.

In general cases of ferromagnetic bodies the situation is not so simple. If an irregularly shaped body is magnetised, even a uniform distribution of magnetisation gives rise to non-uniform demagnetising fields. This leads in return to an irregular magnetisation distribution and the demagnetising factor cannot be defined. However in the case of an ellipsoid a uniform demagnetising field results for a uniform magnetisation distribution. Despite the calculated formulae of demagnetising factors being quite complex the

equations are fairly simple and clear for special cases. One of these special cases is a flat ellipsoid with two long axes of similar dimension (same order of magnitude) and a short axis. Figure 1.1 shows an illustration for the case  $y > x \gg z$ .

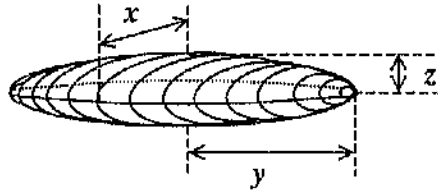


*Figure 1.1*

*Schematic of a flat ellipsoid.*

The demagnetising factors parallel to the  $x$  and  $y$  axes are approximately given by

$$N_x = \frac{\pi}{4} \cdot \frac{z}{y} \left[ 1 + \frac{5}{4} \frac{y-x}{y} + \frac{21}{16} \left( \frac{y-x}{y} \right)^2 \right] \quad (1.10a)$$

$$N_y = \frac{\pi}{4} \cdot \frac{z}{y} \left[ 1 - \frac{1}{4} \frac{y-x}{y} - \frac{3}{16} \left( \frac{y-x}{y} \right)^2 \right] \quad (1.10b)$$

(Chikazumi, 1964). It should be noted that the demagnetising factor of compact bodies is often well approximated by the corresponding demagnetising factors of the inscribed ellipsoid (Hubert et al, 1998). Even numerical calculations of the demagnetising energy for arbitrary bodies can be checked by comparing them with the result for a suitable ellipsoid.

### **Induced Anisotropy**

In a polycrystalline random magnetic alloy such as permalloy ( $\text{Ni}_{80\text{at}\%}\text{Fe}_{20\text{at}\%}$ ) where the stoichiometry results in near zero magnetocrystalline anisotropy, it is possible to induce significant uniaxial anisotropy by different means. The most common options, especially in the case of continuous thin films are to either deposit the material in a magnetic field or to anneal the sample after deposition in the presence of a field. This induced anisotropy is caused by a preferential ordering of atom pairs in the otherwise random alloy (Chikazumi, 1964). During deposition an interaction between the local magnetisation and the atom pairs tends to align the "pair axis" with the magnetisation vector. This results in a "pair axis" throughout the sample, which remains after deposition as so-called induced anisotropy.

### 1.3.4 ZEEMAN ENERGY

In the presence of an external field  $\vec{H}$  there is also a magnetostatic contribution from the interaction between the magnetisation and the applied field. This is known as the Zeeman energy  $E_h$  and is given by

$$E_h = -\mu_0 \int_V \vec{M} \cdot \vec{H} dV. \quad (1.11)$$

In the minimum energy state the magnetic moments of a ferromagnet align parallel with the applied field.

### 1.3.5 MAGNETIC DOMAINS AND WALL ENERGY

The net magnetisation of a ferromagnetic body is often substantially less than the saturation magnetisation of the magnetic material which it is made from. In an attempt to explain this, Becker (1930) introduced the concept of magnetic domains. This hypothesis, which was later confirmed by Bitter (1931), assumes that within a sample there are volume fractions of spontaneously aligned magnetisation, each of them possessing a different direction of magnetisation. Such volume fractions are termed domains and the different directions of magnetisation lead to a reduction of the overall net magnetisation of the body. The boundaries between domains are known as domain walls and the magnetisation vector gradually rotates within a wall between the two directions of magnetisation in the adjacent domains. Depending on how the magnetisation vector rotates the wall is either referred to as a Bloch, Néel or cross-tie wall (Fig. 1.2). A Néel wall possesses an in-plane rotation of magnetisation (Fig. 1.2(a)) whilst in a Bloch wall the magnetisation rotates out of the sample plane as shown schematically in Fig. 1.2(b). For further theoretical elaboration see Landau et al (1935), Néel (1944), Lifshitz (1944), Hubert et al (1998).

Important in this context is the term 'polarity' of a domain wall, which describes the 'mean direction of magnetisation' within the wall. The polarity is positive in a certain direction and negative opposite to it (illustrated for x-direction in Fig. 1.2(a)). In the case of 180° Néel walls it does not make a difference which polarity the wall has as both possibilities are equivalent in terms of energy considerations. Therefore the polarity of a wall is the result of the magnetisation direction in adjacent domains for all other wall

angles. This means that in the case of positive magnetisation components in the two adjacent domains positive polarity is favourable for the wall whilst negative polarity is the result for negative magnetisation components in neighbouring domains. It should be noted that the polarity of a wall will not simply 'flip' not even during magnetisation reversal processes and that walls of opposite polarity will not annihilate but instead form so-called  $360^\circ$  walls (Heyderman et al, 1994), (Gillies et al, 1995).

A cross-tie wall (Huber Jr et al, 1958) is an intermediate structure with sections of Néel walls and parts of Bloch walls (Fig. 1.2(c)). The parts of a cross-tie wall with out of plane component of magnetisation are singularities commonly known as Bloch lines which are located (i) at the crossings of walls and (ii) in the centre of magnetisation rotation (vortices) (Middelhoek, 1963), (Feldtkeller et al, 1965), (Hubert et al, 1998). It should be noted that the orientation of the Bloch lines need not alternate as shown in Fig. 1.2(c). Instead all Bloch lines could point in the same direction.

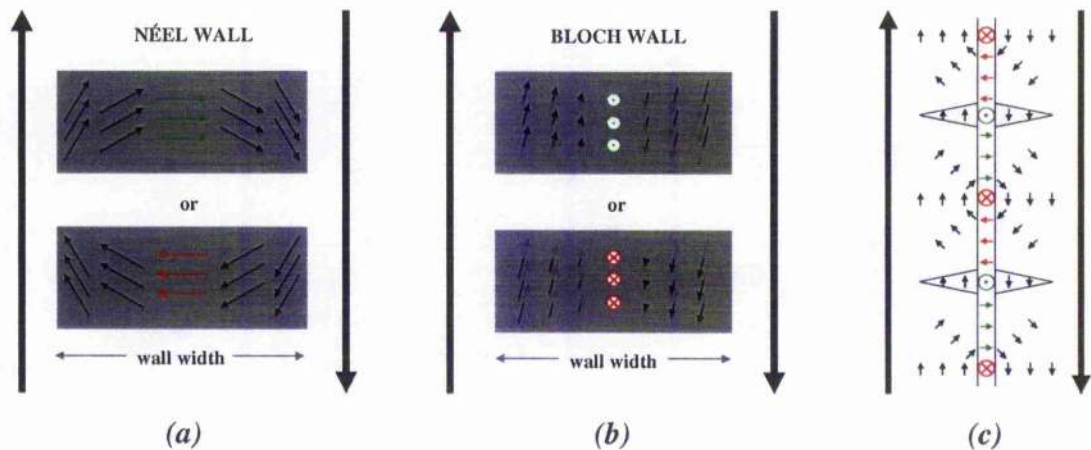


**Figure 1.2**

*Planar schematics of domain walls. (a) Néel wall, (b) Bloch wall, (c) cross-tie wall.*

*Big black arrows indicate magnetisation direction in adjacent domains.*

*→ magnetisation components of Néel walls with positive/negative polarity.*

*⊙, ⊗ components of Bloch walls (i.e. Bloch lines) pointing out and in the plane of the sample.*

The rotation of magnetisation across a domain wall results in contributions to the exchange energy  $E_{ex}$ , the anisotropy energy  $E_K$  and in some cases magnetostatic energy  $E_s$ .

For a Bloch wall in a bulk material it is possible to define the domain wall energy per unit area of the wall

$$\sigma_{wall} = 4\sqrt{AK} \quad (1.12)$$

with  $A$  being the exchange constant (section 1.3.1) and  $K$  the anisotropy constant (section 1.3.2).

Although the wall energy is a combination of previously introduced energies it is valid to consider it as a separate entity  $E_w$ . The type of domain wall depends on the film thickness and Fig 1.3 shows the expected wall type in permalloy as a function of film thickness. The reason for the different variations of the energy densities of different wall types depending on the film thickness is that a Bloch wall has  $\nabla \vec{M} = 0$  but it creates surface charges and is therefore less favourable for thinner films. Néel walls on the other hand have a  $\nabla \vec{M} \neq 0$  but do not create magnetic surface charges which is preferable for thinner films. As cross-tie walls are the intermediate wall type its energy density does not vary with film thickness.

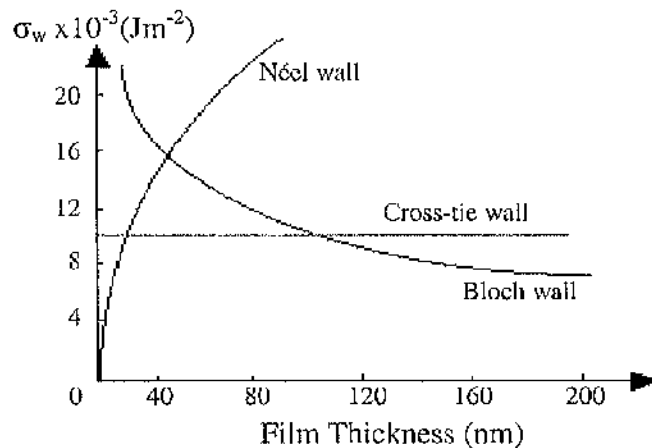


**Figure 1.3**

*Comparison between energy densities of Néel, Bloch and cross-tie walls versus permalloy film thickness (Prutton, 1964).*

### 1.3.6 TOTAL ENERGY

The total energy of a magnetic system  $E_{tot}$  is given by the summation of all the energies introduced above,

$$E_{tot} = E_{ex} + E_K + E_s + E_h + E_w \quad (1.13)$$

It should be noted that the magnetostriction energy is not taken into account in the energy considerations here as it does not play an important role for the materials and material systems discussed in this work.

In order to determine a possible magnetic state of a system the total energy must be minimised. Micromagnetics and domain theory are based on the same variational principle which is derived from thermodynamic principles as established initially in Landau et al (1935) and as reviewed for example in Hubert et al (1998). The energy terms are inter-related and the balance between them is the factor, which controls the micromagnetic state (domain configuration) of the sample. For example, in many cases the magnetostatic energy may be lowered, or even averaged to zero by the formation of flux closure domains. This, on the other hand, leads to an increase of other energies.  $E_w$  may be increased as a result of different wall configurations and  $E_K$  is increased since flux closure domains are often orthogonal to the easy axis direction. Hence, several low energy states exist for a system and it is easily possible to determine a local energy minimum instead of the absolute minimum state. In a demagnetised state the magnetic system will be such that there is a global minimum in the total whilst the remanent state is only a local minimum. Thus the energy of the system is dependent on its magnetic history. This dependence is known as hysteresis and is dealt with next.

### 1.4 HYSTERESIS

The hysteresis effect of the magnetisation  $M$  versus the applied magnetic field  $H$  is a fundamental characteristic of ferromagnetic materials and therefore the hysteresis loop is the most common way to represent (bulk) magnetic properties (Jiles, 1991). An example of a typical hysteresis loop is shown in Fig. 1.4. Crucial values of hysteresis loops are the saturation magnetisation  $M_S$ , the remanence  $M_R$  and the coercivity  $H_c$  as these values

determine the usefulness of a material for certain applications. Permanent magnets for example require high coercive values (i.e. need to be magnetically hard) whilst transformer cores need to be soft magnetic materials. In the magnetic recording industry it is necessary to carefully balance  $M_S$ ,  $M_R$  and  $H_c$  depending the application to achieve high performance and reliability.

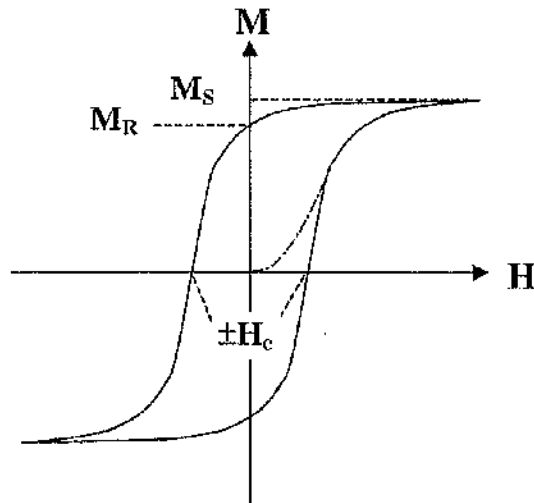


**Figure 1.4**

*Hysteresis loop;*

*dashed curve: virgin curve*

*$M_S$ : saturation magnetisation,*

*$M_R$ : remanent moment,*

*$H_c$ : coercive field.*

## 1.5 SMALL MAGNETIC ELEMENTS

In the case of soft magnetic micro- and nano-structured thin films as investigated in this work the main energy terms are exchange and magnetostatic self-energy (in zero field conditions). The exchange energy is minimum for parallel alignment of the magnetic moments whilst magnetostatic energy favours alignment of the magnetic moments parallel to the nearest edge (and surface for thin films) and the interplay between both energies determines the equilibrium state of magnetisation for small magnetic elements. It should be noted that in the case of a hard magnetic material the crystal anisotropy would also contribute non-negligibly to the total potential energy.

Figure 1.5 shows schematics of favourable domain configurations of elements depending on the geometry of some small magnetic elements (dimensions in the micron and sub-micron range) of permalloy with a film thickness in the range  $\approx 20 - 30$  nm. Such configurations were not only observed in this work but can also be found in McVitie et al (1988), Kirk et al (1997a, b) and Gomez et al (1999) and further geometries are discussed in a recent review article by Cowburn (2000).

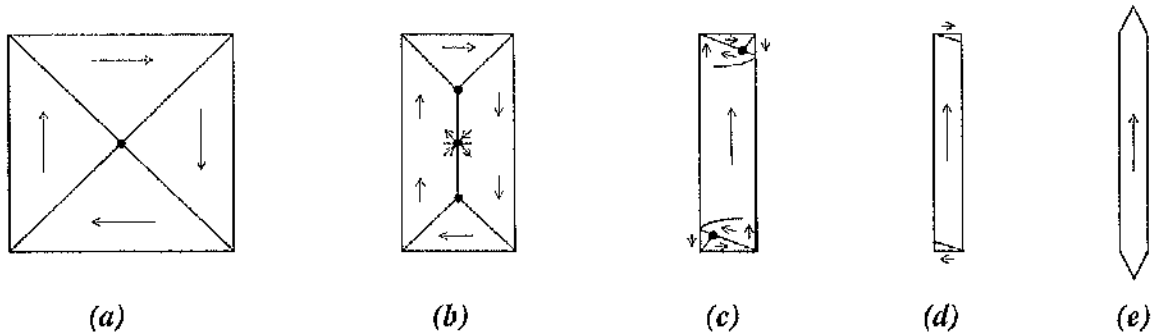


**Figure 1.5**

*Schematics of favourable domain configurations of small magnetic thin film elements. (a), (b) Flux closure structures, (c), (d) end domains, (e) single domain state.*

Squares and rectangles of certain dimensions are known to support flux closure structures (Figs. 1.5(a), (b)). Such configurations result in a minimum for  $E_s$  on the expense of  $E_{ex}$ . More elongated rectangles (Figs. 1.5(c), (d)) clearly possess a net magnetisation parallel to the element length whilst end domains form in order to reduce magnetic charge at the element ends. This domain configuration is near to an absolute minimum of  $E_{ex}$  but it is not favourable in terms of  $E_s$ . The situation differs again for double pointed elements (Fig. 1.5(e)) where end domains are suppressed and the element is in a single domain state. Therefore the system is at the absolute minimum for  $E_{ex}$  whilst  $E_s$  is maximised.

It should be noted that due to the finite lateral dimensions (micron and sub-micron range) of small magnetic elements the demagnetising factor out of the sample plane  $N_z$  is slightly  $<1$  even for thin films (thickness 20-30nm). As the dimensions are of suitable magnitude and proportion one can work out that the demagnetising factor  $N_z$  for the inscribed ellipsoid is  $\approx 0.99$  by means of eqns. (1.10a), (1.10b). Despite this value being that close to one it does reduce the confining effect of the magnetisation direction in the sample plane. The magnetisation direction depends on the cosine of  $N$  and this means that the magnetisation can easily be tilted a few degrees out of the sample plane in the case of small magnetic elements as discussed in this work. This should be taken into account when carrying out magnetising experiments in the way described in section 2.2.5 (magnetic fields applied orthogonal to the sample plane).

## 1.6 MULTILAYER STRUCTURES - GMR

The great interest in magnetic multilayer systems originated with the discovery of the so-called giant magnetoresistance (GMR) effect arising from the exchange coupling between successive magnetic layers separated by non-magnetic spacer layers. Generally magnetoresistance (MR) is the change in electrical resistance of a material in the presence of an external magnetic field. This property can be utilised as a magnetic field sensor in various devices such as magnetic read heads or electrical compasses. Commonly one distinguishes between anisotropic (AMR), the above mentioned giant (GMR) and colossal magnetoresistance (CMR) which is found in mixed valence manganese oxides (Ramirez, 1997). The former two MR effects are described in the following sections.

### **Anisotropic Magnetoresistance**

AMR was discovered by Thomson (1851) and arises upon the application of an external field to a ferromagnetic body. The underlying mechanism is the following: In the absence of an applied field the conduction electrons within a ferromagnetic body experience a Lorentz deflection which is proportional to the component of magnetisation, orthogonal to the electron motion. When the direction of current is orthogonal to the average direction of magnetisation, the Lorentz deflection is a maximum and, in the case of a thin film, this leads to strong electronic scattering from the film surfaces. Upon the application of an external field, which is non-parallel to the magnetic vector, the magnetisation rotates towards the field direction. Consequently there is a decrease in the component of magnetisation orthogonal to the electron path and the Lorentz deflection is lowered. This results in a cosine squared dependence for the AMR amplitude for fields applied orthogonal to the zero field direction of magnetisation.

### **Giant Magnetoresistance**

GMR was reported for the first time in 1988 by Baibich et al for a Fe/Cr multilayer superlattice. The investigated sample was grown by molecular beam epitaxy (MBE) and it was found that at  $T=4.2\text{K}$  the resistance was lowered by almost a factor of 2 upon the application of a 2T magnetic field. The origin of GMR was correctly suggested by the authors to be due to spin-dependent scattering of conduction electrons, predominantly at the interfaces of the multilayer. Upon variation of the thickness of the Cr layer, oscillations in the coupling constant between the adjacent layers were observed. This effect was

interpreted as a change from ferromagnetic (FM) to antiferromagnetic (AF) exchange coupling between the magnetic Fe layers depending on the Cr layer thickness.

The same effects have later been observed for a variety of sputtered multilayer systems (Parkin et al, 1990), (Grünberg et al, 1991) with one of the most common ones being Co/Cu multilayers. The oscillatory dependence of the GMR on the thickness of the non-magnetic spacer layer is shown in Fig. 1.6 for layer systems with a constant Co thickness of 10 Å. The measurements were taken at room temperature with the current in plane (CIP) and the experiments were carried out at the University of Leeds using the standard four probe method (Marrows et al, 1999). The trend of a theoretical curve (dashed line) is included in the diagram.

It is important to specify whether the direction of the current is in the plane of the layers (current in plane (CIP)) or perpendicular to the layers (current perpendicular to plane (CPP)) when quoting magnetoresistance values for GMR multilayer materials. In general CPP geometries give rise to a larger change in resistance since the current is directed across the interfaces rather than along the layers. It should be noted though that in CPP the total resistance of the multilayer is very low (typically  $10^{-8}\Omega$  for a  $1\text{mm}^2$  multilayer). This is a considerable drawback for the application of the CPP geometry as the contact leads commonly have a much higher resistance than the sensor itself and therefore swamp the effect.

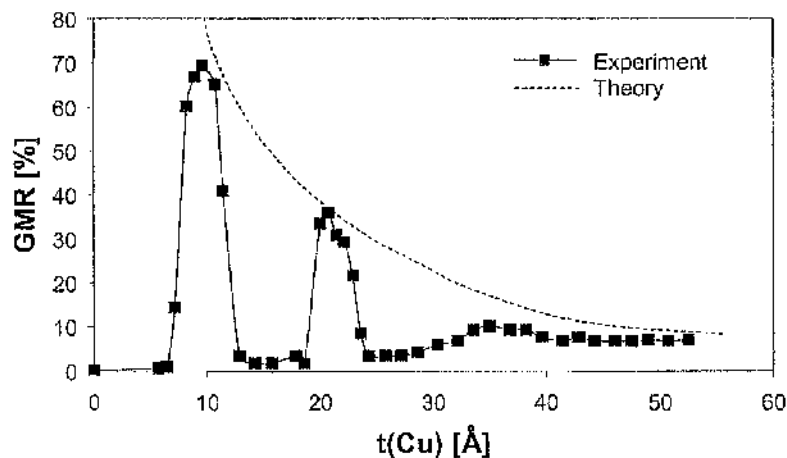


**Figure 1.6**

*GMR as a function of the Cu layer thickness.*

*Data set from C. Marrows; Co layer thickness constant 10Å, GMR measured at room temperature.*

Despite many efforts to determine the reason for the marked variation of resistance with variation of the external field, theoretical physicists are still working on a universal theory to describe different GMR varieties. Some theoretical explanations, however, are already generally accepted:

If the spacer layer thickness does not exceed the 'spin conserving' mean free path of the electrons, an additional spin dependent scattering mechanism can occur. Depending on the magnitude of other electrical scattering processes this spin dependent scattering may have a considerable influence on the total resistance of such systems. Spin dependent scattering can take place at interfaces as well as within the magnetic layers. The main points are summarised in a phenomenological model:

Exchange interaction in a ferromagnet results in a spin dependent band shift dividing the electrons into two 'groups' (Fig. 1.7). One group are the majority electrons (in the fully occupied d-band, black in Fig. 1.7) and the second group are the minority electrons (red in Fig. 1.7 in the d-band with unoccupied states).

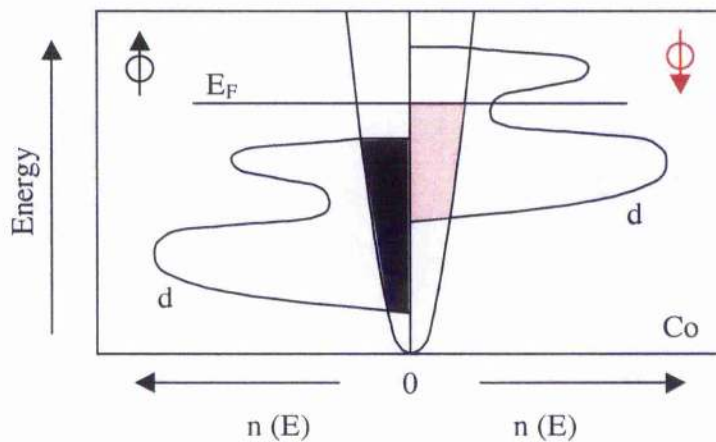


**Figure 1.7**

*Schematic of densities of states for a typical band ferromagnet (here Co).*

⬆ Majority electrons, ⬇ minority electrons;  $n(E)$ : density of states;  
*d*: d-band,  $E_F$ : Fermi level.

Figure 1.8 shows schematics of the scattering behaviour of electrons with different spin for FM (Fig. 1.8(a)) and AF (Fig. 1.8(b)) alignment of the magnetisation in a Co/Cu multilayer together with the corresponding circuit diagrams. In the case of a multilayer system the spin of the majority electrons corresponds to the magnetisation direction in the ferromagnetic layers. As a result of the different densities of states at the Fermi level the

scattering probability is higher for minority electrons than for majority electrons (Smits, 1992). This means that for parallel (FM) alignment in the multilayer stack, the main carriers are the majority electrons and the resulting total resistance of the layer system is low. For antiparallel (AF) alignment, however, the scattering probability is high for both groups of electrons therefore resulting in an increase of total resistance.

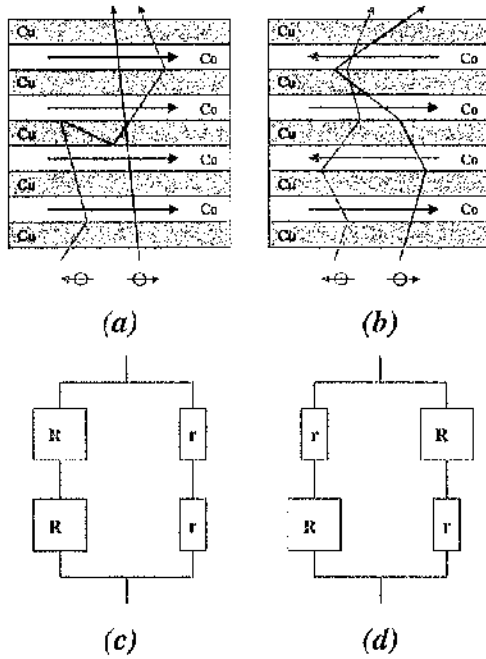


**Figure 1.8**

*Schematics of spin dependent electron transport in Co/Cu multilayers for (a) FM (b) AF alignment.*

*Corresponding circuit diagrams for (c) FM alignment: high and low resistance branches, (d) AF alignment: similar resistance in both branches.*

**CHAPTER 2:****INVESTIGATION OF MAGNETIC MICROSTRUCTURE****2.1 INTRODUCTION**

In this chapter various techniques are described on how to image magnetic domains. Particular emphasis will be paid to Lorentz electron microscopy because this is the main investigation method applied to collect data for this work. At the end of this chapter, there is a brief discussion about Kerr microscopy as the magneto-optic Kerr effect (MOKE) was used for magnetic measurements at the University of Leeds. It was, however, not the aim to visualise the domain configuration of the investigated Co/Cu multi-layers this way.

The simplest technique for imaging magnetic domains was first demonstrated by Bitter (1931) and involved coating the magnetic material with a colloidal suspension of fine ferromagnetic particles. Due to the stray magnetic field emanating from domain walls the particles accumulated at domain boundaries and thus revealed information about the magnetic state at the surface of the sample. This technique has relatively low resolution (only a few  $\mu\text{m}$ ) and does not yield further information about either the wall structures or the direction of magnetisation within the domains.

A further method to obtain information about the magnetic microstructure of a specimen is photoemission electron microscopy (PEEM). PEEM utilises the phenomenon of magnetic dichroism: The absorption coefficient and therefore the number of emitted photoelectrons depends on the polarisation of the incident light and the magnetisation direction within the sample. High energetic light (a laboratory ultraviolet lamp or synchrotron radiation) is used to generate photoelectrons via photoemission and an electrostatic lens system images the emitted electrons. Such a set-up was developed already in 1933. Nowadays PEEM is becoming an important mesoscopic imaging technique for surface physics and chemistry as well as biology (Swiech et al, 1997). With the easier access to synchrotron radiation sources which are much better suited as illumination source than UV lamps, PEEM is developing into a versatile analytical tool in surface and materials science (Kortright et al, 1999).

Another approach to visualise the magnetic microstructure of sample surfaces is magnetic force microscopy (MFM) (Hubert et al, 1998). The first MFM images were obtained by Martin et al (1987) from a magnetic recording head with the instrument operated in static mode. The MFM offers nowadays a resolution in the sub-100nm range

without the need of sample preparation (Dahlberg et al, 1999). MFM images are formed by detecting the interaction between the magnetisation of the tip and the magnetic stray field emanating from the sample respectively the interaction between the magnetisation of the sample and the MFM tip stray field. The resulting force is the negative gradient of the

interaction energy  $\vec{F}(\vec{r}) = -grad E_{inter}(\vec{r})$  with  $E_{inter} = -\int_{tip} \vec{M}_{tip} \cdot \vec{H}_{sample} dV$  respectively

$E_{inter} = -\int_{sample} \vec{M}_{sample} \cdot \vec{H}_{tip} dV$ . Thus the obtained images are highly dependent on the

magnetic characteristics of the tip. In order to extract quantitative data from MFM images the magnetic structure of the tip needs to be known and stable. The most significant effects of the magnetostatic interaction between the tip and the specimen's stray field are depending on the operating mode: (i) Deflection of the cantilever by the magnetic force according to Hooke's law or (ii) change of the resonance frequency of the oscillating cantilever due to the force gradient.

In a transmission electron microscope the Lorentz deflection of an electron beam caused by a magnetic specimen may be utilised in order to image the sample's magnetic microstructure. This was first achieved by Hale et al (1959) and has since spurred the development of a variety of imaging modes. As several modes of so-called Lorentz microscopy have been used extensively to study the magnetic configuration of thin film samples, a detailed review is given dealing with the requirements (instrumentation) in section 2.2 prior to the description of the different imaging modes of Lorentz microscopy in section 2.3.

## 2.2 TRANSMISSION ELECTRON MICROSCOPY - TEM

The physical and magnetic microstructure of thin film samples was investigated for this work using two transmission electron microscopes (TEMs). The machines were modified in order to optimise magnetic imaging conditions. The first microscope was based on a JEOL 2000 FX (Tsuno et al, 1984), (Hefferman et al, 1991) and the second one was a modified Philips CM20 FEG microscope (Chapman et al, 1994). Both instruments enable the experimenter to observe the magnetic microstructure of samples in a field free environment (section 2.2.2) but additionally possess in-situ magnetising capabilities (section 2.2.5).

### 2.2.1 ELECTRON GUN

The above mentioned microscopes had different types of electron guns. Whilst the JEOL microscope possessed a thermionic cathode (i.e. tungsten hairpin with  $\approx 0.1-0.2\text{mm}$  diameter of wire) the Philips microscope was equipped with a field emission gun (FEG).

Thermionic guns consist of three electrodes (triode structure). The first electrode is the heated filament which forms the cathode at a potential  $-U$ . In the case of tungsten the cathode is directly heated as the electrical resistivity is low enough. The second electrode is the Wehnelt electrode with a potential even more negative than the cathode and the third electrode is the earthed anode. The minimum diameter of the (first) crossover is limited by the lens like effect of the electric field in front of the cathode and the radial components of the electron exit momenta. Due to the Maxwell distribution of exit velocities the radial distribution of the current density in the crossover possesses an approximately Gaussian shape.

A field emission gun consists of an even more pointed cathode tip which is held at a potential  $-U$  and at least two anodes ( $U_1 < U_2$ ). A tungsten wire of  $\approx 0.1\text{mm}$  diameter is spotwelded on a tungsten hairpin cathode before being etched to a radius of curvature of  $\approx 0.1\mu\text{m}$  (Reimer, 1997). The resulting electric field strength at the tip is high enough not to depend on (excessive) heating to emit electrons. Instead emission occurs by means of quantum mechanical tunnelling. The first anode is called the extraction anode and generates a field  $|\vec{E}| \equiv \frac{U_1}{r}$  at the filament tip. The electrons are then accelerated further to their final energy  $E = eU$  by the voltage  $U$  between the filament tip and the second anode (earthed). Ultrahigh vacuum (pressure  $\leq 5 \times 10^{-7}\text{Pa}$ ) needs to be maintained in order to avoid damage of the tip due to ion bombardment as the field emission current depends not only on the work function but also on  $|\vec{E}|$ . A focused electron probe (first crossover) with a diameter of  $\approx 10\text{nm}$  is formed as an image as the anodes act as an electrostatic lens.

Compared to thermionic guns, field emission guns have the advantage of higher brightness and considerably less energy spread. These parameters are of interest for all work that requires high coherence and high current densities, e.g. high resolution phase contrast, electron beam holography, scanning transmission electron microscopy (STEM)

and last but not least Lorentz microscopy. The acceleration voltage of both microscopes was  $U=200\text{kV}$  corresponding to an electron wavelength  $\lambda = 2.5 \cdot 10^{-12} \text{ m}$ .

### 2.2.2 MICROSCOPE COLUMN

The microscope column encapsulates the path of the electron beam from the gun to the viewing screen. In contrast to the gun region a higher pressure of  $\approx 10^{-6}\text{-}10^{-5}\text{Pa}$  can be tolerated in the column. The basic principle is the same as in every cathode ray tube: Several electromagnetic lenses (coils) are mounted along the electron path and interact with the beam electrons. A schematic of the column of the modified Philips CM20 FEG microscope is given in Fig. 2.1.

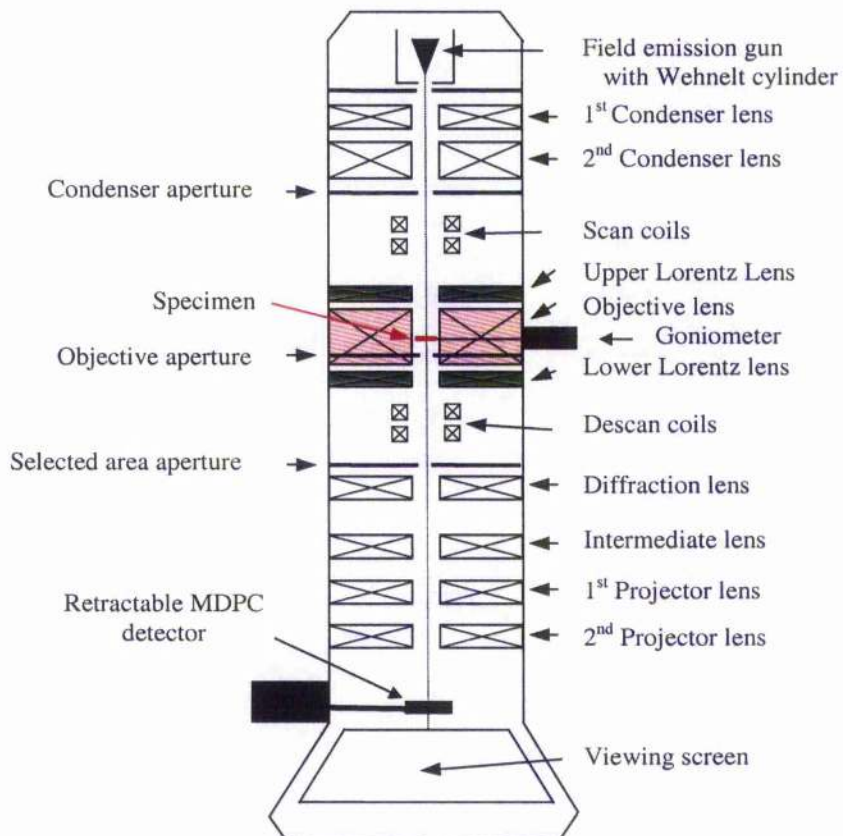


**Figure 2.1**

*Schematic of the Philips CM20 FEG transmission electron microscope.*

The electron source is the field emitting gun on top of the column. The emitted electrons are firstly focused following the trajectories of the  $\vec{E}$ -field surrounding the tip

and successively in the anode system (Wehnelt cylinder). This crossover is then demagnified by the 1<sup>st</sup> condenser lens in order to approximate a point source (virtual electron source). This virtual source lies in the focal plane of the 2<sup>nd</sup> condenser lens and the beam is therefore in good approximation parallel after passing through this lens. The quality of beam parallelism is enhanced further by means of the condenser aperture as divergent beam parts are masked. The described procedures are important alignment steps as they result in the best possible approximation of ideal imaging conditions (i.e. point source, parallel beam, coherence).

The scan and descan coils are used in scanning mode of the microscope. The first set of coils scan the electron probe across the specimen and the second set (descan coils) is necessary to align the scanning signal with the detector.

The Lorentz lenses (green in Fig 2.1) and the standard objective lens (red in Fig 2.1) in the CM20 are described best together as the objective lens system. An objective lens focuses the electron beam to produce a diffraction pattern in its back-focal plane. As in optical microscopy it is aberrations within the objective lens which determine the final resolution of the microscope. The commonly used immersion lenses produce a high magnetic field orthogonal to the sample plane. Usually this vertical field does not cause any problems in terms of interaction with the specimen as many samples are non-magnetic or one is not interested in the magnetic information of the sample (e.g. bright field imaging, electron diffraction, high resolution (Reimer, 1997)). In our case, however, with the observation of the magnetic microstructure and the investigation of the behaviour of the sample under the influence of well-defined magnetic fields being the main aims, the common field values for standard objective lenses (0.5-1.0T) are not tolerable. Precautions are necessary not to expose the samples to unwanted magnetic fields which would perturb, falsify or swamp the micromagnetic characteristics of the specimens. A possible solution is to leave the objective lens unexcited and use the diffraction lenses in order to form the image. The problem with this approach is that one is limited to low resolution studies. In order to image magnetic structures with a reasonably high resolution it is necessary to physically modify the objective lens.

In the case of the Philips CM20 FEG microscope the problem is solved by the incorporation of additional lenses (green in Fig. 2.1) above and below the standard objective lens (red in Fig. 2.1). The additional lenses are referred to as the upper and lower Lorentz lenses and can be used instead of the objective lens in order to achieve field free magnetic imaging with a point resolution of 2.1nm and a line resolution of 1.0nm for in-

focus imaging techniques. In the JEOL 2000 FX the sample is kept in field free space by replacing the original objective lens with a split pole-piece lens creating a field free specimen area (Tsuno et al, 1983).

All lenses below the selected area aperture simply magnify the image and the diffraction pattern of the sample as appropriate and the result can be monitored on the viewing screen.

There are several apertures in the column which often range in diameter from 10-500 $\mu\text{m}$ . The first aperture in the column is the condenser aperture. As already mentioned it defines the diameter of the electron probe and since it is at the top of the column it is crucial that it is aligned with the optical axis of the microscope. The next aperture is the so-called objective aperture, which is situated near the back focal plane of the objective lens. The main purpose of this aperture is to enhance diffraction contrast but it is also necessary to implement Foucault imaging (section 2.3.2). The final aperture is the selected area aperture, which allows diffraction patterns to be collected from specific areas of the sample.

### 2.2.3 ABERRATIONS IN A CTEM

As in light optics there are different kinds of lens aberrations also in the case of electromagnetic lenses. Amongst these there are spherical and chromatic aberration and astigmatism which are discussed in this section.

#### Spherical Aberration

The effect of spherical aberration is to reduce the focal length for electrons passing through outer zones of the lens. This means that electron rays which are not parallel to the optical axis will intersect the Gaussian image plane (image position for very small apertures) at certain distances from the paraxial image point (Reimer, 1997). Therefore a conical electron beam with angular aperture  $\alpha_c$  does not produce a sharp image point but a disc of confusion. Referred back to the specimen the beam possesses a minimum radius  $r_{s,\min}$  given by

$$r_{s,\min} = C_s \alpha_c^3 \quad (2.1)$$

with  $C_s$  being the spherical aberration coefficient. Eqn. (2.1) shows the importance of a parallel beam as the angular aperture governs the resulting diameter of the disc of least confusion. Typical values for  $C_s$  of standard objective lenses are of the order of 0.5-2mm. It should be noted that the  $C_s$  of Lorentz lenses lies in the range of some centimeters up to a few meters due to the higher focal length of those lenses.

### Chromatic Aberration

The term chromatic aberration summarises the adverse effects of energy spread of the electrons and fluctuations of the acceleration voltage as well as lens current instabilities on the imaging quality. Whilst lens current fluctuations lead to variations of the focal length of the affected lens, electrons of different energy have different focal lengths even for a perfect lens. Generally electrons with lower energy are focused more easily (i.e. are stronger deflected). For a thick lens the radius of the disc of least confusion in the object plane is

$$r_{c,\min} = C_c \alpha_a \frac{\Delta E}{E} \quad (2.2)$$

where  $\Delta E$  is the energy dispersion and  $C_c$  is the chromatic aberration coefficient which is usually slightly less than the focal length  $f$  of the lens (Reimer, 1997).

### Astigmatism

Astigmatism will be observed if the lens field is not exactly rotationally symmetric (Fig. 2.2). Due to the different focal lengths in the two lens axes object point P is imaged in a vertical and a horizontal line ( $P_v' P_h'$ ). The disc of least confusion is located between the two lines. Reasons for such asymmetries are inhomogeneities of the pole pieces, ellipticity of the pole piece bores or electric charging of apertures. In effect these inhomogeneities lead to different focal lengths for paraxial rays. Fortunately astigmatism can easily be compensated in electron optics by means of so-called stigmators. Such a stigmator system consists of two quadrupole lenses which are mounted with a relative rotation of  $45^\circ$  around the optical axis (Reimer, 1997).

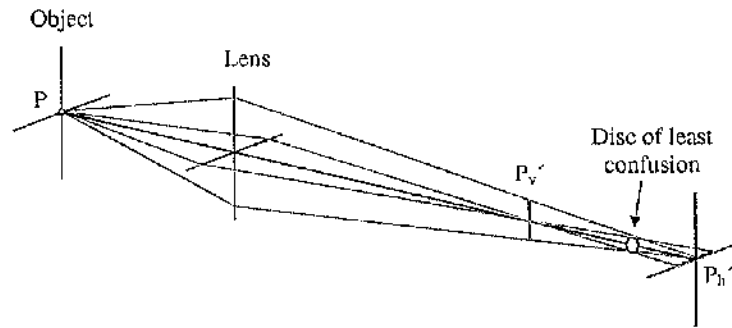


**Figure 2.2**  
*Astigmatism.*

### 2.2.4 IMAGE RECORDING

Micrographs can be recorded on photographic plates, a video camera or by means of a slow scan CCD camera. For this work a CCD camera and two types of photographic film (CEA Reflex-15 and at a later stage Kodak DEF-5 as the other film was no longer available) were used. A major drawback associated with the films is that time consuming processes are involved: The preparation of the material (cut, degas) as well as the development of the negatives and the production of hard copies (either prints or scanning of the negatives). All these disadvantages can be overcome by using the CCD camera and it also offers further advantages as for example real time observations and comfortable digital processing of the images/results. The camera used for this work was a Gatan slow scan CCD camera. A schematic of a CCD chip is shown in Fig. 2.3.

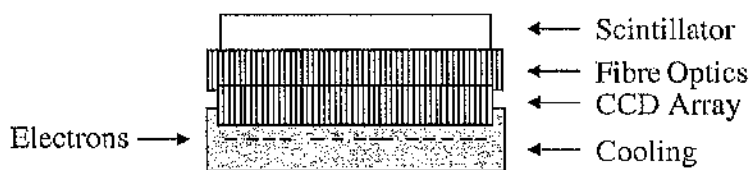


**Figure 2.3**  
*Schematic of CCD chip.*

CCD sensors consist of arrays of silicon-based photodiodes that define the picture elements (pixels). The CCD cannot be irradiated directly with the electrons owing to the generation of defects which would result in a long-time fading of the sensitivity and also because of limited number of recordable electrons per diode. Thus the electrons are converted to photons in a scintillator first which are then transferred through a fibre optical plate. The photons generate electron-hole pairs in the CCD array where they accumulate. By applying sequences of different biases to adjacent diodes the charges are transferred

into a serial shift register and the signal is read out. Cooling of the chip by means of a Peltier element decreases the background dark currents markedly with the result of considerable increase of the signal-to-noise-ratio.

### 2.2.5 MAGNETISING EXPERIMENTS

When investigating the micromagnetic state of samples by means of a TEM it is important to be able to carry out zero field observations (section 2.2.2). However, it is also desirable to carry out in-situ magnetising experiments in well-defined fields. At the University of Glasgow two methods are commonly used to generate magnetic fields at a specimen: (i) A custom made magnetising stage enables the experimenter to apply pure in-plane fields to a sample in the JEOL microscope whilst (ii) in the Philips microscope in-plane components of magnetisation are generated simply by exciting the standard objective lens and tilting the sample in this field (Fig. 2.4).

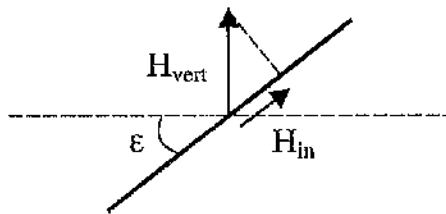


*Figure 2.4*

*Generation of in-plane components of magnetic field in the modified Philips CM20 FEG microscope.*

The in-plane component of the magnetic field can be calculated if the vertical field value  $H_{vert}$  and tilt angle  $\epsilon$  are known:

$$H_{in} = H_{vert} \cdot \sin \epsilon \quad (2.3)$$

The advantage of this method is that it is easy to implement and convenient to use as there are no beam deformations (astigmatism) or shifts associated with this technique. It should be noted though that significant out of plane components of magnetisation can be present at the sample. This is not expected to perturb the behaviour of continuous film samples, it might, however, alter details in the behaviour of small magnetic elements. This is due to the different demagnetising effects for these two groups of samples as discussed in sections 1.3.2 and 1.5. In order to rule out such uncertainties the use of magnetising stages as described by Hefferman et al (1991), Uhlig et al and Heumann et al (University

of Regensburg) is recommended. Apart from difficulties like realigning the electron path, another major disadvantage of such custom made magnetising stages is their limited field range, which especially for small magnetic elements is often not sufficient to saturate the specimens. An overview of the characteristic parameters for the above mentioned methods to generate defined fields in the sample area in a TEM is given in table 2.1.

field generation	constant field	pulsed field	possible directions	
	$H_{in, max}$ [Oe]	$H_{in, max}$ [Oe]	in-plane	out of plane
CM20; tilt sample	$\approx 6000$	no	optional	yes
JEOL magnetising stage	$\approx 125$	$\approx 800$	one	no
Regensburg magnetising stage	65	65 for $f \leq 16.5\text{kHz}$	optional	no

**Table 2.1**

*Comparison of different methods of magnetic field generation in a TEM.*

### 2.3 OBSERVATION OF MAGNETIC DOMAINS BY MEANS OF ELECTRON MICROSCOPY

In this section a number of methods are described to image the magnetic domain structure of thin film samples making use of the interaction between transmitted electrons and a magnetic specimen.

#### 2.3.1 ELECTRON BEAM AND SPECIMEN INTERACTION

##### Lorentz deflection - classical approach

Passing through a magnetic sample, electrons with velocity  $\vec{v}$  interact with the magnetic induction  $\vec{B}$  of the specimen due to the Lorentz force  $\vec{F}_L$

$$\vec{F}_L = -e (\vec{v} \times \vec{B}) \quad (2.4)$$

where  $e$  is the elementary charge. The result of such an interaction is the Lorentz deflection  $\beta_L$ , which can be calculated according to Reimer, 1997 by means of

$$\beta_L = \sqrt{\frac{e}{2m_e}} \frac{4 \pi B_{\perp} t_{mm}}{\sqrt{U \left(1 + \frac{eU}{2m_e c^2}\right)}} \quad (2.5)$$

where  $m_e$  is the rest mass of an electron,  $B_{\perp}$  is the component of the magnetic induction vertical to the incident electron beam,  $t_{mm}$  is the thickness of the magnetic material,  $U$  is the acceleration voltage of the TEM and  $c$  is the speed of light in vacuum.

Alternatively  $\beta_L$  can be calculated for a parallel beam of electrons incident perpendicular to the plane of the film by means of

$$\beta_{L,x} = \frac{e\lambda}{h} \int_{-\infty}^{+\infty} B_y(x,z) dz \quad (2.6)$$

where  $\beta_{L,x}$  is the Lorentz deflection in x-direction,  $e$  is the electric charge of an electron,  $\lambda$  is the wavelength of the electrons,  $h$  is Planck's constant and  $B_y(x,z)$  is the y-component of magnetic induction at a point  $(x,z)$ . For a magnetic film with constant thickness  $t_{mm}$  and on condition that there is no stray field emanating from the film, eqn. (2.6) becomes

$$\beta_L = \frac{e \lambda B_{\perp} t_{mm}}{h} \quad (2.7)$$

where  $B_{\perp}$  is the component of the magnetic induction vertical to the incident electron beam.

Figure 2.5 shows a schematic of the beam deflection when electrons pass through a magnetic sample with three  $180^\circ$  domains.

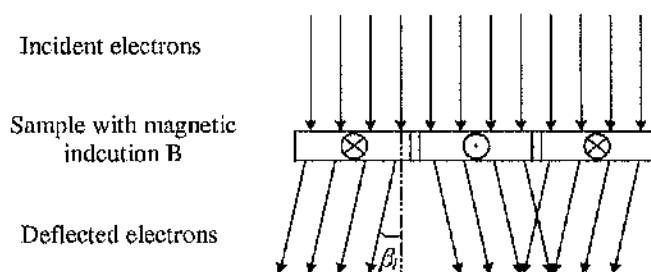


**Figure 2.5**  
Lorentz deflection –  
classical approach.

The incident electrons are deflected by an angle  $\beta_L$  due to the Lorentz force and the beam consists of convergent and divergent parts at the exit plane of the specimen.

With eqn. (2.6) it is clear, that the resulting Lorentz deflection is an integrative effect of the magnetic induction and the corresponding film thickness. This means that  $\beta_L$  not only scales with  $B$  but also with  $t_{nm}$ . Different results of Lorentz deflection due to different samples and magnetic microstructure are illustrated in Fig. 2.6. It should be noted that the Lorentz deflection in magnetic material is drawn in linear approximation in the figure despite the actual trajectory being circular.

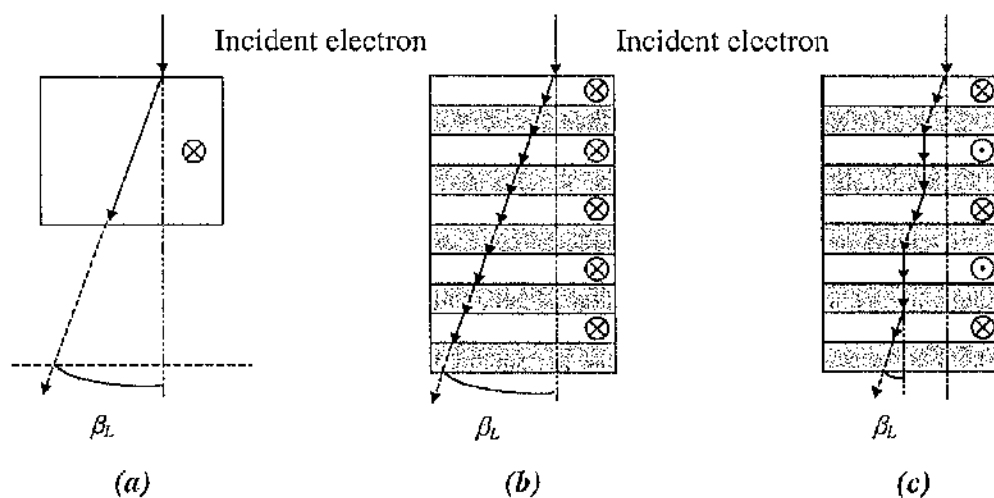


**Figure 2.6**

Lorentz deflection  $\beta_L$  in (a) a single layer sample, (b) a multilayer system with parallel alignment of  $\vec{M}$  in successive magnetic layers respectively (c) antiparallel alignment of  $\vec{M}$  in adjacent magnetic layers.  $\square$  Magnetic material  $\blacksquare$  non-magnetic material.

Incident electrons are deflected by  $\beta_L$  when passing through magnetic material and propagate without any further deflection (dashed arrows) while passing through non-magnetic material or free space. Therefore  $\beta_L$  of a multi-layer with ferromagnetic (FM) alignment of the magnetic layers is the same as for a single layer of the same magnetic material if the thickness of  $t_{nm}$  is identical for both cases. This is illustrated in Fig. 2.6 where the magnetic induction of the material is the same in the single layer (Fig. 2.6(a)) as in all magnetic layers of the multi-layer system (Fig. 2.6(b)). After identical distances (total thickness of multi-layer = thickness of single layer + distance through free space equal to thickness of non-magnetic material) the Lorentz deflection is identical for both

cases. The resulting  $\beta_L$  is however markedly reduced in the case of antiparallel alignment of the magnetisation in successive magnetic layers (i.e. antiferromagnetic (AF) coupling, Fig. 2.6(c)). In the case of perfect AF alignment and an even number of magnetic layers, the resulting Lorentz deflection  $\beta_L \equiv 0$ .

It should be noted that the deflection angle after passing through a soft magnetic thin film sample is very small (in the range  $10^{-6} - 10^{-5}$  rad). This is the reason why no contrast variation due to magnetic structure is detectable in the micrograph when the sample is imaged in focus. Examples of magnetic imaging techniques due to Lorentz deflection in a TEM are described in section 2.3.2.

### Aharonov and Bohm theory - quantum mechanical approach

In order to interpret TEM images correctly one needs to take into account the interactions between the beam electrons and the sample as well as the effects of the imaging system. In the following section a quantum mechanical approach will be used to explain the image formation in a TEM considering the wave properties of electrons. With respect to the effect on an incident normalised plane electron wave a specimen is characterised as an amplitude and/or a phase object. Pure amplitude objects merely alter the amplitude of the wave function whereas pure phase objects solely change the phase. The general description of the normalised wave function of the electron is

$$\Psi_{in} = e^{i(\vec{k} \cdot \vec{r} - \omega t)} \quad (2.8)$$

where  $\vec{k}$  is the wave vector,  $\vec{r}$  is the spatial vector,  $\omega$  is the angular frequency and  $t$  is time. The modulation which a wave  $\Psi_{in}$  suffers by passing through a specimen can be described by means of a 2-dimensional transmission function  $q(x, y)$  (Cowley, 1981). The wave vector  $\vec{k}$  is orthogonal to the  $x$ - $y$ -plane of the sample and the transmission function is given by

$$q(x, y) = e^{i\phi(x, y) - \mu(x, y)t_s} \quad (2.9)$$

where  $\phi(x, y)$  describes the local phase shift,  $\mu(x, y)$  is the local absorption coefficient and  $t_s$  is the thickness of the sample. The local absorption  $\mu(x, y)t_s$  results in a change

of the amplitude of  $\Psi_{in}$  whilst the local phase shift  $\phi(x, y)$  has the effect of a phase modulation. The exit wave  $\Psi_{out}$  of the electrons after passing through the sample is given by

$$\begin{aligned}\Psi_{out}(\vec{r}) &= \Psi_{in}(\vec{r}) \cdot q(x, y) \\ &= e^{i(\vec{k}\vec{r} - \omega t + \phi(x, y)) - \mu(x, y) t_s}\end{aligned}\quad (2.10)$$

If the imaging system transferring this exit wave in the image plane would be perfect, the detectable intensity  $I(x, y)$  would be

$$I(x, y) = |\Psi_{out}|^2 = e^{-2\mu(x, y) t_s}, \quad (2.11)$$

and variations of intensity ( $\equiv$ contrast) would only arise due to changes in the local absorption. As the absorption of specimens which are suitable for TEM is in most cases very low (very thin samples) and the fluctuation of the absorption within small sample areas is also negligible, most thin film samples can in good approximation be regarded as pure phase objects. The resulting transmission function is therefore given by

$$q(x, y) = e^{i\phi(x, y)}. \quad (2.12)$$

Aharonov and Bohm described in 1959 the quantum mechanical interaction between the beam electrons and a magnetic specimen: Electrons with the same start and end points which travel along different paths of equal length suffer a phase difference  $\phi$  which is proportional to the magnetic flux  $\Phi$  enclosed by the two paths (Fig. 2.7).

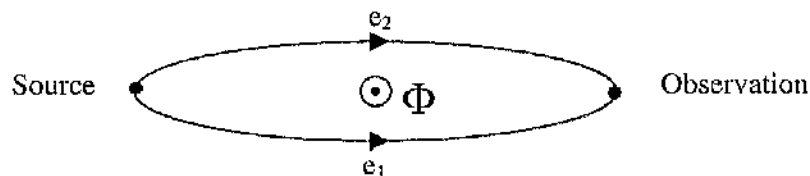


**Figure 2.7**

*Two electron paths of equal length enclosing the magnetic flux  $\Phi$  (Aharonov Bohm effect).*

This phase difference is given by

$$\phi = \frac{2\pi e \Phi}{h} \quad (2.13)$$

In the case of a plane incident wave on a magnetic thin film sample (as illustrated in Figs. 2.5 and 2.6) the phase shift between two points  $x_1$  and  $x_2$  is

$$\phi(\Delta x) = \frac{2\pi e t_{\text{film}}}{h} \int_{x_1}^{x_2} B_y(x) dx \quad (2.14)$$

It should be noted that this phase shift is very small, usually too small to generate contrast in the image. This problem can, however, be overcome by an 'additional' phase shift. This additional phase shift is realised simply by defocusing the image forming lens as illustrated in Fig. 2.8.

### 2.3.2 CONVENTIONAL TRANSMISSION ELECTRON MICROSCOPY MODES - CTEM

Three magnetic imaging modes of conventional transmission microscopy were applied in the course of this work. These were the so-called Fresnel and Foucault modes as well as low angle diffraction (LAD). A brief description of these techniques is given in the following sections. For further information see Chapman (1984) and Reimer (1997).

#### Fresnel Mode

The Fresnel mode of Lorentz microscopy is an out of focus imaging technique which shows domain wall locations as either black or white lines (wall contrast) within a grey background. Considering  $180^\circ$  domains as in Fig. 2.8(a) the magnetisation in such domains leads to a deflection of the electron beam either in positive or negative  $x$ -direction. This results in regions where the transmitted electron beam is either convergent or divergent at a certain distance below the specimen plane. Imaging such a plane by means of defocusing the image forming lens as appropriate ( $+\Delta f$ ), the locations of domain walls are visible as black and white lines within a grey background. If the electron beam is of sufficient coherence, interference effects will occur (Fig. 2.8(b)). Magnetic and electrostatic contrast in a Fresnel image is reversed when the virtual image ( $-\Delta f$ ) is viewed whilst absorption

contrast is the same in over- and underfocus. Magnetisation ripple also gives rise to contrast (fainter than wall contrast) in Fresnel images. As this ripple contrast is directional (i.e. orthogonal to the mean direction of magnetisation) it is possible to deduce the average direction of magnetisation from such image areas therefore allowing a qualitative assessment of domain structures.

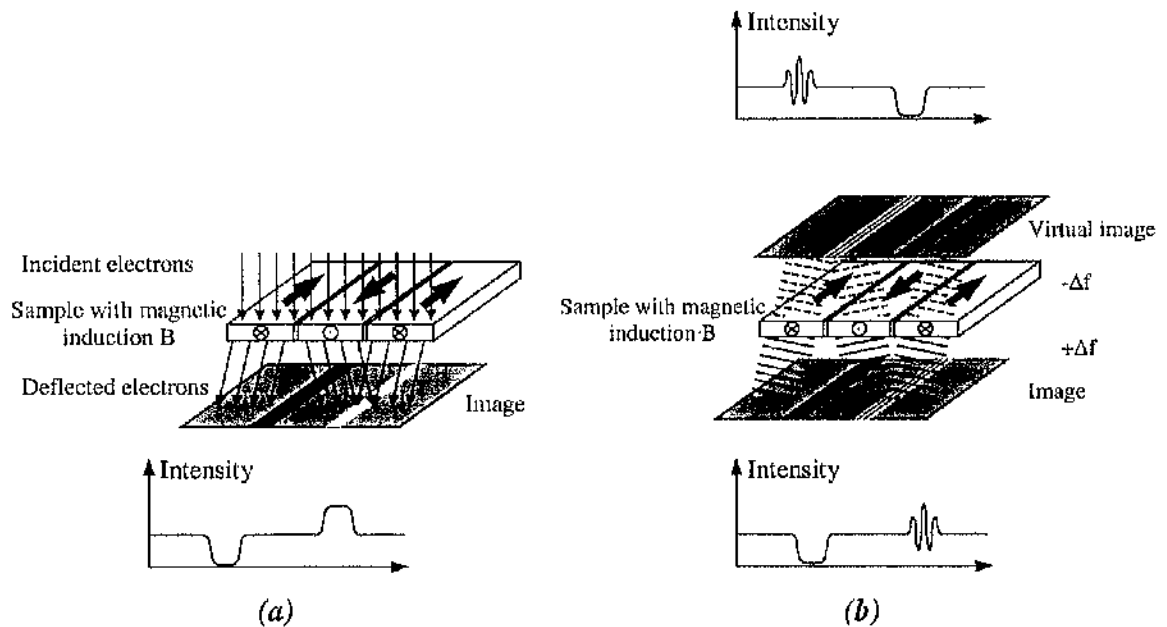


**Figure 2.8**

*Fresnel imaging.*

(a) Classical, (b) quantum mechanical approach.  $\Delta f$ : Defocus.

The principal advantages of the Fresnel mode are the ease with which it can be implemented, the high contrast which can arise at domain walls and the option of real time image recording. Therefore Fresnel imaging is very well suited for (qualitative) observation of dynamic processes. The main disadvantage is that it is an out of focus technique with the drawback of poor resolution and difficulties in relating magnetic structure with topographical contrast. As the transfer function is non-linear it is also difficult to deduce quantitative information from Fresnel images.

### Foucault Mode

Another magnetic imaging technique is the Foucault mode of Lorentz microscopy. In contrast to Fresnel imaging the Foucault mode is an in focus technique and the classical

theory of image formation is illustrated in the schematic in Fig. 2.9. The main principle of image formation in the Foucault mode is the fact that electrons passing through a certain domain (with  $\approx$ constant  $B$ ) are deflected by the same angle. Therefore all these electrons as well as electrons passing through domains with identical direction of magnetic induction are focused in the same point in the back focal plane of the image forming lens. Insertion of the objective aperture, which is situated near the back focal plane, in such a way to mask certain spots results in zero intensity for corresponding domains in the image (i.e. black areas).

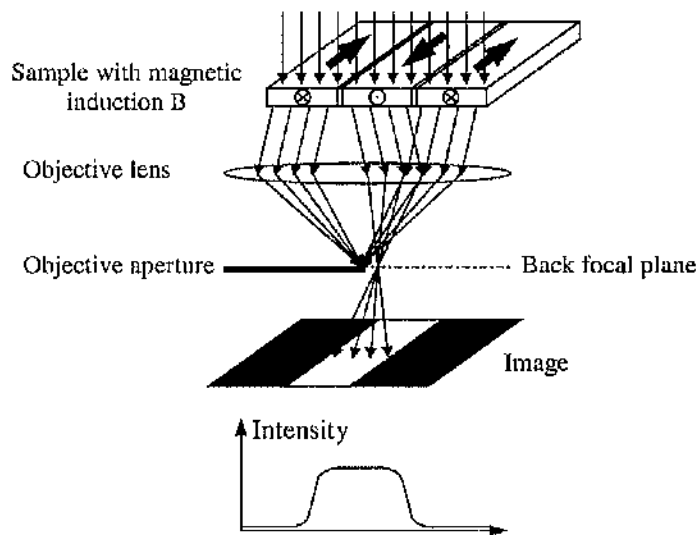


**Figure 2.9**

*Schematic of Foucault mode, classical approach.*

Foucault imaging gives rise to domain contrast and domains with magnetisation in opposite directions show up in the image as black respectively white areas on suitable imaging conditions. Intermediate grey levels belong to domains with magnetisation directions between these antiparallel directions. The positioning of the objective aperture can be set in order to 'map' in different directions and it is standard to always collect at least a pair of images, which have orthogonal mapping directions. Although this technique is relatively simple to implement and does not suffer from the same poor resolution which limits Fresnel imaging, the intensity variations which can be brought about by small movements in the positioning of the objective aperture make it ill-suited for quantitative studies. A further problem is that real time observations of dynamic processes can only be made for one mapping direction at a time.

### Low Angle Diffraction

As discussed in the previous section with respect to Foucault imaging, all electrons passing through a given domain are deflected by the same angle and thus are imaged in the same point near the back focal plane of the image forming lens. In the mode of low angle diffraction (LAD) the configuration of the post-specimen lenses are changed so that this plane is projected onto the viewing screen. This is of interest for magnetic studies when the central spot, which is unscattered by the crystal lattice, is considered. In a sample which contains several domains the central unscattered spot is split into several sub-spots. Each of these sub-spots corresponds to a different direction of magnetic induction in the sample. The intensity of the spots is indicative of the relative fractions of induction in the sample, which have a direction which lie perpendicular to a line which joins the spot with the position of an undeflected beam (Fig. 2.10).

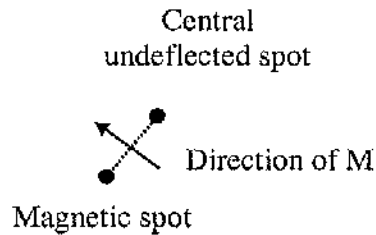


**Figure 2.10**

*Schematic illustration of a low angle diffraction (LAD) pattern.*

The difference between 'standard' and low angle diffraction is the option to choose very high camera lengths in LAD. For this work a camera length of 170m was set in the experiments with Co/Cu multilayers (section 8.5.3.2). Such quite enormous values are necessary in order to clearly image different spots instead of a conglomeration of hardly discernible spots due to the small Lorentz deflection angles (in the range  $10^{-6} - 10^{-5}$  rad compared to typical Bragg deflection angles which are of the order of  $\approx 10^{-2}$  rad). As only one image is necessary to 'image' the distribution of magnetisation directions of a sample within the field of view, real time observations of dynamic processes are possible. If the sample thickness is known quantitative conclusions can be drawn by means of eqn. (2.7) about the magnetic induction within the sample.

### 2.3.3 SCANNING TRANSMISSION ELECTRON MICROSCOPY MODES - STEM

The reciprocity theorem was discussed first by Helmholtz (1860) in light optics. In geometrical optics it is known as the reciprocity of ray diagrams. In wave optics, however, it also implies that the excitation of a wave at a point P by a wave from a source Q is the same as that detected at Q with the source P (Fig. 2.11), (Cowley, 1969, 1981), (Reimer, 1997). Therefore the ray diagram of STEM is the reciprocal of TEM.

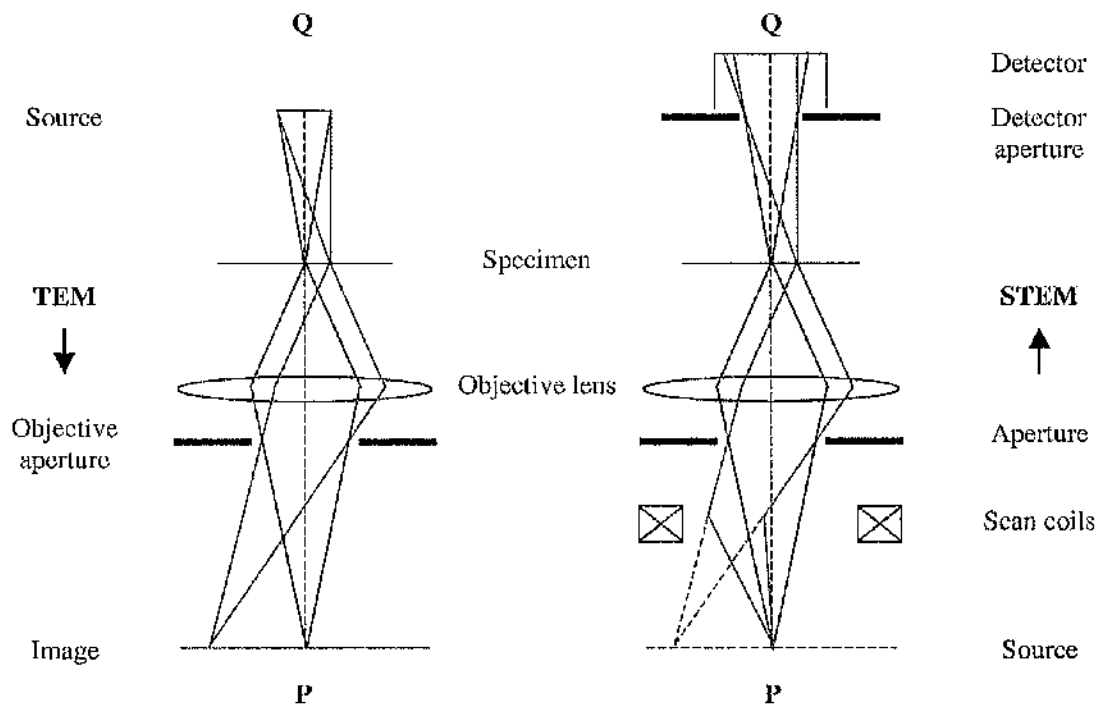


**Figure 2.11**

*Illustration of the theorem of reciprocity.*

Due to this theorem of reciprocity any imaging mode which can be performed on a CTEM can also be implemented on a Scanning Transmission Electron Microscope (STEM). Although it is often simpler to implement many of the standard magnetic imaging modes on a CTEM, the versatility of a STEM often allows modes which would be otherwise impractical. One of these is differential phase contrast (DPC). This technique, which was first suggested by Dekkers et al (1974) and further developed by Rose (1977), requires a configured detector split into quadrants and contrast is generated by taking the difference signal from opposite segments. The technique has been developed for studying magnetic materials predominantly by Chapman et al (1983), at the University of Glasgow.

### Image Formation

Image formation in a STEM differs markedly from that in a CTEM. In the former instrument a small, often coherent, probe of electrons is scanned in a regular raster across the specimen and some portion of the scattered or unscattered beam is detected (Fig. 2.12). In contrast to a CTEM the detected signal is collected sequentially and a digital image is constructed. The physical size of each sample point is usually defined by the probe size.

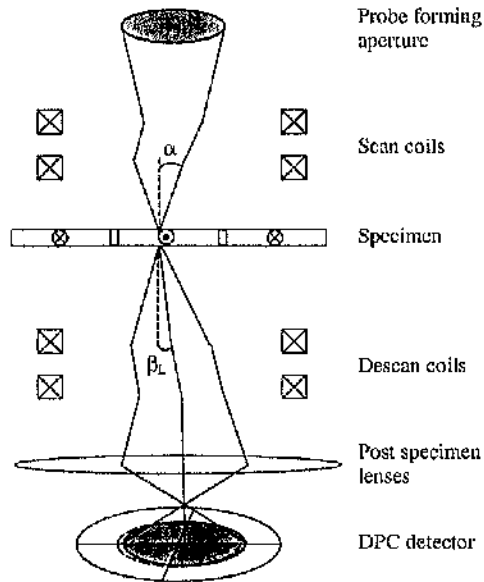


**Figure 2.12**

*Schematic of DPC imaging mode in a STEM.*

*$\alpha$ : Probe angle,  $\beta_L$ : Lorentz deflection angle.*

In the scanning mode of the Philips CM20 FEG, which was used exclusively for the acquisition of so-called (M)DPC images (next section) in this work, the illumination of the specimen is controlled by the two condenser lenses and depending on whether a field free specimen area is required, either the objective or upper Lorentz lens (Fig. 2.1). Although the upper Lorentz lens is the final pre-specimen lens and demagnifies the source onto the specimen it is not this lens which is varied to focus the probe. The reason for this is that focusing a lens (i.e. changing the excitation current of the lens) gives rise to thermal changes in the lens core which in turn results in a thermal drift. Since the upper Lorentz lens is situated immediately above the specimen even small thermal changes in the lens characteristic could result in notable blurring of the final image due to thermal drift. To limit this problem the upper Lorentz lens is set to a pre-determined value and in STEM it is the second condenser lens, which is considerably further away from the sample area, which is varied in order to focus the probe onto the specimen. The electron beam is rastered over the scan area by the scan coils and after passing through the sample descan coils

compensate for the raster motion (Figs. 2.1, 2.12) so that in the absence of a specimen there is no lateral beam movement. The beam is then finally projected onto the detector, which is situated in the far field with respect to the specimen.

Although this classical approach explains the image formation in scanning mode, a more rigorous quantum mechanical approach as given by Chapman (1984) is often required to explain the finer issues or to interpret images.

### Modified Differential Phase Contrast Imaging - MDPC

The detector which is fitted to the CM20 is a sensitive eight segment photodiode (Oxford Instruments) and is shown schematically in Fig. 2.13(b). This detector geometry allows the option of implementing Modified DPC (MDPC) which is discussed in the next section. Firstly, however, a general discussion of standard DPC is given.

### DPC

Standard DPC requires only a four segment detector (Fig. 2.13(a)) and allows two orthogonal maps of magnetic induction to be collected simultaneously. Each segment is a p-n junction in silicon separated by inactive strips  $\approx 200\mu\text{m}$  wide.

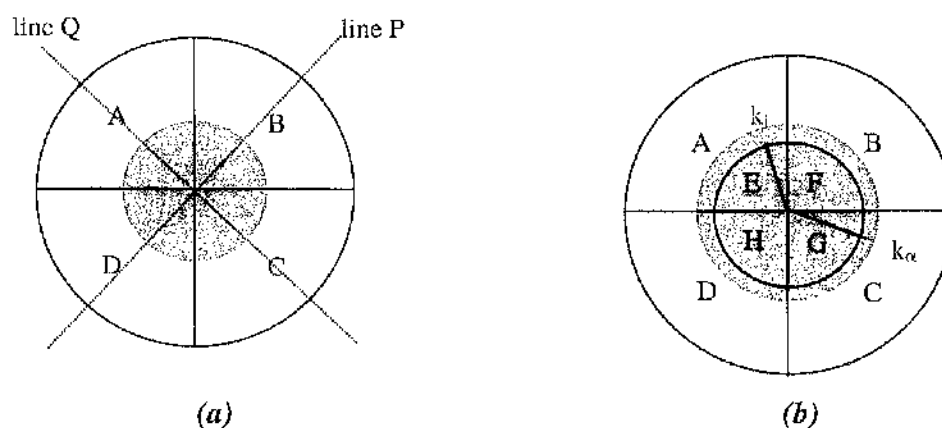


**Figure 2.13**

*Schematic of detector geometry. (a) Four segment detector with probe location (DPC).*

*(b) Eight segment detector with probe location (DPC and MDPC);  $k_\alpha$ : Maximum spatial frequency in the probe,  $k_i$ : largest spatial frequency component falling on inner segments.*

For alignment purposes the post-specimen lenses (Figs. 2.1, 2.12) are used to centre the electron beam on the detector in the absence of a specimen. Therefore equal amounts of electrons are falling on each of the segments and the difference signals, A-C and D-B,

are zero. If however a magnetic specimen is present, the beam is deflected by the Lorentz deflection angle  $\beta_l$  (Fig. 2.12) and the signals on each segment are no longer equal. Provided that the deflection is small compared to the probe angle, then the difference signal of A-C is proportional to the component of in-plane magnetic induction which lies along line P in Fig. 2.13(a). Similarly the D-B signal is proportional to the component of magnetic induction along line Q (Fig. 2.13(a)). The two difference signals provide maps of orthogonal components of magnetic induction, i.e. a complete quantitative description of the in-plane magnetic induction.

### MDPC

A serious problem in determining the magnetic microstructure by means of any mode of Lorentz microscopy is due to contributions of contrast of non-magnetic origin such as surface topography or from the crystallites which make up a polycrystalline thin film. In this case the expression for the phase gradient of the specimen must also consider the changes of the inner potential at crystallite boundaries as it can conceal the magnetic structure (Chapman et al, 1992). The spatial frequencies of the crystallites contributing to the image signal are generally much higher than those containing most of the magnetic information and this can be exploited to substantially alleviate the problem.

The solution adopted in modified differential phase contrast (MDPC) imaging involves replacing the four channel detector by an eight channel device as shown in Fig. 2.13(b). The images formed by taking the differences of currents falling on the outer detector segments (i.e. A-C and B-D) are referred to as MDPC images. Standard DPC images can also be obtained with the MDPC detector using the signal combinations (A+E)-(G+C) and (D+H)-(B+F). When imaging is intended with the eight segment detector, the excitation of the post specimen lens has to be adjusted in such a manner that the radius of the bright field disc is slightly larger than the radius of the inner annular detector (Fig. 2.13(b)). Thus the earlier mentioned problem that the spatial frequencies originating from crystallite boundaries can swamp the magnetic signal can be overcome: Adjusting the probe size in a way that  $k_i/k_\alpha \geq 0.8$  (Fig. 2.13(b)) leads to considerable damping of the phase gradient transfer function for high spatial frequencies and is therefore beneficial for the imaging conditions of magnetic structures (Chapman et al, 1991). Another advantage of the MDPC imaging mode is that through the removal of the contribution of the inner detector the signal-to-noise-ratio at low spatial frequencies is enhanced (Chapman et al,

1990). Thus, using the modified detector geometry results in considerable enhancement of the magnetic information of a sample whilst the unwanted contribution of the crystallite boundaries is markedly reduced.

## 2.4 OBSERVATION OF MAGNETIC DOMAINS

### UTILISING THE MAGNETO-OPTICAL KERR EFFECT (MOKE)

Two techniques of light microscopy are based on Faraday and Kerr magneto-optic (MO) effects (Chikazumi, 1964), (Hubert et al, 1998). Whilst the Kerr effect may be utilised on any metallic or otherwise light absorbing magnetic material with sufficiently smooth surface, the Faraday effect is restricted to transparent media. In both cases the rotation of the polarisation of plane polarised light upon interaction with the specimen is detected. Measurements based on the magneto-optical Kerr effect were carried out on Co/Cu multi-layers at the University of Leeds and some principles of the Kerr rotation are discussed next.

#### Magneto-optical Rotation

The rotation of the plane of polarisation of light can be explained in terms of the Lorentz force acting on light-excited electrons. Depending on the orientation of the polarisation plane of the incident light as well as the plane of incidence four cases of magneto-optical Kerr and Faraday effects are known. There are two geometries for the longitudinal effects (Figs. 2.14(a), (b)), a polar configuration (Fig. 2.14(c)) and the transversal arrangement (Fig. 2.14(d)). Generally the magneto-optical amplitudes can be understood as generated by the Lorentz motion  $v_L$ .

For the longitudinal effects, the magnetisation direction is parallel to the plane of incidence and parallel to the specimen surface. The light beam needs to be inclined relative to the surface and the effect scales with  $\sin \vartheta_0$ . In the case of perpendicular polarisation (with respect to the plane of incidence) as well as in the case of parallel polarisation, magneto-optical rotation is the result for the Kerr effect as well as for the Faraday effect. The sense of rotation is however opposite in the two cases (Figs. 2.14(a), (b)). For  $\vartheta_0 = 0$ , the Lorentz force either vanishes (longitudinal case) or points along the beam (perpendicular case). Thus no detectable radiation is generated.

In the case of the polar effects (Fig. 2.14(c)) the magnetisation is pointing normal to the sample surface and the effect is strongest for perpendicular incidence ( $\vartheta_0 = 0$ ). It should be noted, that the polar effects are largely independent of the direction of polarisation  $E$ .

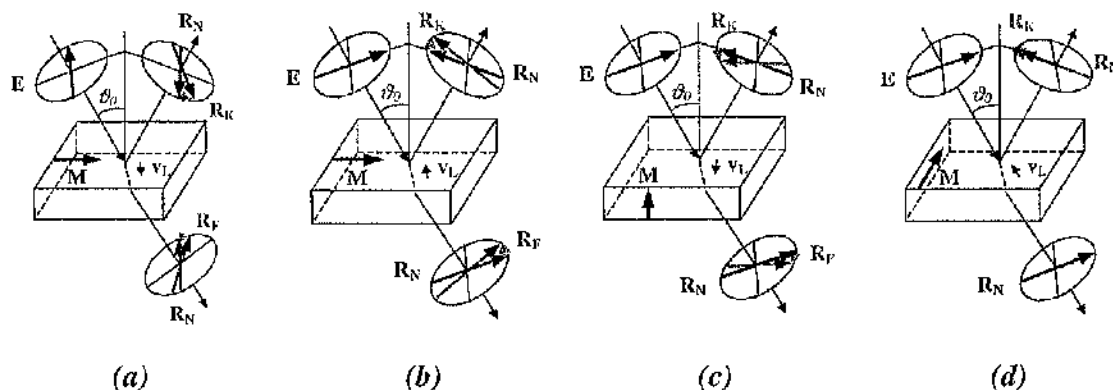


**Figure 2.14**

*Magneto-optical Kerr and Faraday effect.*

(a) Longitudinal  $\perp$ , (b) longitudinal  $\parallel$ , (c) polar, (d) transversal.

$\vartheta_0$ : angle of incident light,  $E$ : direction of polarisation of light,  $M$ : magnetisation direction,  $R_N$ : regularly reflected electric field amplitude,  $R_K$ ,  $R_F$ : magneto-optical amplitudes,  $v_L$ : Lorentz motion

For transverse orientation (Fig. 2.14(d)) where the magnetisation direction is perpendicular to the plane of incidence, no magneto-optical effect occurs in transmission. In reflection, however, a Kerr amplitude is generated for light of parallel polarisation since the reflected beam has a different direction. The effect scales again with  $\sin \vartheta_0$  and the polarisation is constant. The result is therefore a variation of the amplitude of the light which can be measured, but in terms of imaging of the domain structure the transverse effect is not very useful as it produces only little contrast. In order to generate a 'visible' rotation, the polarisation of the incident beam is chosen between the parallel and perpendicular orientation. Thus the perpendicular component is constant whilst the parallel component suffers an amplitude modulation with the result of a detectable polarisation rotation.

### Kerr Microscopy

In a Kerr microscope the light passes first through a polariser, setting the polarisation angle and is then reflected from the sample experiencing regular amplitude reflection  $R_N$  as well as Kerr amplitudes  $R_K$  according to the respective geometry (Fig. 2.14). Finally the light passes through an analyser leading to the total signal amplitude relative to the incident amplitude before the image is magnified. For two domains with opposite direction of magnetisation, the Kerr amplitudes only differ in sign. Aligning the analyser as appropriate, domain contrast becomes visible (Hubert et al, 1998).

The advantages of both Faraday and Kerr microscopy are that they are linear techniques and that in-situ magnetising experiments with large fields can be carried out (Rührig et al 1990), (Rave et al 1990), (Hubert et al 1998). Furthermore large areas can be observed and microscopic information can be imaged on the order of 150nm (Dahlberg et al, 1999). Magneto-optical techniques are well suited for observations of domains which are larger than 1 $\mu$ m.

**CHAPTER 3:****PREPARATION OF PATTERNED THIN FILMS - SMALL MAGNETIC ELEMENTS****3.1 INTRODUCTION**

This chapter deals with the procedures involved to prepare patterned thin film elements and a summary of first results of test patterns. An overview of the fabrication processes is given in sections 3.2-3.4, different types of edge structures of thin film elements are described in section 3.5 and the findings for the test patterns are discussed in section 3.6.

The in-plane dimensions of the small magnetic elements studied here lie in the micron and sub-micron range and are similar in size to state-of-the-art magnetic sensors (de Boeck et al, 1999), (Tondra et al, 1998), (Read-Rite, 1999), (IBM, 1999). Electron beam lithography in combination with lift off techniques was applied to create the patterned thin film elements. As the aim of this work is to assess the influence of structuring the edges of such elements, three different edge structure types were designed which were called types A, B and C (section 3.5). Detailed descriptions of the created test patterns are given in section 3.6.1. The physical microstructure of the elements, with emphasis on the quality of pattern transfer, is discussed in section 3.6.2 and the micromagnetic configurations of some elements are presented in section 3.6.3. It should be noted that no magnetising experiments have been carried out with the test patterns, only the as-grown and ac-demagnetised states have been investigated.

The film thickness of the samples studied in this work lies in the range 20-35nm which is suitable for TEM investigations. However electron transparent substrates were needed to investigate the small magnetic elements by means of TEM and this was realised by using  $\text{Si}_3\text{N}_4$  window substrates instead of standard silicon wafers. The fabrication of such  $\text{Si}_3\text{N}_4$  membranes was the starting point in sample preparation and is described in the following section.

**3.2 FABRICATION OF  $\text{Si}_3\text{N}_4$  MEMBRANES**

The  $\text{Si}_3\text{N}_4$  membranes were fabricated at the University of Glasgow with the membrane production being the first stage of sample preparation (Rührig et al, 1996),

(Khamsehpour et al, 1996). The starting substrate was a 3" (100) silicon wafer of a thickness  $\approx 400\mu\text{m}$  covered with amorphous silicon nitride layers of approximately 50nm on both surfaces. The thin films of  $\text{Si}_3\text{N}_4$  were deposited by low pressure chemical vapour deposition (CVD) at the Edinburgh Microfabrication Facility (University of Edinburgh). The silicon nitride was deposited at  $900^\circ\text{C}$  in a tube furnace, introducing Dichlorosilane ( $\text{SiCl}_2\text{H}_2$ ) and Ammonia gas ( $\text{NH}_3$ ) at a reduced pressure of 250mTorr in a volume ratio 1:4 to ensure complete reaction of  $\text{SiCl}_2\text{H}_2$  (Gundlach, 1999) The silicon wafers were obtained from commercial suppliers. The silicon was grown by means of the Czochralski technique in which polycrystalline silicon is melted in a heated crucible. After the desired initial temperature is reached, crystal growth is initiated by dipping a seed crystal in the melt and a cylindrical single crystal is then pulled vertically from the melt. The wafers were sawn from the cylindrical single crystal parallel to the (100) plane with an accuracy of  $1^\circ$  and the [110] direction of the wafers was marked by flats on the wafer edges. The surface roughness of the wafers due to sawing damage was reduced considerably by means of chemical etching/grinding of both surfaces. After this general polish one wafer surface was polished further applying a chemical/mechanical polishing process using a reactive slurry. Atomic force microscopy measurements, carried out at Edinburgh Microfabrication Facility, indicate an average roughness of this smooth and shiny wafer side in the range of approximately a few  $\text{\AA}$ . After deposition of the  $\text{Si}_3\text{N}_4$  layers the difference in roughness of both sides is still easy to discern as the smooth side is considerably more reflective. The smooth  $\text{Si}_3\text{N}_4$  surface is going to form the  $\text{Si}_3\text{N}_4$  window substrates and will be referred to as the top (sur)face. These  $\text{Si}_3\text{N}_4$  coated wafers were the raw material for the membrane fabrication process, which is described next.

Firstly both surfaces needed to be protected against damage. As the smooth top surface was going to be used as the substrate it was crucial not to damage (e.g. scratch) this surface and to maintain its integrity. Therefore the top surface was protected first and for this purpose photo resist (Shipley S1818) was spun onto the top side of the wafer with 4000rpm for 30s. The resist was then baked for 30min at  $90^\circ\text{C}$ . The resulting protective layer of resist had a thickness of  $1.8\mu\text{m}$  and the same procedure was applied for the bottom surface. Then the wafer was scribed in quarters parallel to the [110] direction using a diamond stylus. At this stage the actual fabrication of the membranes began and an overview of the procedures involved is given in figure 3.1.

Figure 3.1(a) illustrates the patterning process of the bottom face of the (quarter) wafers. Firstly the quarter wafers were cleaned three times for 2min each in the ultrasonic bath using acetone. Then they were rinsed three times also for 2min each in the ultrasonic bath firstly using opticlear, secondly acetone, thirdly methanol and finally RO (reverse osmosis) water before they were blown dry. After the cleaning process the top side of each quarter wafer was again protected with photo resist (Shipley S1805), which was spun onto the substrate with 4000rpm for 30s and baked for 20min at 90°C. Then S1805 resist was also spun with 4000rpm for 30s on the bottom face of the wafer and baked for 30min at 90°C. The thickness of the S1805 resist layers was 0.5 $\mu$ m and the quarter wafer was at this stage ready for the patterning of its bottom face. After aligning the mask BF395-9 $\times$ 9 (short

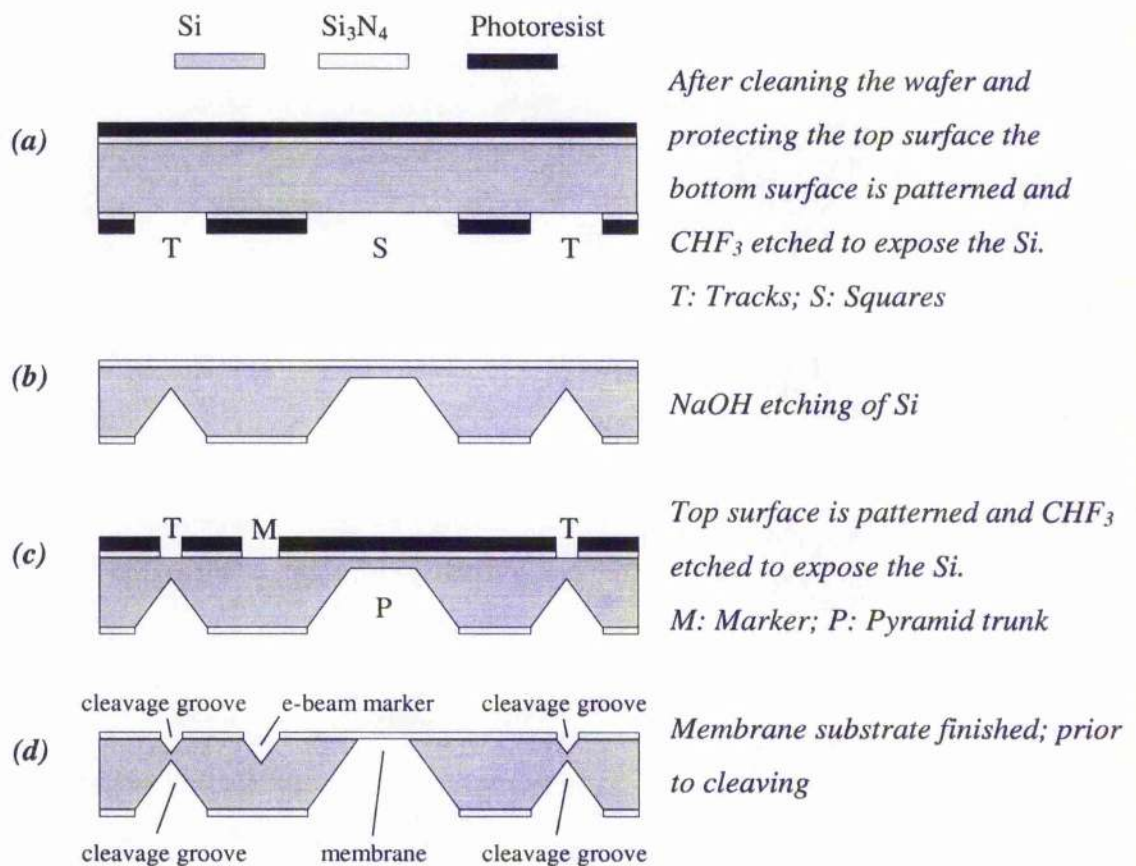


**Figure 3.1**

*Schematic overview of the steps of  $\text{Si}_3\text{N}_4$  membrane fabrication showing a cross sectional view of the wafer.*

for: mask for back face of wafers with  $395\mu\text{m}$  thickness for resulting  $9\times 9\text{mm}$  membrane arrays) with the [110] direction of the substrate by means of an UV mask aligner stage, the photo resist was exposed with UV light of a mercury lamp for 4s. The resist was sensitive to the 394nm wavelength of the mercury lamp. Next the photo resist was developed for 75s using Microposit Developer in a 1:1 mixture with RO water and then rinsed in RO water and blown dry before the quality of the pattern was checked with a light microscope. Then the patterned bottom side was  $\text{CHF}_3$  etched for 5min using the BP80 RIE (reactive ion etching) system. This dry etching process removed the  $\text{Si}_3\text{N}_4$  from the exposed areas of the pattern.

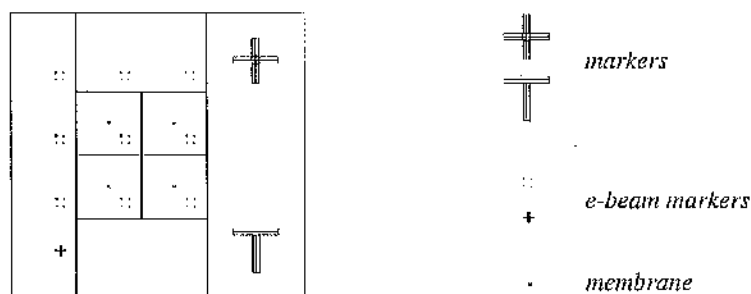
Figure 3.1(b) shows a schematic of the wafer after the next fabrication steps where the exposed silicon was wet etched in refluxed boiling sodium hydroxide solution (20% NaOH in RO water at  $112\pm 1^\circ\text{C}$ ) in order to create pyramid trunks at the membrane areas and cleavage grooves. The etch rate of this process is  $5.5\mu\text{m min}^{-1}$  for Si [100]. After 45min the wet etch was finished by rinsing the quarter wafer in RO water and blowing it dry. Now the etch depth needed to be checked using an optical microscope. The height difference from the bottom face of the wafer to the top of the pyramid trunk should be  $210\text{-}240\mu\text{m}$  at this stage. The wafer was then cleaned by rinsing it firstly in opticlear, secondly in acetone, thirdly in methanol and finally in RO water. Due to the cleavage grooves the quarter wafers were quite fragile and therefore could not be put in the ultrasonic bath.

Next (Fig. 3.1(c)) S1805 was spun on the top side of the wafer with 4000rpm for 30s and baked at  $90^\circ\text{C}$  for 30min and the top face was patterned with the mask TF395-9x9 (short for: mask for top face of wafers with  $395\mu\text{m}$  thickness for resulting  $9\times 9\text{mm}$  membrane arrays) using the UV mask aligner stage. The pattern of the mask needed to be carefully aligned with the etch pattern of the bottom face of the quarter wafers. For this purpose the substrate was not only illuminated with light from above but also with infrared light from underneath so that the pattern of the mask and the etched pattern were visible simultaneously and it was possible to match up both patterns. After the alignment the substrate was exposed with UV light for 4s. Then the resist was developed for 75s in a 1:1 mixture of Microposit Developer and RO water and the substrate was rinsed in RO water and finally blown dry.

Figure 3.1(d) shows a schematic of a finished membrane substrate after the top face of the substrate has been dry etched and the quarter wafer was wet etched for a second time.

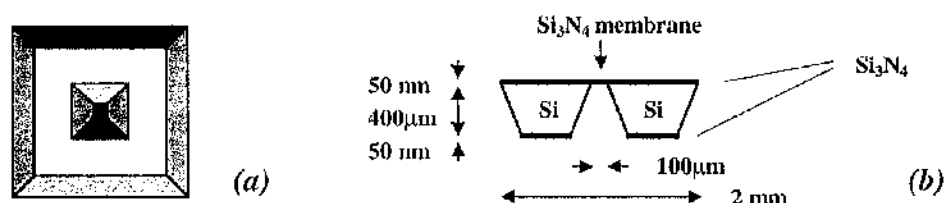
Apart from a reduced duration of the wet etch, the same conditions were applied for both processes as before. The wet etch was complete when the membranes were clearly visible from the front side. At this stage the substrate was very fragile and needed to be handled with great care when it was taken out of the NaOH solution and rinsed in RO water. The substrate was blown dry very gently in order to avoid breaking the thin  $\text{Si}_3\text{N}_4$  windows and finally the substrate was cleaved in arrays of  $2 \times 2$  membranes which were surrounded by a frame for easier handling. The dimensions of such an array were  $9 \times 9 \text{ mm}^2$  and a schematic is shown in figure 3.2.

Figure 3.3 shows schematics of one  $\text{Si}_3\text{N}_4$  window substrate. The size of each membrane was  $100 \times 100 \mu\text{m}^2$ , the membrane thickness was about  $50 \text{ nm}$  and it was lying in the centre of an  $2 \times 2 \text{ mm}^2$  block of silicon covered with silicon nitride on top and bottom.



**Figure 3.2**

Top view of  $2 \times 2$  membrane array with markers and surrounding frame, overall size  $9 \times 9 \text{ mm}^2$ . The markers are for correct loading of the substrates in the e-beam writer and the e-beam markers are used to position the patterns in the centre of the membranes.



**Figure 3.3**

Silicon nitride membrane; (a)  $2 \times 2 \text{ mm}^2$  silicon block with membrane in the centre; looking at bottom side, (b) Schematic of a cross section of a silicon nitride membrane in the surrounding silicon block.

### 3.3 SMALL MAGNETIC ELEMENTS

In small elements of soft magnetic thin film the dominant energy terms are magnetostatic energy which aims to minimise magnetic charge on the surface and exchange energy which is minimal for parallel alignment of the magnetic moments. The balance between these two energies leads to different domain configurations for different shapes of the elements (sections 1.3 and 1.5). Acicular elements are known to support a single domain state at remanence and they reverse very quickly ('switch') at a well defined field value. It is also known that the perfection of the edges of such elements is crucial in determining their switching field values (Gadbois et al, 1995). Therefore we are interested in finding out the effects of deliberately modulated edge structures of acicular elements.

At first, however, test patterns with in-plane dimensions of the elements in the range of 0.5-4.0 $\mu\text{m}$  and aspect ratios up to  $l/w=8$  ( $l$ : length,  $w$ : width of the elements) were designed. The starting dimensions of the edge features were in the range of  $(\frac{1}{2} \times) 500 \times 500 \text{nm}^2$  depending on the shape of the structure features (i.e. triangular or square). The purpose of these test patterns was to look at the large scale effects first. No magnetising experiments were carried out with these samples. Later only acicular elements with aspect ratios between 4 and 16 were designed and investigated. Furthermore the dimensions of the structure features were scaled down and the period and the height of the structure features were varied. In the case of the patterns designed in this work the smallest edge structure features were in the range of 100nm by 50nm (chapters 4-6).

The patterns were designed using a program called WAM, which is short for WaveMaker. This program allows the design of highly complex planar structures with a finest grid spacing of one nanometer. Detailed descriptions of the patterns created in this work are given for the different investigated samples prior to the discussion of the experimental results. It is possible to save the WAM files in \*.dxf format (drawing exchange format) and open them in AutoCAD (Computer Aided Design) programs which are better suited to get high quality hard copies of the designs.

### 3.4 FABRICATION OF PATTERNED THIN FILMS

The patterning of the magnetic thin film elements involved several steps which are divided in two main parts. The first part is electron beam lithography and the second is metal deposition and lift off. Both processes are described in the following sections.

#### 3.4.1 Electron Beam Lithography

Firstly the  $\text{Si}_3\text{N}_4$  membrane substrate was cleaned by gently rinsing it with acetone, methanol and IPA (isopropyl alcohol) before it was blown dry carefully and then a double layer of resist (PMMA: polymethylmethacrylate) was spun on the substrate (Khamsehpour et al, 1996). PMMA is a polymer, which is available in various molecular weights. Polymer molecules are long chains of carbon atoms with various atoms or molecules at the remaining bonds of the carbon atoms. In the case of PMMA the carbon chains are broken when exposed with an electron beam. The statistical process of breaking bonds in long polymer chains and their random distribution in the solution gives rise to the generic edge roughness of electron beam lithography which lies in the range of 5-10nm (Thoms, 1996).

In the USSL (Ultra Small Structures Lab) at the University of Glasgow two standard PMMA brands are currently in use. One is 'ELV' from Elvacite and the other is 'ALD' from Aldrich. They are used in solutions of some percent PMMA in ortho-xylene. The first PMMA layer spun on the substrate was 2.5%ALD and the second layer was 2.5% ELV. The 2.5%ALD was spun on with 3000rpm for 60s and then baked for 1h at 180°C. After letting the sample cool down, 2.5%ELV was spun on with 5000rpm for 60s. The temperature for the following bake was also 180°C, but the duration of the bake was 2h for this layer of resist. The overall thickness of these two layers of PMMA was 110-150nm with the layer thickness of the ALD being 40-50nm and that of the ELV layer 70-100nm. The double layer of resist was applied because the two resists have a different sensitivity and are therefore damaged to different degrees by the electron beam. This results in an undercut profile in the PMMA cross section at the interface of the different resists as illustrated in figure 3.4. The reason for applying a double layer of resist was to enhance the final lift-off stage of the resulting pattern as the thin film elements are not in contact with the PMMA. It should be noted, that electron beam lithography generally results in an undercut profile even for single layers of resist which is due to multiple scattering of the

electrons in solids. This leads to spreading of the beam and therefore the area where the PMMA molecules are broken increases with the thickness of the resist and also depending on the material and thickness of the substrate (Mackie, 1984), (Reimer, 1997). Very thin substrates (as in our case) in combination with thin layers of resist however reduce this effect and therefore the depth of the undercut. This is why the option to enhance the quality of lift off by means of a double layer of resist was chosen.

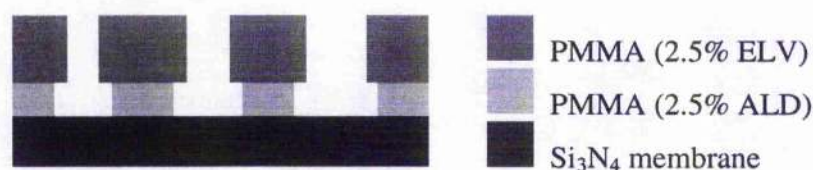


**Figure 3.4**

*Schematic of undercut profile in double layer of PMMA. The overall height of PMMA is  $\approx 110-150\text{nm}$ .*

The designed patterns were transferred to a Leica-Cambridge beamwriter where the PMMA was exposed using 100kV electrons with a spot size of 12nm. The exposure dose was varied between  $1.3 \times 10^7 \text{Cm}^{-2}$  and  $1.7 \times 10^7 \text{Cm}^{-2}$  by an increase of 10% from membrane to membrane for each 2x2 membrane array. This variation led to a reduction of adverse effects of statistical variation of parameters like beam current or changes in the mixture/thickness of resist as well as changes of the developing conditions. Furthermore different doses can be better suited for different parts of the patterns and therefore by changing the dose from one membrane to the other it is more likely to get good results for all features on one membrane or the other. The topological alignment marks, created by the UV-patterning process described in section 3.2, were used to position the patterns. Finally the patterns were developed for 37s in 3:1 IPA-MIBK (methyl isobutyl ketone) solution with a temperature of 23°C. The process was completed by rinsing the samples in IPA before gently blowing them dry.

The actual writing process is illustrated in figure 3.5. As the patterning is realised by sequentially filling in a designed shape with the scanning electron beam, the spot size as well as the dose need to be considered carefully. It should be noted, that not all designed shapes will be transferred in the same quality as far as edge acuity is concerned. Straight edges and step-like features will usually be very true to the actual design. For ellipsoidal or

wedge structures the pattern transfer will be less perfect. The effect of deterioration of edge acuity however is demonstrated exaggeratedly in figure 3.5, as the overlap of the exposed areas of adjacent beam positions is not shown in these schematics. A more realistic description of the writing process is given in figure 3.6, where this overlap is taken into account.

Another limitation in pattern transfer is caused by proximity writing. While this is obvious in the case of wedge structures (Fig. 3.5(d)), it also frequently observed in the case of step structures such as illustrated in Fig. 3.5(b). The reason for this is that the electron beam scans more often in close proximity to the regions marked by the red circles than close to other sections of the edge. Therefore the likelihood of unintentionally damaging the PMMA is considerably increased in the marked areas and can lead to rounding of the corners of step and wedge structures.

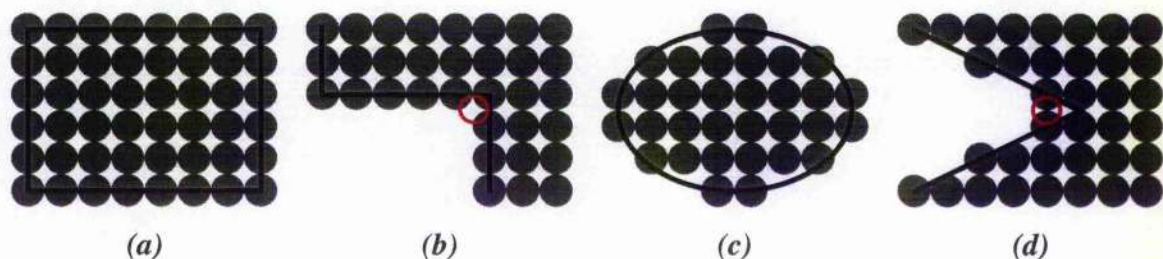


**Figure 3.5**

*Illustration of the patterning process of different shapes by means of an e-beamwriter.*

*Patterning (a) a rectangle, (b) a step structure, (c) an ellipse and (d) a wedge structure.*

*Red circles indicate regions affected by proximity writing.*

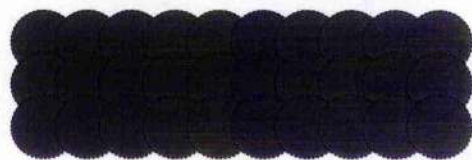


**Figure 3.6**

*Detailed schematic of the e-beam writing process.*

### 3.4.2 Metal Deposition and Lift Off

Schematics to illustrate the processes of metallization and lift off are given in figure 3.7. After developing the PMMA, a thin film of magnetic material was thermally evaporated onto the patterned resist on the substrate (Fig. 3.7(a)).

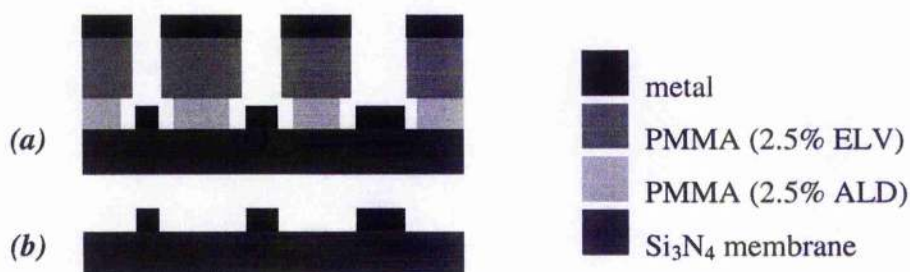


**Figure 3.7**

*Schematic of the patterning of thin films by means of lift off. (a) Metal is deposited on top of the patterned PMMA, (b) Patterned thin film elements after lift off.*

This involved placing pieces of metal in a crucible, which was mounted between high current terminals in a vacuum evaporating stage with a base pressure in the  $10^{-4}$ Pa range. Each alloy or metal was evaporated from a separate crucible and the material itself was cleaned prior to evaporation. It is crucial that any mixing of different pure metals or alloys is avoided. The evaporation process was monitored using a crystal oscillator. The frequency change of the crystal due to the change in its overall mass, as metal is also deposited on the crystal, has to be calibrated for each material and can then be used as a guide for the desired film thickness ( $f \propto m^{-1/2}$ ). It should be noted that the film thickness generally influences magnetic parameters as e.g. coercivity, domain structures, magnetic dispersion and wall type (chapter 1). Therefore the aim was to avoid considerable variations of the film thickness between different samples. The heating, as well as the shutter, was controlled by hand. The shutter was placed between the crucible and the substrate and was opened when a reasonable evaporation rate was reached. It was shut when the crystal oscillator reading reached the desired value. The fact that the controls were not only done by hand but were also dependent on the subjective interpretation of the operator of e.g. reasonable evaporation rate indicates that the deposition parameters could vary for each evaporation process. It is known that different grain sizes of films and stress influence the magnetic parameters (Hubert et al, 1998), (Akhter et al, 1998) and the film parameters depend on growth conditions like vacuum and substrate temperature. While the base pressure was kept as constant as possible, there were certainly changes in deposition time from one run to the next which altered the substrate temperature. However, in the case of small magnetic elements the magnetic properties are much more determined by the element shape than by the intrinsic properties of the material (Hubert et al, 1998).

Therefore the variations due to the deposition process are not expected to perturb the results to an unacceptable extent.

By applying standard lift off techniques the unexposed resist was dissolved by simply putting the samples in acetone and the metal on top of the resist was removed with the resist (Fig. 3.7(b)). The result was a pattern of small elements of metal on top of the membrane, which matched the design. The film thickness of the investigated elements was in the range of 20-35nm and we used mainly permalloy, a NiFe alloy of the composition  $\text{Ni}_{80\text{at}\%}\text{Fe}_{20\text{at}\%}$  for our studies. Permalloy is widely used in the magnetic data storage industry and also for other applications in sensors. This dominance is due to the fact that permalloy not only displays negligible magnetostriction but its magneto-crystalline anisotropy is very small and therefore bulk permalloy is isotropic with no preferred magnetic axis (Jiles, 1991), (Mallinson, 1996).

After lift off the film thickness was determined accurately for each pattern using a Dektak surface profiler. As the patterns consisted of completely isolated metal elements on an insulating  $\text{Si}_3\text{N}_4$  membrane, the substrates needed to be coated with carbon as a conductive overlayer in order to avoid charging of the sample in the microscope. At this stage the patterns were ready for TEM investigation (Rührig et al, 1996), (Khamsehpour et al, 1996).

### 3.5 STRUCTURED EDGES OF SMALL MAGNETIC ELEMENTS

Three different types of edge structure were designed for this project. Examples of elements with structured edges in the test patterns are shown in figure 3.8. The structure types were called A, B and C and they were realised by periodic repeat structures of (a) isosceles and (b) right-angled triangles and (c) rectangles. The in-plane dimensions  $w$  and  $l$  of the elements were in the range of 0.5-4.0 $\mu\text{m}$  and the elements had aspect ratios of  $l/w=1-8$ . The dimensions of the edge features were in the range of  $(\frac{1}{2}\times)500\times 500\text{nm}^2$  and neither the period nor the height of the structures was varied in the case of the test patterns.

As the requirements of the fabrication process and magnetic imaging techniques were met by the test patterns (sections 3.6.2 and 3.6.3) the parameters of the edge structure features could be scaled down at a later stage. Our research was focused on double pointed acicular elements with aspect ratios in the range of 4-16. Schematics of the designs of such elements are given in figure 3.9. In order to achieve a detailed understanding of the effects

caused by structuring the edges different types of edge structure were investigated with variation of period and height of the features (chapters 4-6). Standard elements with straight edges have been fabricated and studied for comparison (Fig. 3.9(d)).

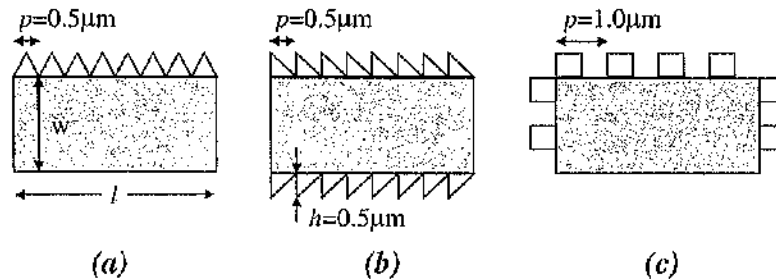


**Figure 3.8**

*Schematic of elements of test patterns. Rectangular elements with width  $w$  and length  $l$  in the range of  $0.5-4.0\mu\text{m}$  and (a) edge structure type A on one edge (b) edge structure type B on two edges (c) edge structure type C on three edges. Neither  $p$  nor  $h$  was varied in the test patterns.*

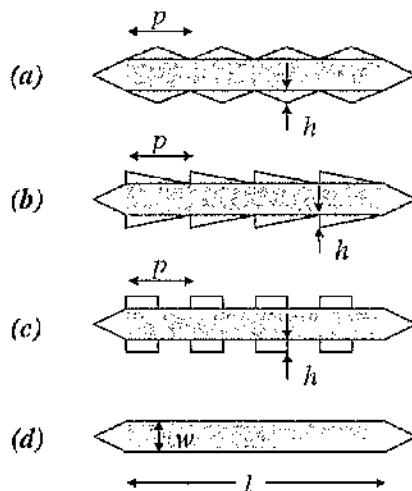


**Figure 3.9**

*Schematic of double pointed acicular small magnetic elements with (a) edge structure type A, (b) edge structure type B, (c) edge structure type C.*

*The period  $p$  is varied from the length  $l$  down to  $0.1\mu\text{m}$  for types A and B and  $0.2\mu\text{m}$  for type C. The height  $h$  is constant for this set with  $0.1\mu\text{m}$ .*

*(d) Standard element with straight edges, parameters width  $w$  ( $0.25$  and  $0.5\mu\text{m}$ ) and length  $l$  ( $2.0$  and  $4.0\mu\text{m}$ ) of base rectangle as indicated.*

### 3.6 TEST PATTERNS - PHYSICAL AND MAGNETIC MICROSTRUCTURE

The test patterns were designed in order to evaluate the fabrication and imaging conditions and to try out different types of edge structure. No magnetising experiments were carried out with these samples, only their as-grown and ac-demagnetised states were investigated. In these test patterns the size of the designed edge structure was

approximately the high resolution limit of photo lithography, the most common commercial patterning technique.

### 3.6.1 DESCRIPTION OF PATTERNS

Three patterns have been designed with different edge structure types A, B and C as described in section 3.5. Figure 3.10 shows the design of one of these test patterns where elements with all three structure types were on a single membrane.

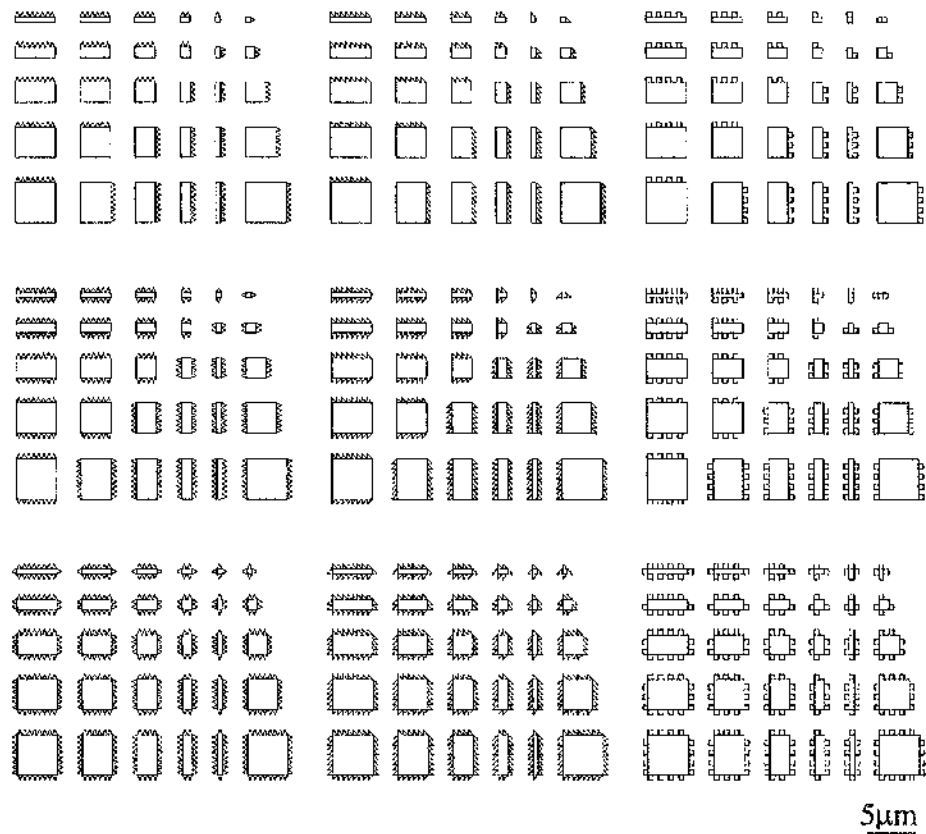


**Fig. 3.10**

*Design of one of the test patterns; all three structure types on one membrane, permutations of numbers of edges structured.*

For this pattern the numbers of edges structured were 1, 2 and 4 with 1 or 2 long edges being structured in this case. The height of the structure features was constant with  $h=0.5\mu\text{m}$  for all types, the period of the triangular shapes was also  $p_{A,B}=0.5\mu\text{m}$ , whereas the

period of the squares was  $p_c=1.0\mu\text{m}$ . On each membrane were nine arrays of 30 rectangles with varying side lengths of 4, 3, 2, 1 and  $0.5\mu\text{m}$ . Each single array was a permutation of the number of structured edges. In another test pattern 1, 2 and 3 (short) edges were structured and in a different set of test patterns the edge structure type was not varied, but instead eight arrays of 30 rectangles with all possible permutations of 0, 1, 2, 3, and 4 structured edges were on a single membrane.

### 3.6.2 PHYSICAL MICROSTRUCTURE

The physical microstructure of the patterned thin film elements was revealed by means of bright field imaging. Figure 3.11 shows examples of bright field images of different samples.

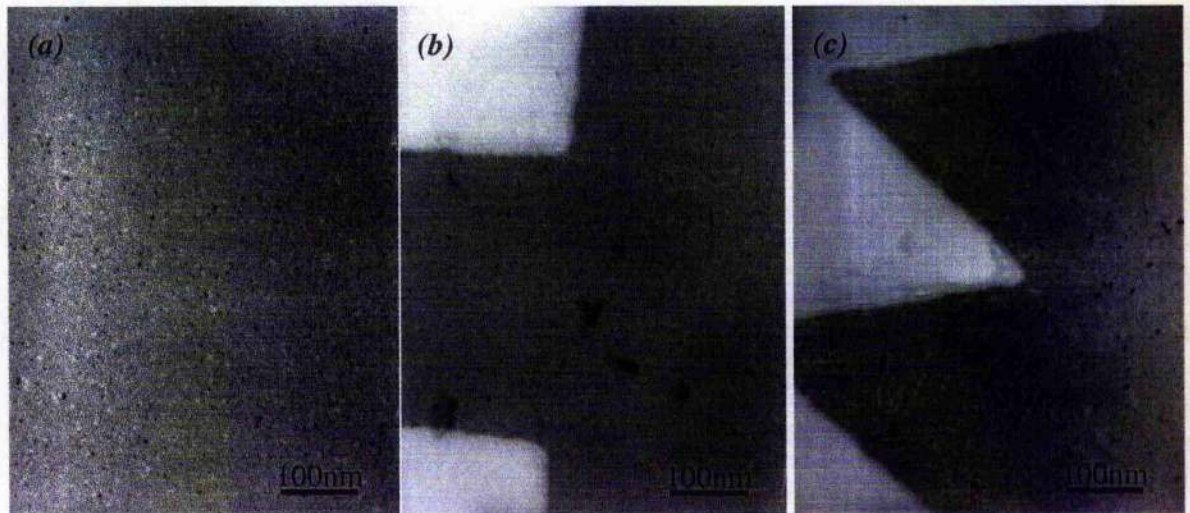


**Fig. 3.11**

*Bright field images of patterned elements of NiFe film.*

*Two samples with a thickness of  $22\pm 2\text{nm}$ , one sample (a), (b) has a much finer grain structure than the other one (c). (a) Central and (b) edge area (structure type C) of patterned elements. (c) Edge structure type A of an element of another sample.*

Figures 3.11 (a) and (b) are images of a sample of the first set. The NiFe film was micropolycrystalline as expected and it had a very fine granular structure with an average grain size of  $\leq 10\text{nm}$ . The edge acuity was very high as can be seen in figure 3.11 (b) and

was of the order of the expected generic edge roughness of 5-10nm due to the PMMA (section 3.4.1). Figure 3.11 (c) shows an example of a pattern of the second set of test patterns. The films of the second set were of the same film thickness and they were also micropolycrystalline, but displayed a much coarser grain structure than the samples of the first set and had a larger average grain size in the range 10-15nm. This variation of the grain size is almost certainly due to the uncontrollable changes of the deposition process as described earlier (section 3.4.2). It should be noted that the increase of the average grain size did not result in a considerable deterioration of the edge acuity. Lift off was of good quality for both sets of test samples with all excess metal having been removed, however there was a layer of PMMA remaining in some areas.

Figure 3.12 shows a set of lower magnification bright field images of the sample also displayed in figures 3.11 (a) and (b).

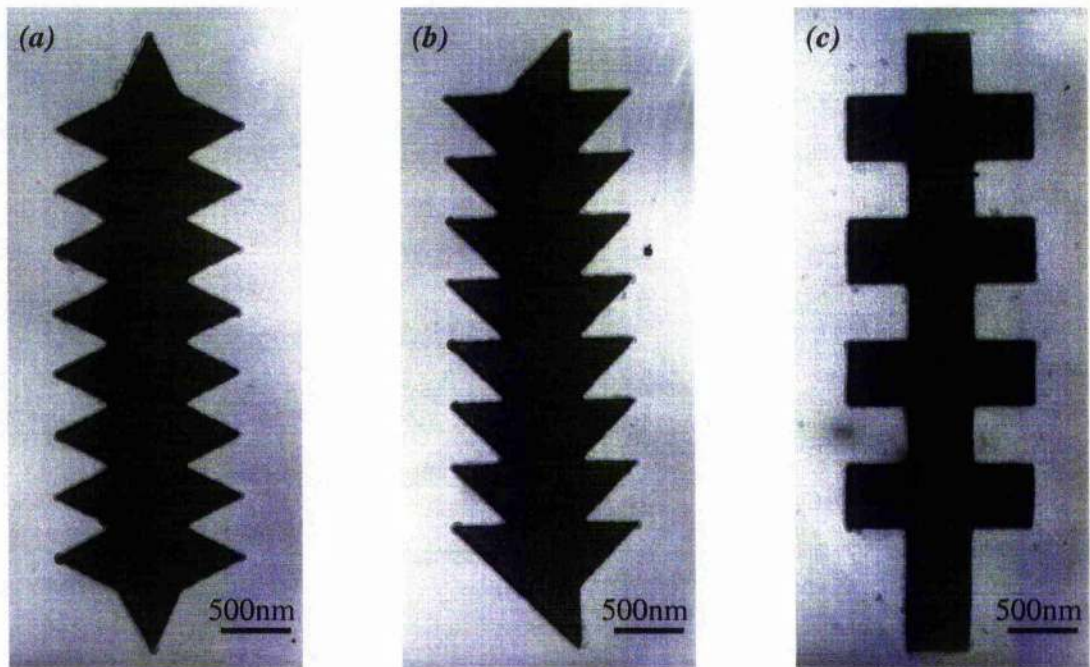


**Fig. 3.12**

*Bright field images of small magnetic elements with edge structure type A (a), B (b) and C (c); material NiFe alloy; film thickness  $22 \pm 2$ nm.*

Figure 3.12 is an overview of elements with all four edges structured and an example is given for each structure type. The pattern transfer was of high quality and the two triangular structure types are easy to distinguish. In the case of the triangular edge

structures the central area of the elements was slightly broadened. This is an artefact of the writing process as discussed in section 3.4.1 (Fig. 3.5).

### 3.6.3 AS-GROWN AND AC-DEMAGNETISED STATE

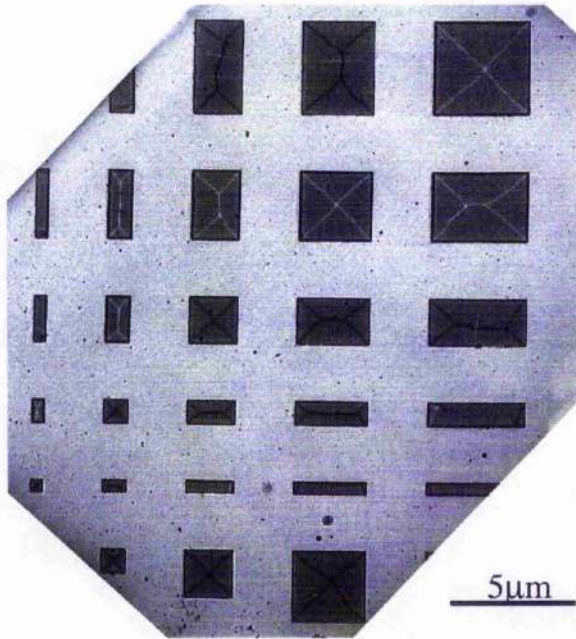
Imaging of the magnetic microstructure of the as-grown and ac-demagnetised states of the samples was realised by means of Lorentz microscopy. The main two imaging modes, which were applied in this work to small magnetic elements are Fresnel and Foucault imaging (section 2.3.2). In general the domain configurations of the elements in their as-grown state were very similar to those after the samples had been ac-demagnetised. However, as expected, the elements often showed even more symmetric domain configurations after demagnetising, as demagnetisation results in a low energy state of a sample, especially the magnetostatic energy component. As the as-grown state is a unique state and because there was very little difference between the as-grown and the ac-demagnetised states, the main focus of this work will lie on the demagnetised state of the samples.

Figure 3.13 shows a Fresnel image of an array of rectangles of an ac-demagnetised test sample. The locations of domain walls were clearly visible as black and white lines within the uniform grey background of the elements. The domain configurations are highly symmetric and in agreement with the work of others (Ziethen et al, 1998), (Swiech et al, 1997), (Kirk et al, 1997 a), (Hefferman et al, 1995), (McVitie et al, 1988).

The square elements supported highly symmetric flux closure structures with four domains of equal size with the four walls being  $90^\circ$  walls of the Néel type. Néel walls with opposite polarity (indicated by green and red arrows in Fig. 3.14) which meet in an element with flux closure structure led to the expected formation of a Bloch line at that location (solid circle in Fig. 3.14(a), (McVitie et al, 1997)). The elements with aspect ratios  $1 < l/w < 4$  also had very symmetric four-domain structures. The four walls of the triangular end domains were  $90^\circ$  walls whereas the wall in the centre of the element was a  $180^\circ$  wall with cross ties observed in some cases (Fig. 3.14(b)). It should be noted that at least one Bloch line ought to be expected due to the reason given above.

The narrow elements with aspect ratios  $\geq 4$  were clearly uniformly magnetised in the central region of the element but displayed walls at the element ends. Small end domains form in order to reduce the magnetostatic energy of such elements (Figs. 3.14(c), (d)). In

Foucault mode stray fields were visible at the ends of these elements which were similar to the field distribution around a bar magnet. This is in agreement with a nearly uniformly magnetised state of this kind of element, which is a result of the strong shape anisotropy of such an element (Kirk et al, 1997 b). It should be noted though that the end domain configurations in Fig. 3.14(c) are vortex structures and therefore Bloch lines form at the intersections of the walls. As the illustration was already quite busy the polarities of the Néel walls were not given in the schematic.



**Figure 3.13**

*Fresnel image of an array of rectangles showing wall contrast; material: NiFe alloy, film thickness:  $22 \pm 2$  nm.*

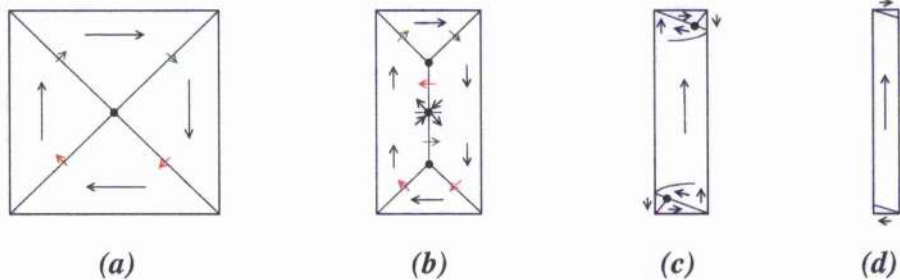


**Figure 3.14**

*Schematics of common domain configurations of rectangular elements depending on the aspect ratio  $l/w$  of the elements; (a)  $l/w = 1$ , (b)  $l/w < 4$ , (c) and (d)  $l/w \geq 4$ . The direction of magnetisation is illustrated by black arrows (shown outside the element for very small domains). Green and red arrows indicate opposite polarity of Néel walls (not in (c) as the schematic is too small). The locations of Bloch lines are given by solid circles.*

As the aim of this work is to study the effects of structured edges on the magnetic microstructure of small elements, Fig. 3.15 shows the Fresnel images of two arrays of elements of ac-demagnetised samples. The first image is of an array of elements with structure type A on all four sides (Fig. 3.15(a)) and the second is of an array with structure type C on three element sides (Fig. 3.15(b)). The most striking observation was that there were many additional walls in all elements which were very localised and clearly associated with the structure features whilst in many cases the larger scale structure seen in the elements with straight edges was retained. Most of the additional walls originated in the corners of structure features, resulting in a predominantly spike like appearance of the walls for both triangular edge structure types and flux closure like configurations for structure type C.

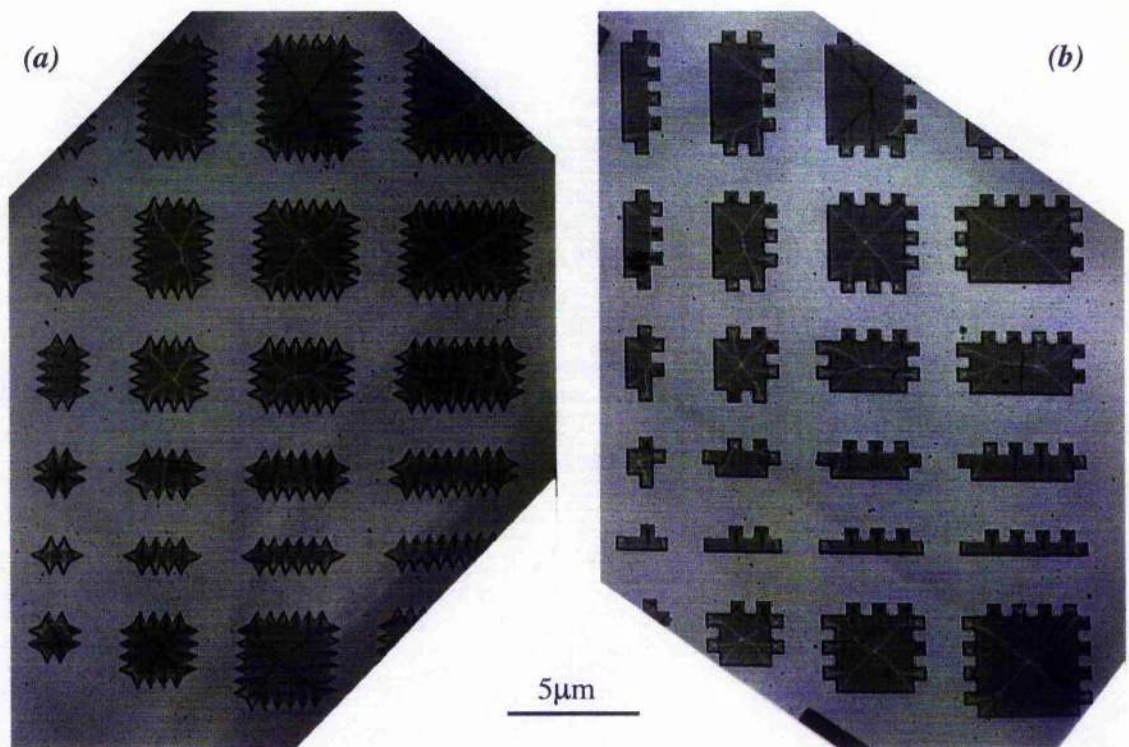


**Figure 3.15**

*Fresnel images of arrays of patterned elements of nickel-iron alloy with (a) edge structure of type A on four sides, (b) edge structure of type C on three sides.*

More detailed information was gained from Foucault images at higher magnification as shown in figure 3.16. Pairs of Foucault images are displayed for rectangular elements with straight edges with  $l=4.0\mu\text{m}$  and  $w=3.0, 2.0$  and  $1.0\mu\text{m}$  (Figs. 3.16(a), (b)) and similar

elements with structure type A, B and C on all four edges of the elements (Figs. 3.16(c)-(h)). The mapping direction for each row is indicated by a double arrow. For the images in the top row, with the mapping direction parallel to the element length, it is found that all elements have a net magnetisation along the length of the element. This can be deduced as the main body of most elements is either black or white. For the narrow two elements with straight edges non flux closure structures were observed as a result of their strong shape anisotropy and stray fields are clearly visible at the element ends in Figs. 3.16(a), (b).

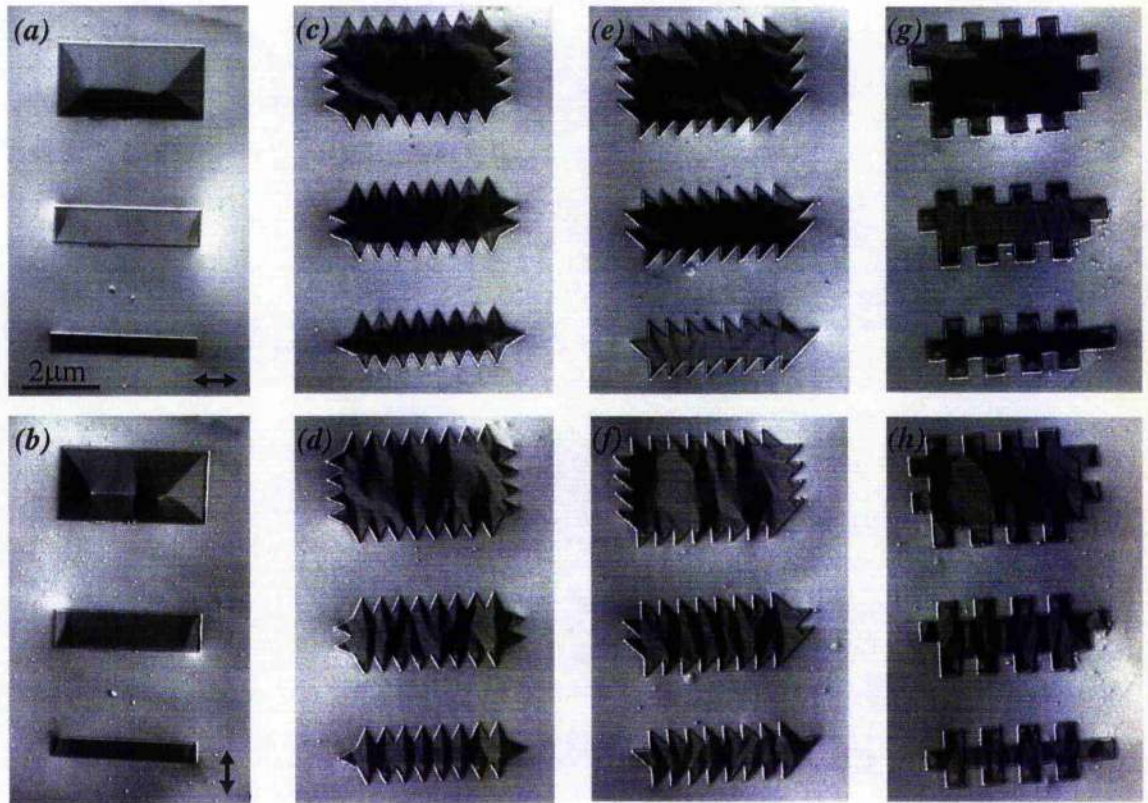


**Figure 3.16**

*Overview of pairs of Foucault images of small magnetic elements with aspect ratios of 2, 4 and 8 of the base rectangle. Mapping direction as indicated by double arrows.*

*(a), (b): Rectangles; (c), (d) Structure type A; (e), (f): type B; (g), (h): type C.*

The Foucault images with mapping direction parallel to the element length (top rows of Fig. 3.16) for elements with structured edges either showed predominantly black or white contrast and therefore their mean direction of magnetisation was parallel to the element length. There were however contrast variations visible in the main body of the elements which got more pronounced with increase of the element width. Even stronger

contrast changes were associated with the structure features, which indicated the existence of magnetisation components antiparallel to the mean direction of magnetisation within these features.

In the set of Foucault images with the mapping direction parallel to the element width (bottom rows of Fig. 3.16) the well known domain structures and stray fields for non flux closure structures were observed in the case of the elements with straight edges (Kirk et al, 1997 a), (McVitie et al, 1988). The central parts of the narrow elements with  $l/w=4$  and 8 did not show any contrast variations and the wider element with  $l/w=2$  displayed the well known contrast variation around a cross tie wall (Hefferman et al, 1995), (Chapman et al, 1991), (Hubert et al, 1998).

In the case of the elements with structured edges the situation changed drastically (Figs. 3.16(d), (f), (h)). Strong contrast variations were associated with the structure features of all three types indicating abrupt changes of the direction of magnetisation parallel to the element width within the features. In the case of the triangular edge structures these strong contrast variations also affected the structure in the main body of the elements with the two highest aspect ratios (Fig. 3.16(d), (f)). These perturbations were less pronounced in the central parts of the wider elements which suggests that the influence of all edge structure types is highly localised. This is in agreement with the observations of the Fresnel images of such elements (Fig. 3.15).

Schematics of the magnetisation distribution were derived within the elements with structured edges. Only the domain configurations within and close to the structure features were considered partly for reasons of clarity but also because the effects of the structure features on the magnetisation distribution were found to be very localised. Figure 3.17 shows an overview of such schematics for all three edge structure types. It was found that corners of structures were common nucleation sites for walls. This was expected as the magnetisation tends to remain parallel to the edges of the elements. The reason for this is that magnetostatic energy is minimal for parallel alignment of the magnetisation to the edge and therefore this kind of alignment is favourable. Observation of the samples showed indeed, that the magnetisation preferably aligned parallel to the nearest edge and parallel to the mean direction of magnetisation of the element. Figure 3.17 shows schematics of the magnetisation distribution together with an indication of their frequency of occurrence. Depending on structure type and number of edges structured between  $\approx 40$  (structure type C, only one small edge structured) and  $\approx 400$  (structure types A and B, all four edges

structured) structure features were evaluated in a negative. Despite the different magnetic configurations observed for the different structure types, certain similarities could be detected which led to the classifications given in Fig. 3.17. The most dominant groups were the 'flux closure' and 'bisector' structures. It should be noted, that 'wall singlet', 'end domain' and 'single domain' were observed too, but less frequently. The latter two were mainly a result of the specific local geometry of certain elements and will therefore not be discussed in detail.

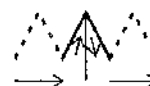
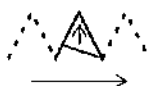
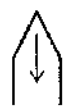
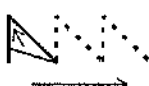
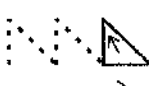
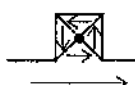
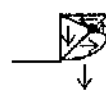
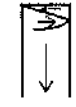
	flux closure	bisector	wall singlet	end domain	single domain
Type A	 ≈20%	 ≈60%	 ≈10%		 ≈10%
Type B	 ≈20%	 ≈50%	 ≈10%		 ≈10%
			 ≈10%		
Type C	 ≈50%	 ≈30%		 ≈10%	
	 ≈10%			 ≈10%	

Figure 3.17

Schematics of magnetisation distribution within edge structure features of types A, B and C with indication of their frequency of occurrence.

The flux closure structures were expected to be the most likely domain configurations if the structure features were isolated. The reasons for this are that (i) the lateral dimensions

of the structure features were too big ( $\geq 500\text{nm}$ ) and (ii) furthermore no shape anisotropy ought to be expected as all edge lengths were of similar magnitude and had (iii) significant corners so that single domain states could almost certainly be ruled out. This was shown experimentally for the case of structure type C, as the smallest elements in the arrays of rectangular elements with straight edges were squares of the same dimensions, which were generally found to support flux closure structure. The reason for this is that flux closure configurations result in a minimum state of the total magnetic energy as the balance between magnetostatic and exchange energy is best. Therefore it is reasonable to assume that isolated triangular elements would support flux closure structures, too (Schneider, 2000), (Cowburn, 2000). If the features are no longer isolated, but joined to a larger element, it should still be possible to form flux closure structures. This was indeed observed for all three investigated structure types, with a majority of this domain configuration in the case of structure type C. It should be noted that for structure type C two kinds of flux closure structures were observed with one of them being much more dominant than the other. To form the less common one, an additional wall needed to be generated (dashed red line in Fig. 3.17). As this results in a higher energy state this configuration is expected to be less common which is in agreement with the observations. The walls, which meet in the centre of the features are modified Néel walls which are in the case of flux closure structures of different polarisation and therefore Bloch lines are expected at the intersections. Due to the geometry of the features the angle of the walls was  $\approx 120^\circ$  for all three walls in the case of structure type A, in the case of type B two walls had an angle of  $\approx 135^\circ$  and the third wall was  $\approx 90^\circ$  while in the case of structure type C all four walls were  $90^\circ$  walls.

The bisector structure was also commonly observed for structure type C, but it was by far the most frequent configuration in the case of the triangular structure types A and B. This was expected as the magnetisation within the structure features was not only parallel to the closest edge (minimum of magnetostatic energy) but also had components parallel to the nearest mean direction of magnetisation (reduces exchange energy) and only one wall needed to be generated. The bisector wall is a high angle wall from  $120^\circ$  in the case of structure type A up to  $180^\circ$  in the case of structure type C. To form the bisector structure in the case of edge structure type C, two more ( $90^\circ$ ) walls are needed but no Bloch line is generated as the Néel walls are all of the same polarity.

Wall singlet structures were only observed in the case of the two triangular structure types A and B and they were not very common. The reason that these states were quite rare is that despite only one wall ( $\geq 90^\circ$ ) being present, the magnetisation within the structure features was almost uniform and therefore generated considerable magnetic charge on the edges.

### 3.7 SUMMARY

This chapter dealt with the procedures necessary for the fabrication of thin film elements suitable for TEM investigation. The preparation of the electron transparent  $\text{Si}_3\text{N}_4$  membrane substrates as well as the fabrication of a set of test patterns of small magnetic elements was described in detail before discussing preliminary results of these test samples. By means of transmission electron microscopy it was found that the pattern transfer was of good quality and that the elements had the common micropolycrystalline structure of evaporated NiFe films. Lorentz microscopy was applied successfully for the study of the magnetic microstructure of the patterned thin films. The domain configurations of the small magnetic elements were investigated in the as-grown and ac-demagnetised states of the samples and only very little difference was found between these two states. In general the magnetic microstructure could be observed in great detail. Even domains as small as  $\approx 0.05\mu\text{m}^2$  were clearly visible and qualitative information about the direction of magnetisation could easily be deduced. As the preliminary results of the test patterns were very encouraging, the fabrication and investigation of acicular elements with smaller edge structure features, as described in section 3.5, was the next step.

**CHAPTER 4:****1<sup>ST</sup> PATTERN: ACICULAR ELEMENTS WITH STRUCTURED EDGES OF TYPES A, B, C****4.1 INTRODUCTION**

This chapter focuses on the physical and magnetic microstructure of acicular elements and their magnetisation reversal behaviour. The thin film elements were fabricated using a combination of e-beam lithography and lift off techniques as described in chapter 3. The length of the elements was in the range of 2.5-5.0 $\mu\text{m}$  and their width was mainly in the sub-micron range. Standard elements with straight edges (Fig. 3.9(d)) were compared with elements with structured edges (Figs. 3.9(a)-(c)). With exception of the control squares all elements were double pointed as acicular elements of this kind are known to support single domain states with the magnetisation being almost uniformly aligned parallel to the element length at remanence (Kirk et al, 1997). Application of an opposite magnetic field parallel to the element length results in a very rapid magnetisation reversal (switch) of such elements at a well defined coercive field  $H_c$ . The resulting hysteresis loop is square with the element width being a crucial parameter for  $H_c$  (Rührig et al, 1996), (Kirk et al, 1999). Two different lengths as well as two widths of elements were investigated in the first pattern. Three different types A, B and C of periodic repeat structures were designed and the period of the structure features was varied over a wide range. Schematics of the designs were given in section 3.5 and a detailed description of the pattern is given in section 4.2.

Transmission electron microscopy was used to investigate the physical and magnetic microstructure of the samples. Bright field imaging (Reimer, 1997) revealed the physical microstructure and is discussed in section 4.3. Lorentz microscopy (Chapman, 1984), (Reimer, 1997), (section 2.3.2) was used to determine the magnetic microstructure of the elements and the observations will be presented in sections 4.4 and 4.5. Investigation of the elements in their as-grown and ac-demagnetised state was performed on the JEOL 2000 FX microscope whereas all in-situ magnetising experiments were carried out on the Philips CM20 FEG microscope. It must be remembered that a significant component of field out of the sample plane  $H_{obj} \times \cos\alpha$  ( $H_{obj}$ : field of objective lens;  $\alpha$ : tilt angle), is present and the effect of the objective lens field in this direction needs to be considered (Chikazumi, 1964), (Scheinfein, 1998), (sections 1.3, 1.5, 2.2.5 and 7.4).

## 4.2 DESCRIPTION OF PATTERN

In the case of the first pattern acicular elements with three edge structure types were designed on a single membrane. The film material of the sample was a thermally evaporated soft magnetic NiFe alloy with a thickness of  $\approx 33\text{nm}$ .

Figure 4.1 shows the design of the first pattern of acicular elements with and without structured edges. The squares were designed for control and alignment purposes. The pattern parameters are indicated by the blue letters. Two widths ( $w_1=250\text{nm}$ ,  $w_2=500\text{nm}$ ) and two lengths ( $l_1=2.0\mu\text{m}$ ,  $l_2=4.0\mu\text{m}$ ) were chosen for the base rectangles (section 3.5) of the elements. All three structure types described in section 3.5 were in this pattern. The pattern was made up of six arrays of acicular elements. The upper three arrays in Fig. 4.1 are the wide elements ( $w_2$ ) and the lower three the narrow elements ( $w_1$ ). The two top rows of each array were standard elements for each width value and control squares. The three columns shown are elements with edge structure types A, B and C going from left to right. The period of the repeat structures was varied from the entire length of the base rectangle ( $2.0\mu\text{m}$  or  $4.0\mu\text{m}$ ) down to  $0.1\mu\text{m}$  in the case of the triangular structure types A and B respectively  $0.2\mu\text{m}$  for the rectangular structure type C. The height of the structure features was  $h=100\text{nm}$  for all types and was not varied in this pattern. Structuring the edges here varied the overall width of the elements and as the width is known to be crucial for the field value necessary to reverse the magnetisation in acicular elements (Kirk et al, 1999), (Rührig et al, 1996), standard elements of four widths have been designed for comparison. The widths of the standard elements were  $w_1=250\text{nm}$ ,  $w_1+2h=450\text{nm}$ ,  $w_2=500\text{nm}$  and  $w_2+2h=700\text{nm}$ . The chosen tip ratio of the double pointed elements was  $t=l_{tip}/w_{tip}=1$ . The tips of the standard elements with  $w_1+2h$  and  $w_2+2h$  of the first pattern however were blunter ( $t=1/2$ ) due to a design error.

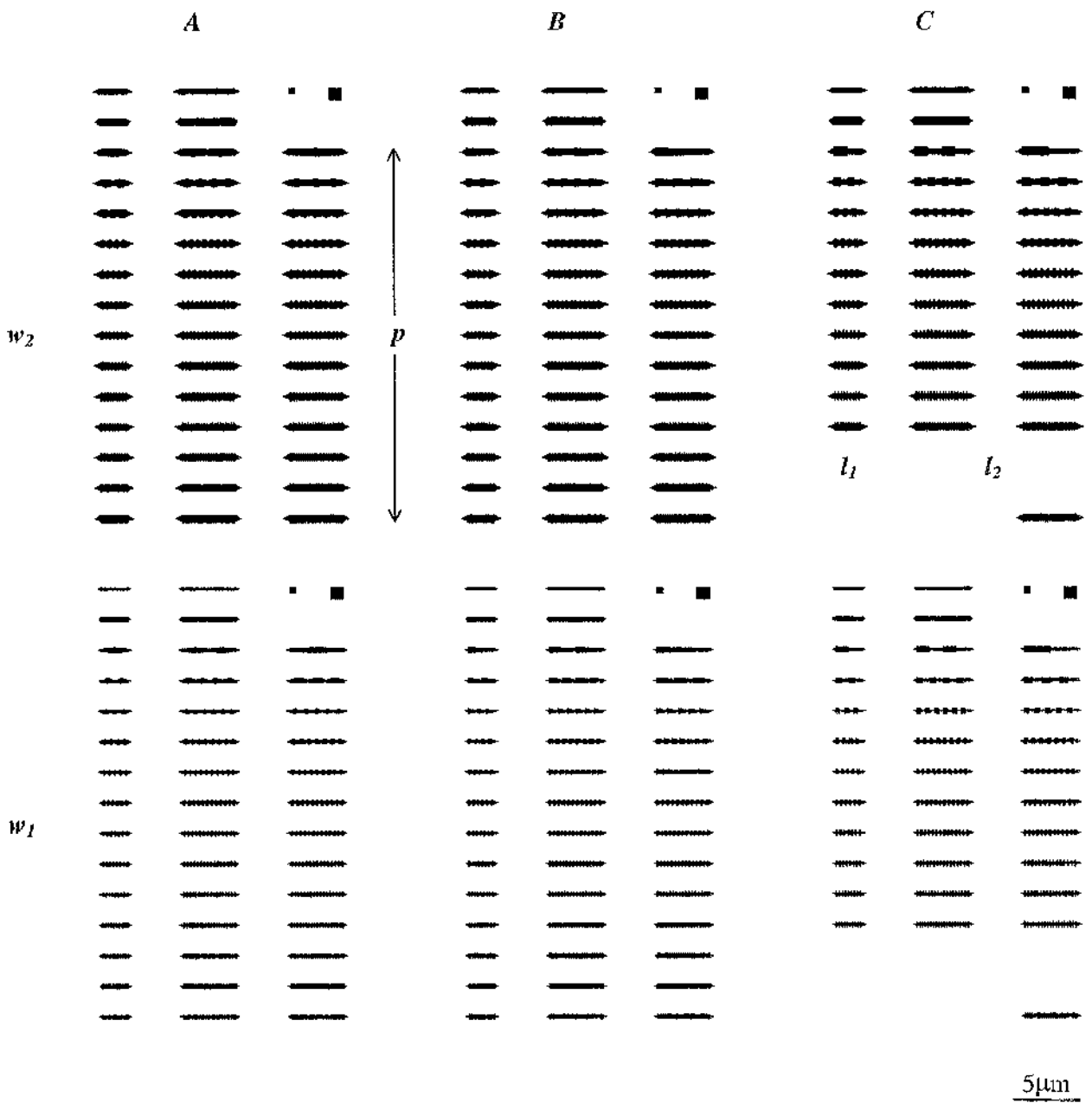


**Figure 4.1**

Overview of first pattern of acicular elements with all three edge structure types.

Type A in first column, type B in second and type C in third column. Blue letters indicate pattern parameters.

### 4.3 PHYSICAL MICROSTRUCTURE

An overview of bright field images of different elements of the first pattern of acicular elements is given in figure 4.2.

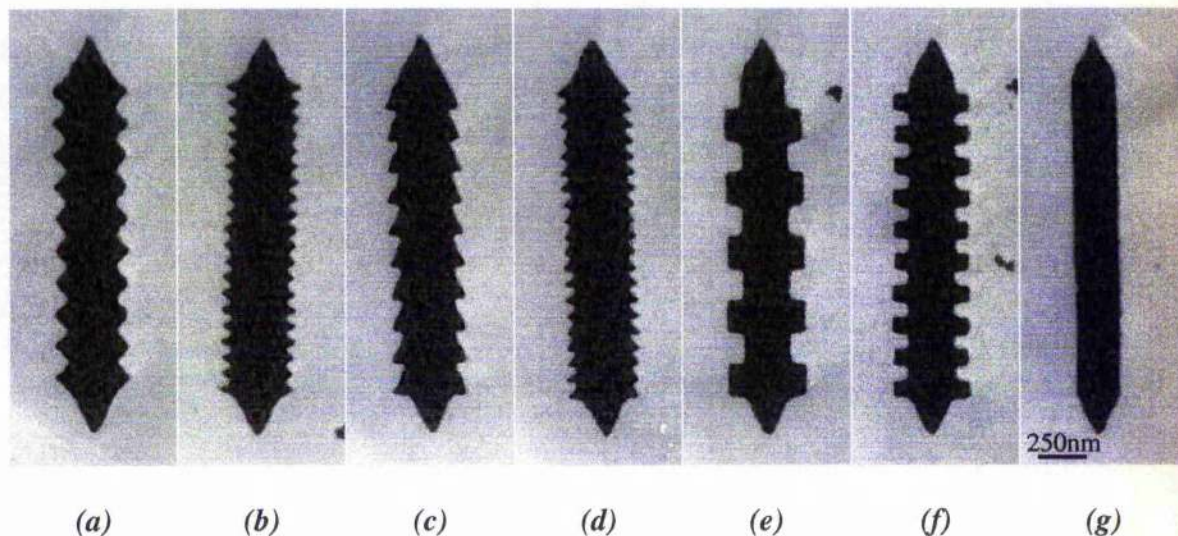


**Figure 4.2**

*Bright field images of short narrow elements of the first pattern of acicular elements;*

*(a), (b) elements with edge structure type A and period  $p=0.2, 0.1\mu\text{m}$ ;*

*(c), (d) type B edge structure with  $p=0.2, 0.1\mu\text{m}$ ;*

*(e), (f) type C edge structure with  $p=0.4, 0.2\mu\text{m}$ ;*

*(g) standard element.*

The NiFe film displayed the expected polycrystalline microstructure. The grains were easily visible and the average grain size was 15-20nm. The pattern transfer was of good quality with the different structure types in general easy to distinguish. The only exceptions were the two triangular edge structures with the smallest period of 0.1 $\mu\text{m}$ , which looked quite similar (Figs. 4.2(b) and (d)). This was due to the fact that not all of the designed right angled triangles appeared exactly right angled but often this angle was slightly smaller and this deviation from the actual design had a more notable effect for smaller periods. Furthermore it should be noted that the height of the structure features decreased by 20-30nm for the elements with the smallest period triangular edge structures whereas the

width of the base rectangle increased by the approximately twice this amount. These were artefacts of the writing process as discussed in section 3.4.1.

#### 4.4 AS-GROWN AND AC-DEMAGNETISED STATE

Initially the magnetic microstructure of the small elements was investigated in the as-grown state and secondly after the elements were ac-demagnetised. Foucault images were taken in the JEOL 2000 FX microscope. The differences between the micromagnetic configurations supported by the elements in these states were very small. As the ac-demagnetised state is a reproducible state of the sample, this is discussed in detail. For the same edge structure the same micromagnetic structures were observed irrespective of element length and width over the range of the elements investigated here. Most of the standard elements with  $w_1+2h$  and  $w_2+2h$  displayed end domain structures similar to those of the very narrow elements with aspect ratios  $l/w \approx 4$  described in section 3.6.3 and the short elements ( $l_1$ ) with  $w_2+2h$  even supported flux closure structures. However as this was a result of the design error of the tips which were too blunt ( $t=1/2$ ) for these elements, this is not discussed further.

As the elements were investigated in the demagnetised state, different directions of net magnetisation of the elements ought to be expected and Fig. 4.3 shows that this was the case. All standard elements with  $w_1$  and  $w_2$  were clearly observed to support a single domain state as shown in the Foucault images Figs. 4.3(a) and (b) for  $w_1$ . The lack of any variation of contrast within the element confirmed uniform magnetisation along its length. Additionally the stray field observed outside the element is consistent with such a magnetisation state and in agreement with earlier observations (Kirk et al, 1997). While the elements with the structured edges retained some similarities to this simple structure, distinct differences were noted. In Figs. 4.3(c)-(l) the stray field contrast outside the elements has a similar form to that of the standard element. This indicates that the mean direction of magnetisation lay parallel to the element length suggesting that the overall shape anisotropy was still quite strong in these elements. For elements with structure type A only small contrast variations were visible close to the structured edges which became more pronounced with decrease of the period as can be seen in Figs. 4.3(f), (h), (j), (l). In the case of the smaller periods (0.4-0.1 $\mu\text{m}$ ) strong contrast variations were observed close to the element ends. Most notably, the elements with  $p=0.1\mu\text{m}$  did not display contrast

variations close to the structured edges and looked in that respect very similar to the standard elements, but they were found to support the domains close to the element ends.

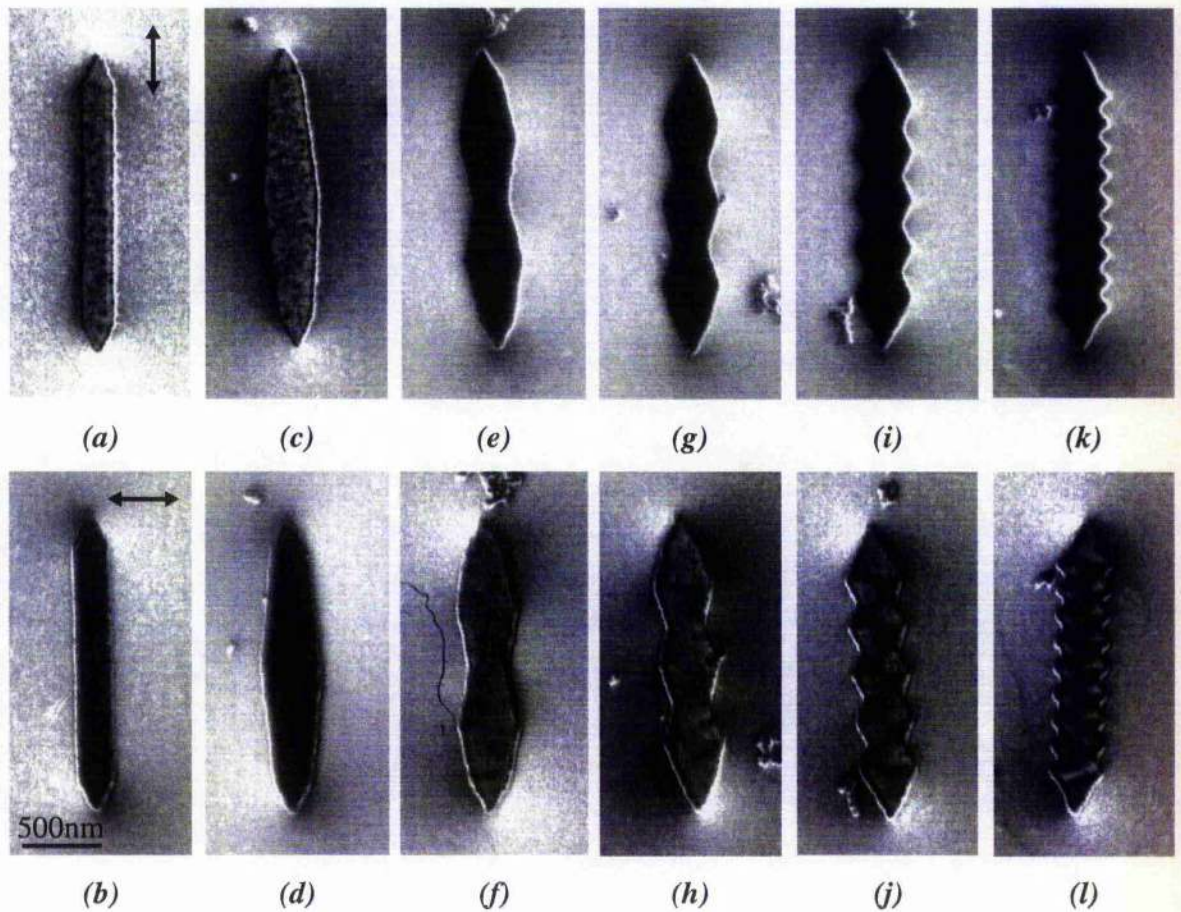


**Figure 4.3**

*Overview of Foucault images of ac-demagnetised elements with edge structure type A of different period. Mapping direction indicated by double arrows.*

Figure 4.4 shows a compilation of Foucault images of a standard element and elements with edge structure type B with different periods. As in the case of structure type A, only negligible contrast variations were detected while mapping parallel to the element length. Therefore only images with the mapping direction parallel to the element width are shown. The contrast variations in the elements with structured edges generally looked very reminiscent to those found in elements with structure type A. The mean direction of magnetisation was parallel to the element length, too, and the contrast variations were also very localised. Apart from the end domain structures, the most pronounced changes in contrast occurred at the sites of the most sudden changes of edge direction. Unlike for

structure type A, no increase of contrast was observed with decrease of the structure period. The reason for this was that in the case of structure type B the major changes of the edge direction were constant ( $\approx 90^\circ$ ) and did not depend on the structure period as they did in the case of structure type A. The magnetic microstructure of the elements with the smallest period of structure B looked very much like that of the elements with the smallest period edge structure A. This is a result of the physical similarities of these shapes as discussed earlier. It should, however, be noted that there was usually only one end domain observed for the elements with  $0.5\mu\text{m} \leq p \leq 4.0\mu\text{m}$  which was due the different end geometry for the two ends as indicated in Fig. 4.4(c). The long end geometry was similar to the long period type A elements ( $p > 0.5\mu\text{m}$ ) where no end domains were detected. The short end had sections of edge orthogonal to the element length, which generally resulted in notable changes in the direction of magnetisation at those locations and even led to the formation of these domains close to the element end.

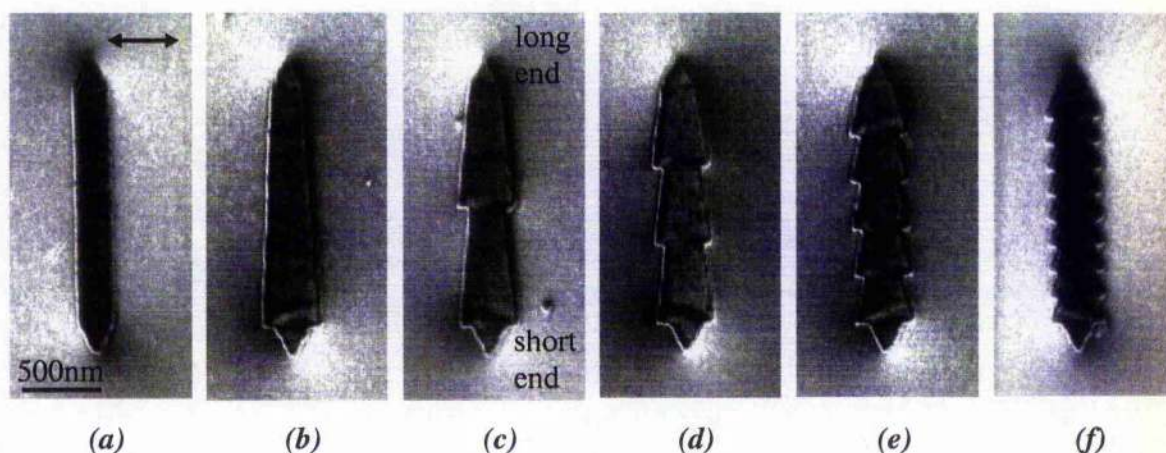


**Figure 4.4**

*Overview of Foucault images of ac-demagnetised elements with edge structure type B of different period. Mapping direction indicated by double arrow.*

In the case of structure type C the mean direction of magnetisation was also found to be parallel to the element length. The contrast variations, however, were much more pronounced than in the elements with the triangular edge structure types and they were not restricted to the edge regions. This is an indication that the rectangular structure type had a more significant impact on the magnetic microstructure (Fig. 4.5). Even domains with the direction of magnetisation antiparallel to the mean direction of magnetisation were

observed in many structure features for  $p \leq 1.0 \mu\text{m}$ . These locations are indicated by single arrows in Fig. 4.5.

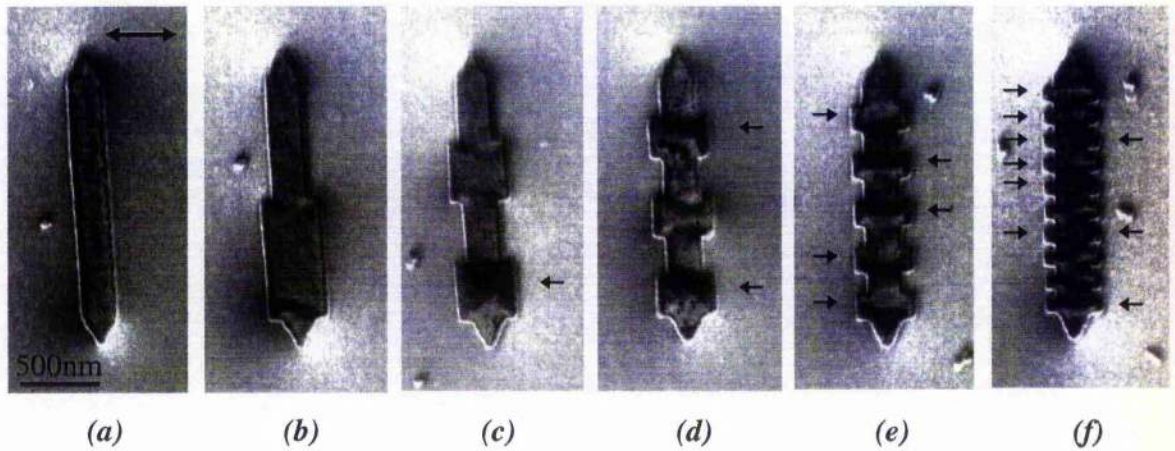


**Figure 4.5**

*Overview of Foucault images of ac-demagnetised elements with edge structure type C of different period. Mapping direction indicated by double arrow. Single arrows indicate domains with magnetisation direction antiparallel to the mean direction of magnetisation.*

As Foucault imaging is sensitive to the in-plane components of the magnetic induction for an untilted specimen, schematics can be derived from the Foucault images as shown in Fig. 4.6. Despite the mean direction of magnetisation (green arrows in Fig. 4.6) being parallel to the element length for all elements, the magnetisation also aligned parallel to the local edge in all cases. For structure type A this resulted in small domain wall sections appearing at the outer vertices of most elements as shown in Fig. 4.6(b). Exceptions were the elements with the longest ( $p=4.0 \mu\text{m}$  and  $2.0 \mu\text{m}$ , see Fig. 4.3(c)) and the smallest ( $p=0.1 \mu\text{m}$ ) structure periods where no such variations were observed.

In the case of structure type B, domain wall sections were associated with the outer vertices of the elements, in agreement with the observations made for structure type A. It was at these vertices where the most abrupt change of edge direction occurred which results in very localised strong contrast variations in the Foucault images as the direction of magnetisation changed by  $\approx 135^\circ$  for type B (Fig. 4.6(c)). This condition did not change with period, which is the reason for the constancy of the contrast variations of the type B structure. The only exceptions were the elements with the smallest period where the central part looked uniformly magnetised and only end domains were visible.

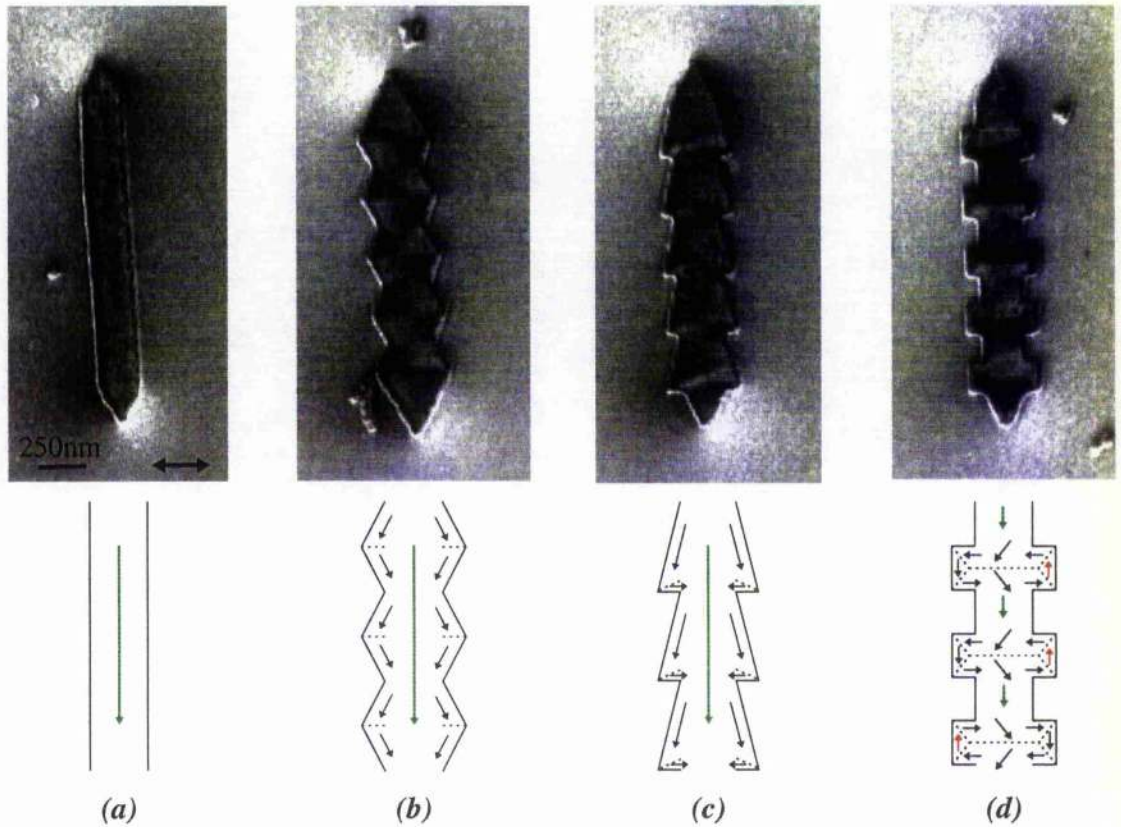


**Figure 4.6**

*Foucault images of elements with corresponding schematics of magnetisation direction in central part of the elements (i.e. the three inner pairs of structure features). Dashed lines show locations of domain walls, green arrows indicate the mean direction of magnetisation of the elements and red ones mark domains with the magnetisation being antiparallel to the mean direction of magnetisation. The mapping direction of Foucault images is indicated by double arrow.*

In the case of edge structure type C the generated wall sections were more pronounced. Small reverse domains (indicated by red arrows in Fig. 4.6(d)) associated with each structure period were observed and walls ran across the entire width of the elements at the widest parts as indicated in Fig. 4.6(d). The domain configurations within such pairs of structure features were similar to the flux closure structures observed in larger rectangular elements where the magnetisation remained parallel to the edges (Kirk et al, 1997), (McVitie et al, 1988) and they were observed in most elements with structure type C: In the case of elements with edge structure periods  $<1.0\mu\text{m}$  such domain configurations formed in several pairs of structure features.

Clearly the walls present in Figs. 4.3, 4.4, 4.5 and 4.6 arise directly due to the presence of the structured edges. Due to the thickness of the film ( $\approx 33\text{nm}$ ) the walls were expected to be of the Néel type (Hubert, 1998), (McVitie et al, 1997). It is however evident that the nature of these walls must be constricted in some way by the presence of the edge modulation. While the Néel walls normally present in permalloy films have widths of the order of hundreds of nanometres, the dimensions of the investigated structure features are smaller than that in many cases, but there was often a number of Néel walls present within these features.

Another important aspect arises from the consideration of the polarity of the Néel walls present in a flux closure like structure, which is illustrated by green and red arrows in Fig. 4.7. The Néel walls on the right hand side clearly possess opposite direction of magnetisation (polarity) and it is known that Bloch lines form where Néel walls with opposite polarity meet (McVitie et al, 1997), (Arrott et al, 1979). Therefore Bloch lines (solid circle in Fig. 4.7) ought to be expected for each flux closure like domain configuration even in the case of very thin films (sections 1.3.5, 1.5). This means, that out of plane components of the direction of magnetisation will be present in the case of flux closure and flux closure like domain configurations in films which are too thin for the generation of Bloch walls.

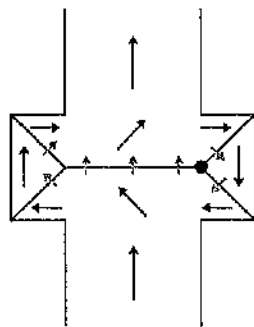


**Figure 4.7**

*Schematic of polarity of Néel walls within a pair of C type structure features. A Bloch line arises (solid circle) where Néel walls with opposite polarisation meet.*

#### 4.5 MAGNETISING EXPERIMENTS

Magnetising experiments were carried out to study differences in the reversal behaviour of the elements. All experiments described here were carried out on the Philips CM20 instrument using the Fresnel mode of Lorentz microscopy. The Fresnel mode was chosen as it is easier to implement than the Foucault mode and shows simple domain wall contrast in a single image in real time and is therefore more suited to dynamic experiments than Foucault imaging or DPC mode. After application of a large field ( $\geq 1000$  Oe) along their length, a reverse field was applied to the elements. In order to get information on reproducibility, the magnetising experiments were repeated several times. An overview of some elements in their remanent state (remanent state here means  $H_{in}=0$  Oe although  $H_{ob}\approx 1200$  Oe for all the images discussed in this chapter; section 2.2.5) as well as their state prior to switching is given in Fig. 4.8. The magnetic microstructure and reversal mechanism of elements with the triangular edge structure types (A and B) are similar for elements with the same period. Therefore the main focus of this discussion is on the standard elements and elements with edge structure types A and C.

As expected, the standard elements with  $w_1$  and  $w_2$  were single domain at remanence (Fig. 4.8(a)) and they were also uniformly magnetised after magnetisation reversal which was in agreement with earlier work (Kirk et al, 1997), (Kirk et al, 1999). In contrast to earlier observations however was the build up of domain structures near the element ends at the two inner corners of the element tips (marked with white arrows in Fig. 4.8(b)). The most likely reason for this difference is that the tip ratios of the earlier investigated elements were higher than for the elements described here. As illustrated in Fig. 4.9, smaller tip ratios result in a more pronounced kink of the element edge and therefore more notable deviations of the mean direction of magnetisation exist even at remanence especially in the case of tip ratios  $t < 2$ . This kink with its considerable change of magnetisation direction in the case of  $t=1$  (Fig. 4.9(a),  $\alpha_1=27^\circ$ ,  $\alpha_2=14^\circ$ ,  $\alpha_3=9^\circ$ ) makes the inner corners of the element tips natural nucleation sites. Another possibility is that the probability of the formation of such domain configurations increases with element width as most of the elements investigated here were wider than the elements in earlier experiments.

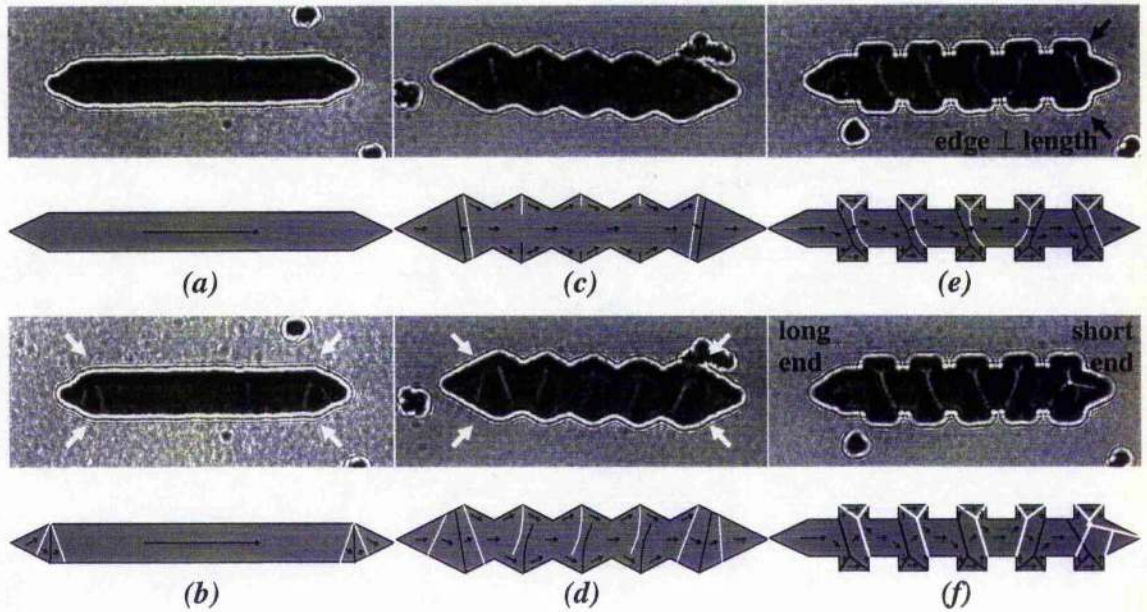


**Figure 4.8**

*Fresnel images taken during magnetising experiments with corresponding schematics showing the distribution of magnetisation within the elements. Upper row shows the elements in their remanent state and lower row just prior to switching. White arrows in the Fresnel images mark inner corners of element tips in (b) and domain configurations near element end in (d). Black arrows in the Fresnel image of (e) mark parts of the edge normal to the element length.*

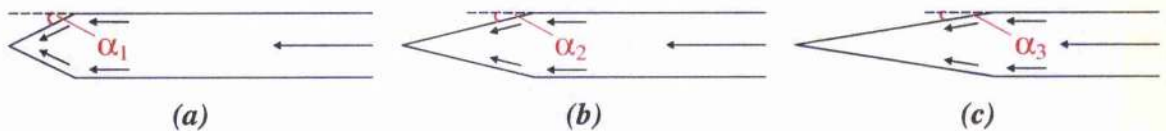


**Figure 4.9**

*Dependence of deviation of magnetisation direction at inner corners of tips on tip ratio. (a) Tip ratio  $t=1$ , (b)  $t=2$ , (c)  $t=3$ .  $\alpha$ : change of edge direction.*

The elements with triangular edge structures supported identical domain configurations in the ac-demagnetised state and at remanence (Figs. 4.3, 4.4 and 4.8). Applying a reverse field led to further development of the existing wall sections (Fig. 4.8(d)). Furthermore an increase of wall contrast was observed while the reverse field was increased indicating an increase in the angle of the domain walls. A pair of walls were observed per period at the widest parts of the element (i.e. one each from opposite outer vertices) and there were also very strong contrast changes noted near the ends of the

elements (marked with white arrows in Fig. 4.8(d)) which was consistent with the reversal mechanism in the standard elements (Fig. 4.8(b)). Notably the elements with the very small period ( $p=0.1\mu\text{m}$ ) of the triangular structure types showed a very similar behaviour to that of the standard elements. No walls were generated in the central part of these elements, not even prior to switching. The reversal itself was too rapid to observe with the elements being uniformly magnetised in the opposite direction after switching. The main difference between the two triangular edge structure types was the asymmetric behaviour of type B as far as the build up of the end domain structures is concerned. As in the case of structure type C the element end geometry was different. There was one long end and one short end (similar to that shown for type C in Fig. 4.8(f); see also Fig. 4.4(c)). Especially in the case of periods in the range  $4.0-0.33\mu\text{m}$  this gave rise to different domain configurations at the two element ends prior to switching.

The elements with structure type C no longer supported the small domains oppositely magnetised to the mean direction of magnetisation at remanence (Figs. 4.6(d), 4.8(e)). After relaxing from the saturated state a micromagnetic structure with a higher net magnetic moment compared to the ac-demagnetised state was observed with a pair of slightly bent y-shaped walls per structure period visible. It should be noted that in this case no Bloch lines needed to be generated as these domain configurations are non flux closure structures and therefore no singularities ought to be expected. Applying a reverse field led to an increase in contrast of these existing walls, indicating an increase in wall angle, with a slight straightening of them (Fig. 4.8(f)). Additional walls were generated only in the short end regions which was merely due to the geometry for structure type C where edge sections perpendicular to the element length exist close to the element end (as indicated by black arrows in the Fresnel image of Fig. 4.8(e)). In the case of structure type C with periods in the range  $4.0-0.33\mu\text{m}$  this was an asymmetric effect, as there is one long and one short end (e.g. Fig. 4.8(f)). For smaller structure periods however, edge sections, which were perpendicular to the element length existed close to both ends and the generation of additional walls became more common in both element ends.

For all the elements investigated here formation of a stable domain structure in the presence of a reverse field was observed. The actual switching process occurred at a well defined field and was too rapid to observe although it is very likely that reverse domains would be formed and grow rapidly in the presence of the external field. Increase of wall

contrast prior to switching indicated that some rotation of magnetisation was also taking place.

Initially, the standard elements with  $w_1$  and  $w_2$  were expected to be the magnetically hardest elements for each set but this was not the result of this experiment. The elements with structure type A with periods  $1.0\mu\text{m} < p \leq 2.0\mu\text{m}$  switched at even higher field values than the standard elements. In this experiment the generation of small domains close to the end of all elements appeared to be the major mechanism in the reversal process. An exception were the above mentioned elements ( $1.0\mu\text{m} < p \leq 2.0\mu\text{m}$ ). Figure 4.10 shows the change in the geometry of the vertex nearest to the tip for the standard element and that with structure type A with  $p=2.0\mu\text{m}$ .

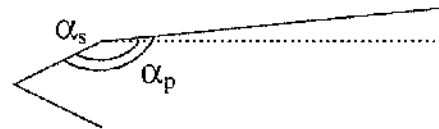


**Figure 4.10**

*Schematic of end geometry of element with structure type A of period  $p=2.0\mu\text{m}$ .  $\alpha_s$  denotes angle subtended at the end of the standard element and  $\alpha_p$  denotes angle subtended at the end of the element with  $p=2.0\mu\text{m}$ .*

The angle  $\alpha_p$  at the inner corner of the tip of the element with edge structure type A of  $p=2.0\mu\text{m}$  is noted to be blunter than the corresponding angle  $\alpha_s$  of a standard element and it would appear that this is the reason that nucleation of walls was found to be inhibited. For most periods of structure type A, a shift of the domain walls from the inner corners of the element tips towards the outer vertices of the edge structure next to the element end was observed (white arrows in Fresnel images of Figs. 4.8(b), (d)). In the case of the elements with periods  $1.0\mu\text{m} < p \leq 2.0\mu\text{m}$  there was no such shift apparent but the walls were formed at higher fields, with a resulting higher switching field.

Further it was found that during magnetising experiments the elements with structured edges not only generated domains near the tip regions of the elements but prior to switching formed reproducible multi-domain states which were strongly dependent on structure type and structure period. After magnetisation reversal, all elements with the triangular structure types supported uniform magnetisation in the presence of the reverse field. In the case of structure type C however, the magnetisation of the element had not

completely saturated for elements with periods  $p=0.2-0.3\mu\text{m}$ . In these cases small antiparallel domains as shown in Figs. 4.11(b) and (c) remained within the edge structures. Further increase of the applied field finally pushed these domains towards the edge before the element was finally saturated.

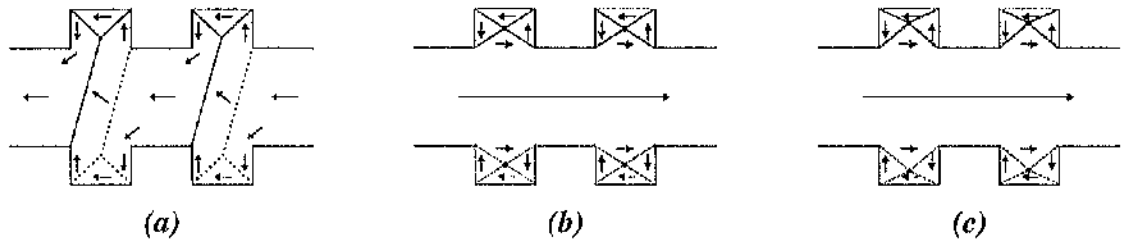
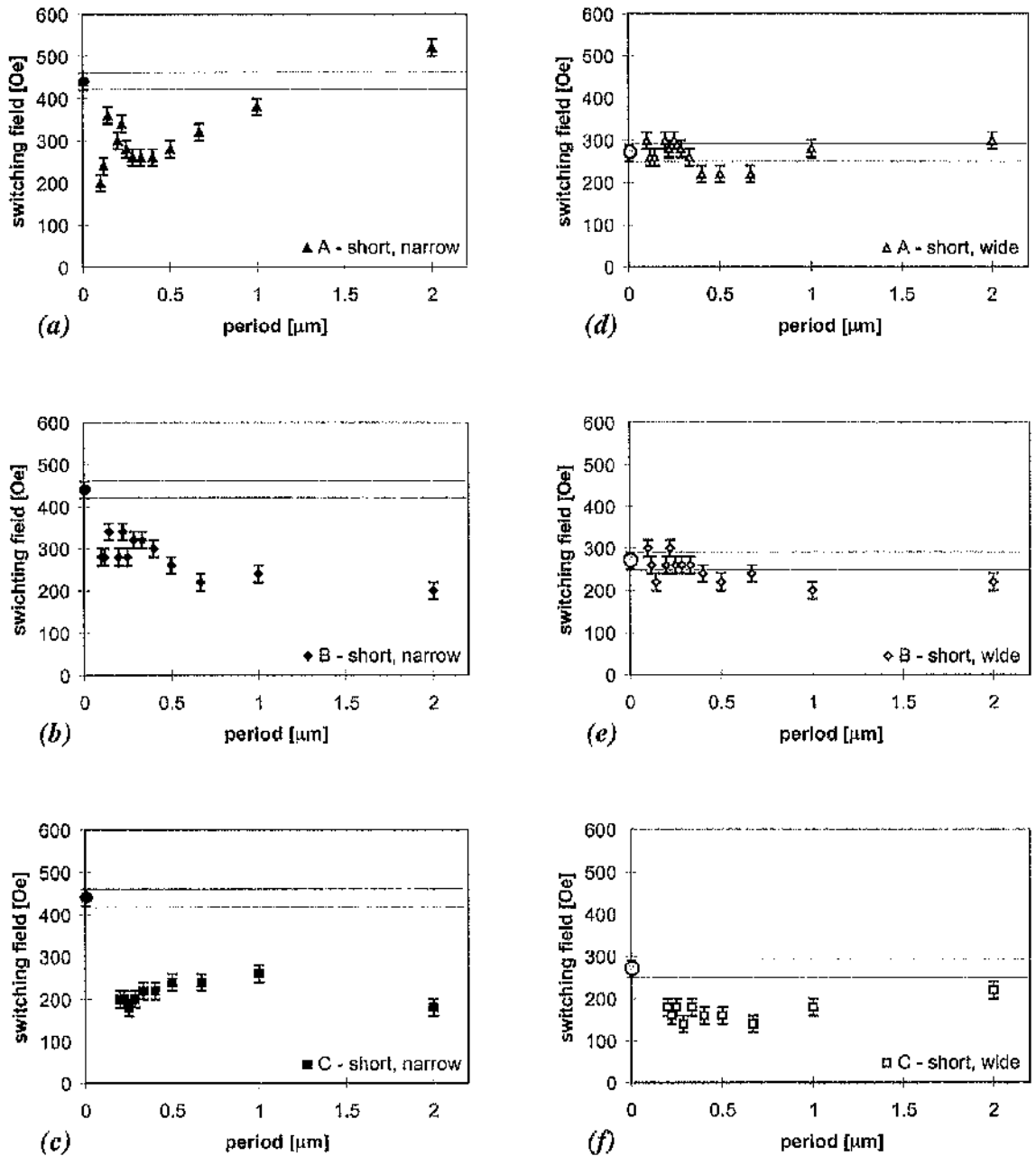


**Figure 4.11**

*Domain structures within the elements with structure type C with periods in the  $0.2-0.3\mu\text{m}$  range (a) prior to reversal, (b) and (c) after magnetisation reversal in the main body. The change from (b) to (c) is due to increase of the applied field.*

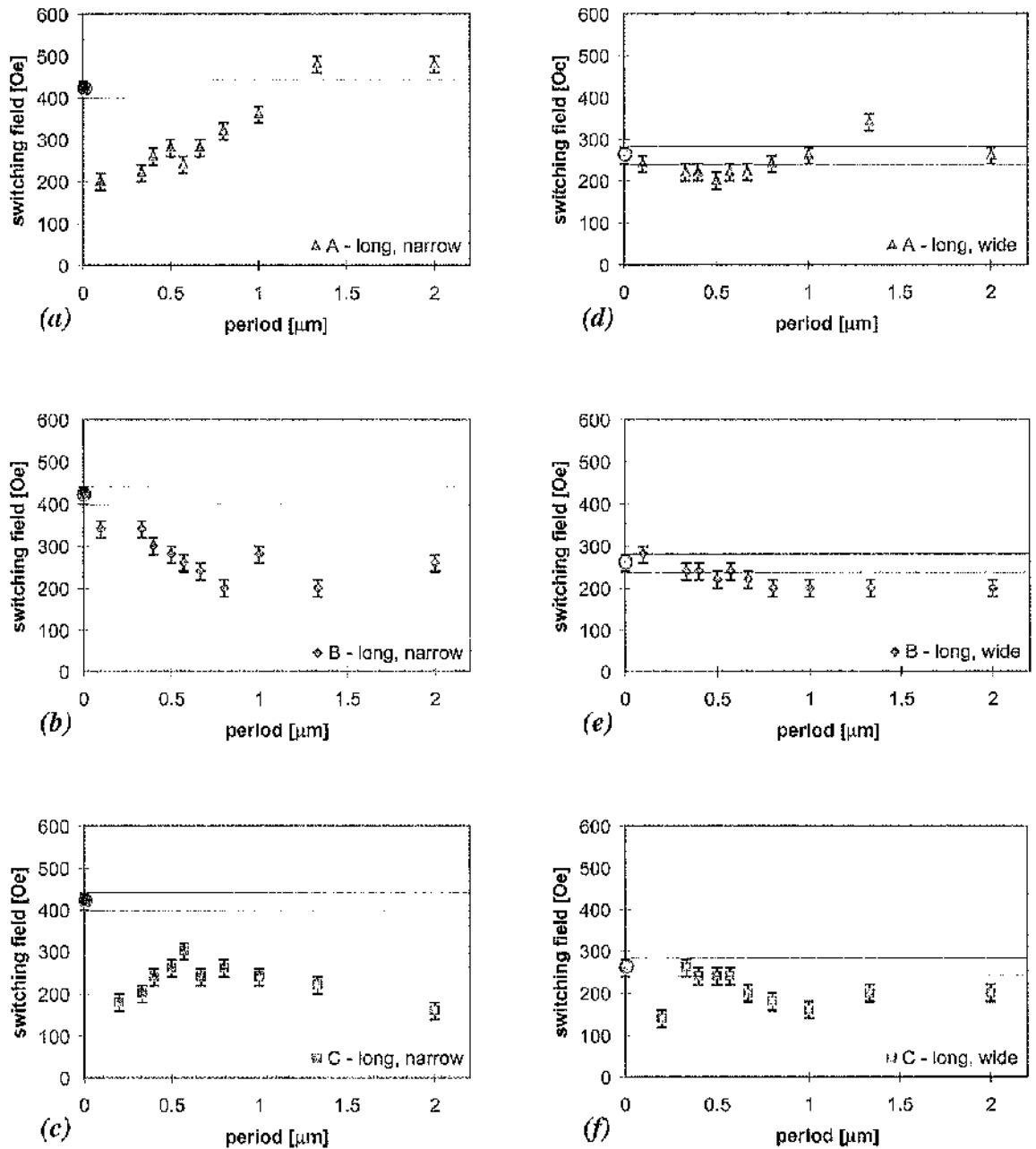
The switching field values for the standard elements with  $w_1$  and  $w_2$  (circles in Figs. 4.12 and 4.13) formed a reference with which to compare the results from the elements with structured edges. Due to the design error for the tips of the elements with  $w+2h$  it was not possible to ascertain the switching field range of the standard elements over the width variation present in the elements with structured edges for this pattern. The error bars mainly reflect the accuracy in the tilt angle setting of the goniometer in the electron microscope.

Fig. 4.12 shows an overview of switching field vs. structure period for short elements for both investigated widths with edge structure types A, B and C and Fig. 4.13 shows the results for the long elements. Apart from the wide elements with structure type C where the longer elements were harder to switch (Figs. 4.12(f) and 4.13(f)), all the other elements did not show a dependence of the switching field values on the element length. The narrow elements with structured edges were clearly easier to switch than their correlated standard elements with the exception of those with type A structure and periods in the range  $1.0\mu\text{m} < p \leq 2.0\mu\text{m}$  as discussed previously. Most wide elements had switching field values within and below the bandwidth of the switching field values (i.e. range of 40 Oe) of their corresponding standard elements.



**Figure 4.12**

Switching field values vs. structure period of short elements ( $l=2\mu\text{m}$ ) of first pattern of acicular elements with structure types A, B and C. (a)-(c) Narrow elements ( $w_1=250\text{nm}$ ); (d)-(f) wide elements ( $w_2=500\text{nm}$ ). Spread of switching field values of corresponding standard elements (circles) given for comparison.



**Figure 4.13**

Switching field values vs. structure period of long elements ( $l=4\mu\text{m}$ ) of first pattern of acicular elements with structure types A, B and C. (a)-(c) Narrow elements ( $w_1=250\text{nm}$ ); (d)-(f) wide elements ( $w_2=500\text{nm}$ ). Spread of switching field values of corresponding standard elements (circles) given for comparison.

## 4.6 SUMMARY

It was found that structuring the edges of acicular elements of a soft magnetic NiFe alloy led to changes in the magnetic microstructure compared to standard elements with straight edges. Magnetising experiments were carried out and in the case of the elements with structured edges variations of the magnetic microstructure were observed which were strongly dependent on the type and period of the edge structure. The main reversal mechanism for all investigated elements prior to switching was the formation of a domain structure near the element ends. In the case of the elements with structured edges reproducible multi-domain configurations were observed prior to switching. Most elements displayed domains close to ends of the elements even at remanence and the elements with edge structure type C were found to support characteristic multi-domain states under zero field conditions.

The observed effects for the switching field values are due to the structured edges themselves and are not associated with differences in the switching fields due to the natural edge acuity of the fabrication technique of the elements studied elsewhere (Gadbois et al, 1995). An interesting aspect of the behaviour of the elements with structured edges is that it appears that the switching field of acicular elements may be tailored by varying the type and period of edge structure.

In order to gain a more quantitative insight in the relevant structure parameters further experiments were carried out including the design of four more patterns. The patterns and the results of the experiments will be described in the following chapters.

**CHAPTER 5:****ACICULAR ELEMENTS WITH STRUCTURED EDGES OF TYPES A AND C****- SECOND AND THIRD PATTERN****5.1 INTRODUCTION**

As the first pattern, the second and third patterns were also designed with the intention to investigate the influence of structured edges on the micromagnetic states and reversal behaviour of acicular elements. All elements were now designed symmetrically in order to avoid the different end domain configurations observed in the previous chapter due to asymmetric end geometry. As the switching of most elements of the first pattern seemed to be triggered by the formation of end domains which nucleated at the inner corners of the element ends (section 4.5 and Figs. 4.8 and 4.9) the effects of more pointed tips needed to be evaluated. For this purpose the elements of these two patterns had different tip ratios. In the second pattern it was  $t_1=l_{tip}/w_{tip}=1$  as for the first pattern and sharper tips with  $t_2=2$  were designed for the third pattern.

It was decided to design short elements only as negligible differences were observed between the elements with the two lengths discussed in the previous chapter. The two widths however were retained. Structure type B was no longer designed and investigated as it was found to have strong similarities with structure type A (sections 4.4 and 4.5). With only two edge structure types and one element length there was enough room to vary the height of the structure features and three different heights were designed and investigated.

Another aim was to improve the statistics of the experiments by having at least five identical elements on one membrane. The material for all the elements discussed from here on was permalloy (Ni<sub>80at%</sub>Fe<sub>20at%</sub>) and the film thickness was  $\approx 22\text{nm}$  in all cases. The constancy of the film thickness was a result of the simultaneous metallization of four samples with the second and third patterns described in this chapter together with the fourth and fifth patterns which are discussed in chapter 6.

A description of the second and third patterns is given in section 5.2 and the physical microstructure of the elements is dealt with in section 5.3. The magnetic microstructure in the as-grown and ac-demagnetised state is discussed in section 5.4 and the results of the magnetising experiments are given in section 5.5. The chapter finishes with the summary in section 5.6.

## 5.2 DESCRIPTION OF PATTERNS

Figure 5.1 shows examples of all acicular elements of the third pattern. The entire pattern consisted of 12 arrays of elements, six arrays were standard elements and elements with structure type A and the remaining six arrays were type C elements and standard elements. In Fig. 5.1 only one row of each of the arrays is given for reference. The length of the base rectangle was  $2\mu\text{m}$  for all elements whereas two widths  $w_1$  and  $w_2$  were designed. The aspect ratio of the element tips was kept constant at  $t_2=2$  in this pattern whilst it was  $t_1=1$  in the second pattern. As a result of the different widths of the standard elements ( $w=250\text{-}1000\text{nm}$ ), the overall length of the standard elements varied from  $3.0\mu\text{m}$  to  $6.0\mu\text{m}$  as the tip length needed to be varied accordingly to keep the tip ratio constant. The lengths of the standard elements are given in the bottom half of Fig. 5.1. All narrow elements with structured edges were  $3.0\mu\text{m}$  long and the length of the wide elements with structured edges was  $4.0\mu\text{m}$ .

Structure features of three heights were designed for both structure types with  $h_1=50\text{nm}$ ,  $h_2=100\text{nm}$  and  $h_3=250\text{nm}$ . The number of different structure periods was reduced to five for each type. For type A they were  $p=2.0, 0.5, 0.33, 0.2$  and  $0.1\mu\text{m}$  and for type C  $p=2.0, 0.67, 0.33, 0.25$  and  $0.2\mu\text{m}$ . As a result of the reduction (no type B, only one (short) element length, reduced number of periods) there was space for 5-30 identical elements for each set of parameters therefore improving the statistics of the experiments. Standard elements of eight different widths were fabricated on one membrane for detailed monitoring of the changes in switching behaviour which were solely due to variation of the element width. The width and length of the standard elements is given in Fig. 5.1. The two left hand side columns in Fig. 5.1 were standard elements having a width ( $w$ ) of either  $w_1$  or  $w_2$  respectively  $w+2h$ . The resulting widths were in the range  $250\text{-}1000\text{nm}$  and they are given for each standard element in the upper half of the figure. Five squares with a side length of  $1.0\mu\text{m}$  were also designed in the middle of the pattern for control and alignment purposes. For an overview of the common parameters of the small magnetic elements see also section 'Symbols and Acronyms'.

The second pattern was similar to the third pattern except for the blunter element tips with an aspect ratio of  $t_1$  and a higher number of standard elements with  $w_1$  and  $w_2$  (30 instead of 20 elements). The overall length of the elements varied from  $2.5\mu\text{m}$  to  $4.0\mu\text{m}$  in

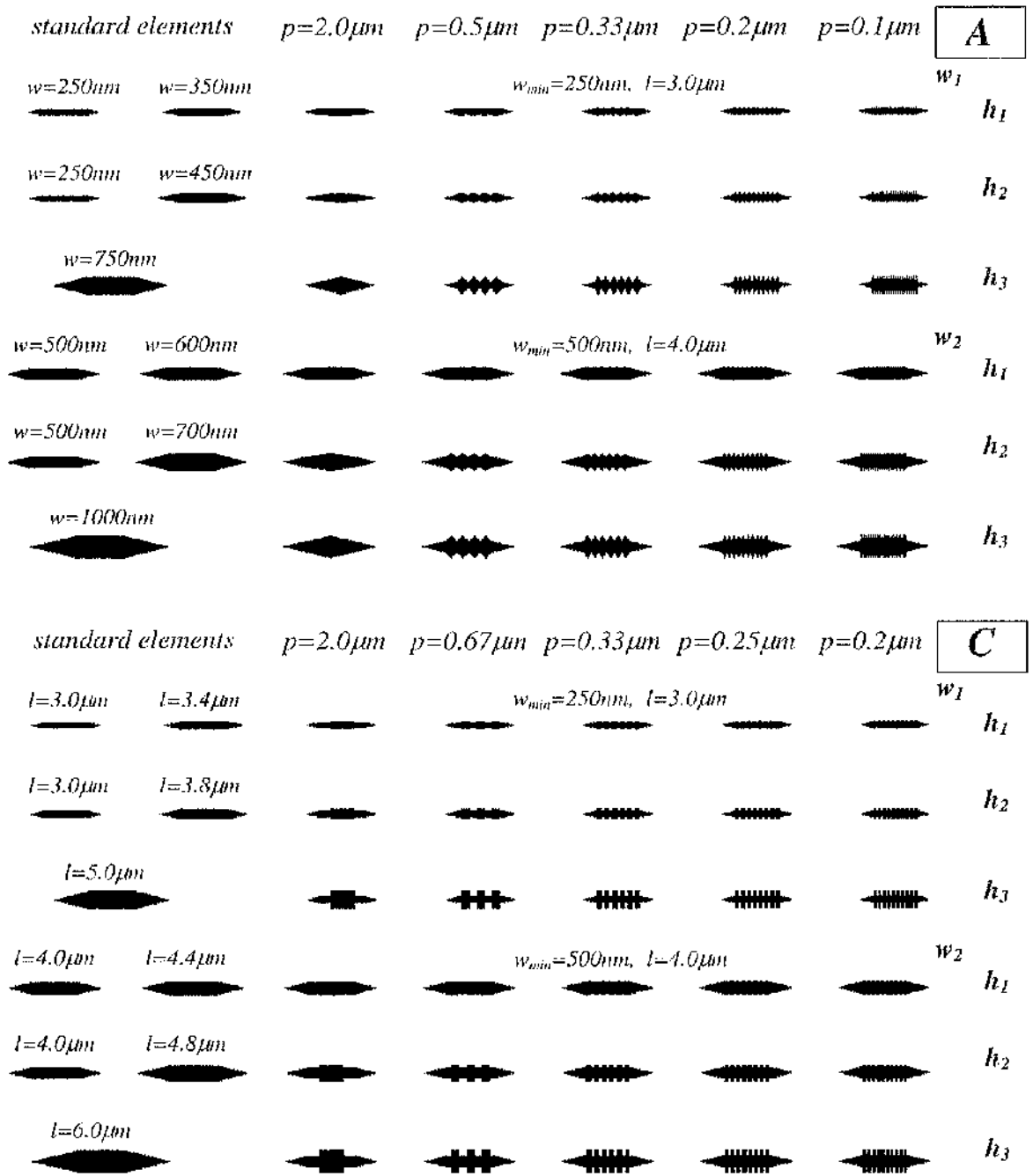


**Figure 5.1**

Standard elements and elements with edge structure types A and C of third pattern ( $t_2=2$ ).

Widths of main bodies ( $w_{\text{min}}$ ) of elements with structured edges:  $w_1=250\text{nm}$ ,  $w_2=500\text{nm}$ .

Heights of structure features:  $h_1=50\text{nm}$ ,  $h_2=100\text{nm}$ ,  $h_3=250\text{nm}$ .

the case of the standard elements and it was  $2.5\mu\text{m}$  for the narrow elements with structured edges and  $3.0\mu\text{m}$  for the wide elements with structured edges. The basic layout of the third pattern was almost identical to that of the second pattern.

### 5.3 PHYSICAL MICROSTRUCTURE

Bright field images of the elements were taken in the JEOL 2000 FX microscope in order to determine the physical microstructure of the film and the edge acuity of the elements. Examples of elements of the third pattern with the sharper tips with  $t_2$  are shown in Figs. 5.2 and 5.3.

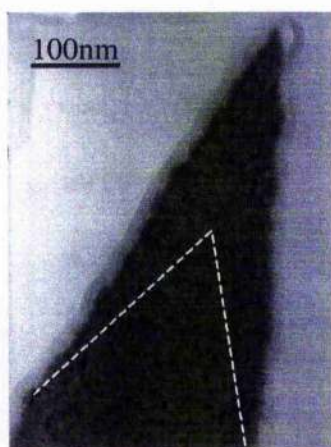


**Figure 5.2**

*High magnification bright field image of the tip of an acicular element with  $t_2=2$ . The dashed line indicates the tip geometry of the elements with  $t_1=1$ .*

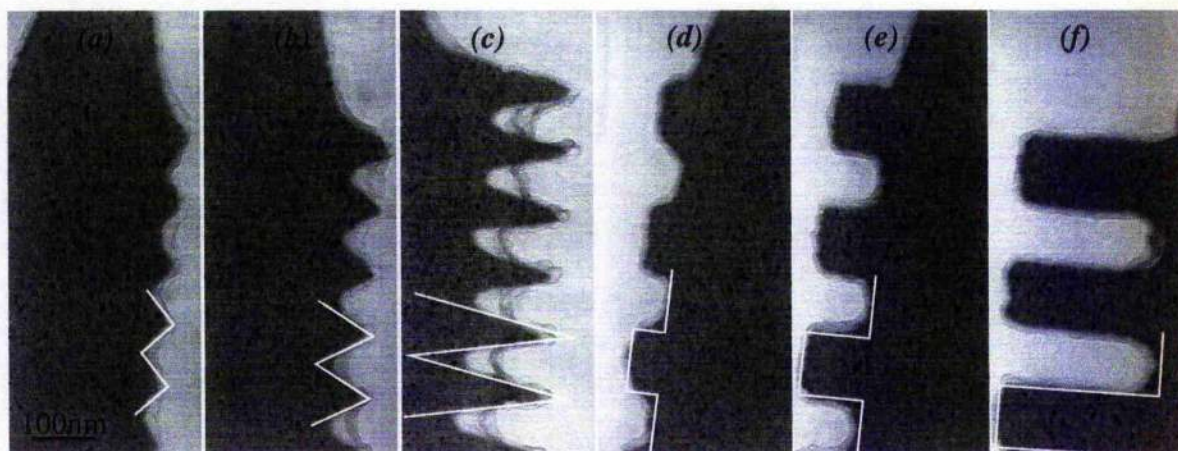


**Figure 5.3**

*Bright field images of elements with different structure height (third pattern).*

*(a)-(c) elements with structure type A; (d)-(f) elements with structure type C. White lines indicate designed edge structure.*

The film was micropoly-crystalline with an average grain size of 5-10nm. The edge acuity of the standard elements was in the usual range of 5-10nm and the pattern transfer was of good quality. The dashed line in Fig. 5.2 indicates the tip geometry of the blunter

tips with  $t_1$  of the second pattern. For the elements with structured edges it was easy to distinguish not only the different types of edge structure but also the variation of the structure height. Schematics of parts of the designed edges are overlaid in Fig. 5.3 in order to gauge the quality of pattern transfer.

In the case of structure type A the quality of the elements was good in terms of structure period, the pattern transfer however was less perfect as far as the actual structure shape and height was concerned. The height was reduced due to the e-beam writing process as discussed in section 3.4.1. The effects became more pronounced with decrease of period and increase of height. The worst case is illustrated in Fig. 5.3(c), where the actual height of the structure features was reduced to about half the designed height. Furthermore the vertices of the structure features were found to be rounded - most notably in the case of the smallest structure period  $p=0.1\mu\text{m}$  which is illustrated in Figs. 5.3(a)-(c). Especially the rounding of the inner vertices is an artefact of the writing process, too (proximity writing, section 3.4.1). This also led to variation of the actual minimum width depending on structure height and period. Values of the measured minimum width of the elements are given in table 5.1 for the narrow elements ( $w_1$ ) with  $h_2$  and  $h_3$ .

Variation of minimum width for elements with structure type A				
period	0.5 $\mu\text{m}$	0.33 $\mu\text{m}$	0.2 $\mu\text{m}$	0.1 $\mu\text{m}$
$w_{\text{min}}(h_2)$	(260 $\pm$ 20)nm	(290 $\pm$ 20)nm	(290 $\pm$ 20)nm	(320 $\pm$ 20)nm
$w_{\text{min}}(h_3)$	(280 $\pm$ 30)nm	(330 $\pm$ 30)nm	(360 $\pm$ 30)nm	(450 $\pm$ 30)nm

**Table 5.1**

*Dependence of minimum width of narrow elements with edge structure type A.*

*Nominal minimum width:  $w_1=250\text{nm}$ ; nominal structure heights:  $h_2=100\text{nm}$ ,  $h_3=250\text{nm}$ .*

The shape of the elements with type C structure was found to be very true to the design with both period and height of the structure features matching well with the designed shapes. The main deviation from the design in the case of structure type C was the rounding of the inner corners of the structure features. This can be seen in Figs. 5.3(d)-(f) where sections of such elements with structured edges are shown together with schematics of the edge design. Again this curvature appears to be an artefact of the writing process due to proximity writing (section 3.4.1).

For all elements there was residual PMMA visible mainly within the gaps of the structure features and often more pronounced for one side of the elements. The reason for this is not clear but higher amounts of remaining PMMA were not found to influence the quality of edge structure for the different element sides.

#### 5.4 AS-GROWN AND AC-DEMAGNETISED STATE

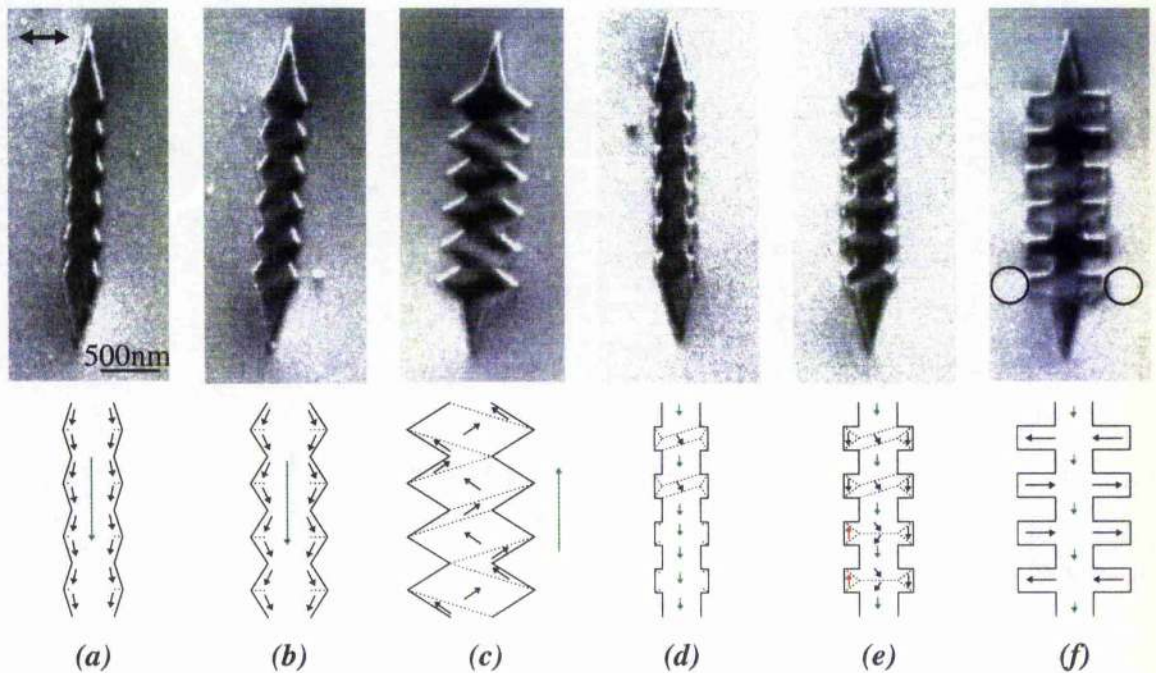
In order to gain insight in the magnetic microstructure of the elements of the second and third patterns Foucault images of the elements were taken in the JEOL 2000 FX microscope of the samples in the as-grown and ac-demagnetised states. As in the case of the first pattern, the differences between the micromagnetic configurations supported by the elements in both states were very small and as the ac-demagnetised state is a reproducible state, the emphasis of the discussion lies on the ac-demagnetised state.

Figure 5.4 shows an overview of Foucault images and schematics of the magnetisation distribution within the central part of the elements (i.e. the middle four structure periods) derived from the pictures. It should be noted that similar micromagnetic configurations were observed for identical structure parameters irrespective of the tip ratio. The elements shown in Fig. 5.4 are of the third pattern and therefore have a tip ratio  $t_2$ . Both structure types are compared in the figure with type A shown in Figs. 5.4(a)-(c) and elements with structure type C displayed in Figs. 5.4(d)-(f). The structure period is constant with  $p=0.33\mu\text{m}$  for all elements but an example is given for each of the three structure heights  $h_1$ ,  $h_2$  and  $h_3$ . The most striking observation was the increase of magnetic contrast with increase of structure height as can clearly be seen in Figs. 5.4(a)-(c) and (d)-(f).

The 'competition' between the overall shape anisotropy of the acicular elements which favoured alignment of the (mean) direction of magnetisation parallel to the element length with the local alignment of the magnetisation parallel to the closest edge led to different micromagnetic configurations within the elements with structured edges.

In the case of structure type A all elements were found to have a net resultant of magnetisation parallel to the element length. This was deduced from the stray fields at the element tips, which can be seen in Figs. 5.4(a)-(c). The mean direction of magnetisation is indicated by green arrows in the schematics. In the cases of the structure heights  $h_1$  and  $h_2$ , variation of direction of magnetisation was restricted to the edge regions with the contrast getting stronger for shorter periods and increase of structure height (Figs. 5.4(a), (b)). The

only exception were the elements with the longest and the shortest structure period ( $p=2.0$  and  $0.1\mu\text{m}$ ) where no contrast variations could be detected. Further increase of the structure height to 250nm led to a drastic change in magnetic microstructure in most cases. Not only were the observed contrast variations much stronger, but, even more important, they were no longer restricted to the edge regions for periods in the range  $0.1\text{-}0.5\mu\text{m}$ . Instead domains which extended over the entire element width were clearly visible in zero field conditions. While the mean direction of magnetisation was still parallel to the element length, strong variations of the magnetisation component parallel to the element width were detected. These were a result of the pronounced changes of the local edge direction leading to changes of the local direction of magnetisation which were strong enough for domain formation. An example for  $p=0.33\mu\text{m}$  is given in Fig. 5.4(c).



**Figure 5.4**

*Overview of Foucault images of ac-demagnetised elements with structured edges with schematics of magnetisation direction within the central four structure periods.*

*Mapping direction indicated by double arrow. Green arrows indicate mean direction of magnetisation. Fine structure in Foucault image of (f) not taken into account in schematic. Circles mark stray fields at the ends of the top pair of structure features.*

*Height of structure features: (a), (d)  $h_1=50\text{nm}$ , (b), (e)  $h_2=100\text{nm}$ , (c), (f)  $h_3=250\text{nm}$ .*

In the case of structure type C, the elements also had a notable resultant of the net magnetisation parallel to the element length with the magnetisation 'following' the local edge. This resulted in the generation of domain walls, which originated at the outer corners of the structure features. In the case of  $h_1$ , this led to the formation of wall sections as well as faint double y-configurations (Fig. 5.4 (d)).

The elements with  $h_2$  were found to support the flux closure like domain configuration in some pairs of structure features, but more commonly the double y-configuration (Foucault image in Fig. 5.4(e)). The small domains with magnetisation direction antiparallel to the mean direction of magnetisation which are associated with the flux closure like domain configuration are again illustrated by red arrows in the schematic of Fig. 5.4(e). The flux closure like configurations were however found to be less common in the second and third patterns than in the first pattern (chapter 4, Fig. 4.5).

Further increase of the structure height ( $h_3$ ) led to a drastic change of the micromagnetic characteristics of such elements. Most notable was the fact that stray fields like those at the ends of the structure features in Fig. 5.4(f) were clearly visible (stray fields at the ends of the bottom pair of structure features are marked by circles in the Foucault image of Fig. 5.4(f)). The intensity of these stray fields was similar to that at the element tips. This is an indication that this kind of edge structure led to the generation of bar magnet like features which were oriented parallel to the element width, i.e. orthogonal to the mean direction of magnetisation. In the case of superposition of these 'bar magnets' with the basic acicular element the bar magnets even seemed to locally outweigh the overall shape anisotropy of such elements. There is some fine structure visible in the Foucault image of Fig. 5.4(f), but it is not clear enough to introduce it in the corresponding schematic. The bar magnet like mean direction of magnetisation within the pairs of structure features, however, is easy to deduce and illustrated by the black arrows in the schematic. The magnetic microstructure of elements with even smaller periods  $p < 0.33 \mu\text{m}$  looked very much like that in Fig. 5.4(f), whereas in the case of  $p \geq 0.5 \mu\text{m}$  flux closure like domain configurations similar to those shown in Fig. 5.4(e) were observed within all these structure features.

With the observation and characterisation of the domain configurations of the elements in zero field conditions completed, the behaviour of the elements when subjected to external fields was investigated next. In-situ magnetising experiments were carried out and these are discussed in the next section.

## 5.5 MAGNETISING EXPERIMENTS

The magnetising experiments were carried out in the Philips CM20 FEG microscope by tilting the sample in the vertical field of the standard objective lens (section 2.2.5). The vertical field was  $\approx 700$  Oe in the case of the second pattern and  $\approx 950$  Oe in the case of the third pattern. The reversal processes were monitored in the Fresnel mode. For some of the elements DPC images were also recorded at different stages of the magnetising experiments.

The discussion of magnetic microstructure focuses on the elements of the third pattern ( $t_2$ ). The main reason for this was that the build up of domain configurations in the standard elements prior to switching could be observed in more detail for the elements with  $t_2$ . In agreement with the standard elements with  $t_1$  it was found that domain formation started at the element ends and in the case of the elements with  $t_2$  these developed into concertina like domain configurations often extending over the entire element. In order to evaluate the effects which are solely due to the edge structure it was then of course necessary to compare the findings of the standard elements with the sharper tips with the observations of the elements with the same tip ratio but structured edges.

For reasons of clarity and comparability with chapter 4 as well as in an attempt to restrict this thesis to a reasonable length, only the magnetic microstructures of the standard elements (section 5.5.1) and narrow ( $w_1$ ) structured elements with  $h_2$  are discussed in detail (sections 5.5.2 and 5.5.3). Overviews of the observed magnetic microstructures are given for all narrow elements and the switching field values are compared for all elements of both patterns.

It should be noted that magnetisation reversal generally occurred very quickly for all investigated elements independently of tip ratio and edge structure variables. The magnetisation was observed to switch in an instant, too rapidly to observe any reversal details in the electron microscope. In the following sections the magnetic behaviour up to the switching field is discussed in detail. Simulations were also carried out in this work in order to shed some light on the reversal processes and they are discussed in chapter 7.

## 5.5.1 STANDARD ELEMENTS

Figure 5.5 shows an overview of Fresnel images of one of the narrowest standard elements ( $w_1$ ) recorded during a magnetising cycle together with schematics of the magnetisation distribution for the different stages.

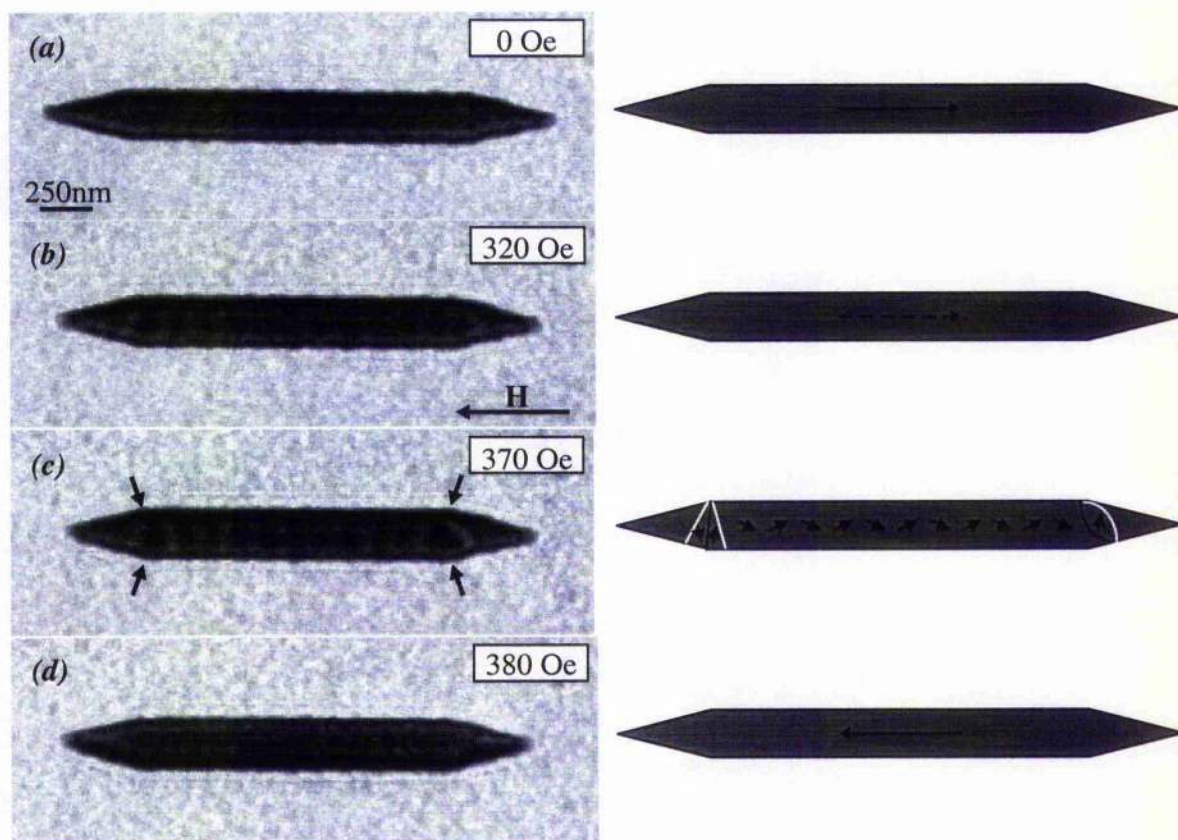


**Figure 5.5**

*Fresnel images of standard element with  $w=250\text{nm}$  recorded during magnetising sequence with corresponding schematics of magnetisation distribution. Arrows in Fresnel image (c) mark inner corners of element tips. The wall configuration at the right hand side of the schematic in (c) is incomplete and is dealt with in detail in Fig. 5.6(c).*

At remanence (Fig. 5.5(a)) the elements were clearly single domain with the magnetisation direction being parallel to the element length. When a reverse field was applied faint contrast variations appeared within the entire element (Fig. 5.5(b)). The intensity of these contrast variations increased with increase of the external field. Especially at the inner corners of the element tips (marked with arrows in the Fresnel

image of Fig. 5.5(c)) walls running across the element width were clearly visible. It appears as if there were different domain configurations present at the two ends of this element which are illustrated in more detail in the schematic of this magnetisation state. The configuration at the right hand side of the element was by far the most commonly observed for the permalloy elements. It should, however, be noted that this domain configuration which was deduced from the Fresnel image in Fig. 5.5(c) is not complete in the corresponding schematic and this is discussed in the following paragraph. The contrast variations in the central part of the element in Fig. 5.5(c) were more pronounced compared to Fig. 5.5(b) indicating ripple like dispersion of the magnetisation / low angle walls. After magnetisation reversal the element was single domain (Fig. 5.5(d)).

In order to describe the build up of domain configurations prior to switching, the convention introduced by van den Berg (van den Berg et al, 1981) is applied. Groups of domain walls are called clusters and the most relevant clusters in our case are so-called edge clusters. An edge cluster is formed where a number of walls intersect in a point at the edge of a sample. In general many walls may be involved in the formation of an edge cluster, but in the case of small magnetic elements, where the magnetisation is known to align parallel to the element edges, two principal cases of wall clusters ought to be expected and these are illustrated in Fig. 5.6.

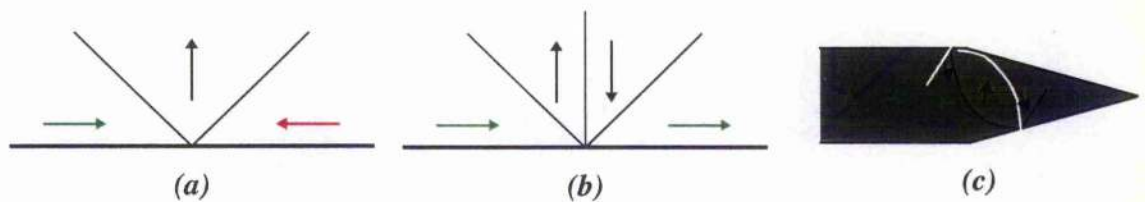


**Figure 5.6**

*Schematics of (a) doublet and (b) triplet clusters and (c) detailed schematic of domain configuration at right hand side end of element in Fig. 5.5(c).*

In the case of antiparallel alignment of the magnetisation either side of the cluster, a doublet cluster (in general: 'even' clusters) will be generated (Fig. 5.6(a)) whereas parallel alignment of the magnetisation direction either side of the cluster leads to the formation of 'odd' clusters, with the most common being triplet clusters (Fig. 5.6(b)). As the direction of magnetisation either side of the edge cluster in the acicular elements is  $\approx$ parallel, triplet clusters ought to be expected as illustrated in Fig. 5.6(c). This does not contradict the

observations in the Fresnel images of Fig. 5.5 as one of the walls can be considerably fainter than the two clearly visible walls which were deduced for the schematic of Fig. 5.5(c). Simulations which were carried out in this work supported the formation of triplet clusters (section 7.4.1.1). Triplet clusters were also clearly observed in the case of wider elements which is discussed next.

Figure 5.7 shows Fresnel images of a wider standard element ( $w_2$ ) recorded during a magnetising experiment. Like the narrow element it was single domain at remanence (Fig. 5.7(a)) with the direction of magnetisation parallel to the element length.

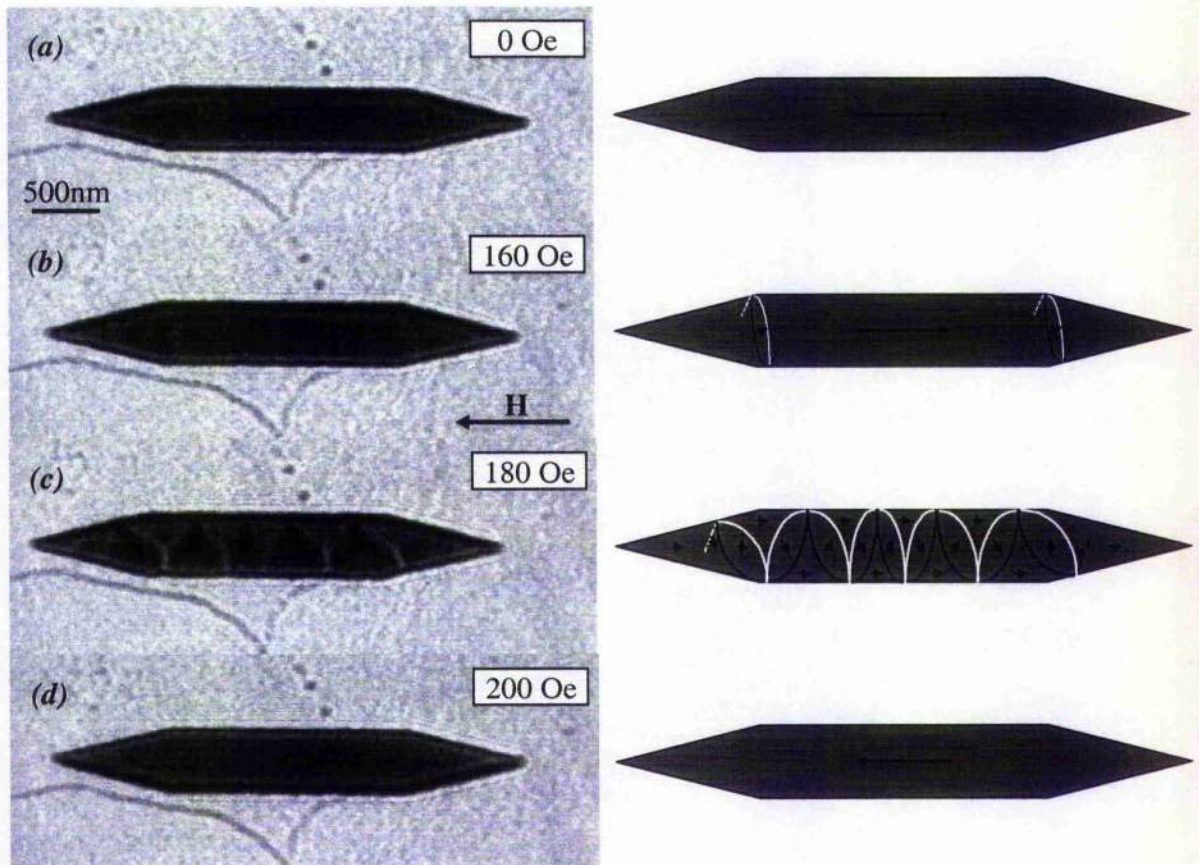


**Figure 5.7**

*Fresnel images of standard element with  $w=500\text{nm}$  recorded during magnetising sequence with corresponding schematics of magnetisation distribution.*

Application of a reverse field led at first to the generation of very faint low angle walls, which originated at the inner corners of the element tips (Fig. 5.7(b)). Further increase of the applied reverse field not only resulted in the build up of a concertina like domain structure prior to switching but all edge clusters were clearly triplet clusters at this

stage (Fig. 5.7(c)). It should be noted that the observed walls were not straight, however the curvature of the walls in the schematic of Fig. 5.7(c) is exaggerated. After magnetisation reversal the element was again uniformly magnetised (Fig. 5.7(d)). Although the concertina structure was observed very frequently in the wider elements, it was a rather volatile state and therefore sometimes difficult to record before switching.

More detailed information about the micromagnetic configurations was revealed by DPC images. Images acquired by DPC are taken point by point (STEM, section 2.3.3) and this means that DPC imaging is considerably more time intensive than taking Fresnel pictures. Therefore only a few DPC images were recorded of interesting magnetisation states which were determined in the Fresnel experiments. Figure 5.8 shows an overview of a square at remanence (to illustrate the contrast variation depending on the mapping direction) and images of the end region of a 500nm wide standard element with  $t_2$  prior to switching.

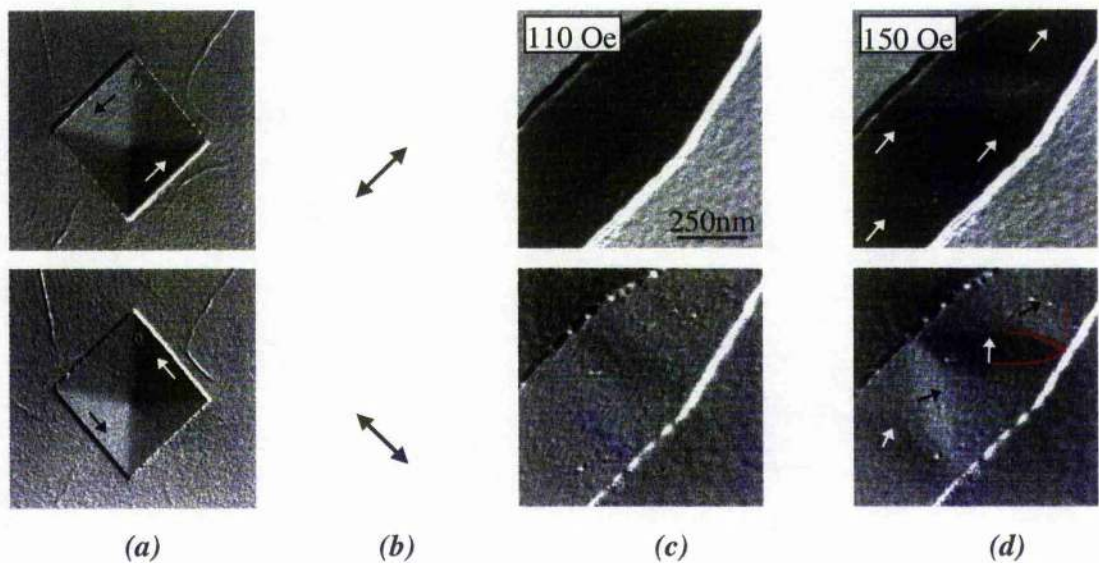


**Figure 5.8**

*DPC images of small magnetic elements.*

*(a)  $1 \times 1 \mu\text{m}^2$  square at remanence; (b) mapping direction; (c), (d) standard element with  $w=500\text{nm}$  and  $t_2=2$  at different field values, arrows in (d) indicate magnetisation distribution. Red lines indicate domain wall sections.*

The contrast variation within the element while mapping parallel to the length was negligible as expected given the strong shape anisotropy of the element and it was also in

agreement with the interpretation of the Fresnel images (Fig. 5.7). Mapping parallel to the element width however clearly revealed the ongoing changes. The build up of the concertina structure starting from the tip regions of the element can clearly be observed as shown in Figs. 5.8(c) and (d). In column (d) of the figure arrows were overlaid to indicate the magnetisation direction present in different parts of the element. Furthermore red lines are used to illustrate wall sections forming a triplet cluster.

All standard elements investigated here were clearly found to form multi-domain states prior to switching. Domain formation started in the transition region between tip and main body of the elements (i.e. 'kinks'; see Fig. 4.9). Domain configurations which were associated with these kink regions of the elements are termed 'end domains' throughout this thesis even if the kink region was not really close to the element ends (as in the case of the wider standard elements with  $t_2$  tips, Fig. 5.9(c)). Extended concertina structures were commonly observed for element widths  $w \geq 350\text{nm}$  with the curvature of the domain walls becoming more pronounced with increase of element width. Figure 5.9 shows the build up of a concertina structure in one of the widest elements fabricated for this work ( $w=1000\text{nm}$ ) of the third pattern. In agreement with the observations of the narrower element discussed in previous sections (Fig. 5.7) it was single domain at remanence. When a reverse field was applied, curved domain walls were generated and a concertina structure formed (Fig. 5.9(b)). The wall curvature was observed to increase considerably during further development of the domain structure (Fig. 5.9(c)). The red ellipse in Fig. 5.9(c) marks the part of the domain structure which was also frequently observed in the case of the widest standard elements of the second pattern ( $t_1$ ). It should be noted that this (end) domain configuration contains two triplet clusters.



**Figure 5.9**

*Fresnel images of standard element with  $w=1000\text{nm}$  and  $t_2=2$  recorded during magnetising sequence; magnetisation reversal occurred at  $(100 \pm 20)$  Oe. End domains similar to that marked with the red ellipse were frequently observed in the case of standard elements with the same width and  $t_1=1$ .*

In agreement with the results discussed so far the standard elements of the second pattern with  $t_1$  were found to be single domain at remanence. Prior to switching the development of end domains similar to those shown in Fig. 5.7(b) was observed for all elements with  $t_1$ . Growth of these end domains and increase of wall contrast was common whereas all three walls of the triplet clusters were only clearly observed in the case of the widest elements. The appearance of such end domains was similar to the domain configuration within the red ellipse in Fig. 5.9(c). No further development in a concertina like domain configuration was however observed in the case of the elements with  $t_1$  before the magnetisation switched. A brief overview of the micromagnetic configurations observed in the standard elements of the second and third pattern is given in table 5.2. The magnetic microstructures of the elements are described at remanence and prior to switching.

Standard Elements		
state	Second Pattern; $t_1=1$	Third Pattern; $t_2=2$
		Figs. 5.5-5.9
R	single domain	single domain
PS	end domains	mainly concertina

**Table 5.2**

*Micromagnetic states of standard elements of 2<sup>nd</sup> and 3<sup>rd</sup> patterns.*

*R: Remanent state, PS: Prior to switching.*

The main difference between standard elements with the same tip ratio but different widths was the monotonic decrease of switching field values for an increase of element width. This is illustrated in Fig. 5.10 for the two sets of standard elements of the second and third patterns. The difference for the two investigated tip ratios was that the elements with the sharper tips ( $t_2$ ) were found to be magnetically harder indicating the importance of the tip geometry. The monotonic decrease of the coercivity with increase of the element width as well as the dependence of the coercivity of acicular elements on the tip geometry is in agreement with earlier work (Kirk et al, 1999). The error bars in Fig. 5.10 are mainly a measure for the uncertainty of the tilt angle of the goniometer.

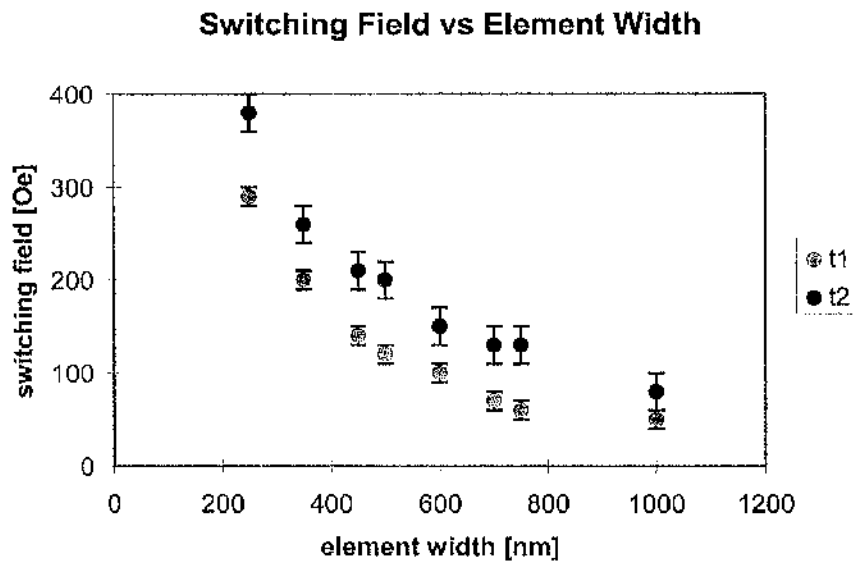


**Figure 5.10**

*Switching field values of standard elements of second and third pattern of acicular elements versus element width; tip ratio  $t_1=1$  (second pattern),  $t_2=2$  (third pattern).*

### 5.5.2 ELEMENTS WITH EDGE STRUCTURE TYPE A

Magnetising experiments involving detailed observation of the magnetic microstructures were also carried out with the elements with structured edges. As already mentioned detailed description is restricted to elements with  $t_2$  and  $h_2$ . It should be noted, that the magnetic microstructures, which were observed at remanence in the case of elements with edge structure type A agreed well with the ac-demagnetised state of these elements (Fig. 5.4).

In order to make presentation of the results easier, a summary is given beforehand in table 5.3. In this table the magnetic microstructures in narrow elements ( $w_1$ ) with edge structure type A of the third pattern ( $t_2$ ) are described for the remanent state and prior to switching. For the benefit of clarity the descriptions used in the table were kept as compact as possible and in agreement with common terminology or terms introduced in this thesis. The emphasis lay on similarities instead of detailed elaboration of small differences. The applied terminology is as follows: 'Single domain' describes uniformly magnetised elements, 'quasi single domain' is used for almost uniformly magnetised elements (e.g. wall segments present at edge vertices due to local variation of magnetisation direction as a

result of the variation of edge direction). 'Concertina' summarises domain configurations with strong similarities to concertina structures when the domain formation started at the element ends as a result of tip geometry. 'Concertina\*' on the other hand describes concertina structures which developed from the centre of the elements due to the structuring of the edge. 'Parallelogram domains' is the term, which was introduced for the most characteristic domain shape observed in the case of structure type A.

Structure Type A, Width $w_1$ - Third pattern				
period	state	$h_1=50\text{nm}$	$h_2=100\text{nm}$	$h_3=250\text{nm}$
2.0 $\mu\text{m}$	R	single domain	single domain	quasi single domain
	PS	concertina	concertina*	concertina*
0.5 $\mu\text{m}$	R	single domain	quasi single domain	parallelogram domains
	PS	parallelogram domains	parallelogram domains	parallelogram domains
0.33 $\mu\text{m}$	R	quasi single domain	quasi single domain	parallelogram domains
	PS	parallelogram domains	parallelogram domains	parallelogram domains
0.2 $\mu\text{m}$	R	quasi single domain	quasi single domain	parallelogram domains
	PS	parallelogram domains	parallelogram domains	walls move and merge
0.1 $\mu\text{m}$	R	single domain	single domain	low angle walls
	PS	concertina	concertina	concertina

**Table 5.3**

*Micromagnetic states of elements with  $w_1$  and structure type A of 3<sup>rd</sup> pattern ( $t_2=2$ ).*

*R: Remanent state, PS: Prior to switching.*

Comparison of elements with identical structure parameters but different tip ratios (second pattern,  $t_1$ ; third pattern  $t_2$ ) showed that any differences were almost negligible. This indicates, that the tip ratio of the elements did not have a marked influence on the magnetic states of elements with structured edges and the overview given in table 5.3 for the third pattern is also valid for most of the elements of the second pattern. Exceptions were the elements with  $p=2.0\mu\text{m}$  and  $h_1$ , where instead of the concertina structure only magnetic dispersion was observed prior to switching. Some of the elements with  $h_2$  and

$p=0.33\mu\text{m}$  and  $p=0.2\mu\text{m}$  were also found to possess faint end domains at remanence (low angle walls similar to those illustrated in Fig. 5.14(a)). The domain configurations, which were observed in the case of the wider elements did not show different characteristics to those described here for the narrow elements. This is in agreement with the investigation of the standard elements with different widths ( $350\text{nm}\leq w\leq 1000\text{nm}$ ), which were also found to generate similar domain structures in our experiments.

This means that it was almost exclusively the edge structure parameters which determined the magnetic microstructure of the small magnetic elements with the characteristic feature of structure type A being the parallelogram domains. As can be seen in table 5.3 these domains were not observed for the longest and the shortest investigated periods ( $p=2\mu\text{m}$  and  $p=0.1\mu\text{m}$ ). This suggests that there is a critical range of values for the edge structure parameters as far as the magnetic microstructure is concerned and that outside this range structuring of element edges does not considerably alter the magnetic microstructure of such elements compared to standard elements.

A first example of the detailed observations made during magnetising experiments with the narrow elements ( $w_1$ ) is given in Fig. 5.11 and shows domain configurations in an element with type A edge structure with  $h_2$  and the longest period ( $p=2.0\mu\text{m}$ ) at different stages of a magnetising cycle. At remanence (Fig. 5.11(a)) the element was uniformly magnetised (single domain). Subjecting the element to a reverse field, low angle domain walls were generated in the central part of the element close to the outer vertices of the structure features. It should be noted, that no end domains were observed for this kind of element. This is in agreement with the findings in section 4.5 (Fig. 4.10) where it was found that a blunter tip angle  $\alpha_p$  inhibited the generation of walls at the tip region. However the domain structure in the centre developed in a concertina\* configuration (Figs. 5.11(b), (c)) and after rapid magnetisation reversal the element possessed a single domain state (Fig. 5.11(d)).

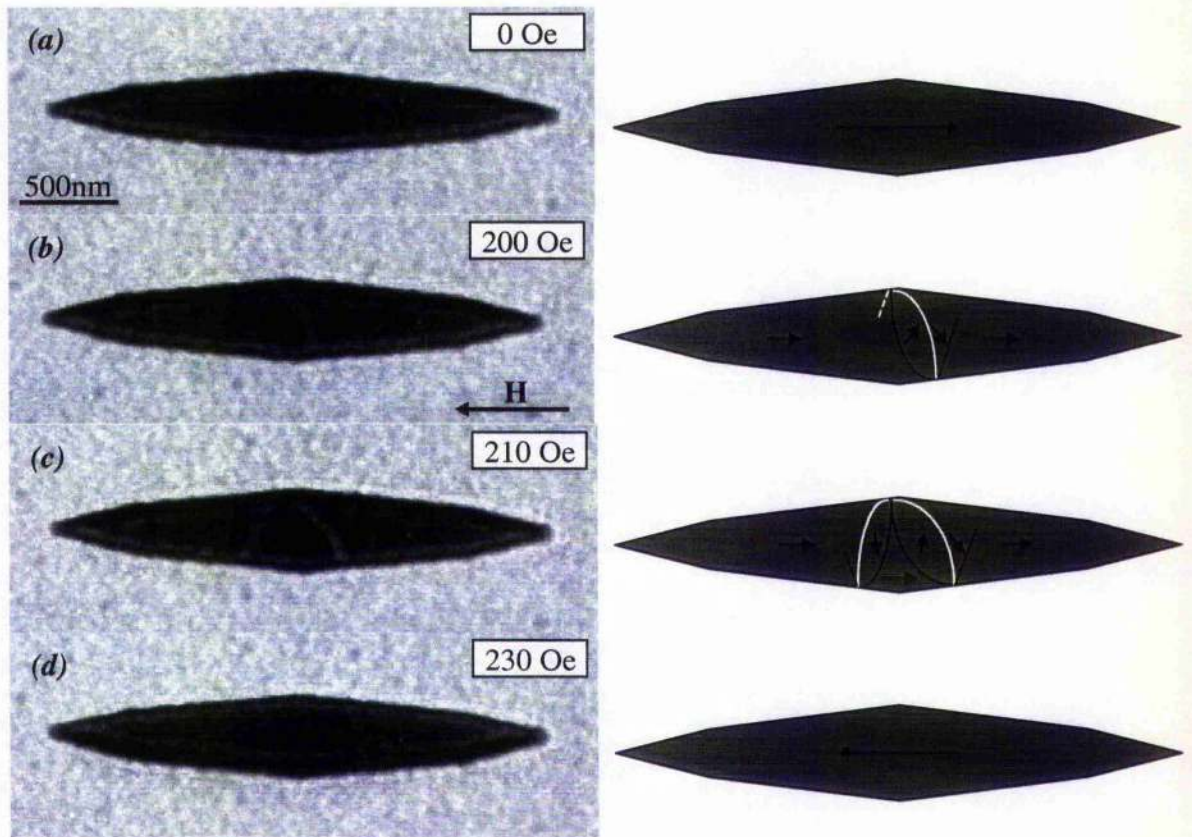


**Figure 5.11**

*Fresnel images of element with structure type A ( $p=2.0\mu\text{m}$ ) recorded during magnetising sequence with corresponding schematics of magnetisation distribution.*

Decreasing the period of the edge structure changed the micromagnetic states of the elements. Fig. 5.12 shows some images of an element with edge structure type A of a period  $p=0.5\mu\text{m}$  taken during a magnetising cycle. Despite the different tip ratio the magnetic microstructure looked very much like that observed in similar elements of the first pattern of acicular elements (section 4.5, Fig. 4.8).

At remanence the elements were quasi single domain with only very faint wall sections visible originating at the outer vertices of the structure features (Fig. 5.12(a)). The wall sections developed in length until they ran across the entire width of the element when subjected to a reverse field. Thus, two walls per period were generated which were  $\approx$  parallel to each other and therefore resulted in one 'parallelogram domain' per period. At a higher field, the wall contrast increased which was an indication for magnetisation rotation and there was also some change of the domain sizes observed; the parallelogram domains (one of them is highlighted by the red area in the schematic of Fig. 5.12(c)) grew

at the expense of the other domains (Figs. 5.12(b), (c)). The domains close to the element ends were associated with the structure features themselves instead of the tip. This was due to the geometry of the element as there was hardly a corner or kink present at the transition from the element tip to the main body of the element. The resulting change of edge direction and correspondingly the change of magnetisation direction was therefore less abrupt at the 'inner corners' of the tip (marked by 'c' in Fig. 5.12(b)) than at the outer vertices of the structure features (i.e. where wall segments already existed at remanence; marked by 'o' in Fig. 5.12.(b)). It should be noted, that this observation agrees with findings discussed in section 4.5 where a shift of the domain walls from the inner corners of the element tips to the outer vertices of the nearest structure feature was also observed for certain elements.

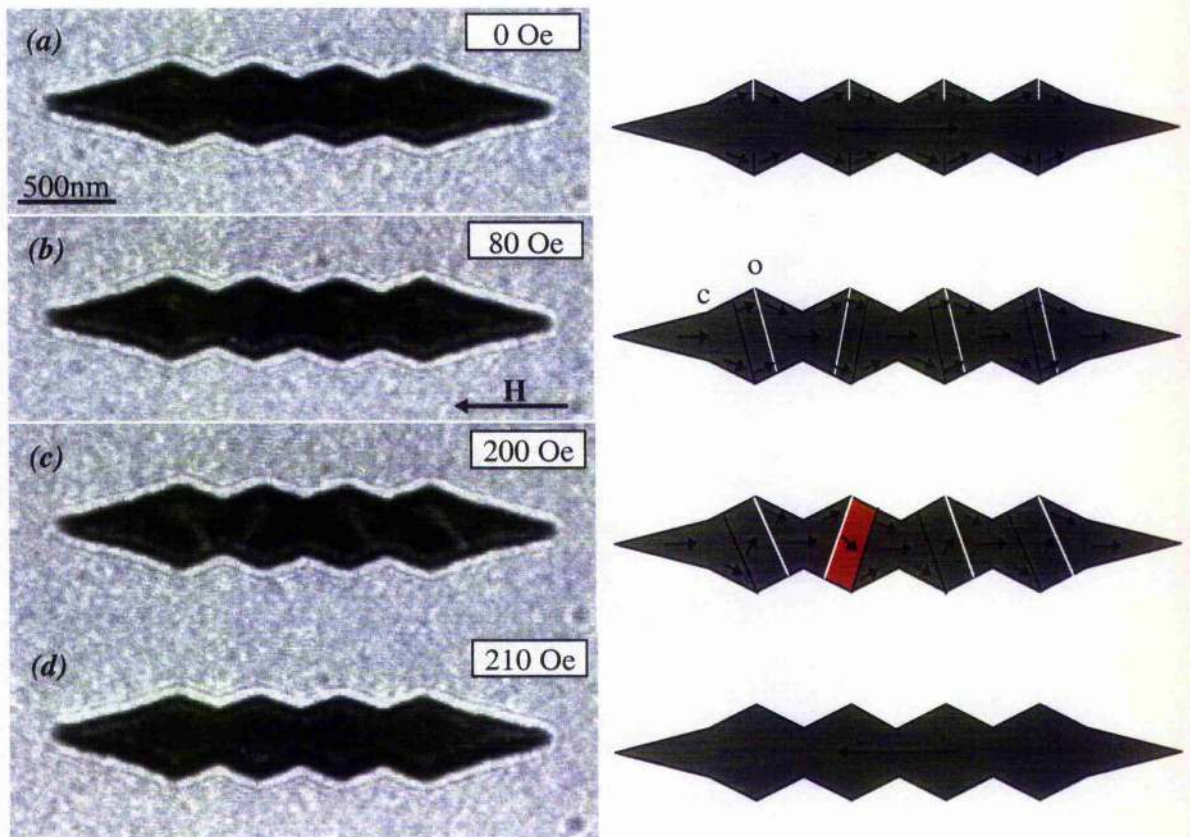


**Figure 5.12**

*Fresnel images of element with structure type A ( $p=0.5\mu\text{m}$ ) recorded during magnetising sequence with corresponding schematics of magnetisation distribution. 'c' marks an 'inner corner' and 'o' marks an 'outer vertex'. Red area highlights a 'parallelogram domain'.*

DPC images were taken to get a more quantitative picture of the ongoing changes. Two stages of the build up of the domain structure prior to switching of an element with type A structure of a period of  $p=0.5\mu\text{m}$  are shown in Fig. 5.13. The mapping direction was parallel to the element width as indicated by the double arrow.

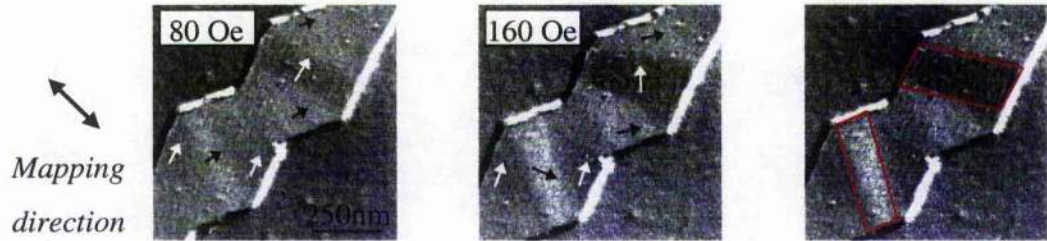


**Figure 5.13**

*DPC images of an element with structure type A ( $p=0.5\mu\text{m}$ ,  $h_2=100\text{nm}$ ) at different field values, with schematics of magnetisation distribution and parallelogram domains (red frames).*

The increase in contrast, which was associated with the increase of the applied field was due to magnetisation rotation which was already suggested in the discussion of the Fresnel images of this element (Fig. 5.12). It was within the parallelogram domains, indicated by red frames in Fig. 5.13, where the most considerable change of magnetisation direction took place. It should be noted that the parallelogram domains next to the element end were often observed to grow more than the others. The schematics derived from the Fresnel images agreed very well with those obtained by DPC imaging.

Reduction of the structure period down to  $p=0.2\mu\text{m}$  did not lead to major changes in the characteristics of the domain configurations observed prior to switching. At remanence the elements were quasi single domain. However, apart from wall sections, which originated at the outer vertices of the structure features, faint end domains were already present at remanence (Fig. 5.14(a)). When a reverse field was applied, two parallel domain walls (i.e. one parallelogram domain) per period were observed which had developed from the wall segments at the outer vertices. In the schematic of Fig. 5.14(b) one of these parallelogram domains is highlighted by the red area. After magnetisation reversal only faint wall sections were visible (Fig. 5.14(c)).

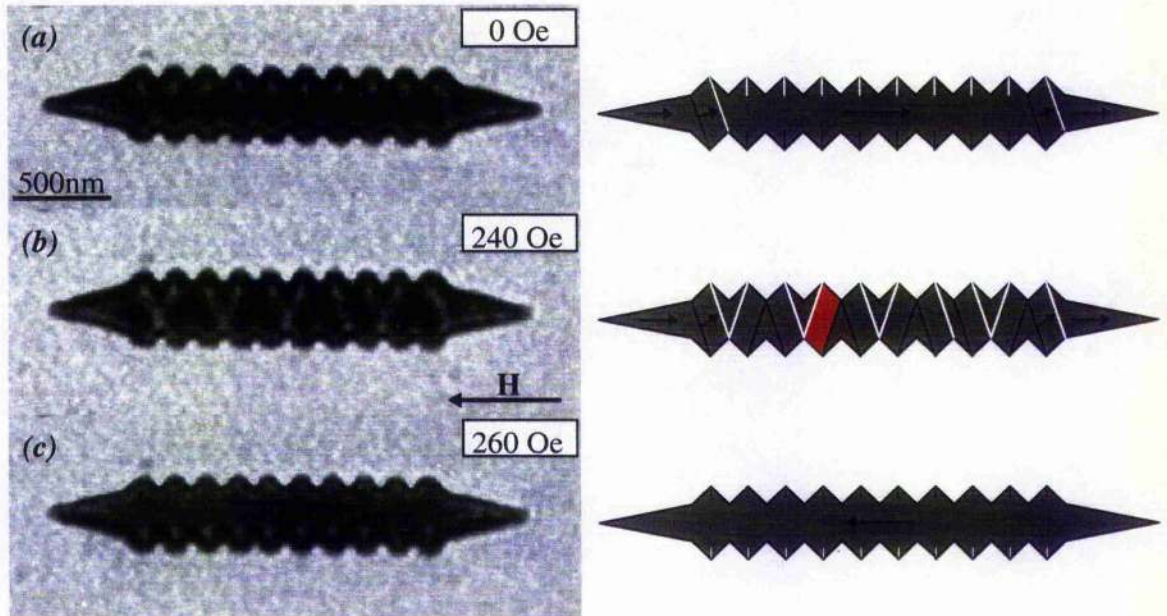


**Figure 5.14**

*Fresnel images of element with structure type A ( $p=0.2\mu\text{m}$ ) recorded during magnetising sequence with corresponding schematics of magnetisation distribution. Red area illustrates a parallelogram domain.*

Different behaviour was observed in the elements with the smallest period ( $p=0.1\mu\text{m}$ ). Not only did the elements look single domain in the remanent state as it was difficult to see whether there was any magnetisation dispersion present at all (Fig. 5.15(a)), but the domain configurations which built up prior to magnetisation reversal (Fig. 5.15(b)) strongly resembled the concertina structures which were commonly observed in the standard elements (Fig. 5.7(c)).

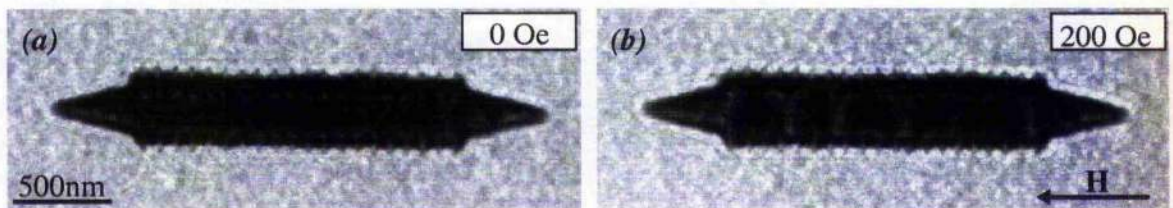


**Figure 5.15**

*Fresnel images of element with structure type A ( $p=0.1\mu\text{m}$ ) recorded during magnetising sequence.*

DPC images were taken in order to gain a more detailed insight in the differences of the magnetisation distribution of the elements with the two smallest periods of structure

type A ( $p=0.1\mu\text{m}$  and  $0.2\mu\text{m}$ ). The formation of parallelogram domains was not only observed in the Fresnel image of Fig. 5.14(b) but also in the DPC images of such an element in Figs. 5.16(a) and (b). Before magnetisation reversal, magnetisation rotation and little wall movement were observed. Therefore the mechanisms of domain formation prior to switching were the same for structure periods in the range of  $0.2\text{-}0.5\mu\text{m}$ .

Examples of the domain configurations which were generated prior to switching in the elements with the smallest period  $p=0.1\mu\text{m}$  are shown in Figs. 5.16(c) and (d).

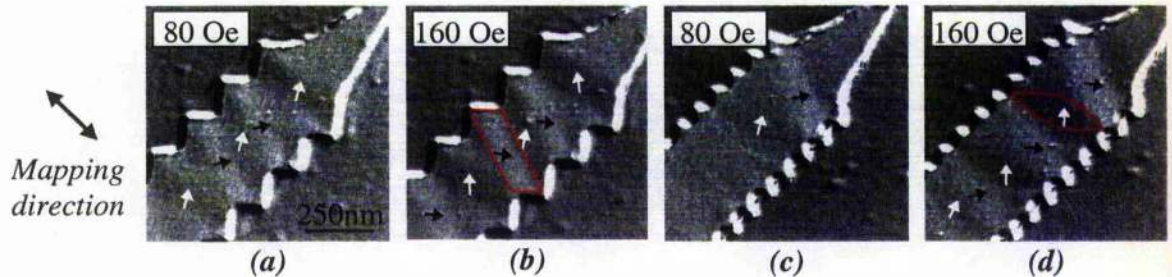


**Figure 5.16**

*DPC images of acicular elements with structure type A ( $h_2=100\text{nm}$ ) at different field values. (a), (b)  $p=0.2\mu\text{m}$ ; (c), (d)  $p=0.1\mu\text{m}$ . Single arrows indicate magnetisation direction. Red frames illustrate characteristic domain shapes.*

Under the influence of a reverse field faint domains were visible at the element ends. These domain structures then developed in a concertina like configuration with the element being uniformly magnetised after magnetisation reversal. Therefore the overall behaviour of an element with the smallest period ( $p=0.1\mu\text{m}$ ) of edge structure type A with  $h_2$  was very similar to that of the standard elements. This suggests that the characteristic effects of structuring the edges of acicular elements on their micromagnetic states were suppressed for the smallest investigated structure period in the case of  $h_2$ .

Whilst the main focus of the description of the magnetic configurations observed in elements with edge structure type A during magnetising experiments lay on narrow ( $w_1$ ) elements with  $h_2$  and  $t_2$ , the effects of the structure parameters on the coercivity is described for all elements. Figures 5.17 and 5.18 show overviews of switching field values versus structure period for all investigated elements with edge structure type A.

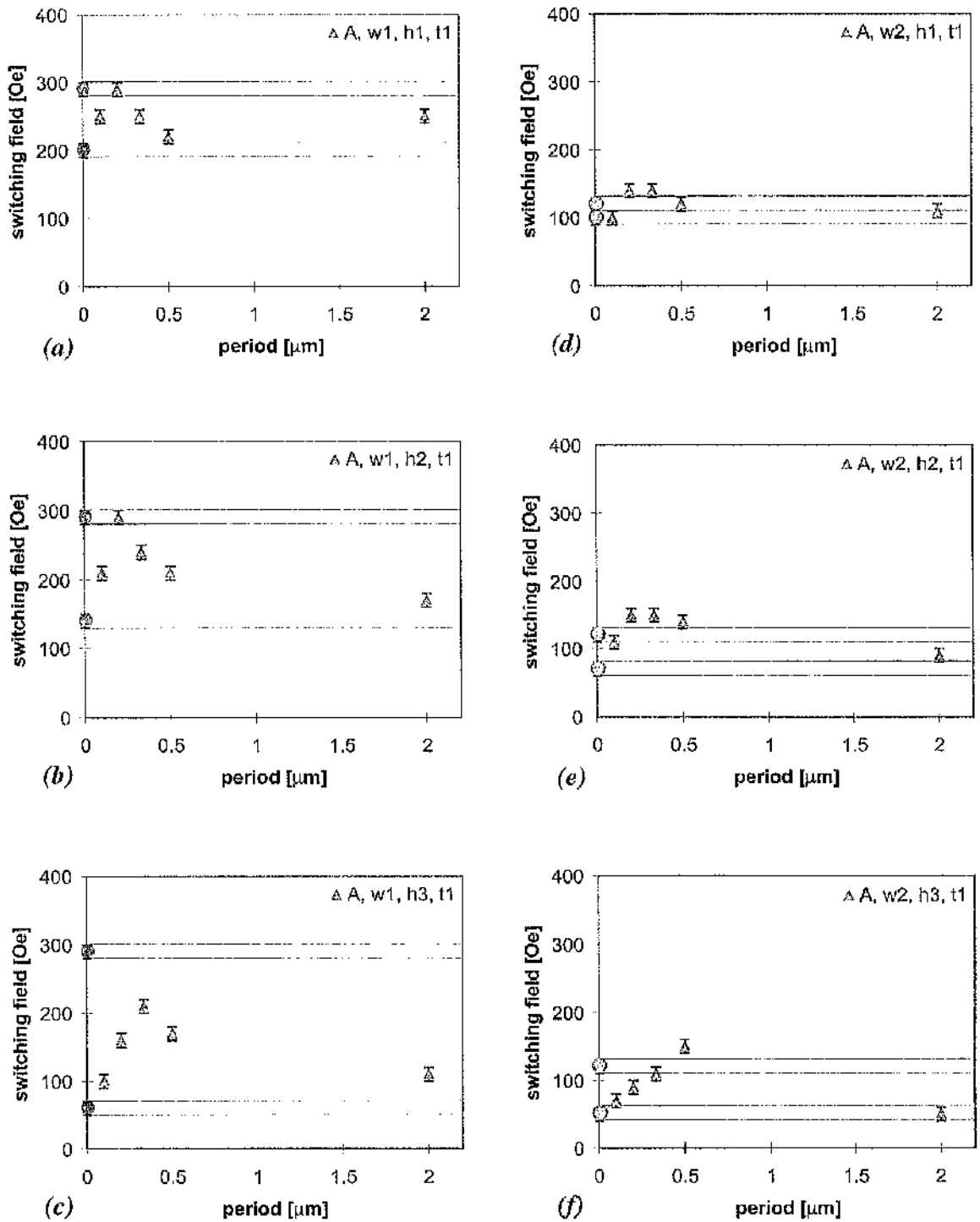


**Figure 5.17**

Overview of switching field values of elements with structure type A of second pattern.

$\Delta$ : type of edge structure,  $t1$ : tip ratio = 1 for the elements of this pattern,

$w1$ : narrow elements,  $w2$ : wide elements, structure heights  $h1=50\text{nm}$ ,  $h2=100\text{nm}$ ,  $h3=250\text{nm}$

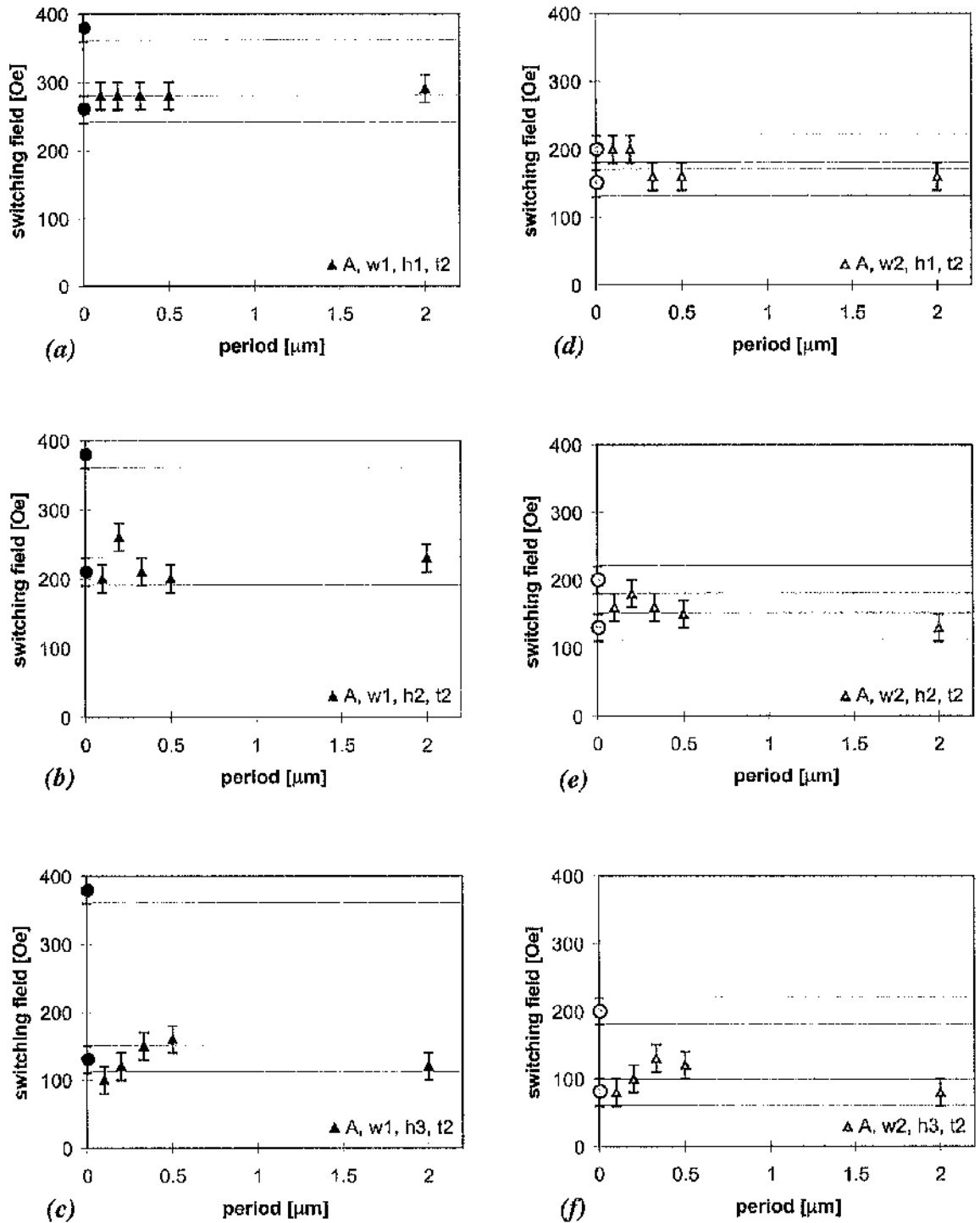


**Figure 5.18**

Overview of switching field values of elements with structure type A of third pattern.

A: type of edge structure, t2: tip ratio =2 for the elements of this pattern,

w1: narrow elements, w2: wide elements, structure heights h1=50nm, h2=100nm, h3=250nm

The effects of the two investigated widths ( $w_1$ ,  $w_2$ ) as well as the three structure heights ( $h_1$ ,  $h_2$ ,  $h_3$ ) are compared. In the left column of the figures the results for the narrow elements ( $w_1$ ) are displayed and in the right column the graphs for the wide elements ( $w_2$ ) are given. The three structure heights are dealt with in the three rows of the overviews. The switching field values of standard elements with the maximum ( $w+2h$ ) and minimum width ( $w_1$ ,  $w_2$ ) were also plotted for each graph and they are marked by circles at a period of zero and vertical lines indicate the spread of these values.

Figure 5.17 shows a compilation of the switching field values for the elements with structure type A of the second pattern ( $t_1$ ). Comparison with the graphs for the first pattern (Figs. 4.2(a), (d)) shows that the elements of the second pattern were magnetically softer than those of the first pattern. Another difference is that none of the elements with a period  $p=2.0\mu\text{m}$  was harder to switch than the standard elements for the upper limits. It is not clear what caused these differences, it could however be a result of the change of material (here permalloy, before soft magnetic NiFe alloy) or due to the different film thicknesses (here 22nm, before 33nm). Simulations were run for 20nm and 30nm film thickness of the elements, and it was found that for a thickness of 20nm the switching fields were indeed reduced. However, none of the elements with structured edges, including those with  $p=2.0\mu\text{m}$ , was found to be harder to switch than the 'upper limit' standard elements in the simulations, but the elements with structure type A and  $h_2$  with  $p=2.0\mu\text{m}$  had the highest coercivity of the elements with structured edges (chapter 7, Fig. 7.8).

The notable increase in coercivity for periods of  $\approx 0.2\mu\text{m}$  which was observed in the case of Fig. 4.12(a) was also detected in Fig. 5.17(b) and even in Fig. 5.17(a) despite the different structure height. It was noted that with the change of period from  $p=0.2\mu\text{m}$  down to  $p=0.1\mu\text{m}$  the characteristic parallelogram domains were no longer generated (section 5.5.2, Figs. 5.14-5.16). However, no such maximum was found in the simulations, which were carried out for the narrow elements with  $t_1$  and structure type A with  $h_2$  (chapter 7, Fig. 7.8(b)).

As expected, the narrow elements in Fig. 5.17 (left column) were generally harder to switch than the wide ones. This effect decreased with increase of the structure height. The reason for this is that in the case of  $h_3$  the 'narrow' elements were fairly wide at the maxima ( $\leq 750\text{nm}$  and  $\leq 1000\text{nm}$ ). In agreement with Fig. 5.10 the decrease in switching field values was less pronounced for wider elements even in the case of structured edges.

All narrow elements with structured edges reversed at values in the range between the two corresponding standard elements with the already mentioned distinct maximum for small periods. In the case of  $h_1$  and  $h_2$  this maximum in switching field values occurred at  $0.2\mu\text{m}$  whereas it was  $0.33\mu\text{m}$  in the case of  $h_3$ . The reason for this shift is not clear. It might however be due to the decrease of perfection in the pattern transfer, which was observed for the small period structures with  $h_3$ . This led to the most pronounced broadening of the minimum width in these elements (see Fig. 5.3(c) and table 5.1) which could explain a further decrease of the switching field. Therefore this drop in coercivity is more likely to be an artefact of the patterning process than a result of the designed edge structure.

The wider elements were found to behave differently compared to the narrow ones as many of them reversed at slightly higher fields than their upper limit standard elements (Figs. 5.17(d)-(f)). However, a moderate maximum in the graphs for elements with small period structures appeared, too, and it was at that part of the graphs, where the switching field values of elements with structure heights  $h_1$  and  $h_2$  exceeded those of the standard elements with  $w_2$  (Figs. 5.17(d) and (e)). The graph for the elements with  $h_3$  (Fig. 5.17(f)) on the other hand shows a totally different characteristic, with the maximum found at  $0.5\mu\text{m}$  and a monotonic decrease for smaller periods.

The behaviour of the elements with the sharper tips  $t_2$  (third pattern) is shown in Fig. 5.18. As known from Fig. 5.10, the standard elements with  $t_2$  were magnetically harder than those with  $t_1$  and therefore the limits determined by the standard elements were higher as well. This characteristic was however not found generally for all elements with structured edges: In the case narrow elements with edge structure heights  $h_2$  and  $h_3$ , however, the elements with the blunter tips  $t_1$  were harder to switch than those with  $t_2$  (Figs. 5.17(b), (c) and 5.18(b), (c)).

In the case of the sharper tips, even the wide elements ( $w_2$ ) with structured edges had switching field values which were in the range between the two standard elements (Figs. 5.18(d)-(f)). Further it should be noted that only the graphs for the elements with structure height  $h_2$  (Figs. 5.18(b), (e)) show a similar trend of the graphs of comparable elements of the second pattern (Figs. 5.17(b), (e)). However, structuring the edges of elements with the sharper tips  $t_2$  had a dramatic effect on the coercivity of the investigated elements as most of them were found to have switching field values in the range of the coercivity of the wider ( $w+2h$ ) standard elements (lower limit). Furthermore the variation of switching field values versus period was very little and, considering the error margins,

almost negligible for all elements of Fig. 5.18. In the simulations, which were carried out for elements with  $w_1$ ,  $t_2$ ,  $h_2$  and structure type A the variation in coercivity was much more pronounced but the drop in coercivity for the smallest period was not found. However there was a distinct minimum for  $p=0.33\mu\text{m}$  (chapter 7, Fig. 7.8(e)).

### 5.5.3 ELEMENTS WITH EDGE STRUCTURE TYPE C

The second investigated edge structure type of the third pattern was type C. As in the case of structure type A, the main focus of the discussion lies on the elements with  $h_2$  but a brief overview of the observed micromagnetic states of all narrow elements ( $w_1$ ) of the third pattern ( $t_2$ ) is given in table 5.4 before the detailed description.

Structure Type C, Width $w_1$ - Third pattern				
period	state	$h_1=50\text{nm}$	$h_2=100\text{nm}$	$h_3=250\text{nm}$
2.0 $\mu\text{m}$	R	quasi single domain	(Figs. 5.19, 5.20(a), (b)) quasi single domain	multi-domain (centre)
	PS	concertina*	concertina*	multi-domain (centre)
0.67 $\mu\text{m}$	R	quasi single domain	(Figs. 5.20(c), (d)) multi-domain	double y-configurations
	PS	multi-domain	multi-domain	double y-configurations
0.33 $\mu\text{m}$	R	quasi single domain	(Fig. 5.21) double y-configurations	double y-configurations
	PS	double y-configurations	double y-configurations	double y-configurations
0.25 $\mu\text{m}$	R	quasi single domain	double y-configurations	double y-configurations
	PS	double y-configurations	double y-configurations	double y-configurations
0.2 $\mu\text{m}$	R	double y-configurations	(Fig. 5.22) double y-configurations	double y-configurations
	PS	double y-configurations	double y-configurations	double y-configurations

**Table 5.4**

*Micromagnetic states of elements with  $w_1$  and structure type C of 3<sup>rd</sup> pattern ( $t_2=2$ ).*

*R: Remanent state, PS: Prior to switching.*

Domain configurations at remanence and prior to switching are described again with the emphasis on similarities. The terminology is consistent with table 5.3 apart from the introduction of 'double y-configurations' which stands for the characteristic domain

configurations observed in the case of structure type C (i.e. one double y-configuration per period). 'Multi-domain' describes either a state like that in Fig. 5.19(b) (for  $h_3$  and  $p=2.0\mu\text{m}$ ) or in the cases of  $h_1$  and  $h_2$  with  $p=0.67\mu\text{m}$  domain configurations like those in Figs. 5.20(c) and (d). As in the case of structure type A, only small differences were observed between sets of elements with identical structure parameters but different tip ratio. The elements with  $p=2.0\mu\text{m}$  and  $h_1$  of the second pattern ( $t_1$ ) were not only observed to generate a domain structure in the centre of the element but also to form end domains. Apart from that, table 5.4 is also valid for the narrow elements of the second pattern. No striking differences were observed between the magnetic microstructures of the narrow and the wide elements which was in agreement with the results of elements with structure type A as well as standard elements with different widths.

Figure 5.19 shows Fresnel images of an element with the longest period of edge structure type C ( $p=2.0\mu\text{m}$ ) with  $h_2$  and  $t_2$ .

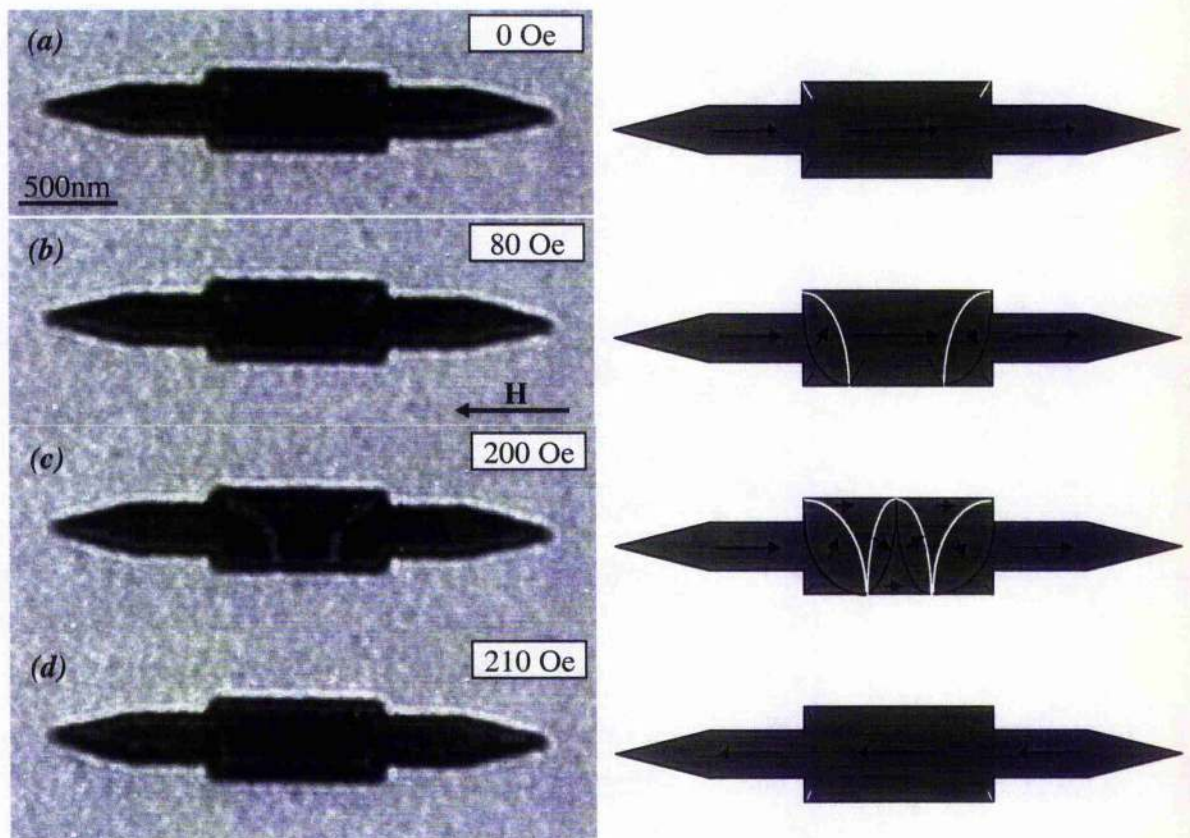


**Figure 5.19**

*Fresnel images of element with structure type C ( $p=2.0\mu\text{m}$ ) recorded during magnetising sequence with corresponding schematics of magnetisation distribution.*

The images were recorded during a magnetising experiment and schematics were derived for the magnetisation distribution for the different stages and are given along with the Fresnel images.

At remanence the elements were almost uniformly magnetised (quasi single domain) along their length with faint wall sections barely visible at the corners of the edge structure features (Fig. 5.19(a)). These walls increased in length and two of them extended over the maximum element width when a reverse field was applied (Fig. 5.19(b)). No contrast changes were visible at the tip regions of the elements. Further increase of the applied field led to the formation of a concertina\* structure within the part of the elements with the structure features but there was still no trace of domains close to the element ends (Fig. 5.19(c)). After magnetisation reversal the elements were almost uniformly magnetised with very faint wall sections visible in the corners of the structure features (Fig. 5.19(d)).

The DPC images in Figs. 5.20(a) and (b) show the similarity of the domain structures which were generated in the widest part of elements with structure type C with  $p=2.0\mu\text{m}$  and  $h_2$  and the concertina structures observed in the standard elements (Fig. 5.8). Domain formation and wall movement as well as magnetisation rotation were clearly observed. In the case of the smaller period,  $p=0.67\mu\text{m}$ , domains which were already present at remanence mainly increased in contrast with little wall movement observed (Figs. 5.20(c), (d)). This suggests that the dominant mechanism prior to switching in this case was magnetisation rotation within existing domains.

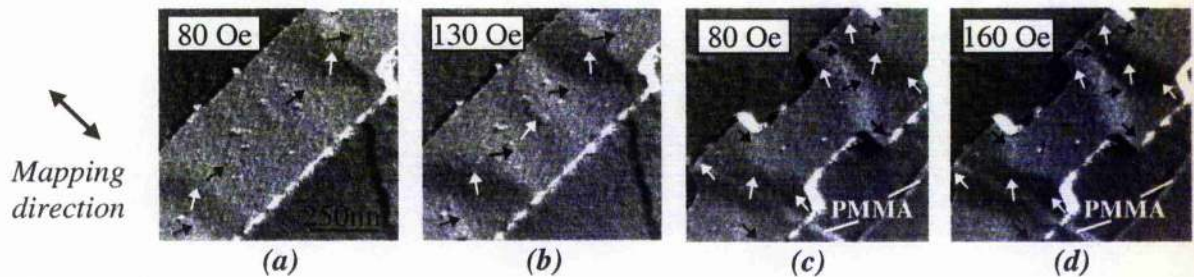


**Figure 5.20**

*DPC images of acicular elements ( $w_1=250\text{nm}$ ) with structure type C ( $h_2=100\text{nm}$ ) at different field values with schematic of magnetisation distribution.*

*(a), (b)  $p=2.0\mu\text{m}$ ; (c), (d)  $p=0.67\mu\text{m}$ . PMMA faults indicated.*

In the case of the smaller structure periods in the range  $0.2\mu\text{m} \leq p \leq 0.33\mu\text{m}$  similar domain configurations were observed at remanence. An example of the typical magnetic microstructures detected in Fresnel mode is given in Fig. 5.21 for different stages during a magnetising experiment. The structure period is  $p=0.33\mu\text{m}$  and schematics of the magnetisation distribution are given for each image.

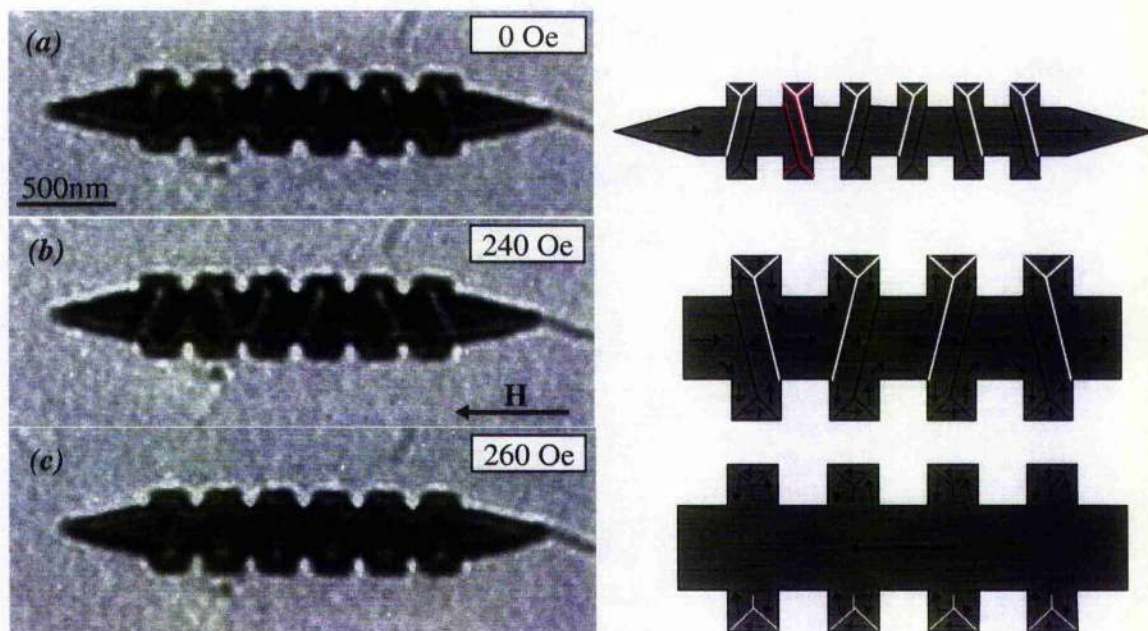


**Figure 5.21**

*Fresnel images of element with structure type C ( $p=0.33\mu\text{m}$ ) recorded during magnetising sequence with corresponding schematics of magnetisation distribution. Red lines indicate double y-configuration.*

At remanence the elements supported one double y-configuration per period (one of them is highlighted by red lines in the schematic of Fig. 5.21(a)). In agreement with the observations for the first pattern (chapter 4) no flux closure like configurations were found in the remanent states of elements with structure type C while such configurations were observed in the ac-demagnetised state of these elements (Figs. 4.6, 4.8 and 5.4). When a reverse field was applied, the contrast of the domain walls increased indicating magnetisation rotation while wall movement played only a minor role (Fig. 5.21(b)). The schematics derived from the Fresnel images (b) and (c) only illustrate the magnetisation distribution in the middle section of the element (i.e. the four central structure periods). After magnetisation reversal the elements were uniformly magnetised in the main body,

while faint bisector domain wall configurations were visible within the structure features (Fig. 5.21(c)).

A series of DPC images of an element with  $p=0.2\mu\text{m}$  is given in Fig. 5.22. The images show that the elements with the smallest structure period were behaving exactly the same as deduced for the elements with the longer period  $p=0.33\mu\text{m}$  in the Fresnel experiment (Fig. 5.21).

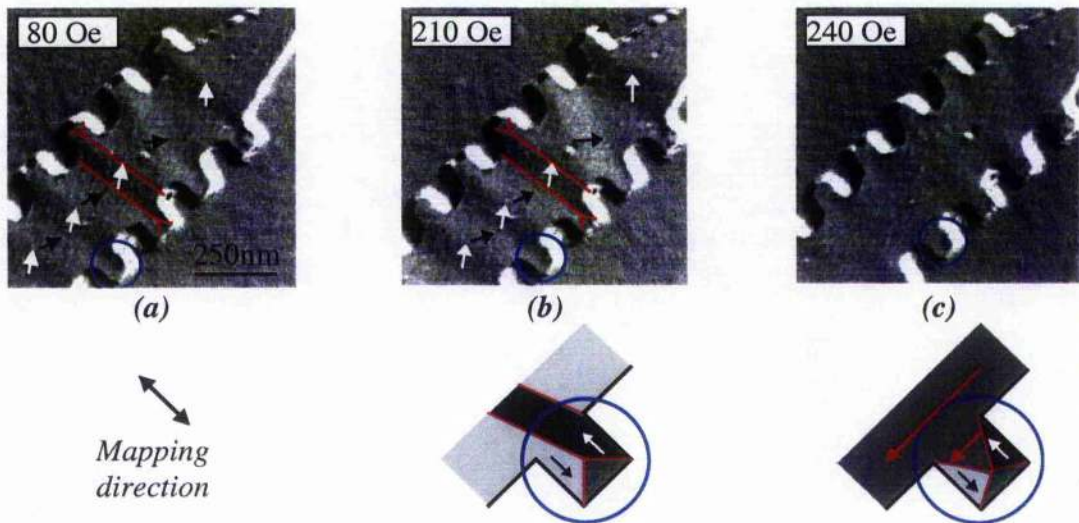


**Figure 5.22**

*DPC images of acicular elements with structure type C ( $h_2=100\text{nm}$ ,  $p=0.2\mu\text{m}$ ) at different field values. (c) shows the element after magnetisation reversal. Red lines indicate double y-configuration. Schematics of the domain configurations of the area within the blue circles are given for (b) and (c).*

Most notably one double y-configuration per period was observed even for this smallest period as indicated by the red lines in Figs. 5.22(a), (b). Increase of the reverse field mainly led to magnetisation rotation prior to switching. It should be noted that, after magnetisation reversal occurred in the main body of the elements with  $0.2\mu\text{m} \leq p \leq 0.33\mu\text{m}$ , the magnetisation was not always reversed in the entire element. This is illustrated in detail in the schematics of Figs. 5.22(b) and (c). The domain configuration within the structure feature marked by the blue circle was found to change from a bisector like (b) to a flux closure like configuration (c). These flux closure like configurations within the small structure features were found to be very stable and it took sometimes a much higher field (up to twice as high) to saturate the elements completely.

The influence of the structure parameters on the coercivity of acicular elements with edge structure type C was also investigated and the results for the second and third patterns are displayed in Figs. 5.23 and 5.24. The layout of the figures is the same as for Figs. 5.17 and 5.18. Figure 5.23 shows the graphs for elements with edge structure type C of the second pattern ( $t_1$ ). It should be noted that the main characteristics of these graphs are very similar to those of the graphs for type A of this pattern (Fig. 5.17): The increase of  $H_c$  for small periods (Figs. 5.17(a), (b), and 5.23 (a), (b)), which in the case of many of the wider elements even lead to an increase of coercivity compared to the standard elements (Figs. 5.17(d), (e), and 5.23 (d), (e)) was observed for both structure types.

Comparison of the graphs for the C type elements of the first pattern with those with  $h_2$  of the second pattern shows that in the case of the narrow elements (Figs. 4.12(c) and 5.23(b)) the main characteristic - all structured elements reversed at lower fields than the upper limit standard elements - agreed well. In the case of the wide elements (Figs. 4.12(f) and 5.23(e)), the different behaviour of these elements of the first pattern - being the only set of wide elements with distinctly lower switching fields than the standard elements - was not confirmed. It was not possible to pinpoint the reason for this difference, because there was not only a change of material but also a considerable difference in film thickness and in the case of type C structure even the geometry of the elements was altered from asymmetric to symmetric.

The behaviour of the elements with the sharper tips ( $t_2$  for third pattern) is shown in Fig. 5.24. As can be seen from Figs. 5.10 and 5.18, the standard elements with  $t_2$  were magnetically harder than those with  $t_1$  and therefore the limits determined by the standard elements were higher as well. In agreement with the findings for structure type A, most elements with  $t_2$  switched within the range of the limits defined by the standard elements with the majority of elements having switching field values closer to the lower limits. Structuring the edges therefore had again stronger effects on the coercivity of elements with the sharper tips  $t_2$ : The reduction of the switching field values of the elements with structured edges compared to those of the 'upper limit' standard elements was more pronounced than in the case of the elements with  $t_1$ .

Simulations which were carried out for the narrow elements ( $w_1$ ) with  $h_2$  and structure type C for both tip ratios not only produced similar trends for the graphs. Both sets of simulated elements were found to have coercivities closer to the lower limit standard elements - in the case of  $t_2$  even below (chapter 7, Figs. 7.10(b), (e)).

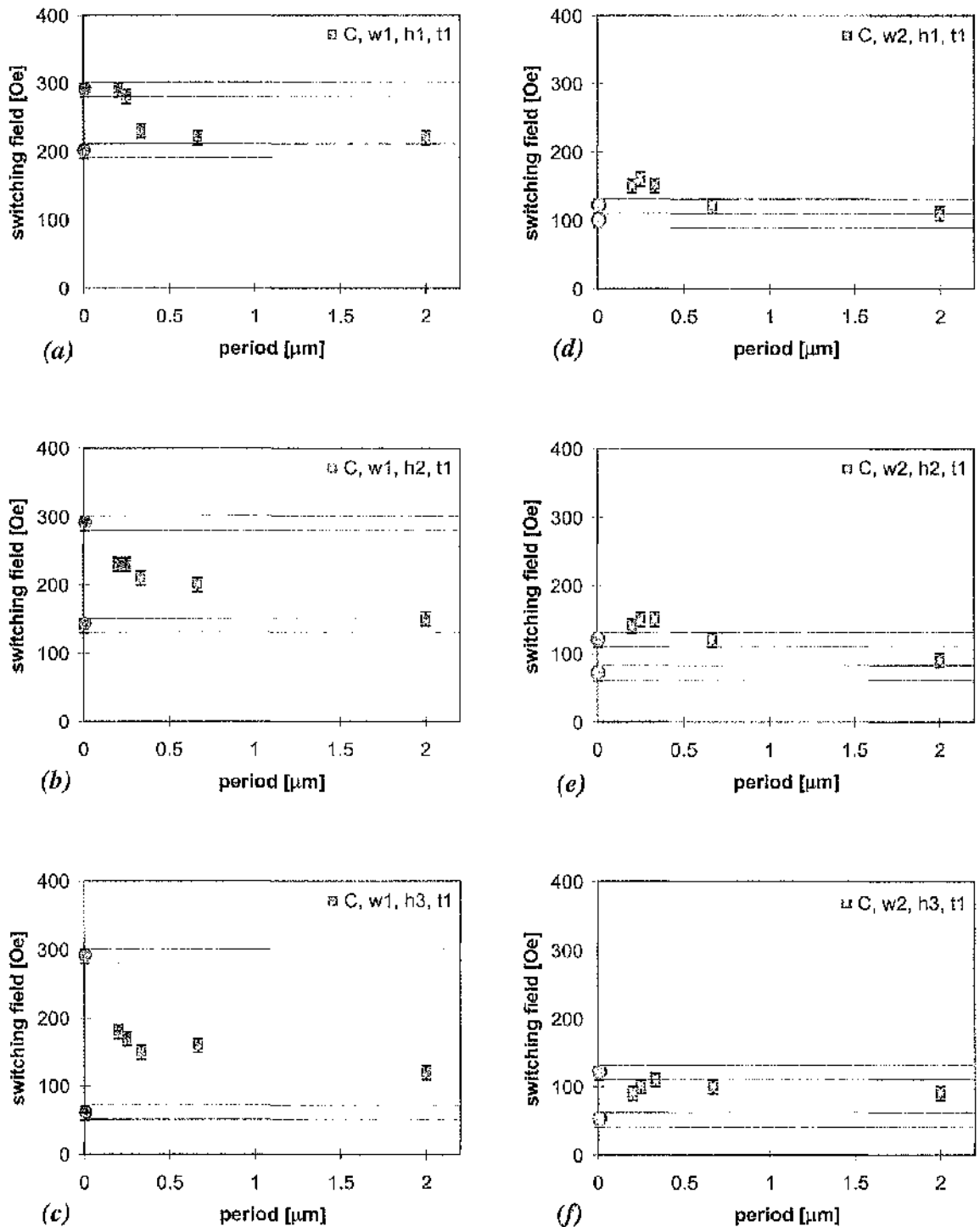


**Figure 5.23**

*Overview of switching field values of elements with structure type C of second pattern.*

*C: type of edge structure, t1: tip ratio =1 for the elements of this pattern,*

*w1: narrow elements, w2: wide elements, structure heights h1=50nm, h2=100nm, h3=250nm*

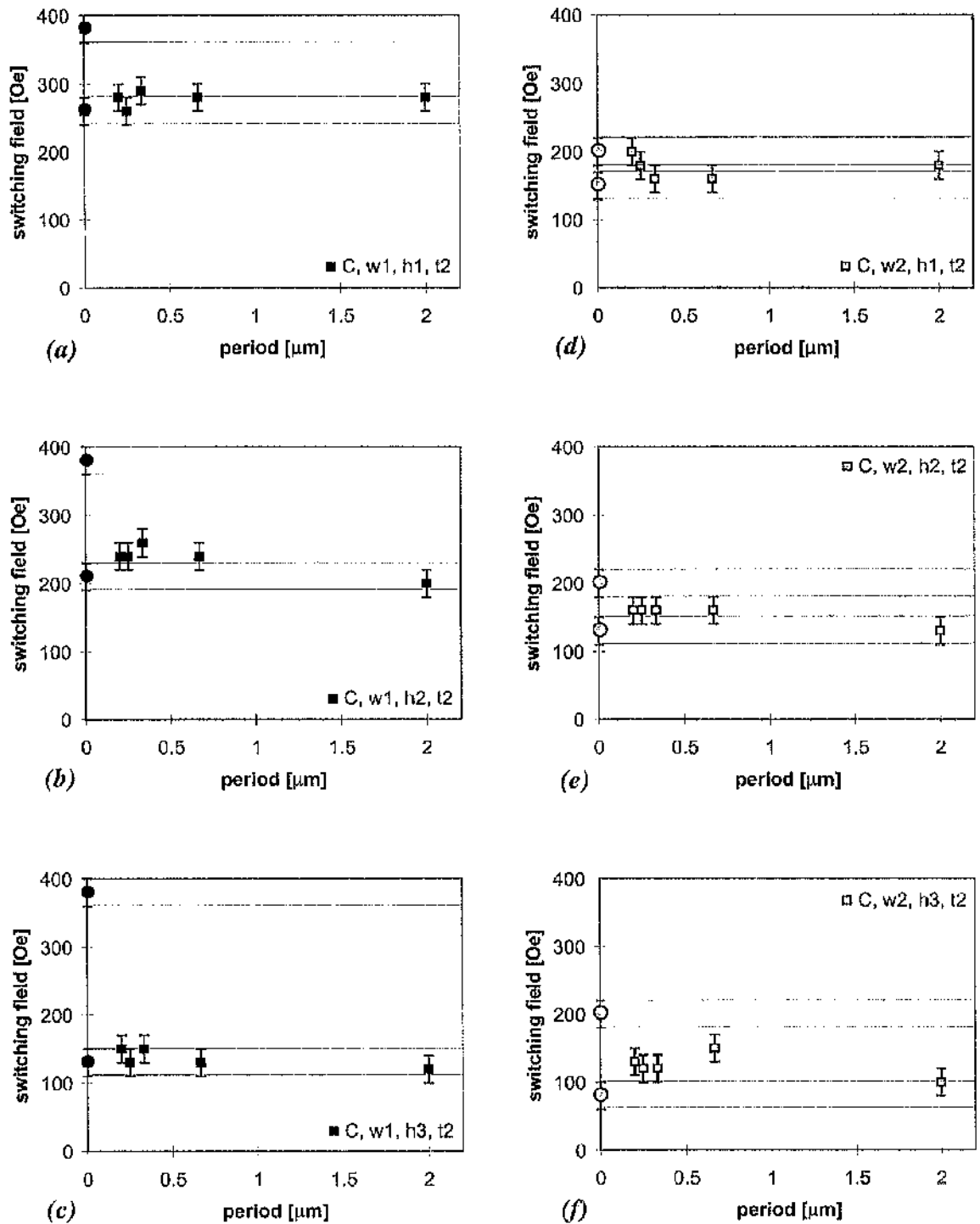


**Figure 5.24**

Overview of switching field values of elements with structure type C of third pattern.

C: type of edge structure, t2: tip ratio =2 for the elements of this pattern,

w1: narrow elements, w2: wide elements, structure heights  $h1=50\text{nm}$ ,  $h2=100\text{nm}$ ,  $h3=250\text{nm}$

## 5.6 SUMMARY

Two patterns of acicular thin film elements with different tip ratios ( $t_1, t_2$ ) and various edge structures were fabricated and investigated in order to ascertain the dependence of the magnetic microstructure and magnetisation reversal behaviour on the geometry of such elements. Standard elements (without deliberate edge structure) of eight widths were designed along with elements with two edge structure types A and C. These edge structures had five different periods and three different structure heights ( $h_1, h_2, h_3$ ). The two minimum widths of the elements with structured edges were  $w_1$  and  $w_2$ .

The physical microstructure of the elements was evaluated first and it was found that pattern transfer was in most cases of high quality. However, in the case of edge structure type A, the quality of the structure features was found to deteriorate for the smallest investigated period ( $p=0.1\mu\text{m}$ ) in addition with increase of structure height (both due to proximity writing).

Investigation of the magnetic microstructure in the as-grown and ac-demagnetised states of the samples showed that there was negligible difference between the two states. As expected all standard elements were clearly single domain with the mean direction of magnetisation parallel to the element length.

In the case of structure type A, variation of direction of magnetisation was observed for all elements with structure periods in the range  $0.2\mu\text{m} \leq p \leq 0.5\mu\text{m}$ . The mean direction of magnetisation of such elements was still parallel to the element length, but locally the magnetisation direction was found to follow the nearest edge. For  $h_1$  and  $h_2$  these effects were highly localised and restricted to the structured edges of the elements while in the case of  $h_3$  domains were observed which extended over the entire element width.

Most of the elements with structure type C however were found to support multi-domain states with the most common feature being double  $\gamma$ -configurations in the case of  $0.2\mu\text{m} \leq p \leq 0.67\mu\text{m}$  but flux closure like configurations were also observed. The mean direction of magnetisation was again parallel to the element length. For elements with  $h_3$  and short periods ( $p \leq 0.33\mu\text{m}$ ) a bar magnet like behaviour was observed for pairs of structure features with their magnetisation direction being orthogonal to the mean direction of magnetisation of the entire element. For both structure types neither the different widths ( $w_1, w_2$ ) nor the different tip ratios ( $t_1, t_2$ ) were found to alter the magnetic microstructure.

In-situ magnetising experiments were carried out and the development of the magnetic microstructure was carefully monitored up to the switching field values. Magnetisation reversal itself was too rapid to gain any insight into the reversal mechanisms by means of TEM, although all elements were clearly found to be multi-domain prior to switching. As in zero field conditions neither the width nor the different tip ratio were found to influence the magnetic microstructure for both structure types.

As expected, the coercivity of the standard elements was found to decrease with increase of element width as well as for the lower tip ratio ( $t_1$ ). The standard elements with  $t_1$  only developed end domains close to the element tips whilst those with  $t_2$  generated concertina structures extending over the entire element. It is thought though that more developed concertina structures were also generated in the elements with the blunter tips  $t_1$  but that those were not observed due to the fact that these domain configurations were even more volatile in the elements with  $t_1$  than in those with the sharper tips  $t_2$ .

The elements with structure type A supported domain configurations at remanence similar to those observed in the ac-demagnetised state. Prior to reversal, most elements with  $0.2\mu\text{m} \leq p \leq 0.5\mu\text{m}$  were found to generate characteristic domain configurations ('parallelogram domains') whilst the magnetic microstructure within the elements with  $p=2.0$  and  $0.1\mu\text{m}$  resembled that of the standard elements.

In agreement with the standard elements the coercivity of the elements with structured edges was found to decrease with the increase of element width and there was also a crucial influence of the tip ratio observed. While in the case of  $t_1$  a characteristic variation with structure period was observed in most cases, the main effect for the elements with  $t_2$  was a more pronounced drop in coercivity compared to corresponding standard elements. The structure period appeared only to have a negligible influence on the coercivity of elements with  $t_2$ .

The most common feature of the elements with edge structure type C were the 'double y-configurations'. These were observed in all elements with  $0.2\mu\text{m} \leq p \leq 0.33\mu\text{m}$  not only prior to switching but in most cases also at remanence. Between remanence and just prior to switching magnetisation rotation was detected but generation and movement of walls only played a minor role for the majority of those elements.

The effects of edge structure type C on the coercivity of the elements were in most cases very similar to the observations made for the elements with structure type A. Furthermore the most common domain configurations for the different edge structure types

showed considerable similarity e.g. the parallelogram domains and the double y-configurations. In both these domain configurations two parallel domain walls were observed per period in the main body of the elements. It should be noted, that structuring the edges resulted in reproducible high densities of modified Néel walls (up to one wall per 100nm was observed for both structure types). The term modified Néel walls describes the fact that Néel walls normally have widths in the order of some hundreds of nanometers whereas in the case of elements with structured edges this width is obviously reduced due to the above mentioned high density of walls.

**CHAPTER 6:****ACICULAR ELEMENTS WITH STRUCTURED EDGES OF TYPES A AND C****- FOURTH AND FIFTH PATTERN****6.1 INTRODUCTION**

The fourth and fifth patterns were designed with the aim to determine the effects of variation of overall width of the elements with structured edges which was present in the former patterns. Therefore elements with structured edges but nominally constant width were designed in the two new patterns. Sets of elements with structured edges were designed with two different widths ( $w_1$ ,  $w_2$ ) and the length of the base rectangle (Fig. 3.9) was the same as in the previous chapter ( $l=2.0\mu\text{m}$ ) as were the two structure types and their parameters. Both new patterns were identical apart from the tip ratio with the fourth pattern having elements with  $t_1$  and the elements of the fifth pattern had sharper tips ( $t_2$ ). The film material was permalloy ( $\text{Ni}_{=80\text{at\%}}\text{Fe}_{=20\text{at\%}}$ ) with a thickness of  $\approx 22\text{nm}$  as in the case of the second and third patterns. As already mentioned in section 5.1, all four samples were fabricated simultaneously in order to achieve the best possible comparability.

The structure of this chapter is as follows: Section 6.2 gives a description of the fourth and fifth patterns and the physical microstructure of the elements is discussed in 6.3. Section 6.4 deals with the magnetic microstructure of the elements in their as-grown and ac-demagnetised states whereas the development of the domain configurations under the influence of external fields is described in section 6.5. The main results of this chapter are then summarised in section 6.6.

**6.2 DESCRIPTION OF PATTERNS**

The basic layout of patterns four and five was very similar to that of the two previous samples. Each pattern consisted of twelve arrays of elements with five identical ones in each row but there was only one row of standard elements in the case of the fourth and fifth patterns. As the overall width was nominally constant even for the elements with structured edges (Figs. 6.1(a), (b)), only two sets of standard elements were investigated. The width of the standard elements was either  $w_1$  or  $w_2$ . For each width there were 30 standard elements on a single membrane. The periods of the edge structures were the same as in the previous

chapter. In the case of type A edge structure they were  $p=2.0, 0.5, 0.33, 0.2$  and  $0.1\mu\text{m}$  and the elements with type C edge structure had periods  $p=2.0, 0.67, 0.33, 0.25$  and  $0.2\mu\text{m}$ . The three structure heights  $h_1, h_2$  and  $h_3$  were also retained. Examples of the element designs and pattern parameters are given in Fig. 6.2.

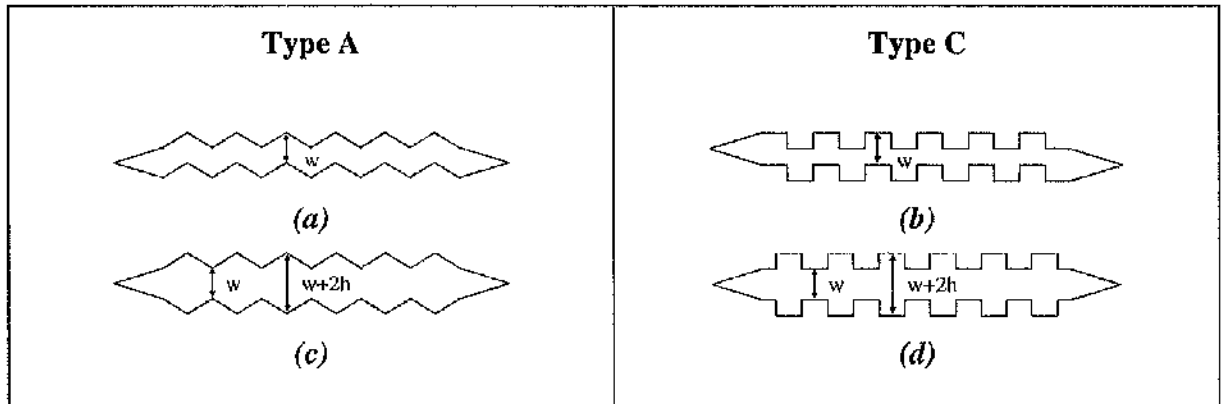


**Figure 6.1**

*Schematic of elements with structured edges with and without variation of the overall width of the elements.*

*(a), (b) Elements of 5<sup>th</sup> pattern ( $t_2$ ) with nominally constant element width.*

*(c), (d) Elements of 3<sup>rd</sup> pattern ( $t_2$ ) with variation of element width between  $w$  and  $w+2h$ .*

!

As the fourth and fifth patterns were identical apart from the tip ratios, only an overview of the elements of the fifth pattern ( $t_2$ ) is given in Fig. 6.2. Each row is one out of the five rows of each of the twelve arrays of the entire pattern. Such a row is made up of elements of nominally constant width and in the case of the elements with structured edges structure type and height are constant in each row.

In order to be consistent with the previous chapter the elements with  $t_2$  are discussed in greater detail with the main focus lying again on the narrow elements ( $w_1$ ) with structure height  $h_2$ . The designs of these elements are shown in the second rows of the top (type A) and bottom (type C) array of Fig. 6.2.

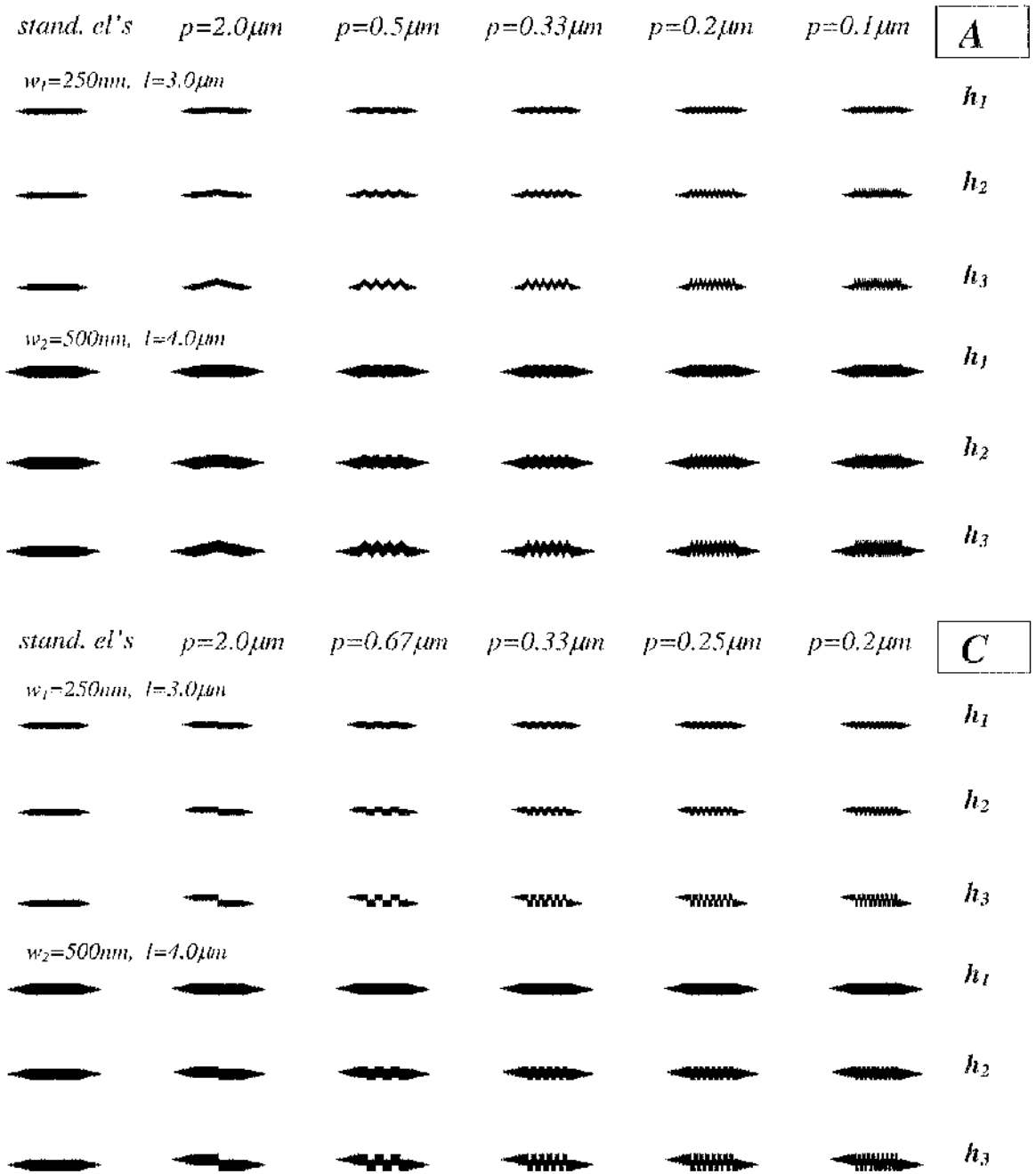


**Figure 6.2**

Standard elements and elements with edge structure types A and C of fifth pattern ( $t_2=2$ ).

Widths of elements:  $w_1=250\text{nm}$ ,  $w_2=500\text{nm}$ . Overall lengths of elements:  $3.0$  or  $4.0\mu\text{m}$ .

Heights of structure features:  $h_1=50\text{nm}$ ,  $h_2=100\text{nm}$ ,  $h_3=250\text{nm}$ .

### 6.3 PHYSICAL MICROSTRUCTURE

Bright field images of the samples were taken in the JEOL 2000 FX microscope. The physical microstructure of the film is the same as for the elements of the second and third patterns (chapter 5) as all four samples were fabricated simultaneously. The  $\approx 22\text{nm}$  thick permalloy film was micropolycrystalline with an average grain size of 5-10nm. Sections of elements with structured edges are shown in Fig. 6.3 and schematics of parts of the designed edge structure were overlaid as reference. Figs. 6.3(a)-(c) display images of elements with structure type A with the smallest period  $p=0.1\mu\text{m}$  and the three different structure heights and elements with edge structure type C with the smallest period  $p=0.2\mu\text{m}$  with  $h_1$ ,  $h_2$  and  $h_3$  are shown in Figs. 6.3(d)-(f). The edge acuity was in the expected range of 5-10nm with the pattern transfer being generally of good quality.

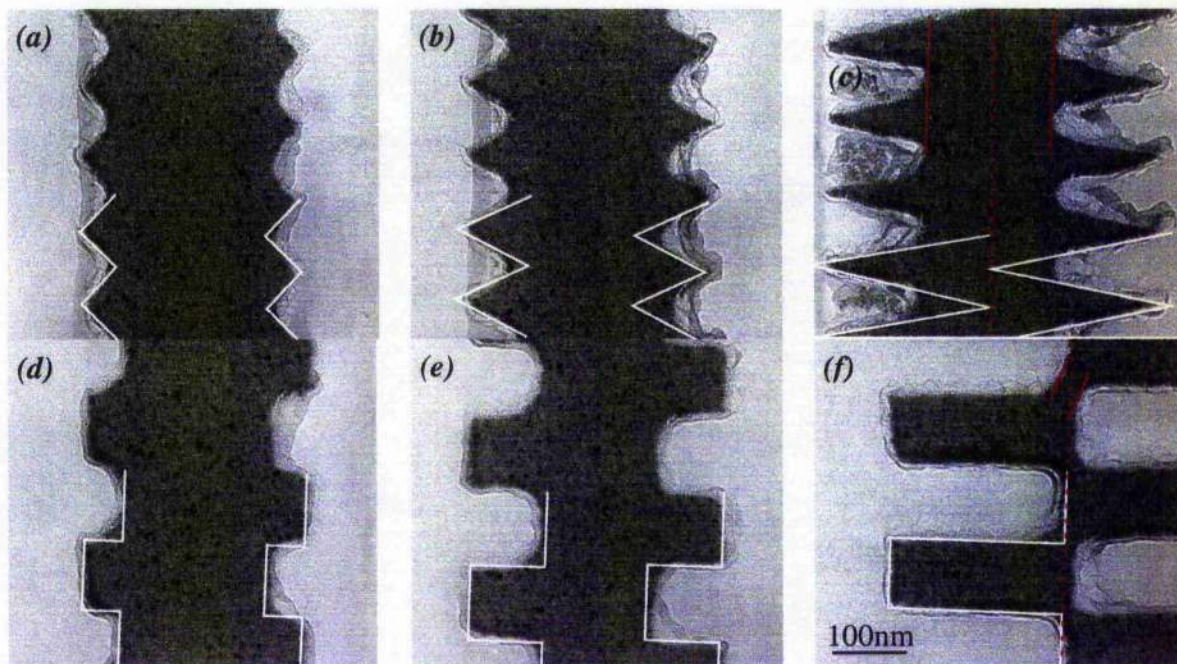


**Figure 6.3**

*Bright field images of elements with different structure height (fifth pattern).*

*(a)-(c) elements with structure type A with  $p=0.1\mu\text{m}$ ; (d)-(f) elements with structure type C with  $p=0.2\mu\text{m}$ . White lines indicate designed edge structure. Red lines mark maximum width of main body of elements, while dashed red lines indicate nominal width of main body ( $=0$  for elements with  $w_1$  and  $h_3$ ).*

As in the previous chapter, the pattern transfer for the elements with edge structure type A was good in terms of period, whereas the actual height of the structure features was often reduced compared to the design due to proximity writing. The effects became again more notable with increase of structure height and in the case of the smallest investigated period ( $p=0.1\mu\text{m}$ ). The worst case is illustrated in Fig. 6.3(c) with red lines marking the actual width of the main body of such an element. Instead of the designed 'zigzag stripe' indicated by the white lines in Fig. 6.3(c) with the nominal width of the main body of the element being equal to zero (illustrated by the red dashed line), the elements had a considerable main body with a width of  $\approx 160\text{nm}$ . Therefore the overall geometry was altered from a zigzag stripe to a rectangle with spikes in the case of structure type A with  $h_3$  and the shortest period  $p=0.1\mu\text{m}$ .

In the case of structure type C the pattern transfer was again superior compared to type A. As in the previous chapter the actual edge structure not only agreed very well with the design as far as the period was concerned but also with the measured structure height. The main imperfection in pattern transfer was again the rounding of the inner corners of the structure features as already pointed out in the previous chapter. This can be seen in Figs. 6.3(d)-(f) and it should be noted, that due to this rounding of the inner corners the rectangles in the case of  $h_3$  were not just tangent to each other in a point but instead there was a transition zone ('bridge') of a width of 20-30nm which is highlighted by the red lines in Fig. 6.3(f). The design of these elements with  $h_3$  had no continuous main body whatsoever (width of main body = 0 as indicated by the dashed red line in Fig. 6.3(f)).

#### 6.4 AS-GROWN AND AC-DEMAGNETISED STATE

In order to evaluate the magnetic microstructure of the elements in their as-grown and ac-demagnetised states, the samples were investigated in Foucault mode in the JEOL 2000 FX microscope. As with the previous samples, no marked differences were observed between the two states and the discussion in this section focuses on the ac-demagnetised state because it is a reproducible state.

Figure 6.4 shows a compilation of Foucault images of narrow elements ( $w_f$ ) with edge structure types A and C together with schematics of the distribution of magnetisation direction. The period is  $p=0.33\mu\text{m}$  and the tip ratio is  $t_2$  for all elements and the effects of the three structure heights ( $h_1$ ,  $h_2$ ,  $h_3$ ) are compared for both structure types. Although

weak, stray field contrast is visible at the element tips for all elements in the Foucault images of Fig. 6.4. The mean direction of magnetisation, which was deduced from these images is indicated by the green arrows in the schematics. The most notable effect of the geometry of these elements is the 'channelling' of the magnetisation through the majority of the elements.

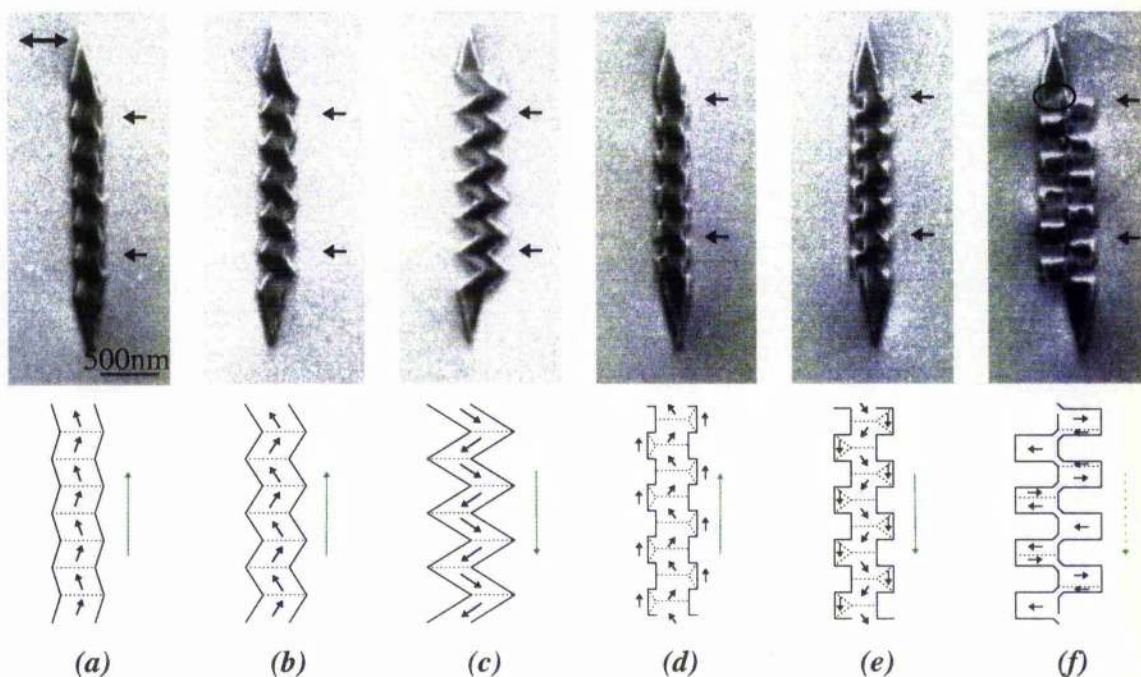


**Figure 6.4**

Overview of Foucault images of narrow ( $w_1$ ) ac-demagnetised elements with structured edges ( $p=0.33\mu\text{m}$ ) and schematics of magnetisation direction within the four structure periods marked by single arrows in the Foucault images. Mapping direction indicated by double arrow. Green arrows indicate mean direction of magnetisation.

(a)-(c) Edge structure type A with  $h_1=50\text{nm}$ ,  $h_2=100\text{nm}$ ,  $h_3=250\text{nm}$ ; (d)-(f) Edge structure type C with  $h_1$ ,  $h_2$ ,  $h_3$ . The ellipse in the Foucault image (f) marks a closure domain.

In the case of structure type A, where the direction of magnetisation simply follows the serpentine like geometry of the elements, this channelling effect is immediately obvious (Figs. 6.4(a)-(c)) and it led to the formation of parallelogram domains in most of the elements even in the as-grown and the ac-demagnetised states of the samples. The parallelogram domains can easily be seen not only in the Foucault images, but also in the associated schematics in Figs. 6.4(a)-(c). In the case of identical period but different

structure height (as for the Foucault images in Figs. 6.4(a)-(c)), the wall angle was found to increase with structure height. For the same structure height, the wall angle was found to increase with decrease of structure period. In both cases the outer vertices of the structure features were getting sharper and therefore the change in edge direction was more abrupt. With the magnetisation aligning parallel to the nearest edge, the associated change in magnetisation direction was also more abrupt and therefore the wall angle higher. Thus the structure parameters did not generally change the characteristic parallelogram domain geometry for structure type A, but the wall angle was found to depend on the structure variables. Exceptions were all elements with the smallest period  $p=0.1\mu\text{m}$ . The elements with  $h_1$  and  $h_2$  appeared quasi single domain while the elements with  $h_3$  were multi-domain but the parallelogram domains were no longer generated for each half period. The same observation was made for the elements with  $h_3$  and the longer period  $p=0.2\mu\text{m}$ . It should be noted that it were also the elements with small period structure type A with  $h_3$  which were found to deviate considerably from the designed zigzag-shape (Fig. 6.3(c)). In agreement with the previous chapter the most common domain shape for edge structure type A was the parallelogram geometry. Whilst in the case of the elements discussed in chapter 5 these parallelogram domains were generated under the influence of reverse fields they often were already present at remanence here.

In the case of structure type C (Figs. 6.4(d)-(f)) the channelling effect was also observed clearly for the two smaller structure heights ( $h_1$ ,  $h_2$ ) but to some degree even in the case of  $h_3$ . Within the elements with  $h_1$  and  $h_2$  with periods  $p\leq 0.33\mu\text{m}$  two y-configurations were observed per period as can be seen in the schematics of Figs. 6.4(d) and (e) for  $p=0.33\mu\text{m}$ . It should be noted that the y-configurations observed here were very similar to the characteristic domain configurations in the case of structure type C in the patterns of chapter 5 (i.e. within the elements with overall variation of width). In the case of the elements with edge structure type C with the longer periods ( $p=0.67$  and  $2.0\mu\text{m}$ ) with  $h_1$  and  $h_2$ , however, only small domains were observed in the step regions of the elements but those did not form y-configurations. These configurations were the same in the ac-demagnetised state and the remanent state of the elements and they are described in section 6.4.2.

The very disjointed elements with structure type C with  $h_3$  displayed different domain configurations (Fig. 6.4(f)) and these were even more dependent on the structure period than in the case of the elements with  $h_1$  and  $h_2$ . A common feature, however, were closure

domains at the blunt end of the tip part as marked with the ellipse in Fig. 6.4(f). As far as the magnetic configurations within the structure features were concerned those strongly depended on the shape of the features. In the case of  $p=2.0\mu\text{m}$  the two nearly separated parts of the element were almost uniformly magnetised along the length of the elements with the exception of small closure domains at the blunt 'ends' in the centre of the elements similar to that marked with the ellipse in Fig. 6.4(f). For  $p=0.67\mu\text{m}$  the structure features supported flux closure structures. In the case of the elements with small structure periods  $p=0.2, 0.25$  and  $0.33\mu\text{m}$  stray fields were visible at the outer ends of the structure features as can be seen in Fig. 6.4(f). In the Foucault image of Fig. 6.4(f) some fine structure is visible within the rectangular structure features. With these stray fields present for most features, flux closure structures could be ruled out for the majority of those rectangles. As the transition areas (bridges) had a notable a width (20-30nm) between the rectangles, the deduced schematic is thought to be quite close to the actual domain configuration.

## 6.5 MAGNETISING EXPERIMENTS

As in the case of the previous patterns the in-situ magnetising experiments were carried out in the Philips CM20 FEG microscope by tilting the sample in the objective lens field. The magnitude of this vertical field was  $\approx 700$  Oe in the case of the fourth pattern and  $\approx 940$  Oe for the fifth pattern. The primary imaging mode was again the Fresnel mode but for some of the elements the magnetic microstructure was recorded in the DPC mode at different stages during magnetising loops. The observations are presented in a similar way to the discussion in chapter 5. However, no description of the behaviour of the standard elements of the fourth and fifth patterns is given as the observations were identical with those of the standard elements of the two previous patterns (section 5.5.1). The development of the magnetic microstructure within the narrow elements ( $w_1$ ) with both structure types is discussed with emphasis on the elements with  $h_2$  of the fifth pattern ( $t_2$ ). A brief overview of the observed magnetic microstructures within all narrow elements is given also and the switching field values are compared for all elements of patterns five and four.

### 6.5.1 ELEMENTS WITH EDGE STRUCTURE TYPE A

As in chapter 5, a summary of the observed domain configurations at remanence and prior to switching is given in advance in order to simplify the discussion of the results. Table 6.1 summarises the observations of in-situ magnetising experiments carried out with the elements of the fifth pattern ( $t_2$ ) for the narrow elements ( $w_1$ ). As in the previous chapter, the overview in the tables was kept as compact as possible and with the emphasis on similarities. The same terminology was used here as for table 5.3. It should be noted, however, that in the case of the fourth and fifth pattern a pair of parallelogram domains were observed per period instead of just one parallelogram domain per period (section 5.5.2).

Structure Type A, Width $w_1$ - Fifth pattern				
period	state	$h_1=50\text{nm}$	$h_2=100\text{nm}$	$h_3=250\text{nm}$
2.0 $\mu\text{m}$	R	single domain	single domain	low angle wall at centre
	PS	concertina	concertina	walls at centre and ends
0.5 $\mu\text{m}$	R	parallelogram domains	parallelogram domains	parallelogram domains
	PS	parallelogram domains	parallelogram domains	parallelogram domains
0.33 $\mu\text{m}$			(Figs. 6.5, 6.6)	
	R	parallelogram domains	parallelogram domains	parallelogram domains
	PS	parallelogram domains	parallelogram domains	parallelogram domains
0.2 $\mu\text{m}$			(Figs. 6.7(a), (b))	
	R	parallelogram domains	parallelogram domains	parallelogram domains
	PS	parallelogram domains	parallelogram domains	walls move and merge
0.1 $\mu\text{m}$			(Figs. 6.7(c), (d))	
	R	single domain	single domain	quasi single domain
	PS	concertina	concertina	multi domain

**Table 6.1**

*Micromagnetic states of elements with  $w_1$  and structure type A of 5<sup>th</sup> pattern ( $t_2=2$ ).*

*R: Remanent state, PS: Prior to switching.*

In agreement with the observations in the previous chapter it was found that the two different tip ratios hardly altered the magnetic microstructure of the elements at all. Therefore table 6.1 is also valid for most of the narrow elements ( $w_1$ ) of the fourth pattern

( $t_1$ ). Exceptions were three sets of elements and the differences were restricted to the observations prior to switching: The elements with  $t_1$  and  $p=2.0\mu\text{m}$  with  $h_1$  and  $h_2$  and also the elements with  $p=0.1\mu\text{m}$  and  $h_1$  did not generate a full concertina structure but instead only end domains were visible prior to switching. Also in agreement with the findings of both previous chapters, the domain configurations which were observed within the wide elements ( $w_2$ ) did not show distinct differences to those of the narrow elements which were described above.

Thus, the main parameters for the determination of the magnetic microstructure of the elements with nominally constant width and structure type A were again the structure parameters  $h$  and  $p$  and the most commonly observed domain geometry was again found to be the parallelogram domains. However, in the case of the elements with nominally constant width, a pair of parallelogram domains were observed for each period instead of just one in the case of the elements with varying overall width in the previous chapter. The absence of the parallelogram domains in the case of the smallest ( $0.1\mu\text{m}$ ) and longest ( $2.0\mu\text{m}$ ) investigated periods was also consistent with the results of the two previous chapters. This supports the idea of critical values for the edge structure parameters to profoundly alter the magnetic microstructure of elements with structured edges compared to standard elements.

Figure 6.5 shows an overview of Fresnel images of an element with  $w_1$  and  $t_2$  with structure type A ( $h_2$ ) with a period  $p=0.33\mu\text{m}$  at different stages of a magnetising experiment. Schematics were derived from the images and are also shown.

At remanence the mean direction of magnetisation was parallel to the element length with the magnetisation being 'channelled' through the element as a result of the local changes of edge direction. Faint low angle walls which were running across the entire element width were already visible (Fig. 6.5(a)) forming a pair of parallelogram domains per period. One of these parallelogram domains is highlighted by the red area in the schematic of Fig. 6.5(a). The walls increased in contrast when a reverse field was applied (Fig. 6.5(b)) indicating magnetisation rotation in adjacent domains. Some degree of wall movement was detected for the walls next to the element tips. All other walls were firmly pinned at (opposite) vertices of the structure features. After magnetisation reversal wall sections were still visible at the outer vertices of the elements (Fig. 6.5(c)).

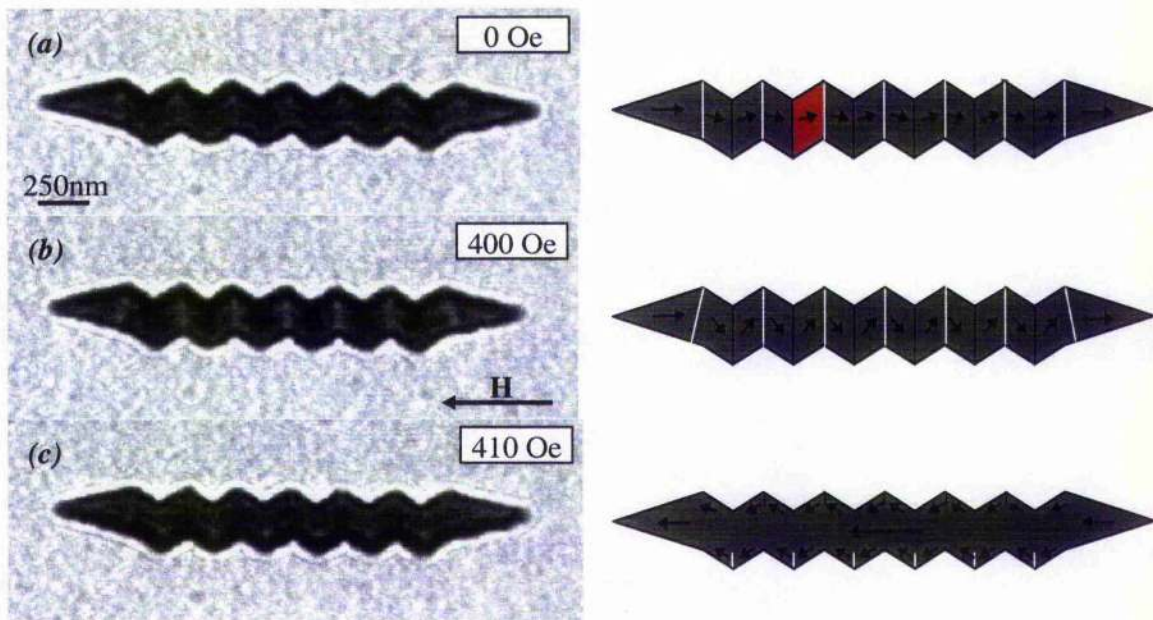


**Figure 6.5**

*Fresnel images of an element with structure type A ( $p=0.33\mu\text{m}$ ) recorded during magnetising sequence with corresponding schematics of magnetisation distribution. The red area in the schematic of (a) highlights a parallelogram domain.*

DPC images of such an element with  $p=0.33\mu\text{m}$  at remanence and prior to switching are shown in Fig. 6.6. The observed increase of domain contrast confirmed magnetisation rotation and the absence of wall movement for all walls but those at the element ends was also corroborated. One of the parallelogram domains is marked by the red frame in Fig. 6.6.

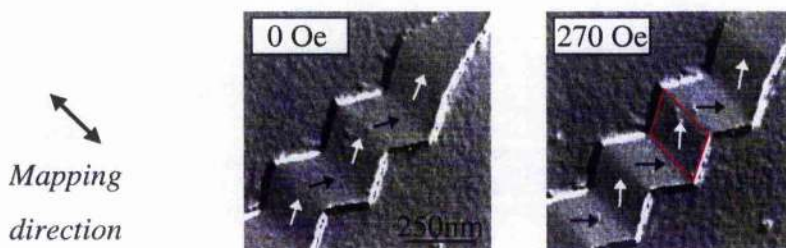


**Figure 6.6**

*DPC images an element with structure type A ( $p=0.33\mu\text{m}$ ,  $h_2=100\text{nm}$ ) at different field values, with schematic of magnetisation distribution. Red frame illustrates a parallelogram domain.*

Similar behaviour was observed for all elements with structure type A with  $h_2$  and small periods ( $0.2\mu\text{m} \leq p \leq 0.5\mu\text{m}$ ). However, the elements with the longest ( $p=2.0\mu\text{m}$ ) and smallest ( $p=0.1\mu\text{m}$ ) periods were again found to behave differently. These elements displayed strong similarities with the standard elements in their magnetic microstructure in zero field and also in their switching behaviour.

In Fig. 6.7 DPC images of elements with structure type A ( $h_2$ ) with  $p=0.2\mu\text{m}$  and  $p=0.1\mu\text{m}$  are compared. The elements with  $p=0.2\mu\text{m}$  (Figs. 6.7(a), (b)) showed the same characteristics as the elements with the longer periods 0.5 and  $0.33\mu\text{m}$  (i.e. parallelogram domains at remanence and almost exclusively magnetisation rotation prior to switching). Elements with the smallest period  $p=0.1\mu\text{m}$  (Figs. 6.7(c), (d)), however, did not show much variation of direction of magnetisation at remanence. When a reverse field was applied to these elements low angle walls were generated with less than two domains per structure period. As already mentioned the domain configurations looked more like the concertina structures, which were observed in the standard elements (section 5.5.1). The magnetic microstructure of the elements with the smallest structure period also resembled very much that of the elements with the same structure parameters of the second and third patterns (section 5.5.2, Figs. 5.15, 5.16(c), (d)). The red frame in Fig. 6.7(b) illustrates one of the characteristic parallelogram domains and the red frame in Fig. 6.7(d) highlights an arbitrary domain in an element where pairs of parallelogram domains per period were no longer supported.

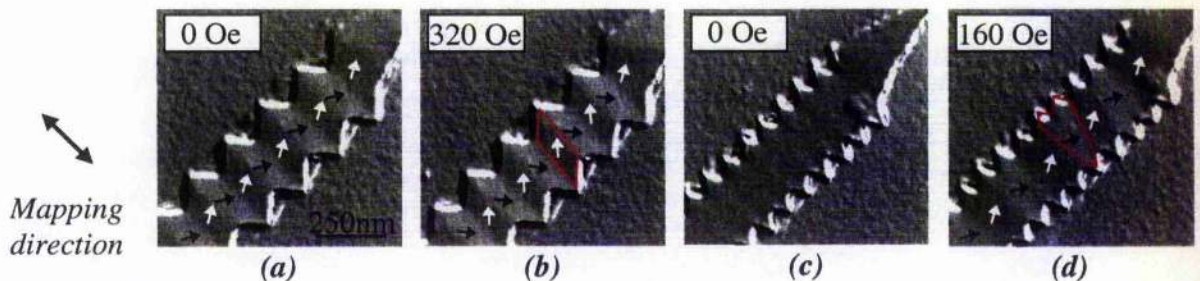


**Figure 6.7**

*DPC images of acicular elements ( $w_1=250\text{nm}$ ) with structure type A ( $h_2=100\text{nm}$ ) at different field values. (a), (b)  $p=0.2\mu\text{m}$ ; (c), (d)  $p=0.1\mu\text{m}$ . Single arrows indicate magnetisation direction. Red frames illustrate domain shapes.*

With the discussion of the domain configurations of elements with structure type A complete the next sections deal with the investigations of the influence of the edge structure parameters on the coercivity of the elements. Overviews of the switching field values of all elements with edge structure type A of the fourth and fifth patterns are given in Figs. 6.8 and 6.9. The layout of the figures is identical to that in sections 5.5.2 and 5.5.3. As the width of the elements was nominally constant in the case of these two patterns (apart from the tip regions) only one set of standard elements was investigated and used for reference in the corresponding graphs. The reference elements for the narrow elements with structured edges were standard elements with  $w_1$  whilst the coercivity of the wide elements with edge structure is compared to the switching field values of the standard elements with  $w_2$ .

The results of these two patterns were in many respects very similar to those for the second and third patterns (see section 5.5.2). The main difference was that the elements with structured edges of the fourth and fifth pattern were generally harder to switch than the corresponding ones of the second and third patterns. The reason for this is almost certainly the fact that the elements of the former patterns did not have wider parts than the (minimum) width (see Fig. 6.1). It should be noted that this increase of coercivity had two main effects on the graphs discussed here. Firstly, the typical maximum of coercivity for small periods, which was detected in the previous patterns with  $t_1$  appeared again (Figs. 5.18, 6.8) but as a result of the general increase of coercivity for the elements with structured edges this maximum lay in most cases even above the coercivity of the standard elements. Secondly, in the case of the sharper tips ( $t_2$ ) the variation of the coercivity with period was again reduced but the drastic drop in coercivity which was detected for the elements with variation of width (Fig. 5.19) was not seen for the elements with nominally constant width (Fig. 6.9). Another difference was that here all elements with the sharper tips  $t_2$  were magnetically harder than the corresponding elements with the blunter tips  $t_1$ .

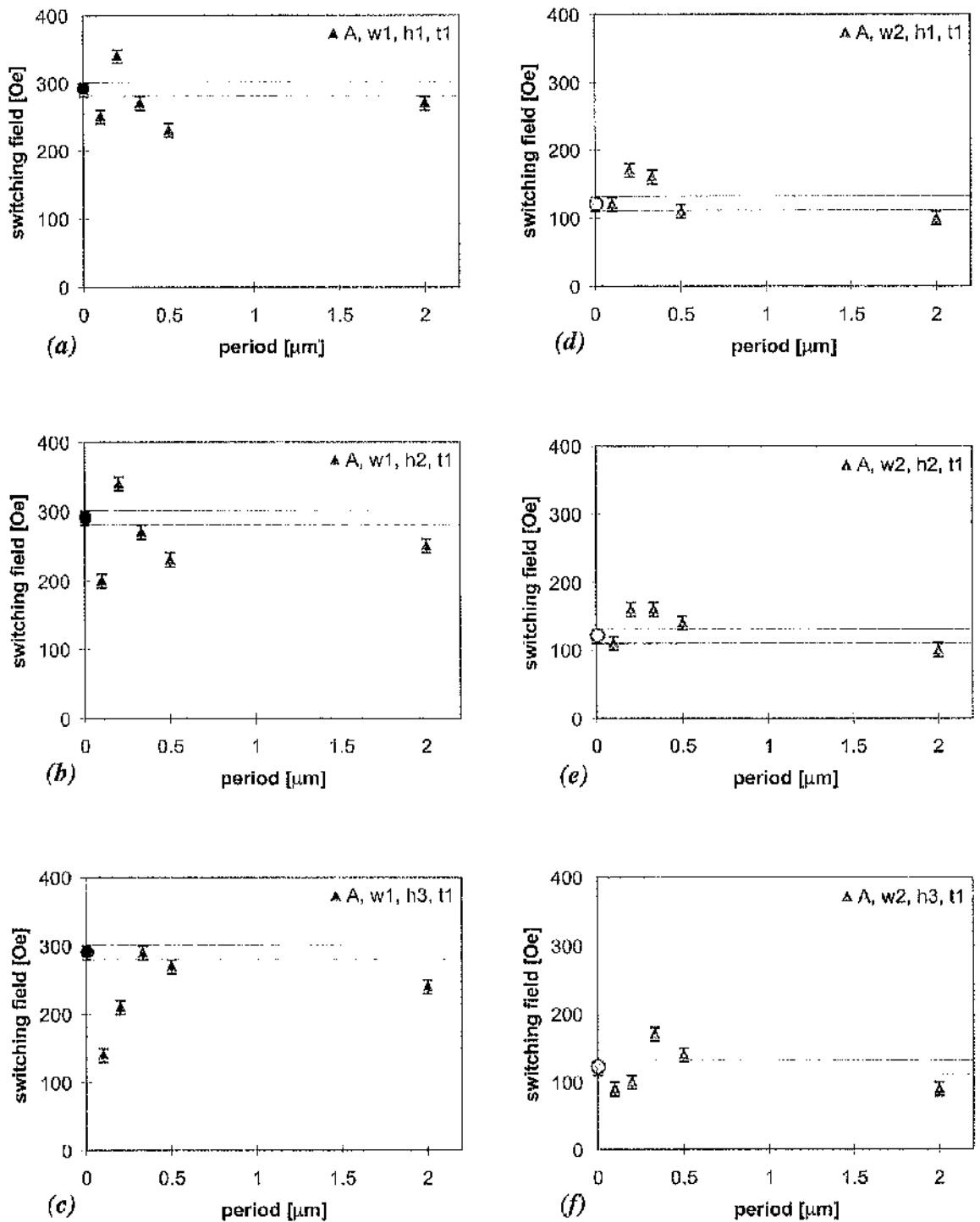


**Figure 6.8**

Overview of switching field values of elements with structure type A of fourth pattern.

A: type of edge structure, t1: tip ratio = 1 for the elements of this pattern,

w1: narrow elements, w2: wide elements, structure heights h1=50nm, h2=100nm, h3=250nm

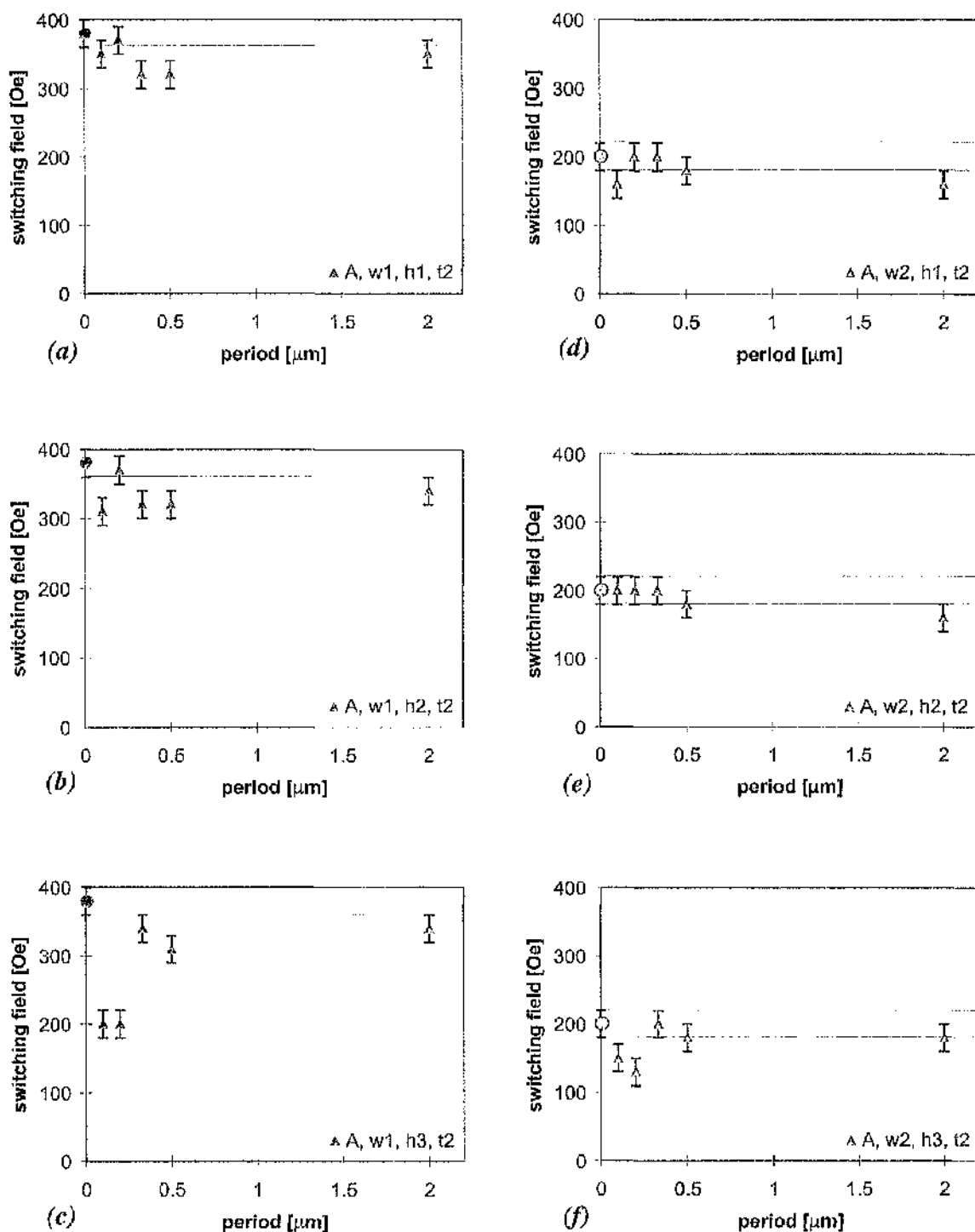


**Figure 6.9**

Overview of switching field values of elements with structure type A of fifth pattern.

A: type of edge structure, t1: tip ratio = 1 for the elements of this pattern,

w1: narrow elements, w2: wide elements, structure heights  $h1=50\text{nm}$ ,  $h2=100\text{nm}$ ,  $h3=250\text{nm}$

## 6.5.2 ELEMENTS WITH EDGE STRUCTURE TYPE C

In accordance with the structure of the previous sections an overview of the observed domain configurations during magnetising experiments is given prior to the detailed discussion of the results. Table 6.2 summarises the micromagnetic states of the narrow elements ( $w_1$ ) with structure type C of the fifth pattern ( $t_2$ ). As before the principle was to determine characteristic similarities rather than minute differences.

Structure Type C, Width $w_1$ - Fifth pattern				
period	state	$h_1=50\text{nm}$	$h_2=100\text{nm}$	$h_3=250\text{nm}$ ('fishbone')
2.0 $\mu\text{m}$	R	quasi single domain	quasi single domain	Figs. 6.3(f), 6.4(f) closure domains
	PS	concertina*	concertina*	closure domains
0.67 $\mu\text{m}$	R	quasi single domain	(Figs. 6.10, 6.12(a), (b)) multi-domain	--
	PS	multi-domain	y-configurations	--
0.33 $\mu\text{m}$	R	y-configurations	(Figs. 6.11, 6.12(c), (d)) y-configurations	--
	PS	y-configurations	y-configurations	--
0.25 $\mu\text{m}$	R	y-configurations	y-configurations	--
	PS	y-configurations	y-configurations	--
0.2 $\mu\text{m}$	R	y-configurations	y-configurations	--
	PS	y-configurations	y-configurations	--

Table 6.2

Micromagnetic states of elements with  $w_1$  and structure type C of 5<sup>th</sup> pattern ( $t_2=2$ ).

R: Remanent state, PS: Prior to switching.

The terminology is similar to that of table 5.4. The only new term is 'closure domains' and describes domains at the blunt end of tip parts (as those marked by the ellipse in Fig. 6.4(f)). The micromagnetic states of the narrow elements with  $h_3$  are only described for  $p=2\mu\text{m}$ . For the other periods the fine structure within the almost isolated structure features was not clear enough in the Fresnel experiments to deduce enough detail and it was not considered worthwhile to carry out the time consuming DPC experiments with

these 'fishbone' elements (Fig. 6.2, third row in lower array). It should be noted though that closure domains were detected at all blunt ends of tip parts in the fishbone elements.

Comparison of the domain configurations observed in the elements of the fifth pattern ( $t_2$ ) with those detected in the elements of the fourth pattern ( $t_1$ ) showed that there was very little difference between the two samples for identical structure parameters. This agrees well with previous observations where it was also found that the two different tip aspect ratios did not show considerable influence on the magnetic microstructure of the elements. Therefore table 6.2 is also valid for most of the corresponding elements of the fourth pattern. Exceptions were all elements with  $p=2\mu\text{m}$  in the state prior to switching: In addition to the domain configurations given in the table end domains were generated in all these elements.

Comparison of the elements with the two different widths did not yield striking differences between the domain configurations for the elements with  $h_1$  and  $h_2$ . However, due to the change of the 'fishbone' geometry ( $w_1$ ) to elements with considerable main body ( $w_2$ ) the magnetic microstructure of the two sets of elements with structure type C with  $h_3$  were different. The wider elements of this kind displayed a similar behaviour to the elements with  $h_2$  (see corresponding column of table 6.2).

In the case of structure type C the mean direction of magnetisation was also found to lie parallel to the element length and the channelling effect which was deduced for the elements with structure type A was observed as well. This is illustrated in Fig. 6.10 where an overview of Fresnel images of an element with structure type C with  $p=0.67\mu\text{m}$  and  $h_2$  is given for different stages during a magnetising experiment together with the derived schematics. At remanence low angle walls which ran across the entire element width were visible due to this channelling of magnetisation (Fig. 6.10(a)). When a reverse field was applied the configurations of these domain walls changed and despite being curved (exaggerated in the schematic), y-configurations were clearly to discern (Fig. 6.10(b)). It should be noted that some non-y-configuration walls were also present. Increase of the applied field led to an increase of wall contrast indicating magnetisation rotation while no further wall movement was observed. After magnetisation reversal faint wall sections which originated in the outer corners of the structure features were still present (Fig. 6.10(c)).

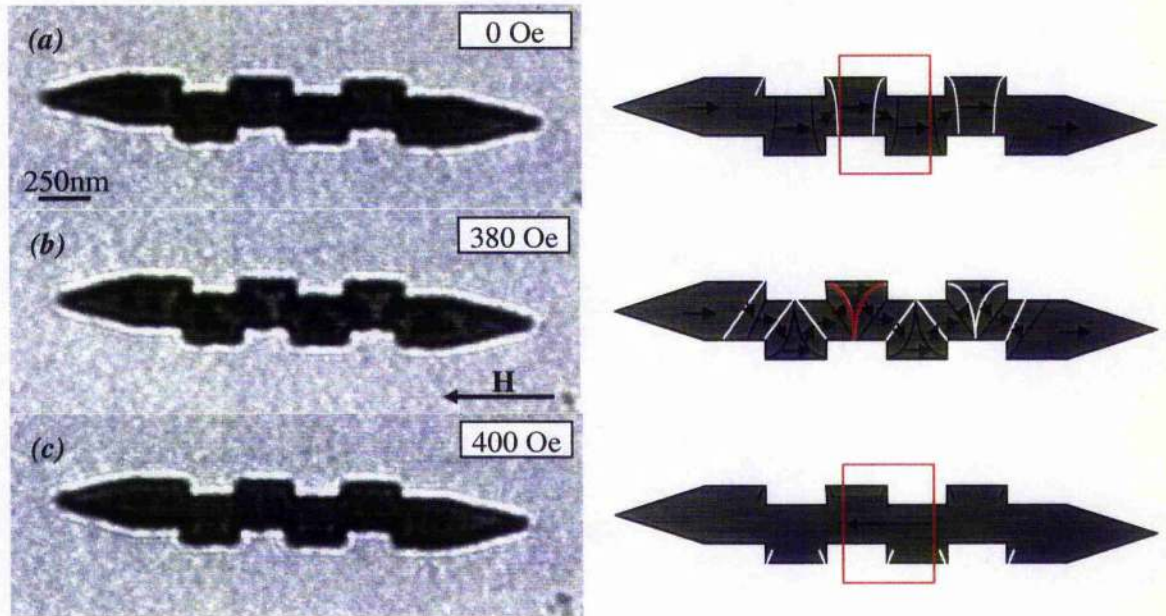


**Figure 6.10**

*Fresnel images of element with structure type C ( $p=0.67\mu\text{m}$ ) recorded during magnetising sequence with corresponding schematics of magnetisation distribution. Red boxes mark domain structures which were also found in the case of  $p=2.0\mu\text{m}$ , while the red lines in (b) highlight a y-configuration.*

In the case of the longest period ( $p=2.0\mu\text{m}$ ) the elements were almost uniformly magnetised at remanence apart from a faint domain structure which was present at the region of the step of such elements. This configuration looked like the one marked with the red frame in Fig. 6.10(a). Application of a reverse field led first to an increase of wall contrast and at a later stage to the generation of a ‘concertina\*’ structure (i.e. a concertina structure which started to develop from the centre of the elements). After magnetisation reversal, the elements were quasi single domain with two faint wall sections visible in the step region (see red frame in Fig. 6.10(c)).

In the case of the structure periods  $0.2\mu\text{m}\leq p\leq 0.33\mu\text{m}$  y-configurations were observed at remanence. One of them is highlighted by red lines in Fig. 6.11(a). It should be noted that there was always a pair of such y-configurations per period observed, which was quite similar to the double y-configurations as discussed in the previous chapter. Under the influence of a reverse field the walls which were already present at remanence merely intensified in contrast indicating an increase of wall angle (Fig. 6.11(b)). After magnetisation reversal faint wall structures were still visible within the structure features

(Fig. 6.11(c)). In the Fresnel image of Fig. 6.11(c) all remaining domain configurations after the switch of magnetisation were of the bisector type. This was not always the case but the remaining of flux closure like domain configurations within the structure features after magnetisation reversal within the main body of the elements as described in section 5.5.3 (Fig. 5.22) was less common here.

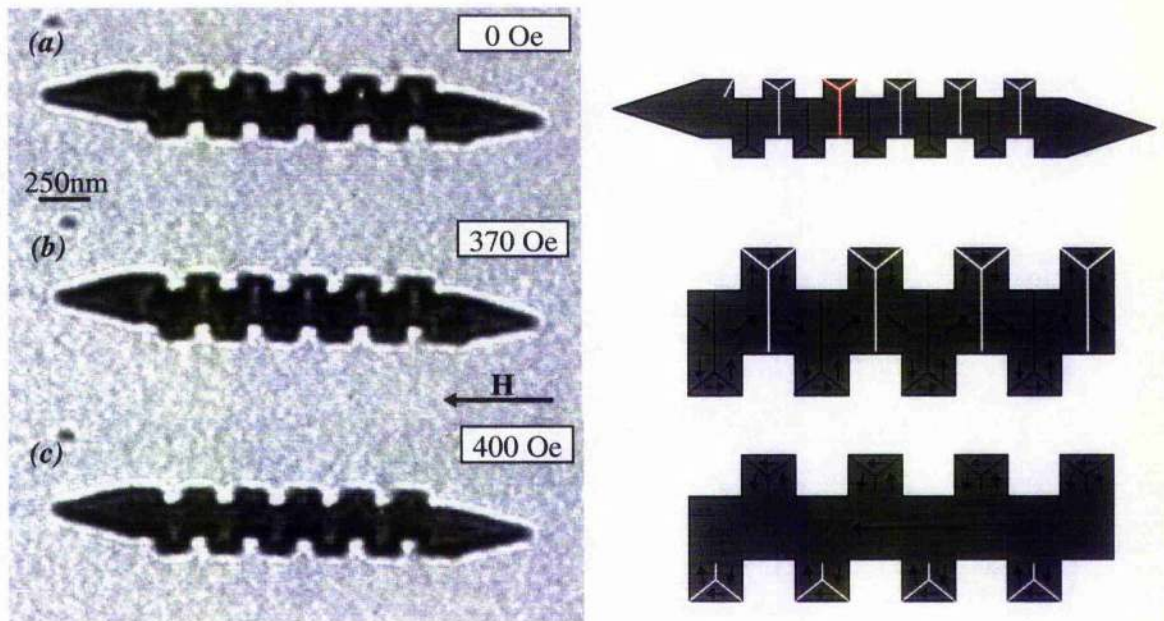


**Figure 6.11**

*Fresnel images of element with structure type C ( $p=0.33\mu\text{m}$ ) recorded during magnetising sequence with corresponding schematics of magnetisation distribution. Red lines highlight y-configuration.*

Figure 6.12 shows a compilation of DPC images of two elements at remanence and prior to switching. It illustrates the characteristic y-configurations as well as the domain configurations which were present at the steps of the longer period elements ( $p=2.0\mu\text{m}$  and  $0.67\mu\text{m}$ ) at remanence (Fig. 6.12(a)). The schematics, which were derived from the Fresnel images agreed very well with the schematics in the DPC images. In the case of the elements with  $p=0.67\mu\text{m}$  transformation of the domains at the steps present at remanence (Figs. 6.10(a), 6.12(a)) into y-configurations when a reverse field was applied was clearly the result in both experiments (Figs. 6.10(b), 6.12(b)). The observation that y-configurations were generally firmly pinned and that there was no movement of such y-configuration walls prior to switching was also corroborated (Figs. 6.11(a), (b) and 6.12(c),

(d)). The observations for the elements with  $0.2\mu\text{m} \leq p \leq 0.33\mu\text{m}$  were basically identical due to the channelling of the magnetisation through the serpentine shapes.

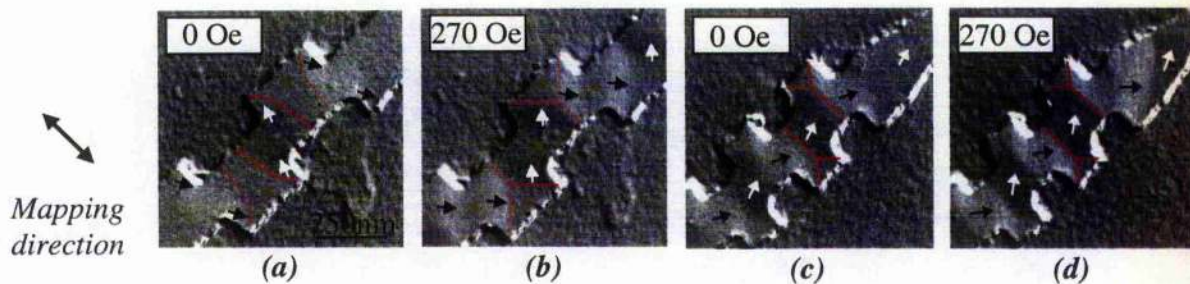


**Figure 6.12**

*DPC images of acicular elements ( $w_1=250\text{nm}$ ) with structure type C ( $h_2=100\text{nm}$ ) at different field values. (a), (b)  $p=0.67\mu\text{m}$ ; (c), (d)  $p=0.33\mu\text{m}$ . Single arrows indicate magnetisation direction. Red lines highlight common domain configurations.*

The investigation of the coercivity of the elements with structure type C is discussed next. The results are illustrated in Figs. 6.13 and 6.14 with the layout being identical to that of Figs. 6.8 and 6.9 (apart from the missing graphs for the ‘fishbone’ elements). The elements with structure type C of the fourth and fifth patterns were also magnetically harder than those of the second and third patterns which was in agreement with the observations for the elements with structure type A. A considerable number of elements with structured edges and  $t_1$  tips were found to have an even higher coercivity than the corresponding standard elements (Fig. 6.13) This was also observed for the type A elements of this pattern (Fig. 6.8).

It should be noted, that in the case of the elements with the sharper tips ( $t_2$ ) the variation of coercivity depending on structure period was not generally found to be markedly reduced compared to the variation of  $H_c$  of the elements with the blunter tips (Figs. 6.13, 6.14). Additionally the characteristic drop in coercivity which was found for the elements with  $t_2$  for both structure types of the elements in the previous chapter (Figs. 5.19, 5.25) was not seen here. This was also observed for the elements with structure type A of the fourth and fifth pattern and is thought to be a result of the nominally constant element width of all elements including those with structured edges.

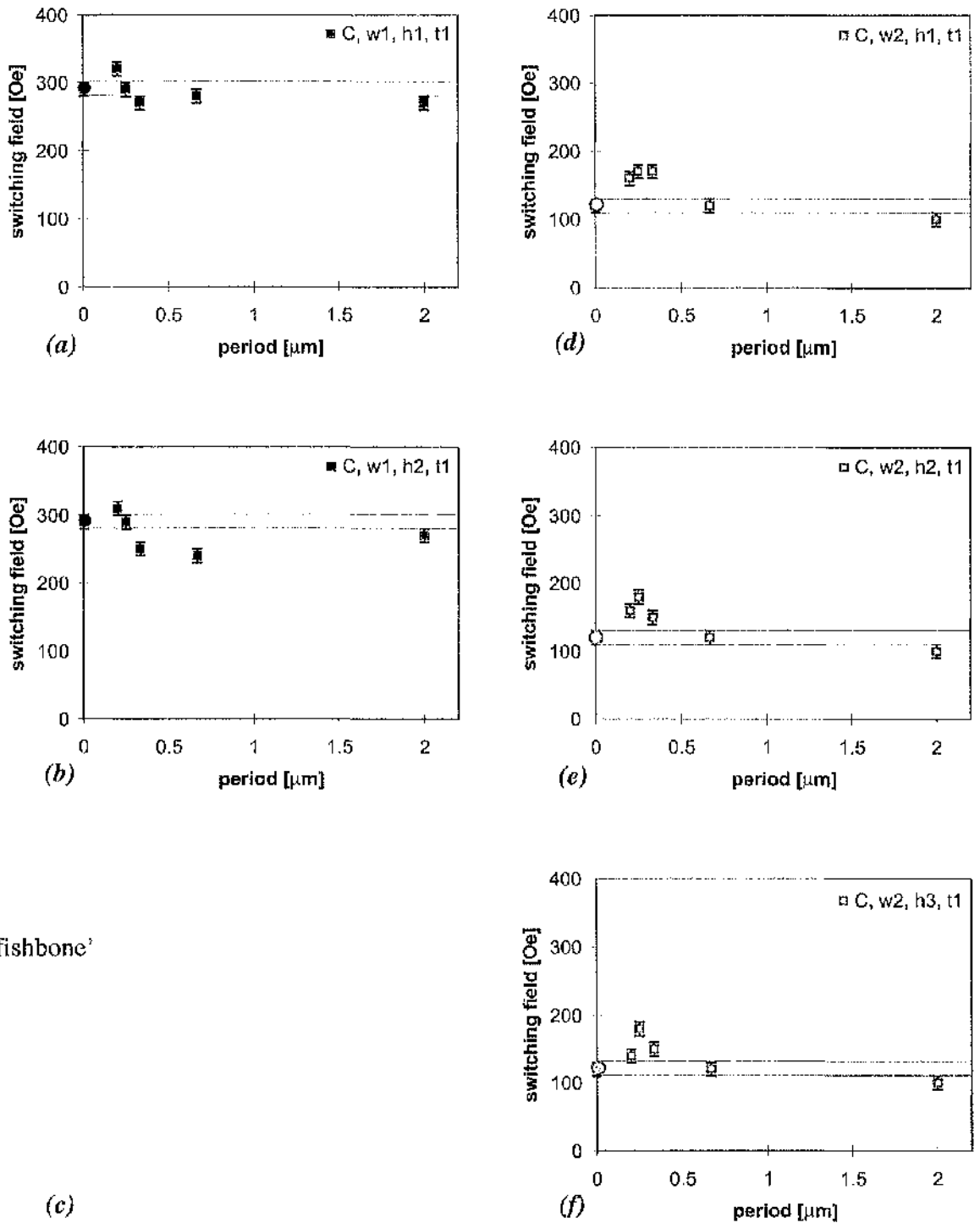
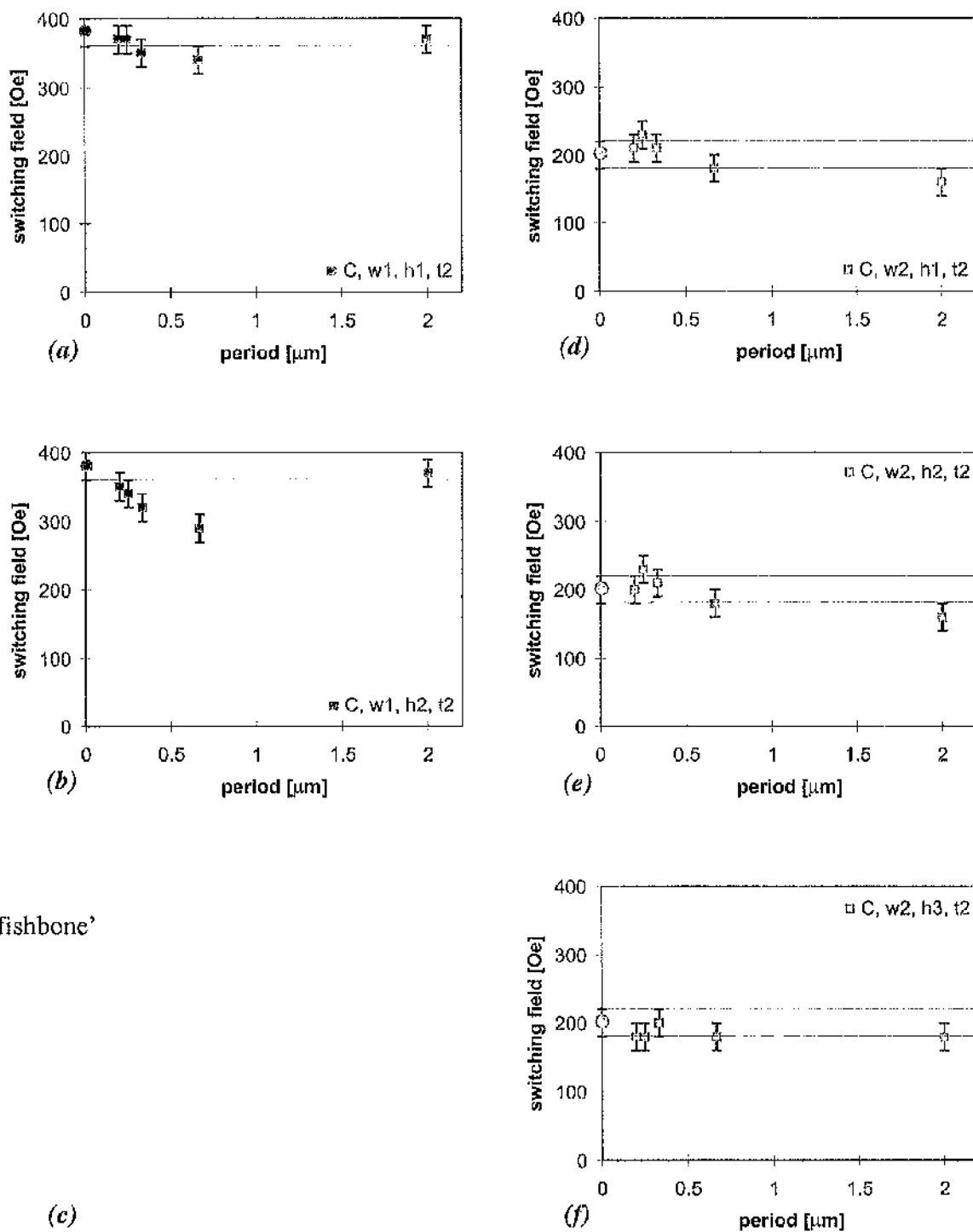


Figure 6.13

Overview of switching field values of elements with structure type C of fourth pattern.

C: type of edge structure,  $t1$ : tip ratio = 1 for the elements of this pattern,

$w1$ : narrow elements,  $w2$ : wide elements, structure heights  $h1=50\text{nm}$ ,  $h2=100\text{nm}$ ,  $h3=250\text{nm}$



**Figure 6.14**

Overview of switching field values of elements with structure type C of fifth pattern.

C: type of edge structure, t2: tip ratio =2 for the elements of this pattern,

w1: narrow elements, w2: wide elements, structure heights h1=50nm, h2=100nm, h3=250nm

## 6.6 SUMMARY

As in the previous chapter, two patterns of acicular thin film elements with different tip ratios ( $t_1$ ,  $t_2$ ) and various edge structures were fabricated and investigated. In order to determine the effects, which were due to the variation of element width in the previous chapters, the elements with structured edges of the fourth and fifth patterns were of nominally constant width ( $w_1$  and  $w_2$ ). Structure types and parameters were kept the same as in the previous chapter.

The physical microstructure of the elements was evaluated first and it was found that pattern transfer was in most cases of high quality. In agreement with the previous chapters the quality of the structure features was however observed to deteriorate in some cases for edge structure type A (i.e. for the smallest period  $p=0.1\mu\text{m}$ ).

Investigation of the magnetic microstructure in the as-grown and ac-demagnetised states of the samples showed that there was negligible difference between the two states. As expected and in agreement with the results of the previous chapters, the standard elements were clearly single domain with the mean direction of magnetisation parallel to the element length. Also in agreement with the observations in the previous chapter the different tip ratios ( $t_1$ ,  $t_2$ ) were generally not found to considerably alter the magnetic microstructure.

In the case of the elements with structured edges, the main observation was the distinct 'channelling' of the magnetisation through the elements as a result of the serpentine like geometry of most of them. Thus, the variation of magnetisation direction within elements with edge structure type A was no longer confined to the edge regions. Instead, a pair of parallelogram domains per period was visible within the majority of these elements. The mean direction of magnetisation of all these elements was clearly parallel to the element length.

In the case of structure type C the channelling effect of the magnetisation was also observed with the mean direction of magnetisation being again parallel to the element length. The channelling was most pronounced in the case of the two small structure heights ( $h_1$ ,  $h_2$ ) but it was also observed to some degree in the case of  $h_3$ . Most of the elements with structure type C were found to support multi-domain states with the most common feature being two y-configurations per period. In the case of structure type C with  $h_3$  and  $w_1$ , the

elements were very disjointed and the magnetisation distribution within the structure features depended on their shape.

In-situ magnetising experiments were carried out and the development of the magnetic microstructure was carefully monitored up to the switching field values. Magnetisation reversal itself was again too rapid to gain any insight in the reversal mechanisms by means of TEM. All elements were clearly found to be multi-domain prior to switching and it is thought that reverse domains were nucleated at some point which then grew rapidly. As in zero field conditions, neither the width nor the different tip ratios was found to alter the magnetic microstructure for both structure types.

It should be noted that as a result of the channelling effect of the elements with structured edges, the majority of these elements were found to be multi-domain even at remanence. While wall movement only played a minor role in the transition between remanence and prior to switching, rotation was clearly observed. The magnitude of the effects depended on the structure parameters. In the case of elements with structure type A with  $h_3$  and the small investigated periods ( $p=0.2\mu\text{m}$  and  $0.1\mu\text{m}$ ) a remarkable change in reversal behaviour was frequently detected: Instead of switching in an instant, the elements were found to reverse in stages.

In agreement with the observations in the previous chapter the coercivity of the elements with structured edges was found to depend on the element width. The main difference was that the elements with structured edges of the patterns of this chapter were generally harder to switch than the corresponding ones in the previous chapter. The reason for this was that the elements of the fourth and fifth patterns were of nominally constant width. This led to the result that some elements with structured edges were magnetically even harder than corresponding standard elements. A second effect was the drastic drop in coercivity, which was detected for the elements with the sharper tips ( $t_2$ ) in the previous chapter was not seen for the elements with nominally constant width. Between remanence and the state just prior to switching magnetisation rotation was detected but generation and movement of walls only played a minor role for the most of these elements.

Also in agreement with the results of the previous chapter, the effects of edge structure type C on the coercivity of the elements were in most cases very similar to the observations made for the elements with structure type A and the similarity of the domain configurations in the main body of the elements (i.e. two parallel domain walls per period) was also corroborated. As in the previous chapters, structuring the edges led to high densities of

modified Néel walls (up to one wall per 100nm was again observed for both structure types). Simulations were carried out for some of the elements discussed in this chapter and the results are presented in the next chapter.

**CHAPTER 7:****SIMULATION OF MICROMAGNETIC STATES****USING LLG MICROMAGNETICS SIMULATOR****7.1 INTRODUCTION**

In the previous chapters the results of in-situ magnetising experiments involving standard elements and elements with structured edges were described. The switching fields of the small magnetic elements were determined with high accuracy and detailed observations of the build up of domain configurations prior to switching were made. Due to the rapid switch of magnetisation it was not possible to observe the reversal mechanisms in detail. It was expected though that reverse domains would be nucleated at the coercive field value and that these would quickly propagate the magnetisation reversal in the elements. There was however no proof for this assumption to be deduced from any of our experiments. Using commercially available software it was decided to model the magnetic microstructure during magnetising cycles for a number of elements which were investigated experimentally (chapters 4-6). Comparison of the micromagnetic behaviour determined by the simulations with the observations made in the experiments (i.e. magnetic microstructure at remanence, domain configurations prior to switching and coercivity) should provide useful insight into the agreement between experimental and theoretical data and the mechanisms behind the rapid magnetisation reversal. The simulations described here were calculated using a finite element package called 'LLG Micromagnetics Simulator' (Scheinfein et al, 1998) which solves the Landau-Lifshitz-Gilbert equation for 3-dimensional problems. Please note that the LLG Micromagnetics Simulator will be referred to as 'LLG' in the following discussion.

In this chapter a brief description of the theory underlying LLG is given in section 7.2 and the set up of problems is discussed in 7.3. A selection of simulation results is presented in section 7.4 with emphasis on narrow elements with  $t_2$  tips. The chapter concludes with the summary in section 7.5.

## 7.2 THEORY OF OPERATION OF LLG MICROMAGNETICS SIMULATOR

In order to calculate the magnetic microstructure in a ferromagnet the time evolution of the magnetisation distribution inside such a system, which is described by the Landau-Lifshitz-Gilbert equation must be solved. The Landau-Lifshitz-Gilbert equation has been examined experimentally and theoretically (Scheinfein et al, 1991 a, b), (Hubert et al, 1998) and was found to yield an accurate description of the time evolution of the magnetic moment of fixed magnitude in a magnetic field. The Landau-Lifshitz-Gilbert equation has the following form:

$$\frac{d\vec{M}}{dt} = \frac{\gamma}{1+\alpha^2} \vec{M} \times \vec{H}_{eff} + \frac{\gamma\alpha}{1+\alpha^2} \vec{M} \times \vec{M} \times \vec{H}_{eff} \quad (7.1)$$

$\gamma$  is the gyromagnetic ratio ( $\gamma = \frac{g\gamma_e}{2}$ ) which is determined by the free electron value of  $\gamma_e$  ( $= \frac{\mu_0 e}{m_e}$ , with  $\mu_0$ : permeability of vacuum,  $e$ : elementary charge,  $m_e$ : rest mass of electron) and the spectroscopic splitting factor  $g$  (Landé  $g$ -factor) which is  $\approx 2$  for ferromagnets.

$\alpha$  is the damping parameter (due to spin wave scattering) and  $\vec{H}_{eff}$  is the effective field which is determined by

$$\vec{H}_{eff} = \frac{-\partial E_{tot}}{\partial(M_s \vec{\beta})} \quad (7.2)$$

$M_s \vec{\beta}$  is the saturation magnetisation multiplied by the direction cosines and represents the value of the magnetisation vector  $\vec{M}(\vec{r})$  at each point within the ferromagnet.

$E_{tot}$  is the total energy of a system and it is determined in LLG by

$$E_{tot} = E_{ex} + E_K + E_{Ks} + E_s + E_h + E_r \quad (7.3)$$

The contributions to the total energy of a ferromagnetic system are

- the mean field exchange energy  $E_{ex}$  between nearest neighbours which is characterised by the exchange coupling constant  $A$  ( $erg/cm$ )<sup>1</sup>
- the magnetocrystalline anisotropy energy  $E_K$  describing the interaction of the magnetic moments with the crystal field which is characterised by the constant  $K_u$  (uniaxial anisotropy) or  $K_c$  (cubic anisotropy) in units of ( $erg/cm^3$ )
- the surface magnetocrystalline anisotropy energy  $E_{K_s}$  correcting for broken symmetry in the interaction of the magnetic moments with the crystal field near surfaces which is characterised by the constant  $K_s$  ( $erg/cm^2$ )
- the magnetostatic self-energy  $E_s$  arising from the interaction of the magnetic fields created by discontinuous magnetisation distributions in bulk as well as at the surface
- the external magnetostatic field energy  $E_h$  due to the interaction of the magnetic moments with external magnetic fields and
- the magnetostrictive energy  $E_t$  arising when mechanical stress or strain is applied to a ferromagnetic material which thereby introduces effective anisotropy into the system and is characterised by  $K_m$  ( $erg/cm^3$ ).

A more detailed discussion of the energy considerations is given in section 1.3. The solution of the Landau-Lifshitz-Gilbert equation for the equilibrium magnetisation distribution is a constrained boundary value problem in two or three spatial dimensions with the constraint of constant magnetisation  $M_s$  (saturation magnetisation). It should be noted that for the analysis of the equilibrium micromagnetic structure the differential equation need not be integrated directly but  $\frac{d\vec{M}}{dt} = 0$  must be fulfilled. This implies that the effective field  $\vec{H}_{eff}$  must be parallel to the magnetisation  $\vec{M}$  and the magnetisation configuration can be relaxed iteratively by positioning each magnetisation vector  $\approx$ parallel to the effective field vector throughout the entire mesh of finite elements.

The initial condition can be selected to provide a suitable start for the iteration procedure and the iteration process is stopped when the largest residual of a single value of

---

<sup>1</sup> LLG Micromagnetics Simulator uses almost exclusively CGS units.

$\frac{\vec{M} \times \vec{H}_{eff}}{|\vec{M}||\vec{H}_{eff}|}$  drops below the chosen convergence minimum. This convergence minimum is the value of the largest relative change in the largest component of the direction cosines. It depends on the size of the mesh and the closeness to a change in magnetisation such as the reorientation close to the coercive field in a hysteresis loop calculation. Equilibrium domain wall configurations determined from this energy minimisation scheme agree generally very well with configurations determined by solving the Landau-Lifshitz-Gilbert equation directly (Scheinfein et al, 1991 b). Therefore in the case of uniform systems the more economical energy minimisation scheme can be used to determine equilibrium configurations. For more complex systems, however, or in the presence of grain boundaries which may serve as nucleation sites it may be necessary to directly solve the Landau-Lifshitz-Gilbert equation for the benefit of accurate results (Scheinfein et al, 1998), (Victoria, 1987).

### 7.3 SET UP OF PROBLEMS

A description of the set up of problems as calculated in this thesis is presented in this section. When the program is loaded the start-up screen is displayed and choosing the '*Begin Simulation*' option activates the main LLG input control dialog for setting up a simulation. The '*LLG Input Control*' dialog box is illustrated in Fig. 7.1 together with the '*LLG Computational Details*' box. In the following discussion emphasis lies on the features which were relevant for this work starting at the top of the '*LLG Input Control*' box (Fig. 7.1(a)).

At this point I would like to acknowledge Prof. M. Scheinfein who not only wrote LLG but also helped a lot in the early stages of the simulations carried out for this work. His advice and tailor-made additions to the program proved very valuable and timesaving.

- ***Read Input Files:***

The '*Input Params*' button in the '*Read Input Files*' box allows to load the input parameters of previous calculations and then quickly change the appropriate values to run the simulation of a similar problem.

- *Dimension, Search, 2D Self Energy and Boundary*

The default settings of these boxes are given in Fig. 7.1(a) and neither of them was changed at any time for the simulations described here.

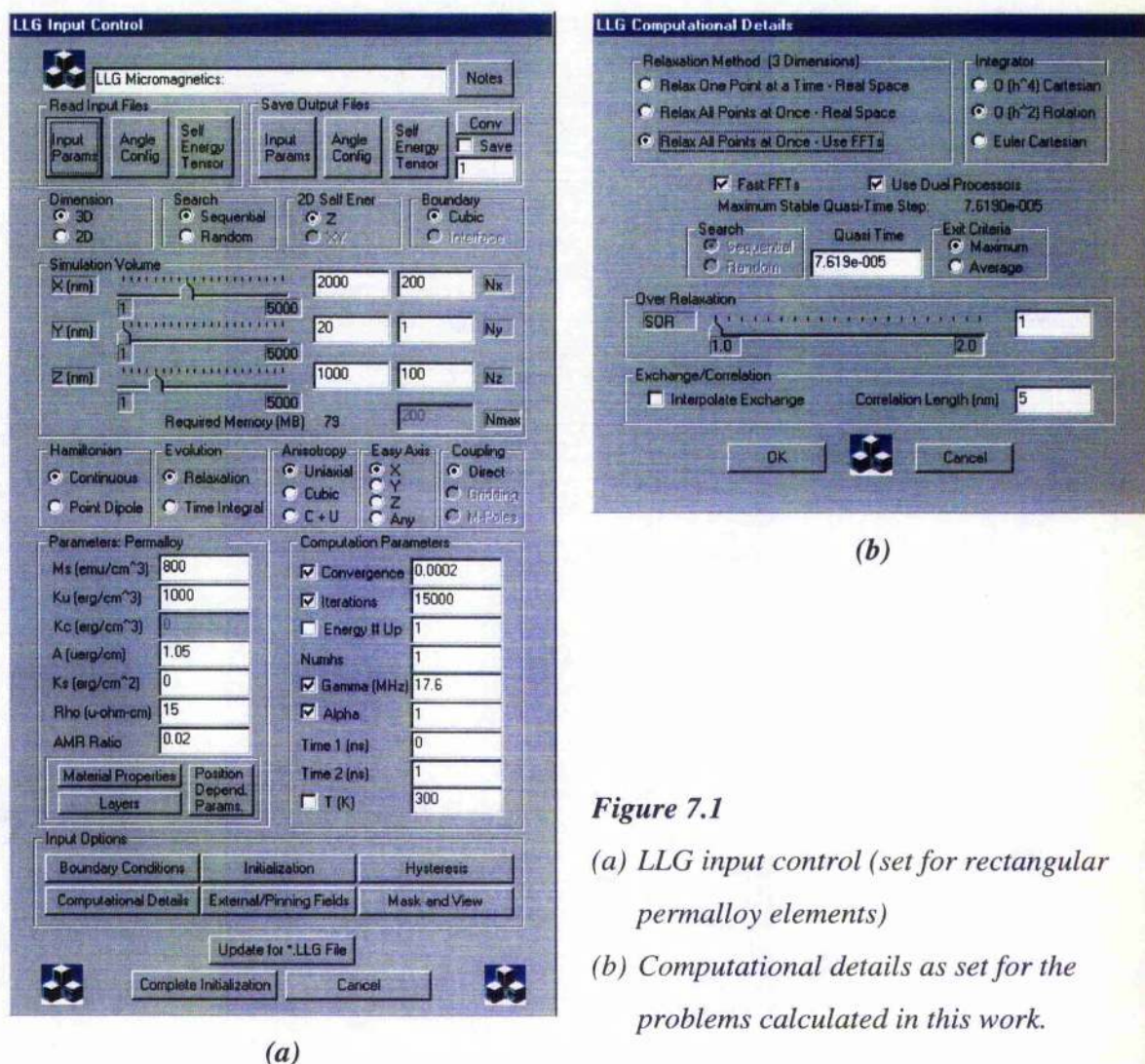


**Figure 7.1**

(a) LLG input control (set for rectangular permalloy elements)

(b) Computational details as set for the problems calculated in this work.

- *Simulation Volume*

In the ‘*Simulation Volume*’ field the overall size of the problem is determined along with the ‘discretisation volume’ of the elements (cell size). The unit of the dimensions is nanometer and the maximal size of a simulation volume is a cube of  $5000^3 \text{ nm}^3$ . It should be noted that the two in-plane dimensions in LLG are the X and Z directions, while the Y-component defines e.g. the thickness of a thin film element. In the case displayed in Fig. 7.1(a) the dimensions are set for a rectangular thin film element with a length of

2000nm, a width of 1000nm and a thickness of 20nm. In the next column of the field '*Simulation Volume*' the size of the discretisation volume is determined by setting the number of cells per axis. Usually the cells need to be cubes with a side length of a few nanometers ( $\leq 10\text{nm}$  in the case of permalloy) in order to avoid intrinsic demagnetisation effects within each sub-element (Scheinfein et al, 1998). However, in the case of thin films of permalloy these effects are very small in the out of plane direction and therefore 'rods' were chosen as discretisation volumes (cells) in order to cut down simulation time. The rods were 20nm high (= film thickness) and had a square base of  $10 \times 10\text{nm}^2$ . It is crucial to retain a square base for the rods as a rectangular base could introduce notable intrinsic demagnetisation effects. Comparison of examples calculated with cubic cells with those consisting of rods did not show differences and therefore it was decided to set up all simulations with rods for this work.

It should be noted that benchmarks were recently done for the cell size of permalloy problems to yield accurate simulation results. It was determined that grid scales of  $\leq 2\text{nm}$  are required to get correct details for vortex dynamics and numbers of walls in the calculations (Scheinfein, 2000). As exchange energy is a next neighbour phenomenon (section 1.3.1) the cell size fixes the corresponding Fourier components. Therefore the micromagnetic simulations are not scale free but depend on the chosen grid scale and the calculated physics changes slightly with the mesh.

- ***Hamiltonian, Evolution, Anisotropy, Easy Axis and Coupling***

The default settings in these boxes are shown in Fig. 7.1(a). Neither of them was changed for the calculations carried out for this work: For 3D problems the continuous '*Hamiltonian*' was recommended. '*Relaxation*' was chosen in the evolution box because we were not interested in real-time-evolutions for this work. The crystal '*Anisotropy*' of permalloy is known to be uniaxial. This setting was applied for our problems although the experimental films were polycrystalline. The direction of the crystal anisotropy was however chosen parallel to the X-axis which coincided with the '*Easy Axis*' (length) of the elements. It should be noted that the shape anisotropy of the elements investigated in this work was expected to control the magnetic behaviour (Hubert et al, 1998) and therefore it was not expected that the setting of uniaxial crystal anisotropy would markedly influence the results. Finally in the version which was used for this work only the direct '*Coupling*' was implemented.

- **Parameters: Permalloy (Magnetic Parameters)**

When the 'Begin Simulation' option is enabled, the box 'Parameters: Permalloy' comes up with its default title 'Magnetic Parameters'. In order to model a problem with permalloy the default settings for permalloy need to be chosen. By doing so the title of the dialog box changes to 'Parameters: Permalloy'. As already mentioned mainly CGS units are used in LLG. It should be noted that LLG uses the 0-K value of saturation magnetisation  $M_s$  of a material and that for most practical systems there is only negligible deviation between the  $M_s$  values at 0K and  $M_s$  at room temperature (i.e. well below the Curie temperature; Scheinfein et al, 1998, Scheinfein et al, 1991 a). No fluctuations in magnetisation due to thermal agitation were considered for the simulations described in this work as temperature as parameter was not enabled (in the 'Computation Parameters' box, next section).  $K_u$  is the uniaxial and  $K_c$  the cubic magnetocrystalline anisotropy ( $K_c=0$  for permalloy),  $A$  is the magnetic exchange coupling constant (stiffness) in modified CGS units (uerg/cm means  $\mu\text{erg/cm}$ ),  $K_s$  is the magnetocrystalline surface anisotropy,  $Rho$  ( $\rho$ ) is the resistivity of the material (u-ohm-cm means  $\mu\Omega\text{cm}$ ) and  $AMR$  stands for anisotropy magnetoresistance ratio.  $AMR$  is the classical anisotropy magnetoresistance effect parameter which characterises the change in resistivity for current density  $\vec{J}$  being either  $\parallel$  or  $\perp$  to  $\vec{M}$  (section 1.6).

The 'Material Properties' button enables the user to change the material parameters while 'Layers' enables the set up of multilayer problems (e.g. GMR). The 'Position Depend. Params.' button was used extensively for this work as one of the options correlated with this field is to accomplish the definition of complex 2D and 3D shapes. Bodies which deviate from purely right angled geometry can be designed by marking certain cells or groups of cells which then can be either turned on or off. All standard elements as well as the elements with structured edges were generated this way.

- **Computation Parameters**

The next dialog box is the 'Computation Parameters' field. It should be noted that the default setting for 'Convergence' needs to be changed for permalloy. As mentioned in section 7.2 this convergence minimum is the value, which the largest relative change in the

largest component of the direction cosines  $\frac{\vec{M} \times \vec{H}_{eff}}{|\vec{M}| |\vec{H}_{eff}|}$  needs to decrease in order to stop

iteration. The LLG default setting is  $1 \times 10^{-3}$  but a value between  $1 \times 10^{-4}$  and  $3 \times 10^{-4}$  is

recommended for simulations with permalloy. It should be noted that it is crucial for accurate results not to choose the convergence criterion too high as iteration might be stopped prematurely before equilibrium is reached. The chosen value for the simulations discussed in this work was  $2 \times 10^{-4}$  as can be seen in Fig. 7.1(a).

Another crucial value is the maximal number of iterations. This is the second exit criterion to stop the calculation and if the number is chosen too small the simulation results are not reliable because the program might stop iterating before equilibrium is reached. '*Iterations*' can either be disabled in order to make sure that calculating is not stopped prematurely or the number needs to be chosen with respect to the problem. For most of the simulations run for this work the chosen value was 15000 (Fig. 7.1(a)) which was found to restrict the number of iterations for some cases while also being high enough to yield reliable results.

The energy criterion '*Energy # Up*' was always disabled and the default setting for '*Numhs=1*' was never changed. LLG computes the effective field rigorously during each iteration cycle, which is the most time consuming part of the computation. Therefore the program offers the option to save computational time by changing the *Numhs* value. Setting it to three for example reduces the calculation time by a factor of three. This option was not chosen for this work as the solution of a problem is rigorous only for *Numhs=1*.

'*Gamma*' ( $\gamma$ ) is the free electron gyromagnetic frequency (Eqn. 7.1) with the most typical value being 17.6 MHz/Oe. '*Alpha*' ( $\alpha$ ) is the phenomenological damping parameter (eqn. 7.1) which governs how quickly a solution converges. The default value is 1 and it was never changed in this work. According to Scheinfein et al, 1998, real materials can have  $\alpha$ -values in the 0.01 range but this component of the relaxation is still an issue as there is not much known about it. It should be noted that setting  $\alpha$  to one provides the same final solution to identical problems as  $\alpha=0.01$  solutions in a fraction of computation time. It is however not recommended to set  $\alpha$  to a value larger than one.

'*Time 1*' is the starting time in nanoseconds for a real time calculation and '*Time 2*' is the ending time but no real time calculations were carried out in this work. '*T(K)*' is for activating the finite temperature solver which was also not used in this work.

- ***Input Options***

The next dialog box is called '*Input Options*'. No '*Boundary Conditions*' were set for any of the simulations done for this work. The '*Computational Details*' however need to be

chosen for every problem and the most common settings for this work are displayed in Figure 7.1(b). As '*Relax All Points at Once - Use FFTs*' (Fast Fourier Transforms) was chosen '*Fast FFTs*' needed to be enabled. The '*Integrator*' default setting was never changed and '*Use Dual Processors*' was always activated in order to reduce computing time. By solving the Landau-Lifshitz-Gilbert equation time appears explicitly as a parameter. The equation can be solved either directly in time or in quasi time. The main difference between these two options is the exit criterion. Pure time methods are integrated for a fixed time sequence whereas quasi time methods are focused on obtaining equilibrium states (as in this work). The '*Maximum Stable (Quasi) Time Step*' is an approximate radius of convergence for the differential equations determined by the program. The program does not allow a higher setting of the time step than the maximum stable limit as otherwise the solution would become intrinsically unstable.

The next button in the '*Input Options*' field in Fig. 7.1(a) is '*Initialization*' with which the starting conditions are set up for a problem. The three main options are (i) uniformly magnetised (in a certain direction), (ii) a vortex structure (in a certain plane) and (iii) random initialisation condition of the magnetisation within the ferromagnetic body. The choice of the initialisation conditions is crucial, especially for problems with high symmetry. An example is given at the end of this section.

Activating '*External/Pinning Fields*' allows calculation of problems with constant external fields. This was an important option in our case as our magnetising experiments were carried out in the Philips CM20 FEG microscope by tilting the sample in an appropriate vertical field of the objective lens. This means that a considerable vertical field component was present at all stages of the experiments, which could be taken into account in the simulations. The value of the objective lens field was  $\approx 700$  Oe for the elements with  $t_1$  and  $\approx 940$  Oe for the elements with  $t_2$ .

In order to calculate magnetising experiments ( $\neq$  constant external magnetic field) the '*Hysteresis*' button needs to be activated and the appropriate maximal field value can then be entered in the hysteresis dialog box. Throughout this work uniform sampling fields (i.e. constant step size) were applied parallel to the X-direction of the elements for hysteresis simulations. This direction was coincident with the length of the elements and therefore along the easy axis of the elements. LLG offers the option to '*Create a Movie*' of hysteresis (and relaxation) calculations. This is a very helpful option as it allows the user to 'abandon' the computer while a simulation is running without missing the reversal details, as the

movie can be replayed after completion of a simulation. The number of saved transition states is chosen by the user by setting the appropriate  $\frac{\Delta M}{\Delta M_s}$  value.

'*Mask and View*' needs to be activated in order to apply designed masks to problems, which deviate from simple right angled geometry.

When the set up of a problem is finished '*Complete Initialization*' is activated and the starting magnetisation tensor is computed. After choosing a suitable '*Render Mode*' (= display mode; exclusively '*Bitmap*' was chosen for this work because of its similarity to Foucault imaging mode) the final step is to start the simulation. It is then useful to watch the development of the problem for some time in order to rule out chaotic behaviour (e.g. if the cell size was set up too big) before switching off graphics (to gain a factor two in computation time!).

- *Examples*

In order to highlight the importance of the starting conditions which need to be set for each problem (Fig. 7.1(a) '*Input Options*' field; '*Initialization*' button), two examples are compared in Fig. 7.2. The problem to solve was in each case a rectangular permalloy element determined by the parameters given in Fig. 7.1 and the aim of the simulations was to determine the equilibrium state of magnetisation for such an element in zero field conditions. The in-plane dimensions were  $2 \times 1 \mu\text{m}^2$ , the film thickness was 20nm and the discretisation volumes were rods of 20nm length (film thickness) with a square base of  $10 \times 10 \text{nm}^2$ . Fig. 7.2(a) gives the scale bar and the colour coding of the magnetisation direction for the three spatial dimensions which are indicated by double arrows and circles in Fig. 7.2. Turquoise illustrates alignment of the magnetisation in positive direction of a cartesian axis while white marks zero components and yellow codes magnetisation direction antiparallel to a certain axis.

Figure 7.2(b) shows the magnetisation distribution within a rectangular element for the starting condition uniformly magnetised in X-direction (i.e. zero Y and Z components with the resulting colour code white). Fig. 7.2(c) shows the converged state of the element for this simulation: Small domains with the magnetisation direction parallel to the edge developed at the element ends (in order to reduce magnetostatic energy) but the element had still a strong net resultant of magnetisation in positive X-direction. The magnetisation direction within the domains is illustrated by single arrows in Fig. 7.2(c). It should be noted, that such a configuration was never observed in any of the elements of this a

geometry and therefore this result of the simulation does not agree with experimental data. Whilst the configuration in Fig. 7.2(c) seems to be some quasi-stable local minimum of the total energy of the element. permalloy elements of this geometry and film thickness are known to possess flux closure structures in zero field conditions (chapter 3, Figs. 3.13, 3.14).

The starting condition, which is closest to such a domain configuration is 'Vortex Magnetisation Y-Plane' as illustrated in Fig. 7.2(d). Relaxation of this initialisation state resulted indeed in a flux closure structure which agreed very well with experimental observations under zero field conditions as the initial four  $90^\circ$  walls developed into four shorter  $90^\circ$  walls originating in the corners and a  $180^\circ$  wall in the centre of the element. Magnetisation distribution within the element in its relaxed state is indicated by the single arrows in Fig. 7.2(e).

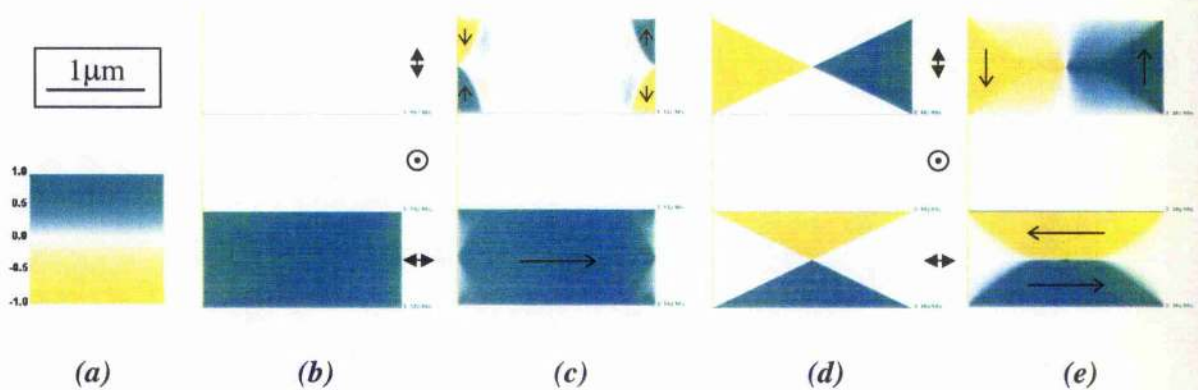


**Figure 7.2**

*Comparison of simulation results for different initialisation conditions.*

*(a) Scale bar and colour scheme;*

*(b) initialisation 'Uniform Magnetisation X-Direction' with result in (c);*

*(d) initialisation 'Vortex Magnetisation Y-Plane' with result in (e).*

*Double arrows and circles indicate 'mapping directions'.*

This example illustrates the importance of the starting conditions as this was the only difference in the set up of these two simulations but only the result of the second simulation was in agreement with experimental observations. This is a well known and common discrepancy which arises for simulations of problems with high symmetry. In such cases the results even for converged simulations often do not have much in common

with experimental data. This is a major drawback of modelling high symmetry problems, which sometimes can be overcome by choosing appropriate starting conditions (Figs. 7.2(d), (e)) or by breaking the symmetry. It should be noted, however, that the uniformly magnetised state of the element in Fig. 7.2(b) would also be the starting condition of the element for a hysteresis calculation and the micromagnetic state of the element in Fig. 7.2(c) would then be the modelled remanent state of the element. As already mentioned, such a magnetisation configuration was never observed in either of our experiments or reported in any publication known to the author. Therefore it is crucial to bear in mind that each model calculates idealised problems (e.g. perfectly straight edges, no grains and grain boundaries, no variation in film thickness, exact field directions) while real conditions are not perfect. When the calculation of a problem reaches a metastable point then the simulation is stopped as the convergence criterion is fulfilled - the modelled system appears to be converged. This stresses the general importance of comparison of modelled with experimental data.

#### **7.4 MODELLING OF MAGNETISING EXPERIMENTS**

##### **WITH AND WITHOUT VERTICAL FIELD:**

##### **MAGNETIC MICROSTRUCTURE AND HYSTERESIS LOOPS**

The emphasis in the simulations of small magnetic elements in this chapter lies in their reversal behaviour rather than pure relaxation calculations or real time behaviour. In accordance with the experimental chapters, the main focus of discussion lies on the elements with the sharper tips  $t_2$  (third and fifth patterns). The simulation results for the switching field values however are compared for both tip ratios. It should be noted that whilst most of the standard elements were set up and modelled only narrow ( $w_1$ ) elements with  $h_2$  were designed and calculated as far as the elements with structured edges are concerned. There were two main reasons why only a selection of elements was modelled: Firstly limited access time on the computer running LLG and secondly and more important the fact that the simulation times for the wider (standard) elements rose considerably as a result of the increased simulation volume of those elements. It was therefore expected that especially calculation of the elements with  $w_2$  would take unjustifiably high amounts of time. This consideration was even more important as simulations were run firstly under similar conditions as the experiments were carried out (i.e. with vertical fields applied to

the modelled elements) and secondly the reversal behaviour was calculated for zero vertical field. The aim was to gauge the influence of the vertical field as present during the in-situ magnetising experiments in the CM20 microscope on the observations discussed in chapters 4, 5 and 6. Both sets of simulation results are presented and compared to the experimental data. The material parameters were for all cases those of permalloy and the film thickness was 20nm for all elements.

## 7.4.1 ELEMENTS OF SECOND AND THIRD PATTERNS

### 7.4.1.1 STANDARD ELEMENTS

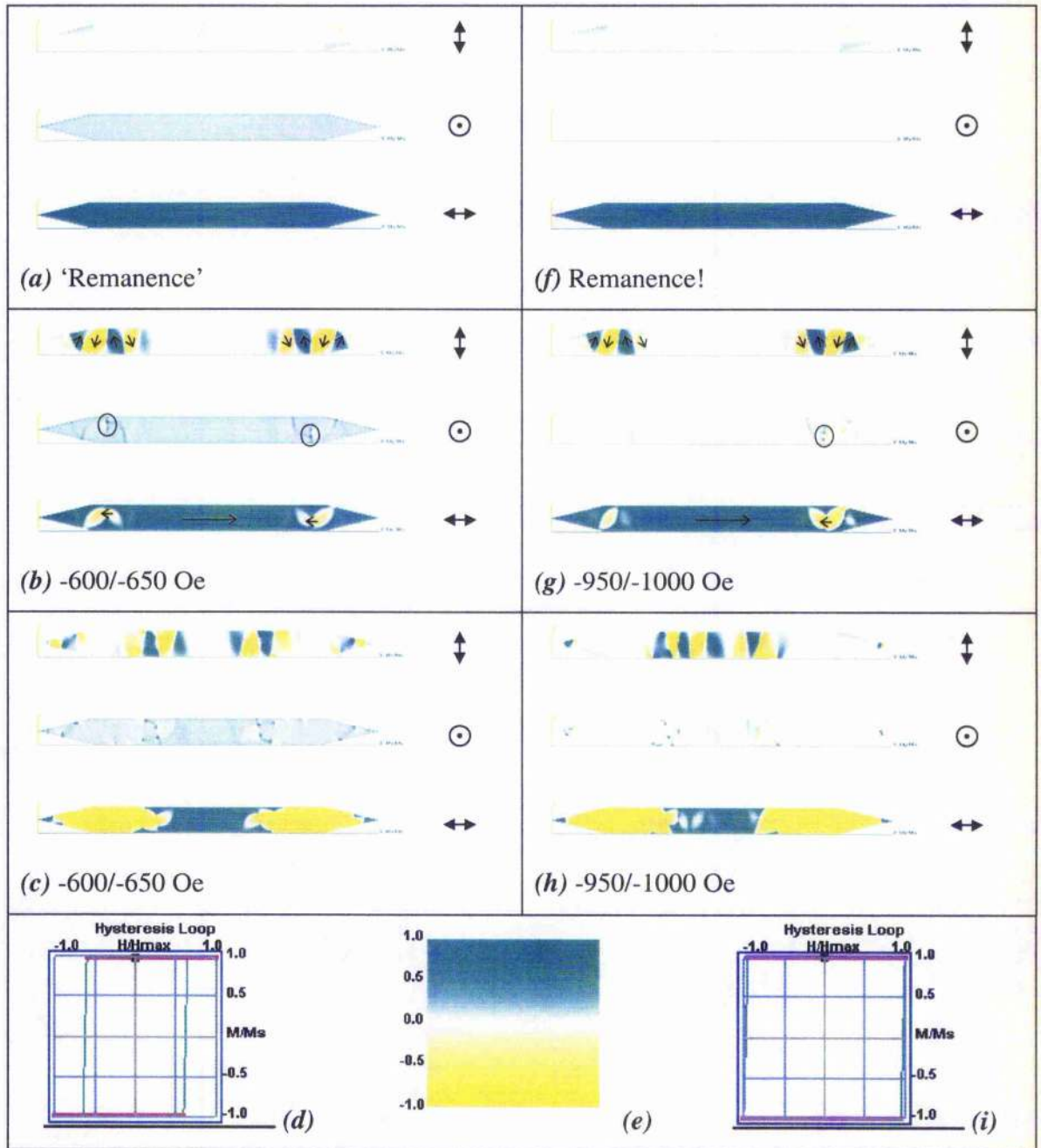
Figure 7.3 shows an overview of some micromagnetic states of a standard element with  $w_1$  and  $t_2$  during hysteresis loop simulations with and without vertical field  $H_y$ . The normalised hysteresis loops for the calculations are shown together with the colour scheme in Figs. 7.3(d), (e), (i). It should be noted that the hysteresis loop had in both cases the square shape expected for acicular double pointed elements. In the case of solely in-plane fields however the hysteresis loop (Fig. 7.3(i)) was considerably wider than calculated for the presence of the vertical field (Fig. 7.3(d)). This means that the same element was harder to reverse for zero vertical field. The varying hysteresis field was applied exactly along the length (= easy axis) of the element (parallel to X-direction). The extreme values were  $H_x = \pm 1000$  Oe and the field was varied in steps of 50 Oe. The 'mapping directions' are indicated by double arrows and circles in Fig. 7.3.

In the first column of Fig. 7.3 extracts of the simulation are presented in which the vertical field, which was present in the experiments was taken into account by applying the constant *external/pinning field*  $H_y = 940$  Oe. The results, which are shown in the second column are from the simulation in which the vertical field  $H_y$  was set zero. All other parameters however were identical for the simulations of the two columns.

The most obvious effect of the vertical field can be seen for example in Fig. 7.3(a) where an out of plane magnetisation component is clearly visible (light turquoise) in the corresponding middle image. The value of  $M_y \approx 0.12 \cdot M_s$  at 'remanence' and this corresponds to a tilting angle of the magnetisation out of the element plane of  $\approx 7^\circ$ . This is evidence that the vertical field component can not be ignored in the case of small magnetic

elements: The magnetisation was no longer confined entirely in the plane of the thin film; it was instead notably tilted out of plane in the simulation. This is a result of the demagnetising effects due to the reduced dimensions of the thin film elements. In the case of continuous thin films of permalloy the out of plane demagnetising factor is  $=1$  but it is  $<1$  for finite in-plane dimensions (section 1.5).

As the in-plane components of magnetisation in both cases (i.e. with and without vertical field) looked very much alike they are discussed together. It should be noted that 'Remanence' here is in agreement with the experiments and means in the presence of a vertical field whilst in the case of zero vertical field the state for zero hysteresis field  $H_x = 0$  Oe is termed Remanence! in the figure. The initialisation condition in both cases was uniformly magnetised in X-direction and calculation of the hysteresis loops started at  $H_x = 1000$  Oe. As these states were very similar to the  $H_x = 0$  Oe states they are not shown in Fig. 7.3. The images in the first row (Figs. 7.3(a), (f)) illustrate the magnetic microstructure for  $H_x = 0$  Oe and the in-plane components look exactly alike with the element being almost uniformly magnetised in X-direction. In both cases there was no change of magnetic microstructure until the onset of magnetisation reversal which occurred at a lower hysteresis field in the presence of the vertical field (Figs. 7.3(b), (g), (d), (i)). As observed in the experiments the situation prior to switching was characterised by the formation of concertina structures (with triplet clusters) in the end regions of the elements (Figs. 7.3(b), (g)). However, unlike in the experiments the concertina structures in the simulations did not extend over the entire element length. Instead reversal was initiated by the generation of areas where the direction of magnetisation seemed to be reversed (yellow in the bottom parts of Figs. 7.3(b), (g)) before the (concertina) domain configuration extended over the entire element. The reverse areas appeared in the wall region between domains in which the magnetisation already possessed reverse X-components after magnetisation rotation. At these sites point-like out of plane components, which are marked by ellipses were visible at the corresponding element ends in the middle parts of the figures. Such singularities (Bloch lines) usually indicate vortex structures and are also found in x-tie walls. It should be noted that despite the thickness of the film (20nm) some domain walls were not 'proper' Néel walls as they clearly displayed out of plane components of magnetisation direction (lines in the middle parts of Figs. 7.3(b), (g)).


**Figure 7.3**

Magnetic microstructure of a standard element with a width of 250nm of the third pattern ( $t_2=2$ ) for different stages of hysteresis simulations. Double arrows and circles indicate mapping directions.  $H_y = \text{constant} = 940$  Oe for (a), (b), (c).  $H_y = \text{constant} = 0$  Oe for (f), (g), (h). Hysteresis loops ( $H_{x(\text{max})} = \pm 1000$  Oe) and colour scheme are given for reference.

Under the influence of the vertical field these out of plane components had the same direction as the Bloch lines and were parallel to the external vertical field (Fig. 7.3(b)). In

the case of zero vertical field however both out of plane directions are clearly visible in Fig. 7.3(g). Domain walls with out of plane components as well as Bloch lines were common features within the element in both cases despite the thickness of the element. A more detailed overview of the calculated magnetic microstructure of the Y-component at the primary reversal sites of the element for both cases is given in Fig. 7.4 and is discussed there.

Figures 7.3(c), (h) show the further development of magnetisation reversal in the simulations. Two sets of concertina structures were pushed towards the centre of the element in front of rapidly growing reverse domains (yellow in the bottom parts of Figs. 7.3(c), (h)) with numerous new Bloch lines being generated during this process (Figs. 7.3(c), (h) centre). In the case of the simulation with vertical field iteration for  $H_x = -650$  Oe stopped when the element possessed a single domain reversed state and the same behaviour was observed for the zero field calculation at the higher hysteresis field value  $H_x = -1000$  Oe.

As already mentioned, the element was considerably harder to switch in the simulation without vertical field component than in the simulation with vertical field (Figs. 7.3(d), (i)). This ties in with the generation of the out of plane components during magnetisation reversal in both cases: Application of a vertical field was found to induce and support out of plane components of magnetisation throughout the magnetising cycle which apparently resulted in a reduction of coercivity.

Detailed sections of the out of plane magnetisation distributions of the standard element at the onset of magnetisation reversal are shown in Fig. 7.4. The first section (Fig. 7.4(a)) is taken from the central part of Fig. 7.3(b) and the second one (Fig. 7.4(b)) is taken from Fig. 7.3(g). Some of the domain wall locations together with the magnetisation direction distribution derived from the images of the in-plane components of magnetisation are overlaid. Circles mark locations of point-like features with increased out of plane component of magnetisation. Structures similar to these are singularities known as Bloch lines, which are present in the centres of vortex structures and in cross tie walls (section 1.3.5).

The central wall configuration in the image of Fig. 7.4(a) consists of crossed walls with cross-tie-like magnetisation distribution in the middle and a vortex structure at the bottom. The calculated singularities (brighter turquoise within the overlaid circles) are consistent with the derived magnetisation distribution. It is still not entirely clear, however,

whether the strong yellow contrast, which was observed in the image of the X-component of the magnetisation of the element in Fig. 7.3(b) (red arrow in Fig. 7.4(a)) was actually due to the existence of a reverse domain at this stage or whether the wall drawn in Fig. 7.4(a) was still present.

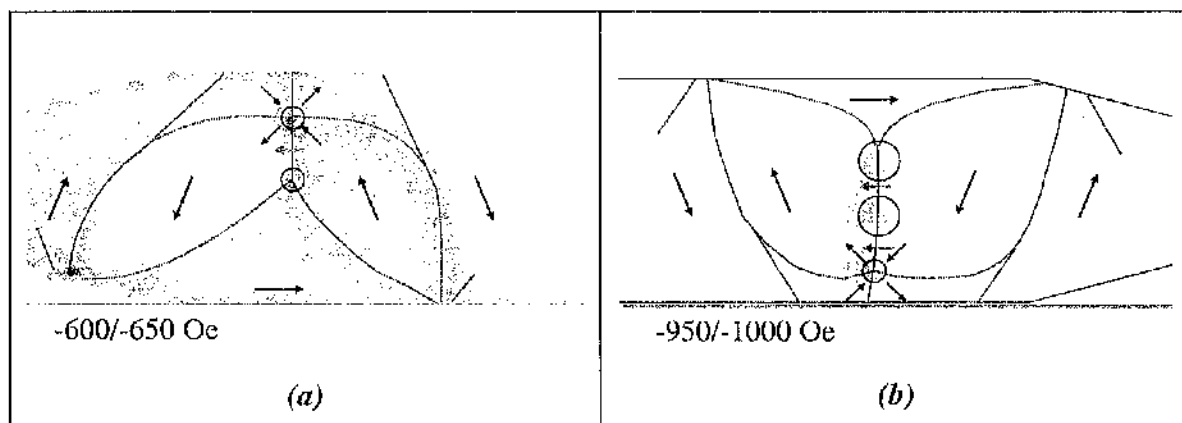


**Figure 7.4**

*Detailed section of the magnetic microstructure (out of plane component) at the end region of a standard element at the onset of magnetisation reversal (Figs. 7.3(b), (g)).*

*(a) Simulation with  $H_y = \text{constant} = 940$  Oe; (b) Simulation with  $H_y = \text{constant} = 0$  Oe.*

*Domain wall locations and magnetisation distribution overlaid.*

The detailed section of the right hand side of the out of plane component of magnetisation in Fig. 7.3(g) is shown in Fig. 7.4(b). In agreement with the simulation with vertical field the calculated walls were not 'proper' Néel walls but possessed out of plane components. Here, however, both polarities of out of plane components were generated in the simulation (turquoise and yellow in Fig. 7.4(b)). In agreement with these findings, Bloch-line-like features were also generated with both polarities. Surprising was again the high number of these features being generated in the process and even more puzzling was that in many cases two such singularities with opposite out of plane components were very close together (marked by large circles in Fig. 7.4(b)). This could be an artefact of the simulation as opposite components cancel out numerically which also explains the low net resultant of out of plane magnetisation in the state shown in Figs. 7.3.(g), 7.4(b) ( $M_y = 0.001 \cdot M_s$ ). There is, however, no explanation at all for the central Bloch-line-like features in Fig. 7.4(b) as the derived directions of magnetisation as well as the wall configurations do not agree with the formation of any singularity at this location (i.e. in

between the two red arrows). It is not entirely clear at this stage whether these deviations resulted due to a principal problem of simulations or if it was simply an artefact of the coarse mesh (10nm instead of  $\leq 2\text{nm}$ ; Scheinfein, 2000).

The domain configurations, which were observed in the magnetising experiments (section 5.5.1) agreed generally well with the corresponding simulated magnetic microstructures. The build up of a concertina structure was calculated for all standard elements starting at the ends of the elements (kink at tip region). In the case of the narrowest calculated element ( $w=250\text{nm}$ ), however, the concertina did not develop over the entire element prior to switching. Instead two 'packages' of concertina structures were pushed through the element until magnetisation reversal was accomplished. In good agreement with the experimental observations and unlike in the case of the simulations with the narrow elements concertina structures which extended over most of / up to the entire element length were calculated for the wider ones ( $w \geq 450\text{nm}$ ). As the field range during which those concertina structures were observed in the experiments was between  $\approx 20$  and  $\approx 50$  Oe it would need further and very detailed (i.e. time consuming) calculations in order to determine unambiguously whether the concertina structures in the simulations would generally be found solely during the switch of magnetisation or if they would be present over a certain field range as observed in the experiments.

Practically identical transition states were calculated for most of the elements with the blunter tips  $t_1$ . This was not entirely in agreement with the experimental results where no highly developed concertina structures were observed prior to switching of those elements. However the build up of end domains with a tendency of formation of concertina structures was also observed in the experiments. As the domain configurations prior to switching in the case of the elements with  $t_1$  were even more volatile in the experiments than those of the elements with  $t_2$  it was hard to determine whether highly developed concertina structures were generated or not. It should be noted though, that the development of concertina configurations seems a very likely possibility.

At first glimpse the modelled reversal mechanism seems reasonable (formation of areas with reverse magnetisation and rapid growth of these areas) and furthermore it appears also to be quite convincing given the good agreement of the experimental and simulated micromagnetic states. However the high number of generated Bloch lines is somewhat surprising as the generation of such singularities is known to be very energy

intensive. It was expected that once a reverse domain was nucleated no more singularities would form.

Further discrepancies emerge when taking a closer look at the polarity of the Néel walls respectively the reversal of the polarity of some of the walls which was the result in the simulations. This is illustrated in Fig. 7.5 for one end region of an element with  $t_2$ .

The experimentally observed domain configuration prior to switching is given in Fig. 7.5(a) (i.e. concertina structure). The mean direction of magnetisation points in positive x-direction (colour coding: green) and all Néel walls have positive polarity (colour code also green). Similar domain configurations to those observed experimentally were calculated for the micromagnetic state prior to switching with the polarity of the Néel walls being the same in both cases (Fig. 7.5(a)).

Figure 7.5(b) shows a simplified schematic of the further evolution of the calculated magnetisation distribution. Whilst the polarity of the domain walls indicated by the dashed green lines may or may not be positive any longer, the excessive rotation of magnetisation within the two domains closest to the element tip not only leads to reverse components of magnetisation within these domains (red arrows) but furthermore implies reversal of the polarity of the (red) domain wall at the bottom of the element. This change in polarity is very puzzling and highly unlikely (section 1.3.5).

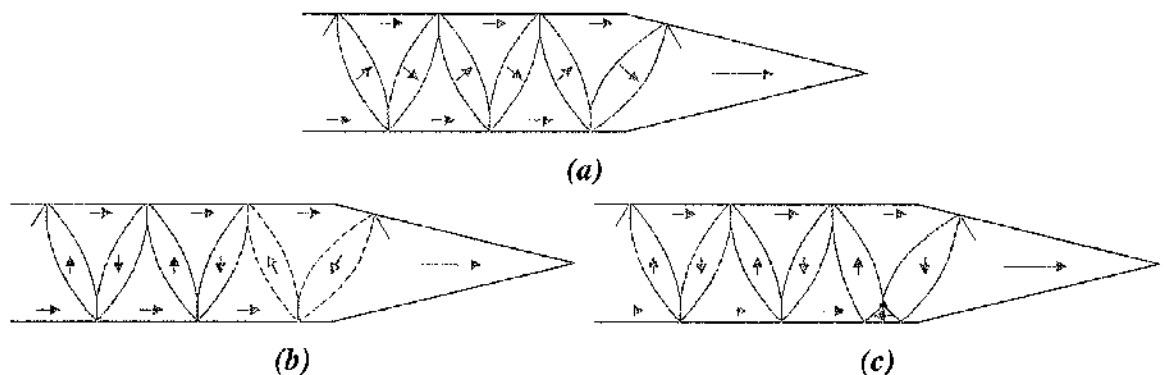


**Figure 7.5**

*Schematics of development of magnetisation reversal.*

*(a) Micromagnetic state prior to switching, (b) calculated reversal mechanism (rotation),*

*(c) theoretical reversal mechanism (nucleation of a reverse domain).*

The reason for this result is that LLG does not consider the concept of the polarity of domain walls and the preservation of this polarity. Instead the magnetic moment of each

cell is freely rotatable and walls evolve naturally as more or less abrupt changes of magnetisation direction from one cell to another. As a result of the minimisation of  $E_s$  discontinuous magnetisation distributions are not preferred solutions. Such a solution would however be required in the case of retained polarity of a Néel wall (wall still green instead of red in Fig. 7.5(b)) between the two domains with reversed components of magnetisation (red arrows in Fig. 7.5(b)). Another problematic area is indicated by the red dashed domain wall in the upper part of the element where the most reasonable polarity of the calculated Néel wall is in negative x-direction which is also opposite to the original polarity.

A more likely reversal mechanism which does not require the reversal of the polarity of domain walls is illustrated in Fig. 7.5(c) and agrees with the behaviour explained by McVitie et al, 1997. In this case magnetisation reversal implicates the nucleation of a reverse domain at the location of a triplet cluster as shown in the bottom part of the element. The magnetisation of this newly formed (nucleated) domain is opposite to the original direction of magnetisation (red arrow) as is the polarity of the newly generated walls (red walls).

Another result to be gained from the simulations was the coercivity of the modelled elements. Figure 7.6 compares the experimental with the calculated switching field values of the standard elements with  $t_1$  in (a) and  $t_2$  in (b). The respective vertical field is given in the diagrams.

The main characteristic of the experimental data, the monotonic decrease of coercivity with increase of element width, was corroborated in most cases of the simulations as was the second finding of the experiments, the higher coercivity of the elements with the sharper tips. The main discrepancy was that the calculated coercivities were in general considerably higher than the experimental results. In the case of the zero vertical field calculations the coercivity was up to  $\approx 3\times$  the experimental values and when the vertical field was taken into account in the simulations the calculated values were still about twice as high compared to the experimental data. The reason for this is not entirely clear but it is very likely that it is simply due to the superior perfection of the modelled elements compared to the real ones and as the elements possess a high symmetry marked deviations between experiment and model can easily arise (section 7.3), (Gadbois et al, 1995). In the work of Gadbois  $1.1\times$  to  $1.7\times$  higher values were also calculated for elements with perfect edges compared to elements with imperfect edges (steps of a height of 10nm). It should be

noted though that those simulations were carried out with rectangular bars instead of double pointed elements. Another possible reason for the deviation is that LLG does not take into account grains and grain boundaries, which are also known to influence the magnetic behaviour of a sample. There is however no explanation at all for the 'odd' drop of both calculated coercivities of the element with  $w=500\text{nm}$  and  $t_2$  (Fig. 7.6(b)) which was found to be reproducible.

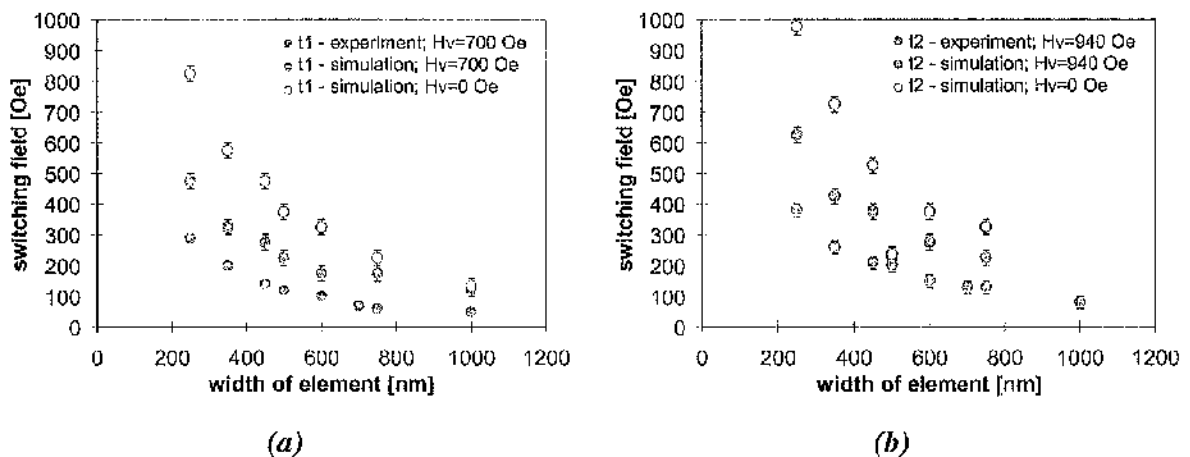


**Figure 7.6**

*Comparison of simulated and experimental switching field values of standard elements with different tip ratios. Vertical field  $H_v$  as indicated.*

#### 7.4.1.2 ELEMENTS WITH EDGE STRUCTURE TYPE A

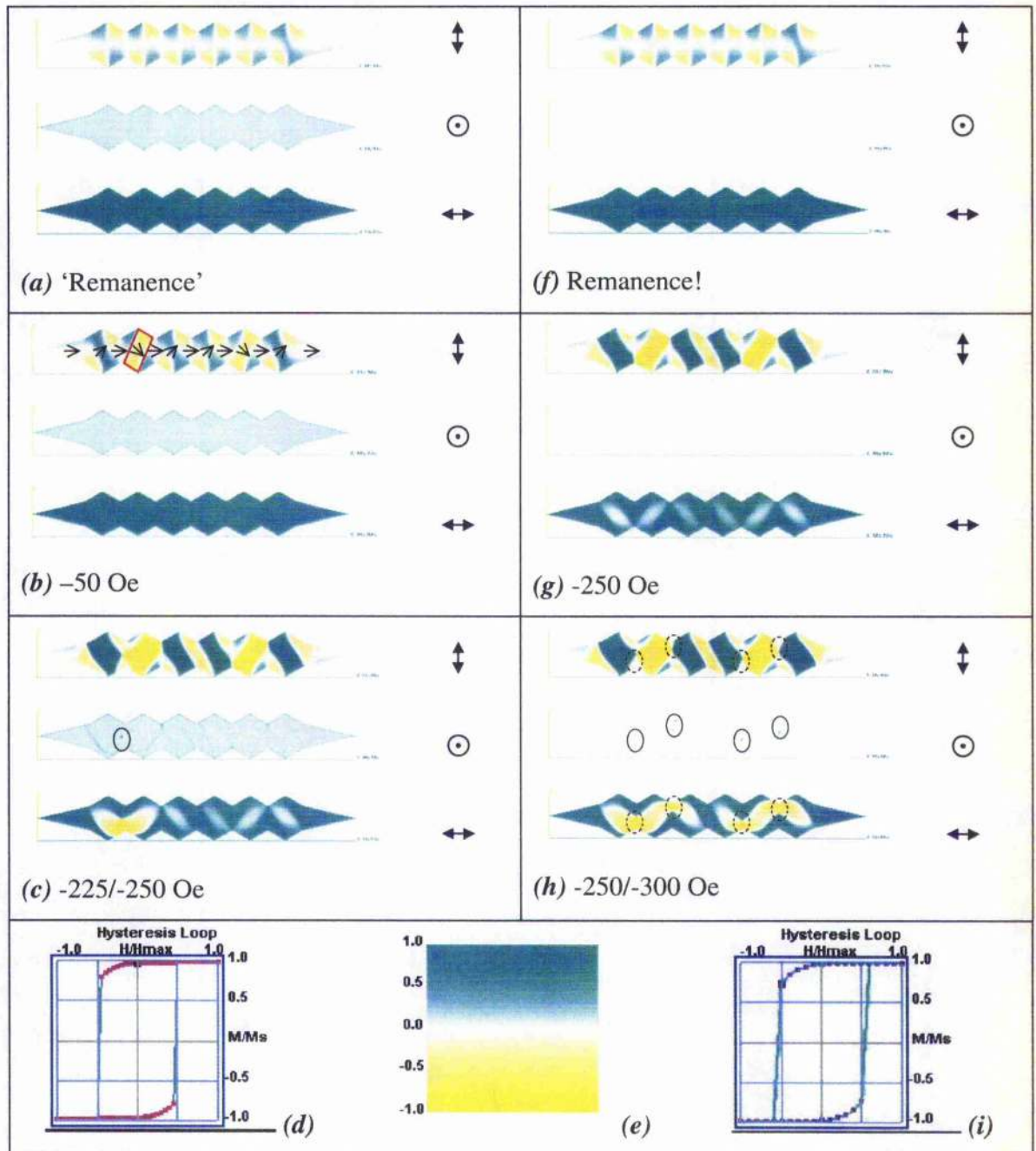
With the discussion of the hysteresis simulations for the standard elements complete the calculated magnetisation reversal behaviour of the elements with structured edges is described next. To begin with masks were designed and hysteresis loops calculated for 4 out of the 24 sets of elements with structured edges from the second ( $t_1$ ) and third ( $t_2$ ) patterns. The elements with width  $w_1$  and structure height  $h_2$  were modelled whilst simulation of the reversal behaviour of the wider elements ( $w_2$ ) was intended too but it was decided to calculate narrow elements only as calculation time increased considerably with element width. Two sets of simulations were again carried out: Firstly the vertical field present in the experiments was taken into account and secondly simulations were run with zero vertical field. In accordance with the previous chapters the magnetic microstructure is

only shown for elements with  $t_2$ . Here the element with  $w_1$ ,  $t_2$ ,  $h_2$  and structure type A with  $p=0.33\mu\text{m}$  is discussed in detail. The coercivity is graphed for both groups ( $t_1$ ,  $t_2$ ) of narrow elements ( $w_1$ ) with structured edges of type A with  $h_2$ .

Figure 7.7 shows a compilation of domain configurations of the described element above during calculated magnetising loops for the two cases with and without vertical field. The hysteresis loops and the colour coding are given in Figs. 7.7(d), (e), (i). The hysteresis field was applied along the easy axis of the element (X-direction) and the extreme values were  $H_x = \pm 500$  Oe with variation steps of 25 Oe for the calculation with vertical field and 50 Oe for the simulation without vertical field. As there were again a lot of similarities for both simulations the results are also presented together.

The main difference between the simulation with and without vertical field was again the clearly notable out of plane component of magnetisation in the simulation with vertical field  $H_y = 940$  Oe (Figs. 7.7(a)-(c) middle parts of illustrations). The details agree well with the results discussed previously for the simulations of the standard elements (section 7.4.1.1). The value of the out of plane component was  $M_y \approx 0.11 \cdot M_s$  for the entire simulation and corresponded to an average out of plane tilting angle of magnetisation of  $\approx 6^\circ$ . Bloch-line-like features were again generated during magnetisation reversal and domain walls also displayed some degree of out of plane component as can be seen in Fig. 7.7(c). In the case of hysteresis simulation with zero vertical field the magnetisation was confined in the plane of the element for most stages of the calculation. In agreement with the discussion in the previous section (7.4.1.1) it was only during magnetisation reversal when out of plane components in the shape of Bloch-line-like features of both polarities (marked by ellipses in Fig. 7.7(h)) were calculated in zero vertical field conditions. The domain walls, however, did not display any out of plane component at any stage of the simulation.

Magnetisation reversal occurred again very rapidly (squarish hysteresis loops) and a notable reduction of the net resultants of magnetisation could already be seen in both hysteresis loops prior to switching (Figs. 7.7(d), (i)). At a hysteresis field of  $H_x = 0$  Oe, however, the net magnetisation of the element was still very close to saturation irrespective of the considered vertical field values. This can be seen in the hysteresis loops and can also be deduced from Figs. 7.7(a), (f) where both X-components were alike with the mean direction of magnetisation in X-direction. Variation of magnetisation in Z-direction,


**Figure 7.7**

Magnetic microstructure of a narrow ( $w=250\text{nm}$ ) element with edge structure type A with period  $p=0.33\mu\text{m}$  of the third pattern ( $t_2=2$ ) for different stages of hysteresis simulations. Double arrows and circles indicate mapping directions.  $H_y=\text{constant}=940\text{ Oe}$  for (a), (b), (c).  $H_y=\text{constant}=0\text{ Oe}$  for (f), (g), (h). Hysteresis loops ( $H_{x(max)}=\pm 500\text{ Oe}$ ) and colour scheme are given for reference.

however, was clearly present in both figures. The variation of magnetisation direction was strongest within the outer vertices of the structure features and gave rise to the also experimentally observed wall sections (section 5.5.2).

When the magnetic microstructure was calculated for reverse fields formation of the characteristic parallelogram domains known from the experiments was also the result of both simulations (Figs. 7.7(b), (g)). The parallelogram domains were found to increase in size and intensify in colour with increase of the reverse field. This is in agreement with the experimental observations of section 5.5.2. One of the characteristic parallelogram domains is highlighted by a red frame and the distribution of magnetisation direction in the main body of the element is indicated by single arrows in Fig. 7.7(b). Under the influence of increasing reverse fields the net magnetisation in X-direction was getting notably reduced in the hysteresis loop due to the areas in which the magnetisation had  $\approx$ zero magnetisation components in X-direction (i.e. the whiteish areas in the bottom illustration of Figs. 7.7(g)). The formation of the areas with reverse direction of magnetisation was again associated with the generation of vortex structures as can be deduced not only from the distribution of the in-plane directions of magnetisation but is also consistent with the Bloch-line-like features in the middle illustrations of Figs. 7.7(c), (h) which are marked by ellipses. At this stage areas with reversed direction of magnetisation appeared (yellow in bottom parts of Figs. 7.7(c), (h)) which then grew on the expense of the other domains.

Figures 7.8(a)-(c) show schematics of the distribution of magnetisation direction around the primary reversal site of the element in Fig. 7.7(c) whilst Fig. 7.8(d) gives an alternative magnetic microstructure for Fig. 7.8(c). Green arrows illustrate magnetisation directions with component in positive x-direction and red arrows indicate negative components of magnetisation direction. Walls with positive polarity are drawn as green lines whilst walls with negative polarity are illustrated by means of red lines.

The two walls in Fig. 7.8(a) move towards each other at the bottom edge of the element. When they meet the micromagnetic situation becomes highly complex at this site (marked by grey ellipse in Fig. 7.8(b)): The wall cluster resembles a doublet cluster (Fig. 5.6) which only forms under the condition of antiparallel alignment of the magnetisation direction either side of the cluster. This is clearly not the case here. LLG solves this problem by introducing an area with reversed magnetisation direction at the bottom edge of the element. The free rotation of the magnetic moment in each cell leads to the magnetisation distribution illustrated in Fig. 7.8(c). It should be noted that the number

of walls resulting in this state is quite high. Especially the black wall would not be necessary considering a slightly modified magnetisation distribution (Fig. 7.8(d)). It is not clear whether the calculated reversal mechanism ought to be expected in reality or if a finer mesh in the set-up of the simulation would allow the calculated walls to coalesce more naturally.

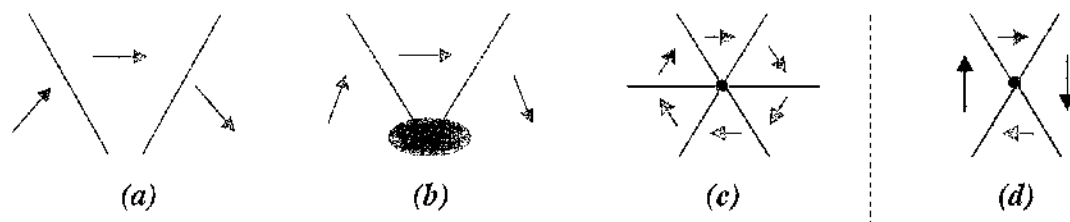


**Figure 7.8**

(a)-(c) Different stages of magnetisation reversal site corresponding to Figs. 7.7(b), (c).

(d) Suggested alternative domain configuration instead of (c).

→ Magnetisation direction with positive/negative component, | Néel walls with positive/negative polarity; ● Bloch line.

An overview of the calculated domain configurations of the elements with  $w_1$  and  $h_2$  of the third pattern ( $t_2$ ) is given in table 7.1 for  $H_y = 940$  Oe. As in the previous chapters the description was kept as compact as possible and with emphasis on similarities and the same terminology was applied as for the corresponding table 5.3. In table 7.1 the domain configurations at remanence are again described along with those prior to switching and additionally the primary switching mechanism is given. The only new term in the table is 'stripe domains' which describes domains, which were perfectly parallel to the element width (Figs. 7.9(a), (b)). The element with the shortest period ( $p=0.1\mu\text{m}$ ) supported almost exclusively such stripe domains at remanence with a frequency of one domain per period. This stripe domain pattern did not change considerably until magnetisation reversal. In the case of these stripe domains the walls originated at the inner vertices of the structure features.

It should be noted that identical domain configurations were often calculated in the case of the elements with the blunter tips ( $t_1$ ) of the second pattern in the 'presence' of the vertical field  $H_y = 700$  Oe and also for both calculations in zero vertical field. Therefore table 7.1 is also valid for most elements with  $t_1$  and irrespective of the vertical field. The

results of all four sets of simulations are summarised in one table: Whilst the catchwords in table 7.1 describe the micromagnetic states of the elements with the sharper tips  $t_2$  under the influence of the vertical field, it is also possible to work out at a glance whether or not the same micromagnetic behaviour was found in the simulations for the elements with the blunter tips and in the simulations without vertical field. The way to proceed is to check the blue parameters in the table. If different observations were made as those summarised in the table then the corresponding blue parameter is cancelled out.

At 'remanence' only the element with  $p=0.1\mu\text{m}$  did not support a (quasi) single domain state and it was only in the case of this shortest period that different domain configurations were found for the element with the blunter tip  $t_1$ : In this case the magnetic microstructure of the element was multi-domain with less orderliness as in the case of the stripe domains. In the simulations with zero vertical field  $t_1(0)$ ,  $t_2(0)$  the elements with  $p=0.1\mu\text{m}$  were in a quasi single domain state at remanence (Fig. 7.9(c)).

Narrow ( $w_1$ ) Elements with Structure Type A ( $t_2$ ) - Third Pattern ( $t_2$ )					
period	2.0 $\mu\text{m}$	0.5 $\mu\text{m}$	0.33 $\mu\text{m}$	0.2 $\mu\text{m}$	0.1 $\mu\text{m}$
<b>state: R</b>	single domain $t_1, t_2(0), t_1(0)$	quasi single domain $t_1, t_2(0), t_1(0)$	quasi single domain $t_1, t_2(0), t_1(0)$	quasi single domain $t_1, t_2(0), t_1(0)$	stripe domains <del><math>t_1, t_2(0), t_1(0)</math></del>
<b>state: PS</b>	concertina* $t_1, t_2(0), t_1(0)$	parallelogram domains $t_1, t_2(0), t_1(0)$	parallelogram domains $t_1, t_2(0), t_1(0)$	parallelogram domains $t_1, t_2(0), t_1(0)$	stripe domains <del><math>t_1, t_2(0), t_1(0)</math></del>
<b>S</b>	propagation of reversed area(s) $t_1, t_2(0), t_1(0)$				

**Table 7.1**

*Micromagnetic states of elements with  $w_1$  and structure type A of 3<sup>rd</sup> pattern ( $t_2$ ) for simulated hysteresis loops with vertical field  $H_v=940$  Oe.*

*State R: Remanent state, State PS: Prior to switching, S: Switching.*

*$t_1$ : Simulation for element with  $t_1$  and  $H_v=700$  Oe;  $t_{1,2}(0)$ : Simulation with  $H_v=0$  Oe.*

*In case of different results for  $t_1, t_2(0), t_1(0)$ :  ~~$t_1, t_2(0), t_1(0)$~~ .*

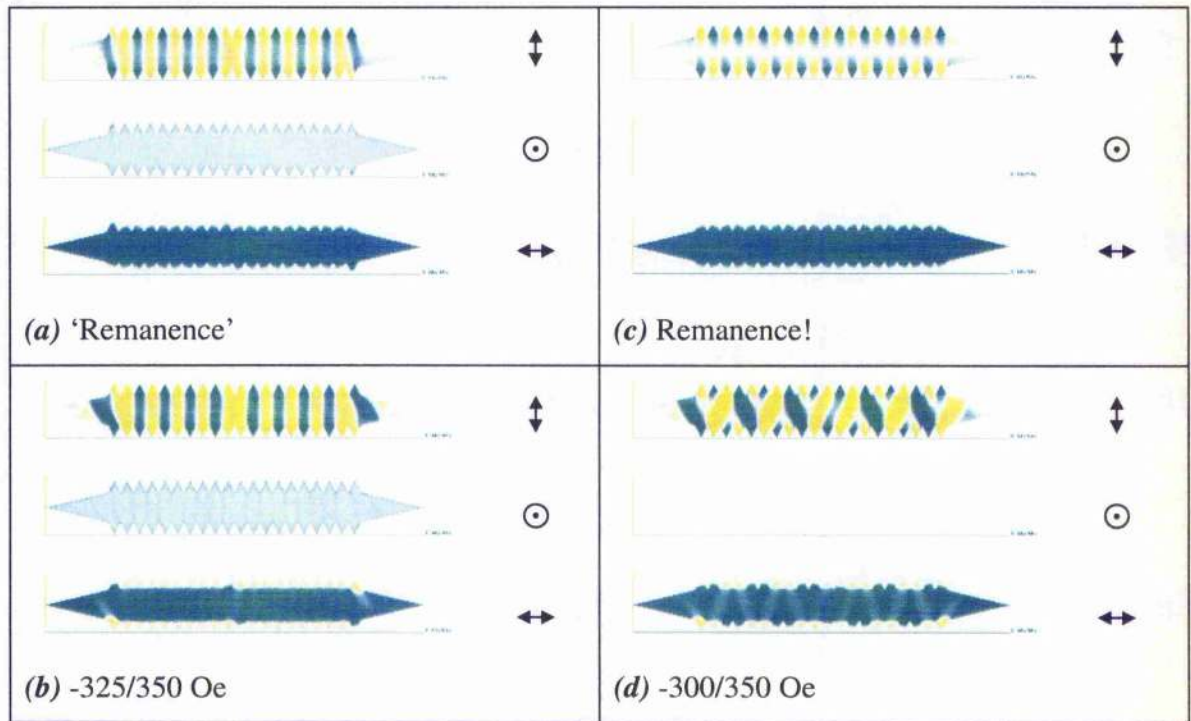


**Figure 7.9**

*Magnetic microstructure of a narrow ( $w_1=250\text{nm}$ ) element with edge structure type A with period  $p=0.1\mu\text{m}$  of the third pattern ( $t_2=2$ ) for different stages of a hysteresis simulation.*

*Double arrows and circles indicate mapping directions.*

*(a), (b)  $H_y=\text{const}=940\text{ Oe}$ ; (c), (d)  $H_y=\text{const}=0\text{ Oe}$ .*

In most simulations the elements developed the characteristic parallelogram domains prior to switching. However, multi-domain states, which could not be described as parallelogram domains were calculated for the elements with the longest and shortest structure period. Stripe domains did not change their configuration whilst (quasi) single domain states developed into concertina-like configurations. Figure 7.9(d) shows the configuration, which was termed '≈concertina'. Magnetisation rotation in adjacent domains was dominant in the stages prior to the calculated switch of magnetisation, which occurred by means of generation and propagation of areas with reversed direction of magnetisation (table 7.1). It should be noted that despite the differences between experimentally observed (table 5.3) and calculated domain configurations for the element with the shortest period  $p=0.1\mu\text{m}$  there was agreement between simulation and experiment as far as the 'density' of walls was concerned: The lowest limit was in each case  $\approx 1\text{wall}/100\text{nm}$ . The different domain configurations in the simulations for the elements with the shortest period resulted

merely due to the (arbitrary) direction of magnetisation within the structure features (Fig. 7.9).

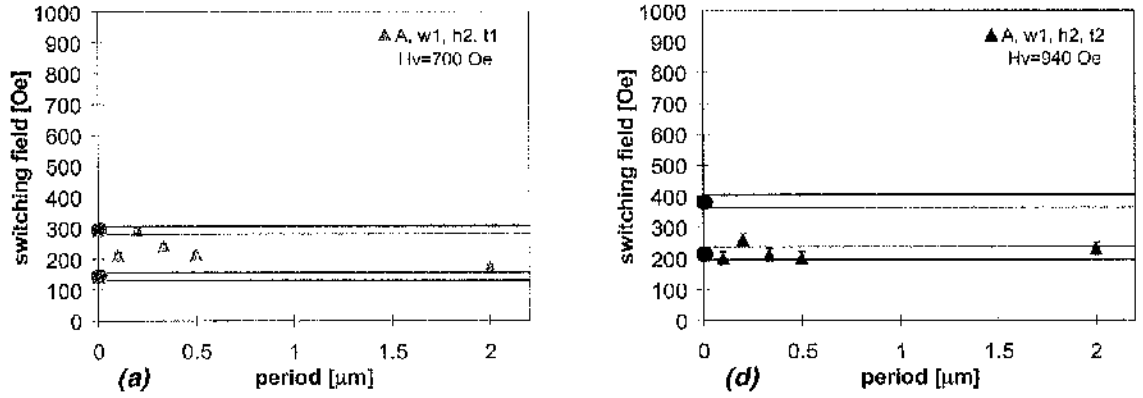
Generally there was good agreement between the experimental and simulated domain configurations at remanence and prior to switching. The modelled reversal mechanism (i.e. generation and rapid growth of areas with reversed direction of magnetisation) appears more plausible here as each reverse domain was only associated with one singularity. It is however surprising that walls were generated which were not really necessary to form a vortex configuration (Figs. 7.8(c), (d)) which might again be an artefact of the coarse mesh. Furthermore there were several reverse domains generated instead of just one which then quickly propagated through the element.

The calculated coercivity of the narrow elements ( $w_1$ ) with edge structure type A ( $h_2$ ) for the cases with and without vertical field is compared with the experimental switching field values of the elements in Fig. 7.10. In Figs. 7.10(a)-(c) the results are graphed for the elements with  $t_1$  and the data for the elements with  $t_2$  is illustrated in Figs. 7.10(d)-(f).

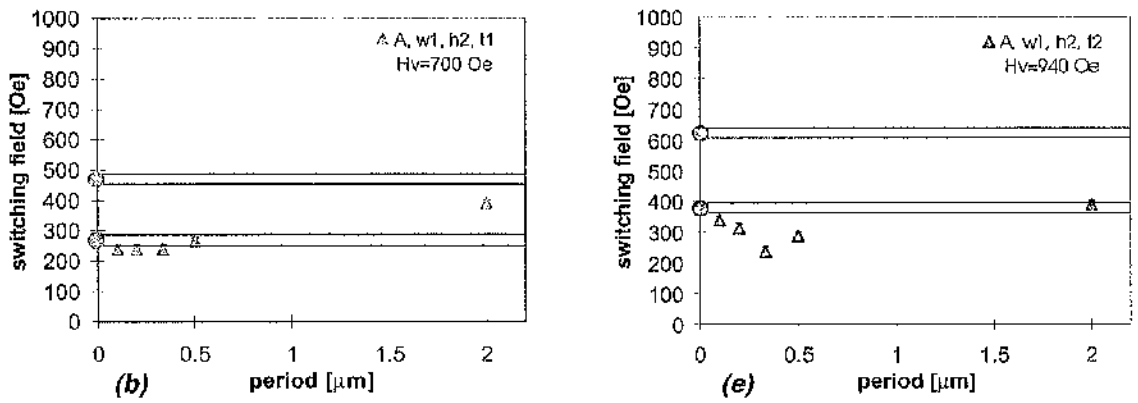
In the case of the elements with the blunter tips  $t_1$  a characteristic maximum appeared for short periods in the experimental coercivity graphs (Figs. 5.18(b), 7.10(a)). This maximum was not reproduced in the simulations (Figs. 7.10(b), (c)). Another difference was that the element with the longest period ( $p=2\mu\text{m}$ ) was the magnetically hardest of all elements with structure type A ( $h_2$ ) in the simulations (Figs. 7.10(b), (c)) whereas the element with  $p=0.2\mu\text{m}$  was the hardest in the experiments (i.e. maximum for short periods). As far as the magnitude of the coercivity is concerned for the elements with structured edges there was quite good agreement between the majority of the experimental and simulated results. It should be noted though that most elements with structured edges were found in the simulations to possess switching field values even below the lower limit of the simulated standard elements. This is due to the fact that the standard elements were generally considerably harder in the simulations than in the experiments (section 7.4.1). This difference is almost certainly due to the fact that elements with structured edges did not have 'perfect' (i.e. straight) edges in the simulations and therefore were a better model for the real elements with structured edges than the modelled standard elements for the real ones.

For the elements with structure type A with  $h_2$  and sharper tips ( $t_2$ ) the most striking observations of the graph of the experimental results, i.e. considerably less variation of the coercivity with structure period and a more pronounced drop of coercivity compared to the

## Experimental Results



## Simulation Results



## Simulation Results

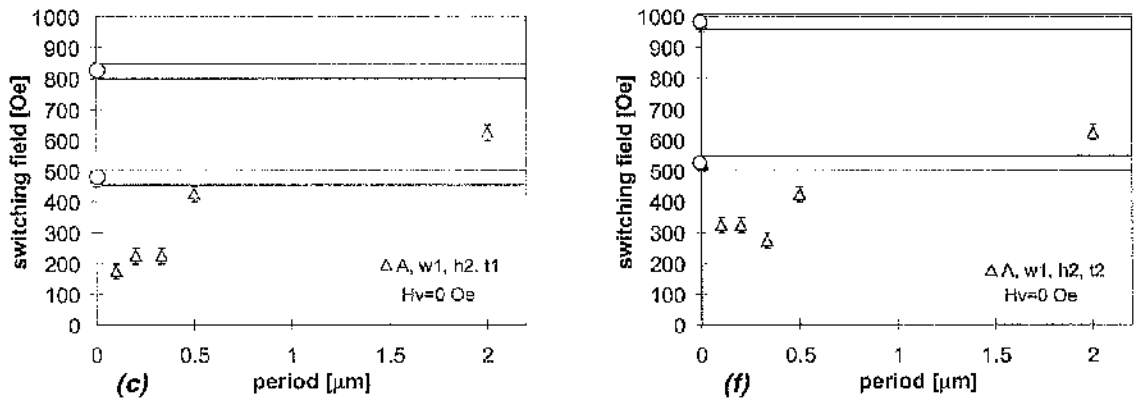


Figure 7.10

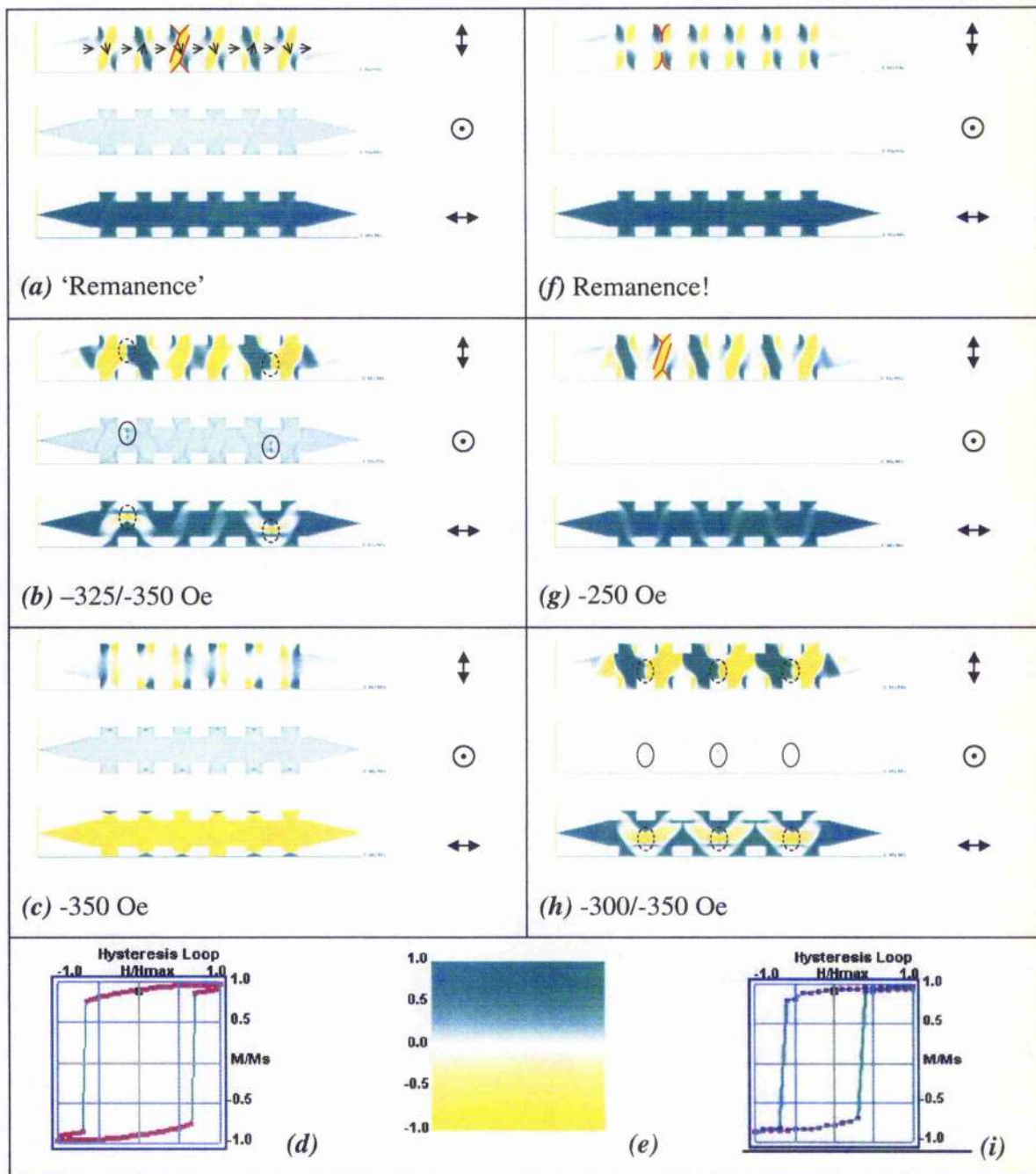
Comparison of experimental and simulated switching field values of elements with edge structure type A of 2<sup>nd</sup> and 3<sup>rd</sup> patterns. Vertical field as indicated. Circles mark switching field values of corresponding standard elements; bandwidth illustrated by horizontal lines.

elements with  $t_1$  (Figs. 7.10(a) and 7.10(d)) were not corroborated in the simulations. On the contrary the variation of coercivity in the simulations was found to be much more dependent on the vertical field as a similar bandwidth of switching field values was the result for simulations (i) with vertical field (Figs. 7.10(b), (e)) and (ii) without vertical field (Figs. 7.10(c), (f)). Thus, the agreement of the simulated switching field values with the experimental results was not as good as the agreement of the magnetic microstructures.

#### 7.4.1.3 ELEMENTS WITH EDGE STRUCTURE TYPE C

The results of the simulations for the elements with edge structure type C ( $h_2$ ) of the third and second pattern are presented next. In accordance with the previous section only the element with  $p=0.33\mu\text{m}$  and  $w_{t_1, t_2}$  is discussed in detail. An overview is given of the results for simulations with and without vertical field for elements with  $t_1$  and  $t_2$ . Fig. 7.11 shows examples of the magnetic microstructure within an element during the hysteresis calculations with the vertical field being  $H_y = 940$  Oe (Figs. 7.11(a)-(c)) respectively  $H_y = 0$  Oe (Figs. 7.11(f)-(h)) together with the hysteresis loops and the colour scheme (Figs. 7.11(d), (e), (i)). The hysteresis field was again applied along the easy axis of the element (X-direction) with the extreme values being  $H_x = \pm 500$  Oe and the variation step was 25 Oe in the case with vertical field  $H_y = 940$  Oe and 50 Oe for zero vertical field.

In agreement with previous observations the vertical field induced a clearly notable out of plane component of magnetisation in the middle parts of the images in Figs. 7.11(a)-(c) and the magnitude of the out of plane component of magnetisation due to the vertical field was  $M_y \approx 0.11 \cdot M_s$  (corresponding to an out of plane tilt of magnetisation of  $\approx 6^\circ$ ). However, in the case of edge structure type C different domain configurations were calculated for the remanent states of the two simulations (Figs. 7.11(a), (f)). In the simulation with vertical field the experimentally observed double y-configurations were calculated. One of these characteristic double y-configurations is highlighted by red lines and the distribution of magnetisation direction in the main body of the element is indicated by single arrows in Fig. 7.11(a). A different magnetic microstructure was calculated in the simulation without vertical field. At Remanence! double v-configurations resulted instead of double y-configurations and one of these double v-configurations is highlighted by the red lines in Fig. 7.11(f). This difference in domain configuration led to a more notable


**Figure 7.11**

Magnetic microstructure of a narrow ( $w=250\text{nm}$ ) element with edge structure type C with period  $p=0.33\mu\text{m}$  of the third pattern ( $t_2=2$ ) for different stages of hysteresis simulations. Double arrows and circles indicate mapping directions.  $H_y=\text{constant}=940\text{ Oe}$  for (a), (b), (c).  $H_y=\text{constant}=0\text{ Oe}$  for (f), (g), (h). Hysteresis loops ( $H_{x(\text{max})}=\pm 500\text{ Oe}$ ) and colour scheme are given for reference.

reduction of the magnetic moment for the element in the calculation with  $H_y = 940$  Oe as can be seen by comparison of the two hysteresis loops (Figs. 7.11(d), (i)).

When the magnetic microstructure of the element was calculated for reverse fields in the simulation with  $H_y = 940$  Oe the domain configuration did not change markedly until the onset of magnetisation reversal. This state is shown in Fig. 7.11(b) where two areas with reversed direction of magnetisation were generated as can be seen in the bottom part of Fig. 7.11(b) and is indicated there by dashed ellipses. The middle part of Fig. 7.11(b) captured the associated changes in the out of plane direction of magnetisation. Bloch-line-like features of exclusively positive polarity (due to the vertical field) were generated at the sites of the reverse domains and these are marked by ellipses. The distribution of magnetisation around the Bloch-line-like features was consistent with the one described in detail in section 7.4.1.1, Fig. 7.4(a) and therefore leads to similar complications as discussed for Fig. 7.5. Another problematic detail is due to the redundant walls which are associated with each Bloch-line-like feature similar to the discussion of Fig. 7.8. Both of these critical points might again be associated with the large cell size.

After magnetisation reversal in the main body of the element small domains with the original direction of magnetisation were still present in eight out of the twelve structure features (Fig. 7.11(c) bottom). It should be noted that the remaining of such domains was also observed in the experiments and the resulting flux closure like domain configurations within the structure features were discussed in detail in Fig. 5.22. The effect on the hysteresis loop can be seen in Fig. 7.11(d) where a higher field was required to saturate the element than necessary to induce the switch of magnetisation ( $H_{switch} = \pm 325/350$  Oe,  $H_{sat} = \pm 475/500$  Oe).

When the magnetic microstructure was calculated for a reverse field in the case of zero vertical field the double v-configurations changed into double y-configurations at a hysteresis field value of  $H_x = -250$  Oe. One of these double y-configurations is highlighted by red lines in Fig. 7.11(g). This domain geometry did not change considerably until switching occurred between  $H_x = -300$  and  $-350$  Oe (Fig. 7.11(h)). The primary switching mechanism was again generation of areas with reversed direction of magnetisation (marked by the dashed ellipses in the bottom part of Fig. 7.11(h)). In agreement with former results it was only at these sites where out of plane components, i.e. Bloch-line-like features of both polarities were generated and these are marked by the

ellipses in the middle part of Fig. 7.11(h). Apart from the two polarities of Bloch-line-like features the details were the same as discussed in the previous paragraph for the simulation with vertical field.

The asymmetric hysteresis loop (Fig. 7.11(i)) resulted from the fact that the magnetisation within the element was not entirely reversed at the maximal negative hysteresis field value ( $H_x = -500$  Oe). An important feature of this hysteresis loop is the step in the upper magnetisation curve between  $H_x = -200$  and  $-250$  Oe: It was at this stage when the change from double v-configurations to double y-configurations occurred and led to a clear reduction of net resultant of magnetisation.

An overview of the magnetic microstructures within the elements with structure type C and  $w_1, h_2, t_2$  (third pattern) calculated with vertical field is given in table 7.2. Whether or not the magnetic microstructures were the same for the elements with  $t_1$  and in both zero vertical field calculations is indicated by the blue parameters. As before a brief description is given for the magnetic microstructures at remanence and prior to switching and the primary switching mechanism is given as well. The terminology is similar to that of table 5.4 apart from the newly introduced double v-configurations. This describes an even more symmetric domain configuration than the double y-configurations. In the case of double v-configurations the central walls do not run across the entire element width (Fig. 7.11(f)).

In good agreement with the experimental observations table 7.2 is also valid for most elements with the blunter tips  $t_1$ . Only for the element with  $p=0.25\mu\text{m}$  slightly different domain configurations were calculated for the 'remanent' state: In the case of the element with  $t_1$  only double y-configurations were calculated instead of double y- and double v-configurations side by side for the element with  $t_2$ . It should be noted that no double v-configurations were observed experimentally.

As far as the simulations with zero vertical field were concerned only little deviation was found compared to the calculated domain configurations with vertical field. In the case of vertical field  $H_y = 0$  no double y-structures were calculated at all for the remanent state of the elements whilst at a sufficiently high reverse field the double v-configurations changed in double y-configurations. The elements with the small periods ( $p=0.33-0.2\mu\text{m}$ ) retained this domain configuration until the onset of magnetisation reversal. All calculated micromagnetic states of the elements with  $0.2\mu\text{m} \leq p \leq 0.33\mu\text{m}$  prior to switching were

identical and they also agreed with the experimental observations (table 5.4). Difficulties arose again for the detailed investigation of the calculated reversal mechanisms (i.e. highly complex wall configurations due to excessive magnetisation rotation rather than nucleation of reverse domains).

Narrow ( $w_1$ ) Elements with Structure Type C ( $h_2$ ) - Third Pattern ( $t_2$ )					
period	2.0 $\mu\text{m}$	0.67 $\mu\text{m}$	0.33 $\mu\text{m}$	0.25 $\mu\text{m}$	0.2 $\mu\text{m}$
<b>state: R</b>	quasi single domain $t_1, t_2(0), t_1(0)$	quasi single domain $t_1, t_2(0), t_1(0)$	double y- configurations $t_1, \cancel{t_2(0)}, \cancel{t_1(0)}$	double y-, v- configurations $\cancel{t_1}, \cancel{t_2(0)}, \cancel{t_1(0)}$	double v- configurations $t_1, t_2(0), t_1(0)$
<b>state: PS</b>	concertina* $t_1, t_2(0), t_1(0)$	multi-domain $t_1, t_2(0), t_1(0)$	double y- configurations $t_1, t_2(0), t_1(0)$	double y- configurations $t_1, t_2(0), t_1(0)$	double y- configurations $t_1, t_2(0), t_1(0)$
<b>S</b>	propagation of reversed area(s) $t_1, t_2(0), t_1(0)$	propagation of reversed area(s) $t_1, t_2(0), t_1(0)$	propagation of reversed area(s) $t_1, t_2(0), t_1(0)$	propagation of reversed area(s) $t_1, t_2(0), t_1(0)$	propagation of reversed area(s) $t_1, t_2(0), t_1(0)$

**Table 7.2**

*Micromagnetic states of elements with  $w_1$  and structure type C of 3<sup>rd</sup> pattern ( $t_2$ ) for simulated hysteresis loops with vertical field  $H_v=940$  Oe.*

*State R: Remanent state, State PS: Prior to switching, S: Switching.*

*$t_1$ : Simulation for element with  $t_1$  and  $H_v=700$  Oe;  $t_{1,2}(0)$ : Simulation with  $H_v=0$  Oe.*

*In case of different results for  $t_1, t_2(0), t_1(0)$ :  $\cancel{t_1}, \cancel{t_2(0)}, \cancel{t_1(0)}$ .*

A comparison of the experimental and simulated switching field values is given next. Figs. 7.12(a)-(c) show the results for the elements with  $t_1$  and in Figs. 7.12(d)-(f) the graphs are given for the elements with the sharper tips  $t_2$ . Whilst the calculated coercivity of the elements was generally higher than the experimentally determined switching field values the agreement between simulations with vertical field (Figs. 7.12(b), (e)) and experiments (Figs. 7.12(a), (d)) was good as far as the trend of the graphed values was concerned. The finding that the experimental coercivity of the elements with  $t_2$  was closer to (even below) the lower limit of the standard elements was also corroborated in the simulations with vertical field. Further agreement between simulation and experiment was that the coercive

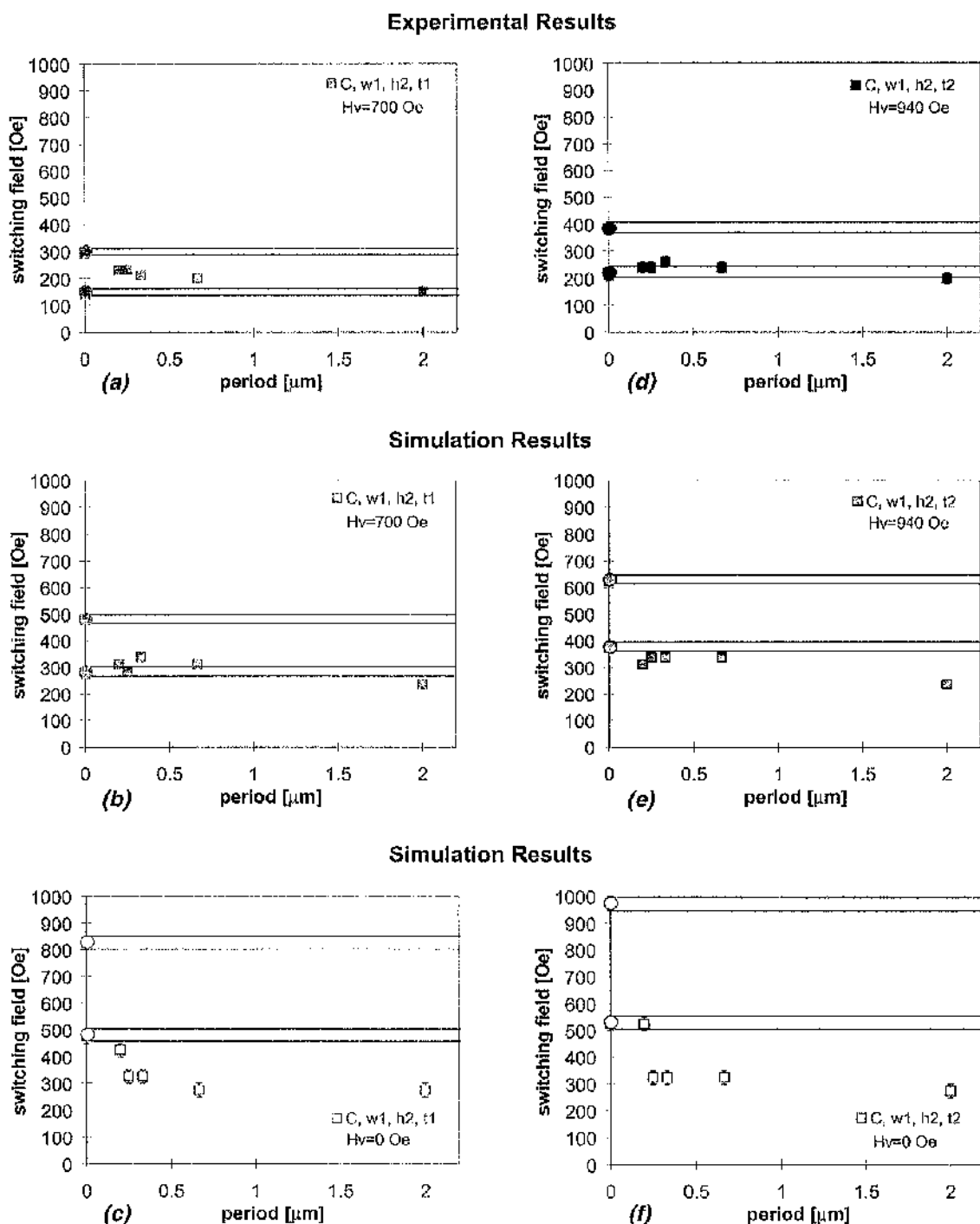


**Figure 7.12**

*Comparison of experimental and simulated switching field values of elements with edge structure type C of 2<sup>nd</sup> and 3<sup>rd</sup> patterns. Vertical field as indicated. Circles mark switching field values of corresponding standard elements; bandwidth illustrated by horizontal lines.*

field values of the elements with structure type C were quite similar for identical period irrespectively of the tip ratio. In all simulations as well as in the experiments the element with the longest period  $p=2\mu\text{m}$  was the easiest to switch. The spread in the calculated coercivities for the zero vertical field calculations (Figs. 7.12(c), (f)) is solely due to the marked increase of  $H_c$  for the element with the smallest period  $p=0.2\mu\text{m}$ .

#### 7.4.2 ELEMENTS OF FOURTH AND FIFTH PATTERNS

In this section the results of the simulations for the narrow elements ( $w_1$ ) with structure types A and C ( $h_2$ ) of the fourth and fifth patterns are presented. In contrast to the elements with structured edges, which were discussed in section 7.4.1 the ones described here were of nominally constant width despite the structuring of the edges. As in the previous sections the emphasis of the discussion lies on the elements with the sharper tips  $t_2$  (here: fifth pattern) and structure period  $p=0.33\mu\text{m}$ . The calculated reversal behaviour of all elements with structured edges with  $h_2$  of both patterns ( $t_1, t_2$ ) is summarised and briefly compared with the experimental findings. In accordance with the previous sections two sets of simulations were run (with and without vertical field) and the results are compared.

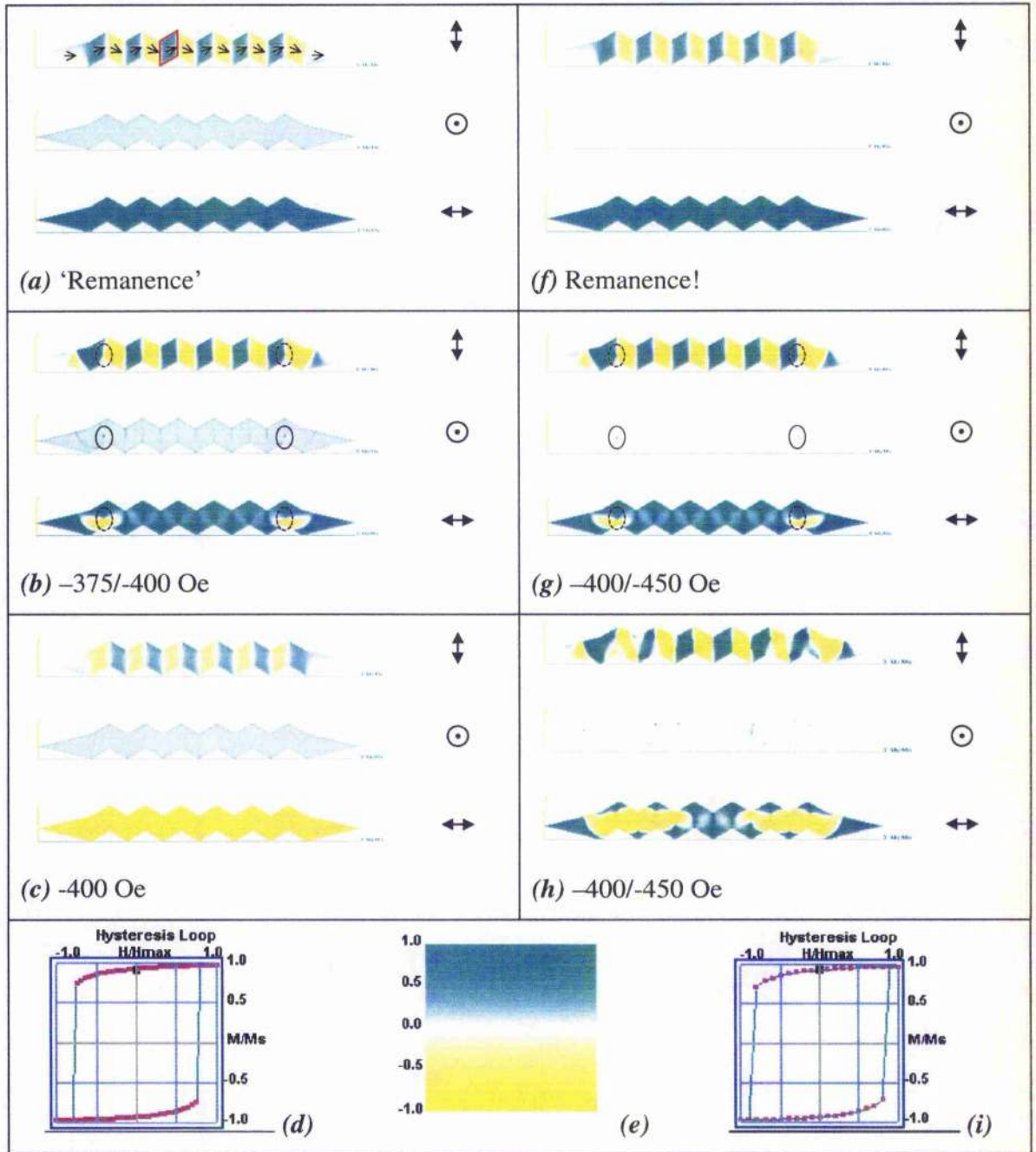
##### 7.4.2.1 ELEMENTS WITH EDGE STRUCTURE TYPE A

The simulations of elements with edge structure type A are discussed first. The set up for the first series of simulations was as follows: The width of the elements was  $w_1$  and was nominally constant in the entire element apart from the tips (double pointed elements). The height of the structure features was  $h_2$  and five different masks with periods between 2.0 and 0.1 $\mu\text{m}$  were designed. Simulations were again run with and without vertical field for both sets of elements ( $t_1, t_2$ ). The vertical field was  $H_y = 940$  Oe in the case of the elements with  $t_2$  and 700 Oe for the elements with the blunter tips  $t_1$  respectively zero for the simulations without vertical field. The hysteresis field was again applied solely along the easy axis of the elements (i.e. X-direction) with the extreme values being  $H_x = \pm 500$  Oe. In accordance with the previous examples the stepwise variation was 25 Oe in the calculations with vertical field and 50 Oe for the simulations without vertical field.

Examples of the magnetic microstructure of the element with  $p=0.33\mu\text{m}$  during a magnetisation reversal simulation with vertical field  $H_y = 940$  Oe are shown in Figs. 7.13(a)-(c) together with the resulting hysteresis loop and the colour code (Fig. 7.13(d), (e)). Some of the domain configurations of the same element for a zero vertical field simulation are given in Figs. 7.13(f)-(h) together with the corresponding hysteresis loop in Fig. 7.13(i). With the vertical field  $H_y = 940$  Oe the magnetisation of the element was again notably tilted out of plane ( $M_y \approx 0.11 \cdot M_s$ , corresponding to a tilt angle of  $6^\circ$ , Figs. 7.13(a)-(c) centre) which is in agreement with analogous results in the previous sections.

The in-plane components of magnetisation distribution looked in both cases exactly alike and as deduced from the Fresnel and DPC images in chapter 6 and are discussed together. Most notably was the corroboration of the experimental result that due to the shape of the elements with structured edges of the fourth and fifth patterns the magnetisation was 'channelled' through these elements. This channelling gave rise to the formation of parallelogram domains even at zero hysteresis field as can clearly be seen in the upper parts of Figs. 7.13(a) and (f). It should be noted that in agreement with the experimental data two parallelogram domains were formed per period. Single arrows indicate the distribution of magnetisation direction in the element and one of the parallelogram domains is highlighted by a red frame in Fig. 7.13(a). Despite the variation of the magnetisation direction the element has a high net resultant ( $M_x \approx 0.93 \cdot M_s$ ) of magnetisation in X-direction at 'remanence' and remanence!. This can be seen in the bottom parts of Figs. 7.13(a) and (f) and in the hysteresis loops (Figs. 7.13(d), (i)).

The magnetic microstructure did not change considerably when the situation was calculated for reverse fields. The main change was that the gradient of magnetisation direction in the parallelogram domains increased (i.e. increase of wall angles). At the onset of magnetisation reversal (Figs. 7.13(b), (g)) two areas with reversed direction of magnetisation were generated at the ends of the element (marked by dashed ellipses in the bottom parts of the figures). Each of these areas was associated with Bloch-line-like features as can be seen in the central part of the image sets (ellipses). The details of the calculated vortex structure is similar to that discussed for Fig. 7.8(c) with the difference that here only one 'green' wall existed. A counterpart to the redundant black wall in Fig. 7.8(c), however, was also calculated here (Figs. 7.13.(b), (g)).


**Figure 7.13**

Magnetic microstructure of a narrow ( $w=250\text{nm}$ ) element with edge structure type A with period  $p=0.33\mu\text{m}$  of the third pattern ( $t_2=2$ ) for different stages of hysteresis simulations. Double arrows and circles indicate mapping directions.  $H_y=\text{constant}=940\text{ Oe}$  for (a), (b), (c).  $H_y=\text{constant}=0\text{ Oe}$  for (f), (g), (h). Hysteresis loops ( $H_{x(\text{max})}=\pm 500\text{ Oe}$ ) and colour scheme are given for reference.

During further development of magnetisation reversal more areas with reversed direction of magnetisation occurred at the inner vertices of the element (also associated with the appearance of further Bloch-line-like features, Fig. 7.13(h)). The fully reversed state of the element is shown in Fig. 7.13(c). Despite the element being  $\approx$ saturated after magnetisation reversal the magnetisation was still not fully aligned with the hysteresis field as can be deduced from the colour variation in the top parts of Fig. 7.13(c). The faint colours however mean that the deviations of magnetisation direction from perfect alignment in X-direction are rather small. It should also be noted that the colour gets even fainter the further it is away from the edges. This agrees very well with the experimental observation that after magnetisation reversal faint wall sections were visible which were restricted to the outer vertices of the elements (Fig. 6.5(c)).

An overview of the magnetic microstructures resulting from the magnetisation reversal simulations for the elements is summarised in table 7.3. The domain configurations are described in catchword style for the simulations of the elements with the sharper tips ( $t_2$ , fifth pattern) under the influence of the vertical field  $H_y = 940$  Oe.

No deviations in the micromagnetic configurations were found in any of the other simulations and therefore none of the blue parameters is cancelled out and table 7.3 is also valid for the elements with the blunter tips as well as for the simulations without vertical field. The terminology is the same as applied for the description of the experimentally observed domain configurations in table 6.1 apart from the  $\approx$ concertina states calculated for the elements with the shortest period  $p=0.1\mu\text{m}$  which were similar to the configuration shown in Fig. 7.9(d). The simulated and experimentally observed domain states during magnetisation reversal cycles agreed very well apart from the elements with the smallest structure period (see table 6.1). There were, however, again problems with the plausibility of the simulated reversal mechanism as similar to the discussion of Fig. 7.8 too many walls were associated with the generation of areas with reverse direction of magnetisation.

Narrow ( $w_1$ ) Elements with Structure Type A ( $h_2$ ) - Fifth Pattern ( $t_2$ )					
period	2.0 $\mu\text{m}$	0.5 $\mu\text{m}$	0.33 $\mu\text{m}$	0.2 $\mu\text{m}$	0.1 $\mu\text{m}$
<b>state: R</b>	single domain	parallelogram	parallelogram	parallelogram	$\approx$ concertina
	$t_1, t_2(0), t_1(0)$	domains $t_1, t_2(0), t_1(0)$	domains $t_1, t_2(0), t_1(0)$	domains $t_1, t_2(0), t_1(0)$	domains $t_1, t_2(0), t_1(0)$
<b>state: PS</b>	concertina	parallelogram	parallelogram	parallelogram	$\approx$ concertina
	$t_1, t_2(0), t_1(0)$	domains $t_1, t_2(0), t_1(0)$	domains $t_1, t_2(0), t_1(0)$	domains $t_1, t_2(0), t_1(0)$	domains $t_1, t_2(0), t_1(0)$
<b>S</b>	propagation of reversed area(s)				
	$t_1, t_2(0), t_1(0)$				

**Table 7.3**

Micromagnetic states of elements with  $w_1$  and structure type A of 5<sup>th</sup> pattern ( $t_2$ ) for simulated hysteresis loops with vertical field  $H_v=940$  Oe.

State R: Remanent state, State PS: Prior to switching, S: Switching.

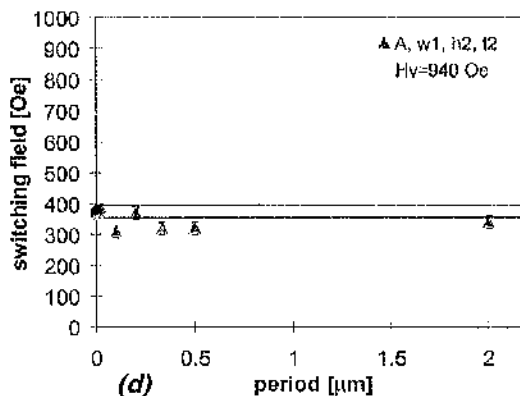
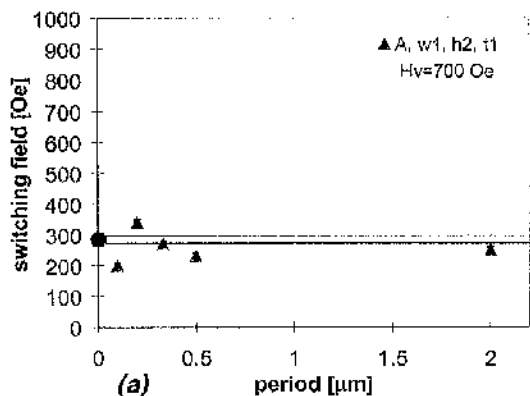
$t_1$ : Simulation for element with  $t_1$  and  $H_v=700$  Oe;  $t_{1,2}(0)$ : Simulation with  $H_v=0$  Oe.

In case of different results for  $t_1, t_2(0), t_1(0)$ :  $\tau_1, \tau_2(0), \tau_1(0)$ .

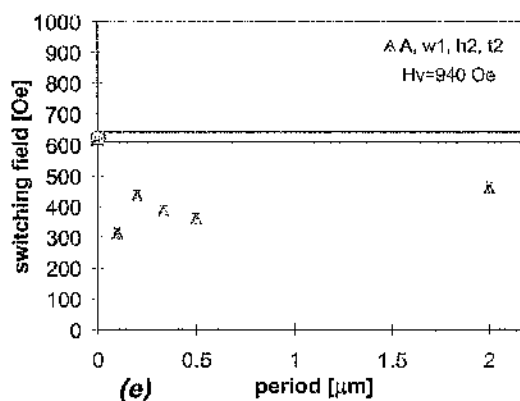
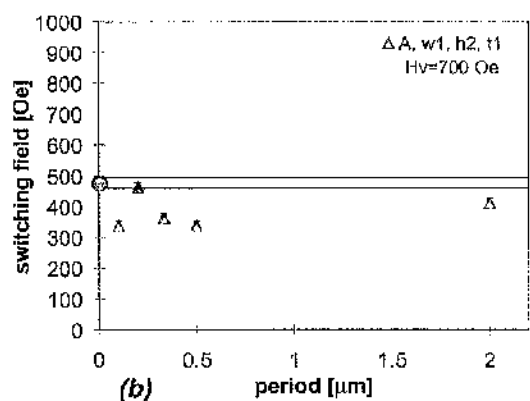
The experimental and simulated switching field values of the elements with edge structure type A with  $h_2$  of the fourth and fifth patterns are compared in Fig. 7.14. The coercive field values of the elements of the fourth pattern are graphed in Figs. 7.14(a)-(c) and those of the fifth pattern are graphed in Figs. 7.14(d)-(f).

The experimentally determined trend of the switching field values especially the maximum for smaller periods (i.e.  $p=0.2\mu\text{m}$ ) was corroborated in all simulations. The calculated switching field values of the elements with the sharper tips  $t_2$  (Fig. 7.12(e), (f)) were very similar to those of elements with the blunter tips  $t_1$  (Fig. 7.12(b), (c)) with identical structure parameters irrespective of the values of the vertical field  $H_v$ . Therefore the result of the experiments that the switching field values of the elements with the sharper tips  $t_2$  did not vary as much as those of the elements with  $t_1$  was not found in the simulations.

Experimental Results



Simulation Results



Simulation Results

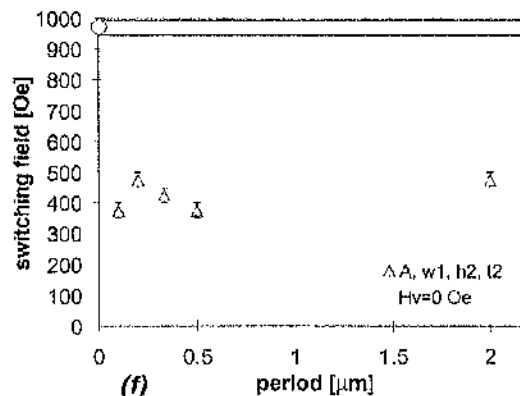
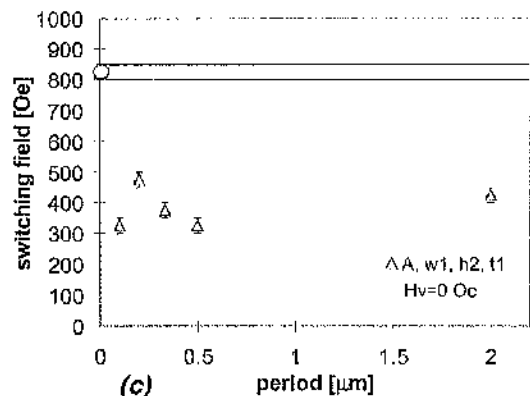


Figure 7.14

Comparison of experimental and simulated switching field values of elements with edge structure type A of 4<sup>th</sup> and 5<sup>th</sup> patterns. Vertical field as indicated. Circles mark switching field values of corresponding standard elements; bandwidth illustrated by horizontal lines.

The increase of coercivity which was observed experimentally for the elements of the fourth and fifth patterns compared to corresponding elements of the second and third patterns, however, was also found in the simulations (Figs. 7.10, 7.14).

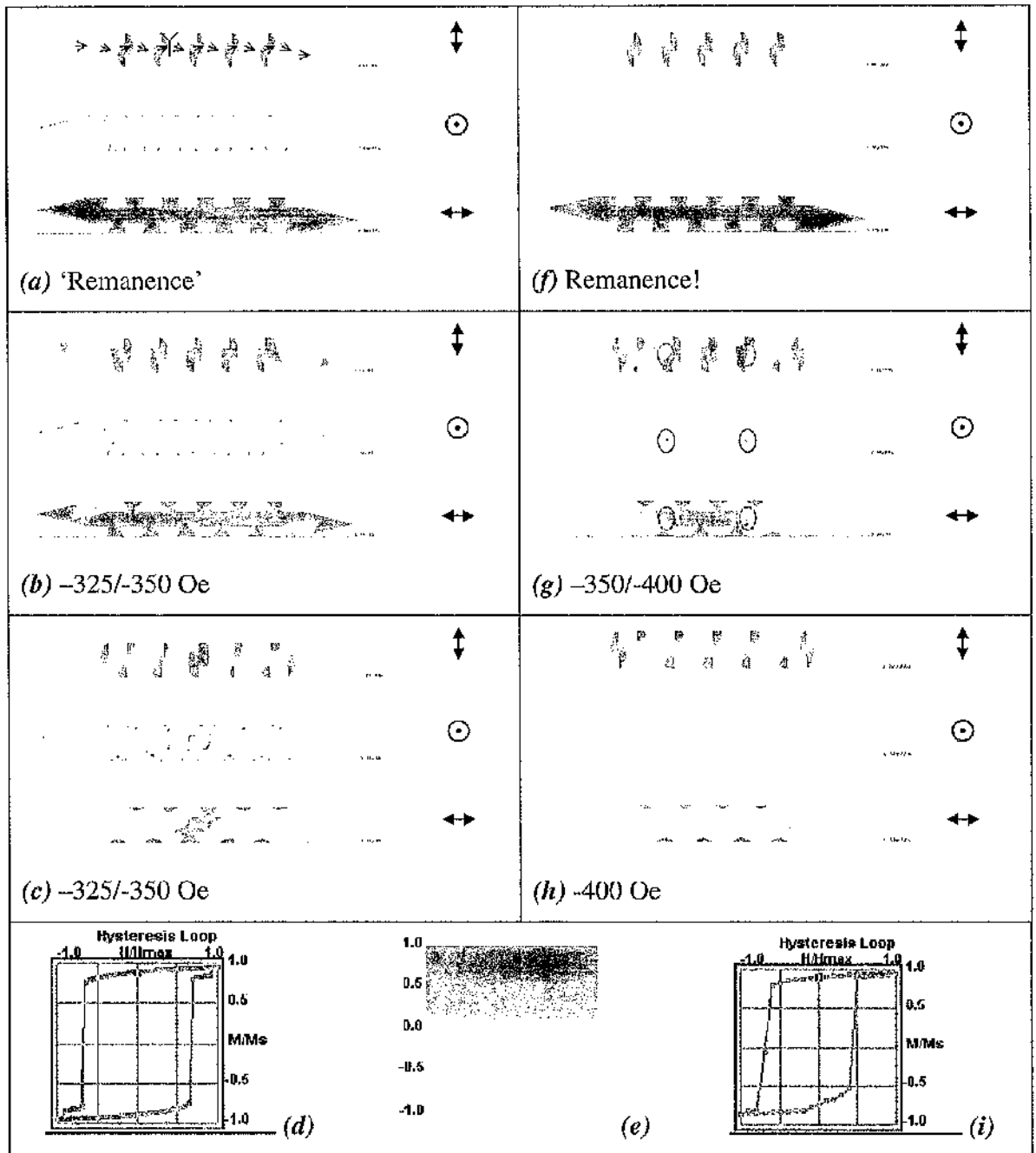
#### 7.4.2.2 ELEMENTS WITH EDGE STRUCTURE TYPE C

In this section the simulations of elements with edge structure type C with  $h_2$  of the fourth and fifth patterns are presented. The set up was the same as for the calculations in the previous section except for the mask to define the shape of the elements. Figure 7.15 shows an overview of magnetic microstructures of the element with  $p=0.33\mu\text{m}$  for different stages during magnetisation reversal simulation with vertical field ( $H_y = 940$  Oe, Figs. 7.15(a)-(c)) and without vertical field ( $H_y = 0$  Oe, Figs. 7.15(f)-(h)). The resulting hysteresis loops and the colour scheme are given in Figs. 7.15(d), (e), (i).

In agreement with the previous section the most notable characteristic of this kind of element with structured edges and nominally constant width is the 'channelling' of magnetisation due to the shape of the element. The out of plane component of magnetisation resulting from the vertical field ( $H_y = 940$  Oe) was again  $M_y \approx 0.11 \cdot M_s$  throughout the hysteresis simulation and is illustrated in the central parts of Figs. 7.15(a)-(c) (average tilt of magnetisation out of plane  $\approx 6^\circ$ ).

In the case of edge structure type C the channelling gave rise to two y-configurations per period in most elements in the experiments (section 6.5.2) as well as in the simulations. These y-configurations were also the result for both hysteresis simulations for the 'remanent' state (Fig. 7.15(a) as well as in remanence! (Fig. 7.15(f)) for the above introduced element. One of these characteristic y-configurations is highlighted by red lines in Fig. 7.15(a) and the direction of magnetisation within the main body of the element is indicated by single arrows. The mean direction of magnetisation was clearly parallel to the length of the element in positive X-direction in both cases (Figs. 7.15(a), (f) bottom) and the magnetisation in X-direction amounted to about  $M_x \approx 0.90 \cdot M_s$  in both zero hysteresis field states.

Modelling the magnetic microstructure for reverse fields did not lead to a change in domain configuration until the onset of magnetisation reversal. This situation is shown in Fig. 7.15(b) where the y-configurations were still present within the region of the element


**Figure 7.15**

Magnetic microstructure of a narrow ( $w=250\text{nm}$ ) element with edge structure type C with period  $p=0.33\mu\text{m}$  of the third pattern ( $t_2=2$ ) for different stages of hysteresis simulations. Double arrows and circles indicate mapping directions.  $H_y=\text{constant}=940\text{ Oe}$  for (a), (b), (c).  $H_y=\text{constant}=0\text{ Oe}$  for (f), (g), (h). Hysteresis loops ( $H_{x(\text{max})}=\pm 500\text{ Oe}$ ) and colour scheme are given for reference.

with the structured edge while areas with reversed direction of magnetisation appeared in both tip regions. No Bloch lines were visible in the central part of the illustration in Fig. 7.15(b) as no vortex magnetisation configurations were present. A later stage of the calculated magnetisation reversal is given in Fig. 7.15(c). At this point the magnetisation in the main body of the element was almost entirely reversed as can be seen in the bottom part of the image. There were however small domains remaining in the outer parts of the structure features where the original direction of magnetisation was still present. This led to flux closure like domain configurations within the structure features and the associated Bloch lines in their centres. Magnetisation distributions of this kind were also discussed in section 7.4.1.3 (Fig. 7.11(c)) of this chapter and in the experimental chapters 5 and 6 (section 5.5.3 (Fig. 5.22) and section 6.5.2.). In order to also reverse the remaining domains a higher field was necessary as can be seen in the calculated hysteresis loop (Fig. 7.15(d), steps in the squarish hysteresis loop for  $H_x = \pm 450 / 475$  Oe). It should be noted that in the case of the elements of the fourth and fifth patterns the remaining of domains with original direction of magnetisation was not as common in the experiments as in the simulations.

In the case of zero vertical field the out of plane component of magnetisation was again always zero except during magnetisation reversal (Fig. 7.15(g)). During magnetisation reversal Bloch-line-like features of both polarities were calculated in the centre of vortex configurations as those marked by ellipses in Fig. 7.15(g).

The calculated hysteresis loop for zero vertical field simulation was asymmetric because the magnetisation of the element was not completely reversed at  $H_x = -500$  Oe. An even more interesting feature was that the first reversal occurred 'stepwise' between  $H_x = -300$  and  $-400$  Oe. An illustration of a domain configuration during the second step of magnetisation reversal is given in Fig. 7.15(g) where ellipses mark locations of Bloch-line-like features in the centre of vortices. The Bloch-line-like features had again both polarities as observed previously for zero vertical field simulations. In contrast to theoretical expectations (sections 1.3.5, 1.5) no out of plane components of magnetisation were detected in the centres of the flux-closure like domain configurations within the edge structure features in Fig. 7.15(h). This is surprising as Bloch lines were clearly calculated for these locations in the simulations with vertical field (Figs. 7.11(c), 7.15(c)) despite the same size of cells in all set-ups.

An overview of the calculated magnetic microstructures for all elements with edge structure type C ( $h_2$ ) of the fifth pattern ( $t_2$ ) is given in table 7.4. The terminology is the same as applied in table 6.2 where the experimental observations were summarised. In accordance with the previous tables in this chapter an overview of the simulation results of all four sets of calculations is given in table 7.4 by means of the blue parameters. An important result was that the main stages of the reversal calculations did not alter with tip ratio or vertical field. Furthermore should be noted that the experimental observations (table 6.2) and calculated results were almost identical with the most characteristic feature of these elements being the y-configurations. In accordance with the previous simulations the switch of magnetisation was initiated by the generation of areas with reversed direction of magnetisation. Magnetisation reversal then progressed by means of rapid propagation of these reversed areas.

Narrow ( $w_1$ ) Elements with Structure Type C ( $h_2$ ) - Fifth Pattern ( $t_2$ )					
period	2.0 $\mu\text{m}$	0.67 $\mu\text{m}$	0.33 $\mu\text{m}$	0.25 $\mu\text{m}$	0.2 $\mu\text{m}$
<b>state: R</b>	quasi single domain $t_1, t_2(0), t_1(0)$	multi-domain $t_1, t_2(0), t_1(0)$	y- configurations $t_1, t_2(0), t_1(0)$	y- configurations $t_1, t_2(0), t_1(0)$	y- configurations $t_1, t_2(0), t_1(0)$
<b>state: PS</b>	concertina* $t_1, t_2(0), t_1(0)$	y- configurations $t_1, t_2(0), t_1(0)$	y- configurations $t_1, t_2(0), t_1(0)$	y- configurations $t_1, t_2(0), t_1(0)$	y- configurations $t_1, t_2(0), t_1(0)$
<b>S</b>	propagation of reversed area(s) $t_1, t_2(0), t_1(0)$				

**Table 7.4**

*Micromagnetic states of elements with  $w_1$  and structure type C of 5<sup>th</sup> pattern ( $t_2$ ) for simulated hysteresis loops with vertical field  $H_v=940$  Oe.*

*State R: Remanent state, State PS: Prior to switching, S: Switching.*

*$t_1$ : Simulation for element with  $t_1$  and  $H_v=700$  Oe;  $t_{1,2}(0)$ : Simulation with  $H_v=0$  Oe.*

*In case of different results for  $t_1, t_2(0), t_1(0)$ :  $t_1, t_2(0), t_1(0)$ .*

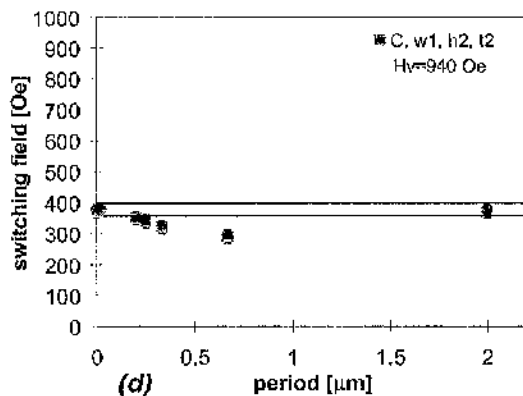
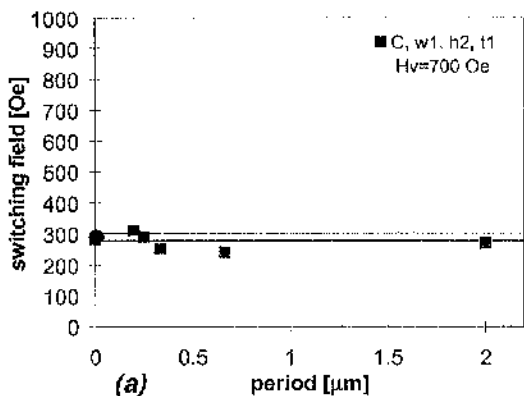
The experimental and calculated switching field values for the elements with edge structure type C ( $h_2$ ) of the fourth ( $t_1$ ) and fifth ( $t_2$ ) patterns are summarised in Fig. 7.16. The trend of the graphed simulation results (Figs. 7.16(b), (c), (e), (f)) agreed well with the experimental values (Figs. 7.16(a), (d)). There was only very little dependence of the coercive field values of the simulations on the two tip ratios and the vertical field. Whilst the agreement between absolute values of the experiments and simulation was very good for the elements with  $t_2$  (Figs. 7.16(d)-(f)) the calculated switching field values were higher than the experimental ones in the case of  $t_1$  (Figs. 7.16(a)-(c)). Furthermore it should be noted that in the experiments the minimum of switching field values was found for  $p=0.67\mu\text{m}$  for both tip ratios whilst in all simulations the minimum occurred for  $p=0.33\mu\text{m}$ .

## 7.5 SUMMARY

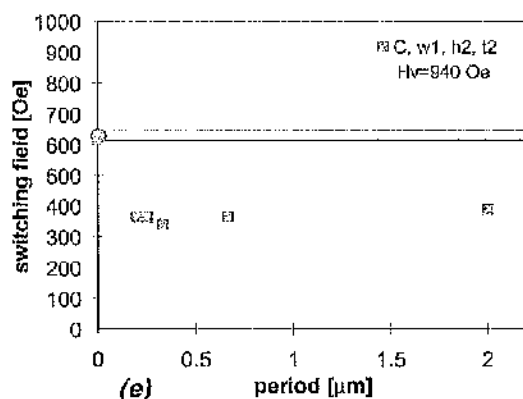
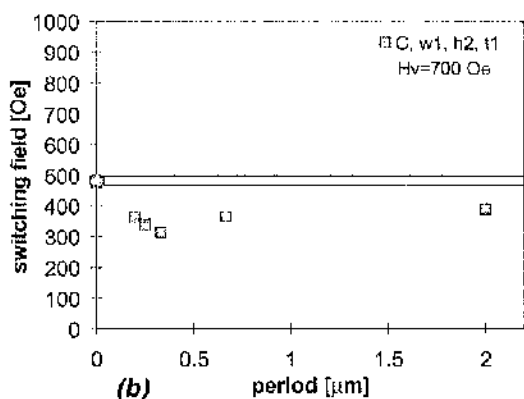
Using a commercially available software package (LLG Micromagnetics Simulator) simulations were run in which the magnetisation reversal behaviour of standard elements and elements with structured edges was calculated. Whilst most of the fabricated and experimentally investigated standard elements were also set up in the simulations only eight out of the 48 groups of elements with structured edges were modelled. Hysteresis calculations were performed for narrow elements ( $w_1$ ) with both tip ratios ( $t_1$ ,  $t_2$ ) and both edge structure types (A and C) with  $h_2$ . Simulations were firstly run with the vertical field present in the experiments taken into account and secondly without vertical field and the modelled results were compared with experimental data.

As far as the magnetic microstructure was concerned there was broad agreement between experimental observations and calculated equilibrium domain configurations. Most notable was the fact that experimentally determined characteristic domain configurations (i.e. concertina structure, parallelogram domains and (double) y-configurations) resulted in the simulations, too. Different domain configurations in the simulations with and without vertical field were only calculated in some cases of the second and third pattern: The elements with edge structure type A with  $p=0.1\mu\text{m}$  ( $t_1$  and  $t_2$ ) and those with edge structure type C with  $p=0.33$  and  $0.25\mu\text{m}$  (both for  $t_1$  and  $t_2$ ) displayed different magnetic microstructures in certain stages of the simulations.

**Experimental Results**



**Simulation Results**



**Simulation Results**

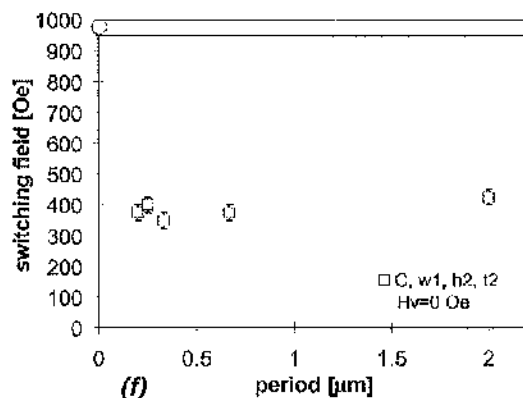
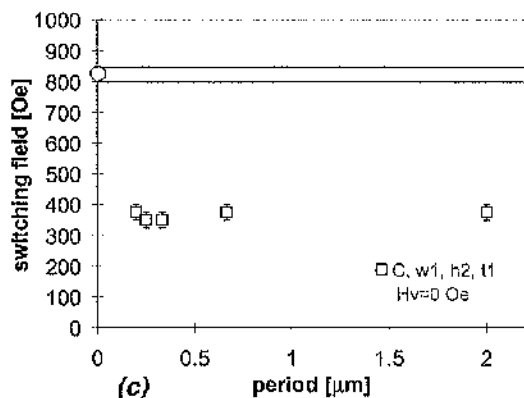


**Figure 7.16**

Comparison of experimental and simulated switching field values of elements with edge structure type C of 4<sup>th</sup> and 5<sup>th</sup> patterns. Vertical field as indicated. Circles mark switching field values of corresponding standard elements; bandwidth illustrated by horizontal lines.

In agreement with the experiments rapid magnetisation reversal was calculated for a vast majority of the elements. The resulting calculated hysteresis loops had a squarish shape and magnetisation reversal progressed rapidly after the generation of areas with reversed direction of magnetisation. Whilst this magnetisation reversal mechanism seemed at first plausible a close look at the calculated magnetic microstructure during the switch of magnetisation showed puzzling details. Surprising was the result that reversal in the simulations was not initiated by the nucleation of a reverse domain but that instead excessive rotation of magnetisation in adjacent domains led to questionable processes at the primary reversal sites. Such processes included the apparent reversal of the polarity of Néel walls, generation of unnecessary walls and a high number of Bloch-line-like features (in the case of zero vertical field calculations even 'pairs of Bloch-line-like features' of both polarities). It is not clear, however, whether these odd processes were merely due to the chosen cell size and whether a finer mesh would have yielded more plausible results for the reversal details. Another striking simulation result was that in most cases more than just one reverse domain were generated and it was also startling that at the locations of the Néel walls out of plane components were detected over notable distances ('not proper Néel walls') despite the thickness of the simulated film of just 20nm. No out of plane components were however detected in the centre of remaining flux closure like domain configurations within edge structure features of type C for zero vertical field calculations. It was suggested that this, too, might be an artefact of the coarse grid.

As far as the standard elements were concerned it was not determined unambiguously whether the calculated concertina structures were stable over a certain field range as found in the experiments or if they were transition states during magnetisation reversal.

The coercivity of the simulated elements was in most cases higher than in the experiments. Whilst the deviations were not so pronounced for the elements with structured edges the calculated coercivities of the standard elements were up to 2× as high as the switching field values of the experiments. When the simulations for the standard elements were run without vertical field the difference between experimental and modelled data got even worse (calculated  $H_c$  up to 3× as high compared with the experimental values). The majority of elements with structured edges however did not display such a pronounced dependence of the switching field on the vertical field. Exceptions were the elements with structure type A with long structure periods ( $p=0.67$  and  $2\mu\text{m}$ ) of the second and third patterns and the elements of structure type C with the smallest structure

period ( $p=0.2\mu\text{m}$ ) of the same patterns. For these elements the switching field rose considerably in the case of zero vertical field calculations.

Apart from that there was generally good agreement between experimental and calculated switching field values of the elements with structured edges of the second and third patterns. Especially the match of experimental and simulated data for elements with edge structure of the fourth and fifth patterns (nominally constant element width) was remarkably good.

**CHAPTER 8:****CO/CU MULTILAYERS – GIANT MAGNETO RESISTANCE (GMR)****8.1 INTRODUCTION**

This chapter deals with another group of magnetic materials with reduced dimensions which are multilayer systems of alternate layers of magnetic and non-magnetic materials with layer thicknesses in the nanometer range (section 1.6). One of the most striking properties of this new generation of artificial magnetic multilayer materials is the oscillatory indirect exchange coupling between two magnetic films separated by a thin non-magnetic spacer (Heinrich et al, 1994). For those thicknesses of spacer layer where the coupling is antiferromagnetic, the application of a magnetic field to such an artificial antiferromagnet can cause the system to undergo a metamagnetic transition. The associated drop in electrical resistivity  $\rho$  as the magnetic configuration changes from antiferromagnetic (AF) to ferromagnetic (FM) is termed the giant magnetoresistance – GMR (Grünberg et al, 1986), (Baibich et al, 1988), (Grünberg et al, 1991), (Dieny, 1994). As the thickness of individual layers in such samples is on the nanometer scale, the preparation techniques for such materials are exacting and few structural defects can be tolerated. In general it appears that the best quality structures are prepared under ultra-high vacuum (UHV) conditions, although there have been few attempts to quantify the effects of background gases on the GMR and coupling of such materials. There is broad agreement that H<sub>2</sub>O and O<sub>2</sub> are particularly damaging (Yoshizaki et al, 1994), (Kagawa et al, 1994) while other authors find a more complex behaviour, with the suggestion that certain low levels of O<sub>2</sub> can be beneficial, at least in spin-valve structures where the interlayer coupling is not necessary to observe GMR (Egelhoff et al, 1997).

The structure of this chapter is as follows: The effects of so-called gas-damage on the GMR performance of different multilayer systems are discussed in section 8.2 and the preparation of three Co/Cu multilayer samples with different degrees of gas-damage which were investigated in this work is described in section 8.3. Sections 8.4 and 8.5 are results sections: In the former GMR measurements and MOKE hysteresis loops are presented and the latter deals with several applied TEM investigation techniques. A summary is then given in section 8.6.

## 8.2 EFFECT OF GAS-DAMAGE ON GMR OF CO/CU MULTILAYERS

It is known that a high level of cleanliness is necessary for a high GMR in Co/Cu multilayers, as residual gases damage the film in such a way as to reduce the AF coupling (Marrows et al, 1997). Moreover, by selectively damaging only certain parts of the sample with gas, it was found that the part of the multilayer most susceptible to damage was the bulk of the Cu spacer. This was accomplished by pausing growth at certain points in the multilayer stack and allowing residual gases from the chamber to adsorb onto the film surface before growth was continued. Multilayers where the spacers were only lightly damaged may still show appreciable GMR, although the remanent moment may be considerable. The GMR ratio was always found to be higher than would be dictated by a simple series circuit of AF and FM coupled regions in the proportions stipulated by the remanent fraction. In fact the GMR ratio was found to have a parabolic dependence on the remanent fraction, suggesting the possibility of non-collinear arrangements of adjacent layer moments at zero field (Marrows et al, 1999 a). Such non-collinear arrangements of layer moments have been observed in a large number of layered magnetic systems and were explained by the introduction of a non-Heisenberg biquadratic (BQ) term into the indirect exchange energy. This needs to be compared with the alternative explanation of the non-zero remanence in poorly AF coupled multilayers, where ferromagnetic bridges or pinholes in the spacer layers are thought to lead to a ferromagnetically coupled volume fraction (Rupp et al, 1993). This would lead to a domain structure at zero field, containing regions with low total moment (AF-coupled) as well as areas with high total moment (FM-coupled).

Biquadratic interactions in multilayered systems continue to attract much experimental and theoretical attention. Almost all investigated coupled multilayer systems were found to exhibit some degree of biquadratic coupling. Recently studied examples include Fe/Cr (Heinrich et al, 1999), (Rezende et al, 1999), Co/Au (Duden et al, 1999), Co/Ir (Yanagihara et al, 1999) as well as systems with semiconducting (Fe/Si), (Endo et al, 1999) and insulating (e.g. Co/Al-O/NiFe), (Yu et al, 1999) spacer layers. Many more can be found in a recent review by Demokritov (Demokritov, 1998).

The aims of the work presented here were twofold: To determine unambiguously the zero field magnetisation configuration of a sample showing reduced GMR and to attempt to find evidence for the gas damage in the physical microstructure. To achieve these goals various modes of transmission electron microscopy (TEM) were employed to image both

the physical and magnetic microstructures of samples showing different interlayer coupling and consequently differing GMR ratios.

Sequences of samples were grown at the University of Leeds on both ordinary Si substrates and Si<sub>3</sub>N<sub>4</sub> window substrates which are suitable for plan-view TEM imaging (Khamsehpour, 1996). By application of different imaging modes it was possible to investigate the physical and magnetic microstructure of the samples grown on the Si<sub>3</sub>N<sub>4</sub> window substrates without any further preparation. As the base pressure of the growth chamber was raised a reduction in both GMR ratio and AF coupling could be observed. These may be linked to changes in the low-field reversal modes of the remanent moment which were investigated magnetometrically and by means of Lorentz microscopy. The layered structure of the sample was examined by cross-sectional transmission electron microscopy (XTEM) at the University of Oxford, imaging vertical slices of samples grown on Si.

### 8.3 PREPARATION OF SAMPLES WITH DIFFERENT DEGREES OF GAS-DAMAGE

Samples were deposited by dc magnetron sputtering in a custom built vacuum system at the University of Leeds. The system was equipped with six sputtering targets and had a base pressure of better than  $2 \times 10^{-8}$  Torr. This was achieved by a combination of cryopumping to  $\approx 1 \times 10^{-7}$  Torr, followed by the filling of a Meissner trap (Meissner, 1960). This is particularly effective in the pumping of water, the main residual gas after cryopumping. The residual gas composition was determined using a quadrupole mass spectrometer. Once the trap was filled the residual gas was mainly comprised of N<sub>2</sub> or CO (mass peak 28). In order to control accurately the level of background gas damaging the film O<sub>2</sub> was introduced through a fine leak valve. The working pressure of 99.9999% purity Ar was 3.0 mTorr, introduced through an ultrahigh vacuum compatible stainless steel line. Typical deposition rates were 2.6 Å/s for Co and 2.9 Å/s for Cu. A magnetic field of 200 Oe was applied in the substrate plane during growth of the whole multilayer stack by a permanent magnet array inside the chamber. To minimise uncontrolled changes in deposition conditions all samples discussed here were deposited in a single growth run.

All multilayers investigated in this work were nominally of the form {Co(8 Å)/Cu(8 Å)}<sub>25</sub>. The Cu thickness was selected to match the first AF coupling peak in the oscillation. No buffers or caps were used as those were found to be unnecessary for

good quality growth and sample longevity. Growth was paused for 10s in the middle of every Cu spacer to allow residual gases to sorb onto the surface.

Magneto-resistance was measured by the conventional four-probe dc technique and magnetisation loops were measured by the Magneto-optic Kerr Effect (MOKE, section 2.4). The field was always applied in the plane of the sample. Low angle x-ray scattering measurements were performed at station 2.3 at the SRS (Synchrotron Radiation Source) at Daresbury laboratory in order to determine the layer roughness and bilayer periodicity of the samples (Daresbury, 2000). All measurements were performed at room temperature.

The samples grown on the window substrates were investigated here at the University of Glasgow. The physical microstructure was studied using conventional (bright field) imaging and diffraction techniques. The magnetic microstructure was investigated using different modes of Lorentz microscopy (section 2.3.2; Chapman, 1984). Samples were also grown on pieces of (001) Si wafer with the native oxide layer left intact for magneto-resistance measurements and for cross-sectional TEM imaging. Meanwhile larger pieces of nitride coated Si wafer were used for GMR and MOKE experiments and some of the measurements were repeated on the membrane samples after completion of the TEM investigations. Sets of samples were mounted side by side on the substrate holders, so that the multilayers were grown simultaneously, allowing their properties to be directly compared.

#### 8.4 GMR MEASUREMENTS AND HYSTERESIS LOOPS

It was repeatedly found that the GMR ratio decreased as the base pressure was raised by the introduction of air or oxygen through the leak valve. For pressures below a transitional band a GMR ratio of  $\frac{\Delta\rho}{\rho_{sat}} \approx 40\%$  was commonly achieved. In the high pressure regime above the transition zone the GMR is very low. The transition region was quite broad ( $\approx 10^{-7}$ - $10^{-8}$ Torr) with a higher base pressure for air than for O<sub>2</sub> alone (Marrows et al, 2000). The saturated resistivities of all samples were comparable, falling in the range  $\rho_{sat} \approx (20 \pm 2) \mu\Omega\text{cm}$ . The changes in GMR were caused by a decrease in the amount of AF alignment in the samples with rise of pressure as borne out by an increase in remanent fraction as observed by MOKE. It was also found that pure oxygen was much

more damaging than air in this regard. This suggests that  $N_2$  is much more inert than  $O_2$  as might be expected.

In Figure 8.1 GMR loops measured at the University of Leeds are graphed for three samples, which were deposited on nitride coated Si wafer at different chamber background pressures. A drop in GMR ratio was observed as  $O_2$  was introduced into the chamber. These multilayers were comparable to similar samples grown directly onto the Si wafer as the nitride surface is similarly smooth.

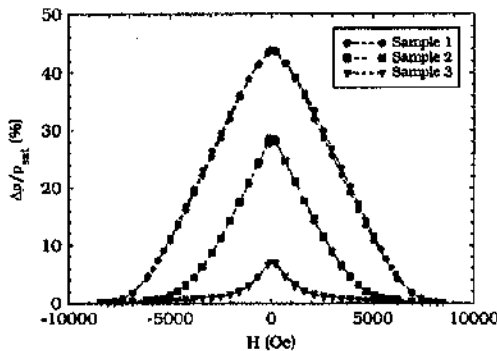


**Figure 8.1**

*Giant magnetoresistance loops for the (large) samples grown on  $Si_3N_4$  at three different base pressures,*

*Sample 1:  $1.8 \times 10^{-8}$  Torr (circles)*

*Sample 2:  $6.2 \times 10^{-7}$  Torr (squares)*

*Sample 3:  $0.9 \times 10^{-6}$  Torr (triangles).*

It should be noted that the shape of the loops is changing in Fig. 8.1. With the leak valve closed ( $1.8 \times 10^{-8}$  Torr) the GMR peak had a convex top close to the parabolic GMR response of an ideally AF coupled multilayer (sample 1). As the background pressure was increased to  $6.2 \times 10^{-7}$  Torr the field required to saturate the samples fell and the GMR peak became more pointed (sample 2). These effects were greater still as the pressure was finally raised to  $0.9 \times 10^{-6}$  Torr for sample 3. While the sample resistivities were all very similar in the magnetically saturated state with values of about  $20 \mu\Omega\text{cm}$  they were of course different at zero field due to the different magnetoresistance ratios. Such changes in GMR loop shape are known to be associated with biquadratic coupling (Kuo et al, 1999).

Grazing incidence specular x-ray scans were carried out with all three samples. It was found that the first order superlattice Bragg peaks were of similar intensity and full width half height maximum (FWHM). The Bragg peaks were not all at the same angle and represented bilayer periods of  $16.1 \text{ \AA}$ ,  $15.2 \text{ \AA}$  and  $16.4 \text{ \AA}$  in order of increasing background pressure (samples 1, 2 and 3). Therefore the sample to sample fluctuation was better than  $1 \text{ \AA}$  from the nominal period of  $16 \text{ \AA}$ . Another result of the x-ray investigation was that the roughness in the samples was low and of very similar amplitude. The rms roughness of all

the layers in the samples was determined to be  $\approx 5.5 \text{ \AA}$ . Simulations were carried out with the result that the fluctuations in the Co layer thickness from sample to sample were much greater than those in the Cu spacer layer. It follows that the changes seen in the GMR in Fig. 8.1 cannot be explained by incorrect spacer thickness - a result corroborated by the fact that the AF coupling peak width and position are not affected by this type of residual gas damage (Marrows et al, 1999 a). Another result from the x-ray measurements was that the conformal roughness on the Co/Cu interfaces was  $\approx 2.5 \text{ \AA}$  for all three samples. For further details about the x-ray measurements and simulations see Marrows et al, 2000.

The changes in GMR amplitude despite the absence of difference in the saturated resistivity is suggestive of a reduction in AF-coupling. This would not affect the saturated resistivity, as the samples are in the same magnetic state with all layer moments aligned parallel to the field. On the other hand the resistivity enhancement at zero field will be much smaller than anticipated if the degree of antiparallel alignment is not high. This is borne out by MOKE loops (measured at the University of Leeds) for the samples, shown in Fig. 8.2. It was possible to explicitly link the drop in magnetoresistance with the rise in remanent fraction (Marrows et al, 1999 a). Two loops are shown together for each sample, one measured with the field applied along the growth field direction and the other perpendicular to it. It can be seen that the shapes of the loops are isotropic in field direction. This is not surprising as any anisotropy induced in Co by the growth field is generally found to be weak (Slonczewsky, 1963), whilst the field required to overcome the coupling is much larger, of the order of a few kOe. However in the low field MOKE loops presented in Fig. 8.3 it is obvious that some anisotropy was present as the remanent moment reversed. For convenience the direction parallel to the growth field will be referred to as the easy axis and the orthogonal direction is termed the hard axis. Although the degree of anisotropy varies from sample to sample, the "easiest" direction was always defined by the growth field. In Figure 8.3(a) both the easy and hard axis loops for sample 1 show considerable rounding. Both loops were somewhat canted and looked very much alike. Therefore the overall behaviour appears almost isotropic with the coercivity being 27 Oe for both axes.

Meanwhile Figs. 8.3(b) and 8.3(c) were quite similar, with a squarer easy axis loop and a canted loop with lower remanent moment for hard axis reversal. The coercive fields were 38 Oe (easy axis) and 35 Oe (hard axis) for sample 2 and 31 Oe (easy axis) and

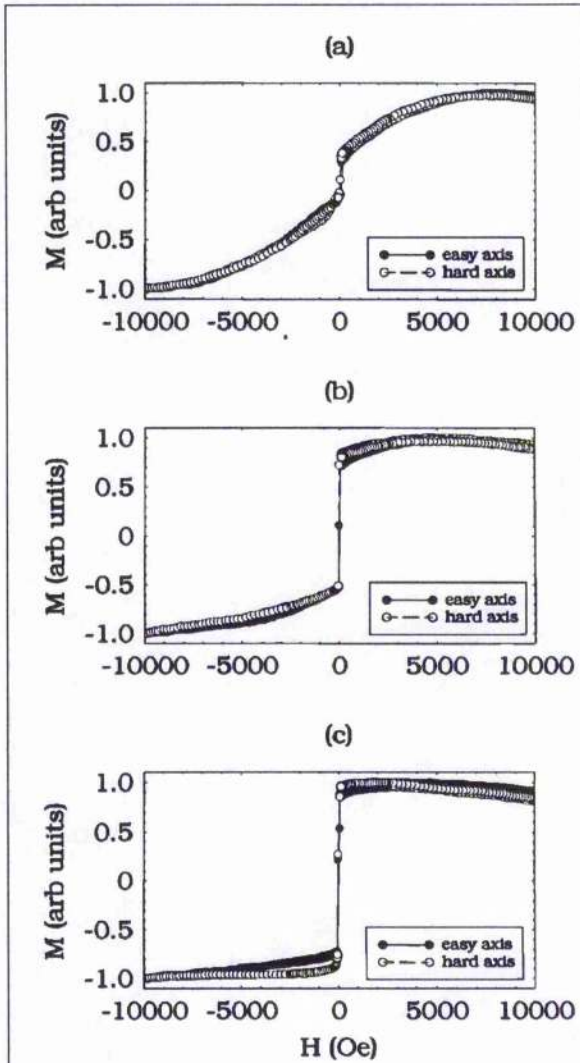


**Figure 8.2**

High field MOKE loops of the large samples grown on  $\text{Si}_3\text{N}_4$  - the remanent moment rises as the GMR falls. Easy axis corresponds to the direction of the growth field and hard axis is perpendicular to it.

(a) Sample 1, (b) sample 2, (c) sample 3.

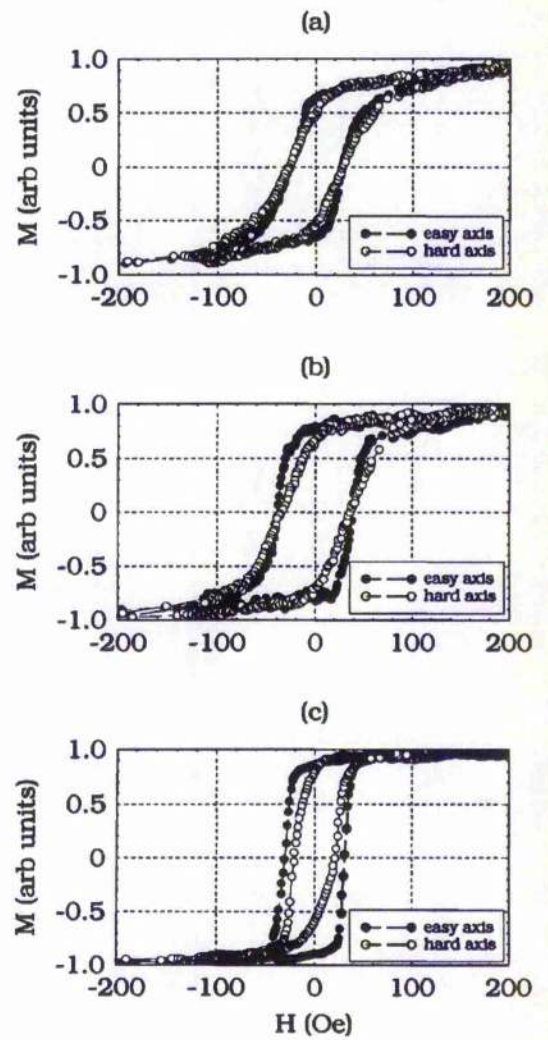


**Figure 8.3**

Corresponding low field MOKE loops of Fig. 8.2.

(a) Sample 1, (b) sample 2, (c) sample 3.

20 Oe (hard axis) for the slightly more anisotropic sample 3. At first it is tempting to link the degree of induced anisotropy in the films with the exposure to oxygen and there have been attempts to do this in the past (Cohen et al, 1960). More recently it was found that the correlation is between the degree of anisotropy and the remanent moment (Marrows et al, 1999 b). For example, samples grown with 15 Å Cu spacers, corresponding to the

second FM peak, were always highly anisotropic in their reversal mechanism, regardless of the degree of exposure to O<sub>2</sub> or any other background gas. For samples with a very low remanence due to excellent AF coupling the anisotropy at low fields can be very small.

## 8.5 TEM INVESTIGATIONS

The samples grown on the Si<sub>3</sub>N<sub>4</sub> window substrates were investigated here at the University of Glasgow in microscopes highly modified to optimise magnetic imaging conditions. The physical microstructure was studied by means of conventional (bright field) imaging and diffraction techniques using a microscope based on a JEOL 2000 FX. The magnetic microstructure of the samples in the as-grown and ac-demagnetised states was imaged in the Foucault mode of Lorentz microscopy (section 2.3.2) also in the JEOL 2000 FX microscope. In-situ magnetising experiments were then carried out in a modified Philips CM20 FEG microscope by tilting the sample in a weak vertical field ( $H_{obj} \approx 90$  Oe) of the objective lens (section 2.2.5). The magnetising experiments were monitored using the Fresnel mode of Lorentz microscopy (section 2.3.2).

### 8.5.1 PHYSICAL MICROSTRUCTURE

As the plan-view bright field images of all investigated samples were indistinguishable only one example is shown in Fig. 8.4(a). The samples were of micro-polycrystalline structure with an average grain size in the range of 15-20nm with no texture present as can be seen in the diffraction pattern of the tilted sample (Fig. 8.4(b)). The majority of the crystallites had fcc structure, but there was evidence for a fraction of hcp crystallites in the diffraction patterns.

It should be noted, that different means have been applied in order to determine any differences in the physical microstructure between clean (AF-coupled) and heavily gas-damaged (almost entirely FM-coupled) samples. Techniques used include synchrotron x-ray analysis, <sup>59</sup>Co nuclear magnetic resonance (Marrows et al, 1997) and high resolution cross sectional (X)TEM (Marrows et al, 2000). All findings were consistent with those described here except for the XTEM investigations where 'very subtle' differences were found. It should be noted though 'that it would prove impossible to infer the level of background gas that the sample had been exposed to only from XTEM images of this sort' (Marrows et al, 2000).

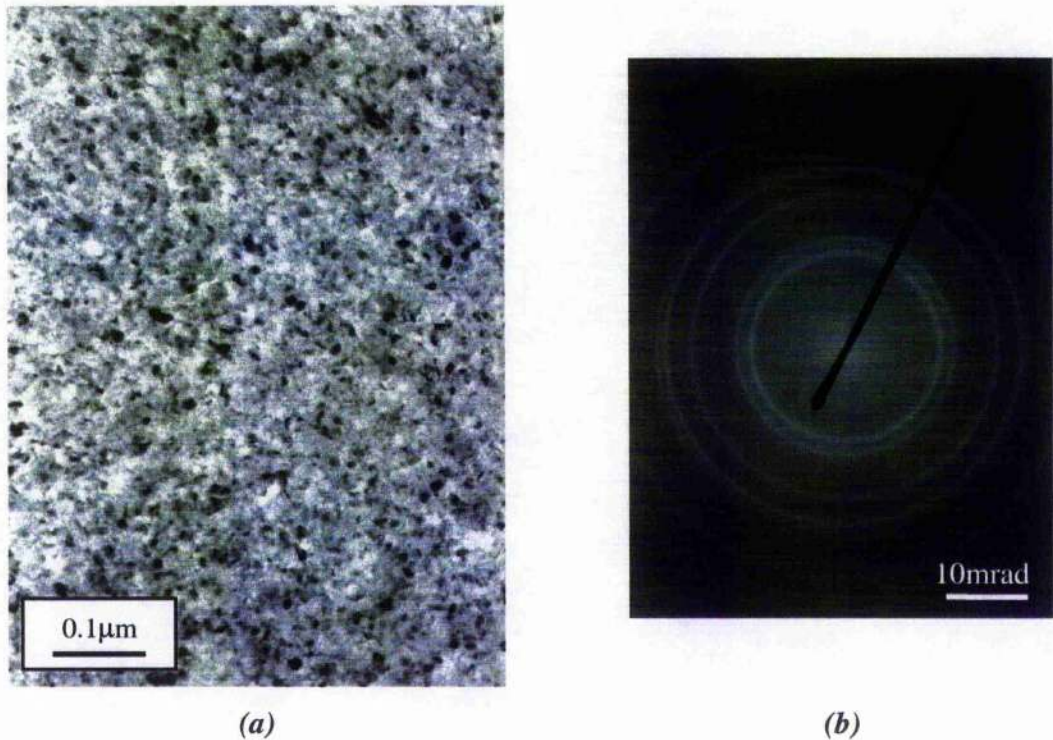


**Figure 8.4**

*Bright field image (a) and diffraction pattern (b) of sample 2. Sample was tilted 30° when the diffraction pattern was imaged.*

### 8.5.2 MAGNETIC MICROSTRUCTURE – AS-GROWN AND AC-DEMAGNETISED STATE

The magnetic microstructure of the Co/Cu multilayers was investigated in their as-grown state before their ac-demagnetised state was studied. In the case of samples 2 and 3 no differences were detected between the as-grown and ac-demagnetised states of the samples and they also looked very much alike. A pair of Foucault images of the ac-demagnetised sample 3 is shown in Figs. 8.5(a) and (b). The sample appeared single domain in the field of view with only magnetic dispersion (ripple) being visible. The entire  $\text{Si}_3\text{N}_4$  window ( $100 \times 100 \mu\text{m}^2$ ) was checked and no domain walls were observed. With such a large area being single domain for samples 2 and 3 in the as-grown and ac-demagnetised states it seems very likely that both samples were single domain.

While the magnetic microstructure of sample 1 (cleanest) in its as-grown state looked also very similar to the other two samples the situation had changed after ac-demagnetisation. The micromagnetic configuration of this state is shown in Figs. 8.5(c) and (d) and domains are easily visible in Fig. 8.5(c). There is directionality of the domains

discernible which was  $\approx$ parallel to the mapping direction in Fig. 8.5(c). The domains were small with the largest domain size lying in the range of  $10 \times 3 \mu\text{m}^2$ .

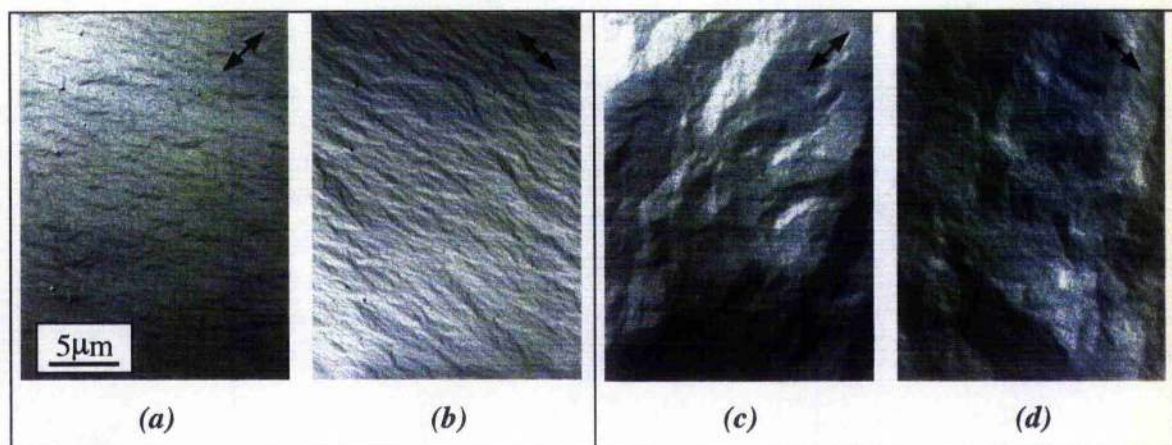


**Figure 8.5**

*Pairs of Foucault images of ac-demagnetised Co/Cu multilayer samples.*

*(a), (b) Sample 3; (c), (d) sample 1. Double arrows indicate mapping directions.*

### 8.5.3 MAGNETISING EXPERIMENTS

As with the small magnetic elements the magnetising experiments were carried out in the modified Philips CM20 FEG TEM (section 2.2). The highest possible field ( $H \approx 6 \times 10^3$  Oe) was applied to the samples first before the objective lens field was reduced to the value suitable for the investigation of the samples ( $H_{obj} \approx 90$  Oe). This small field value was appropriate as the most interesting parts of the hysteresis loops were the low field regions (Fig. 8.3). Therefore the samples were only subjected to a very small vertical field while imaging the magnetising sequences. Taking also into account that the Co/Cu multilayers were continuous film samples, the demagnetising effects due to the vertical field component were expected to be negligible. No observations were made which contradicted this assumption (e.g. no wall movement was observed which was triggered by shifting the samples when the objective lens field was applied).

The Fresnel mode was chosen to monitor the micromagnetic changes in the samples as it is better suited for dynamic observations than Foucault mode or DPC. As mentioned earlier domain wall locations appear as black and white lines (wall contrast) in Fresnel images (sections 2.3.2 and 8.5.3.1; Chapman, 1984). In polycrystalline continuous films the magnetic dispersion gives also rise to ripple contrast which appears within domains as

fine black and white lines running perpendicular to the mean direction of magnetisation (Fuller et al, 1960), (Hoffmann, 1968), (Hubert et al, 1998).

A second series of magnetising experiments was carried out with the same samples and the dependence of the micromagnetic changes on the applied field was investigated using the low angle diffraction (LAD) mode (sections 2.3.2 and 8.5.3.2; Chapman, 1984). LAD is very well suited to obtain quantitative results of magnetising experiments as extremely high camera lengths enable the experimenter to determine the Lorentz deflection angle  $\beta_L$  and then calculate the net induction of the sample  $\vec{B}_{net}$  at different stages of the magnetising experiments. Further elaboration even allows conclusions to be made about the magnetic coupling in the multilayer stack as will be shown later (section 8.5.3.2).

### 8.5.3.1 FRESNEL MODE

In order to gain a more detailed insight into the reversal mechanisms of the samples, magnetising experiments were carried out in which the magnetic microstructure was monitored firstly using the Fresnel mode of Lorentz microscopy. For all investigated samples it was found that the magnetisation reversal processes were dependent on the direction of the in-plane component of the applied field. By applying a field in-situ with the specimen in different orientations the hard axis was identified for all samples. Application of a field in this direction led to the formation of low angle walls which were  $\approx$ orthogonal to the in-plane field direction. Under the influence of reverse fields the magnetisation within the domains was found to rotate. Wall movement was present in all investigated samples and a very common feature was the formation of  $360^\circ$  walls. Furthermore it should be noted that the observed walls were generally not straight. Sequences of Fresnel images recorded during magnetising cycles are presented for all three samples in both axes. Although the directions, which were called hard and easy axes in the discussion of the MOKE loops, the observed reversal processes were different from those known from a simple ferromagnetic film. Therefore these directions are called hard- and easy-axis-like directions in the following discussion. For easier orientation in the sequences of Fresnel images the images taken at remanence are marked by a green frame. Red frames mark images recorded during time dependent processes. The exposure time was 2s for all presented Fresnel images. As the micromagnetic reversal behaviour differed

most markedly for the hard- and easy-axis-like directions of sample 3 and even showed certain similarities with the reversal processes of a ferromagnetic single layer sample 3 is discussed first.

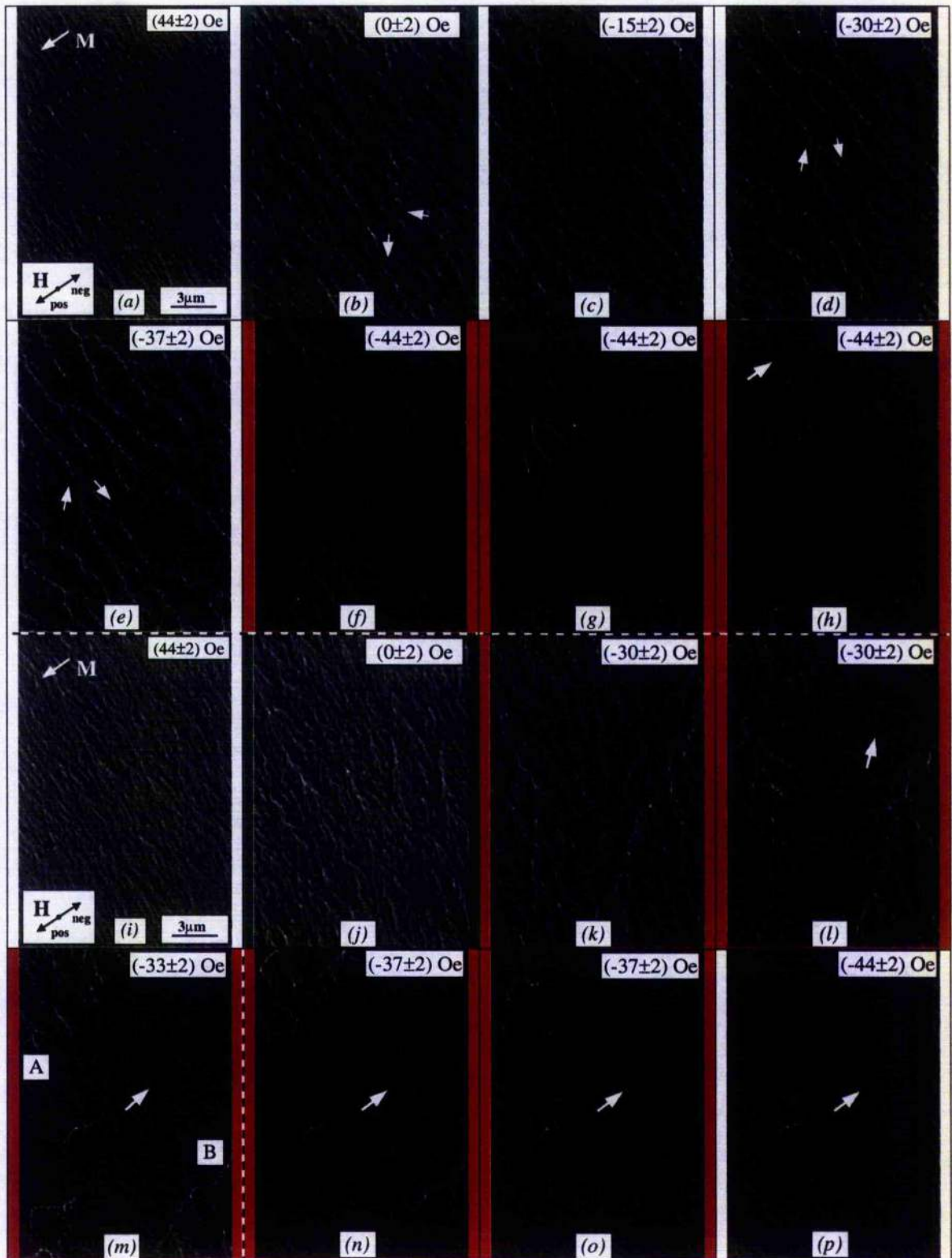
### Sample 3

Figure 8.6 shows sequences of Fresnel images of the micromagnetic states of the 'dirtiest' sample 3 during a magnetising experiment in the hard-axis-like direction (Figs. 8.6(a)-(h)) and in the easy-axis-like direction (Figs. 8.6(i)-(p)). After application of the highest possible field ( $H \approx 6 \times 10^3$  Oe) the objective lens field was reduced and the sample tilt in Fig. 8.6(a) resulted in an in-plane field component of  $(44 \pm 2)$  Oe. The field direction is indicated by the double arrow and only ripple-like contrast was visible in the image. The corresponding mean direction of magnetisation is indicated by the white arrow.

At remanence (Fig. 8.6(b)) low angle walls were clearly visible. The walls were not straight and displayed a strong directionality ( $\approx$ perpendicular to the applied field direction). The resulting domains were very narrow and with the ripple-like contrast within these domains it was possible to deduce the mean direction of magnetisation within some of the broader ones. This is again indicated by white arrows in the image.

Application of a reverse field led to an increase of wall contrast as a result of magnetisation rotation within adjacent domains (Fig. 8.6(c)) and further increase of the field resulted in further magnetisation rotation and wall movement (Fig. 8.6(d)). It should be noted that the fine structure within the bigger domains at that point can hardly be described as ripple-like any longer. Whilst the mean direction of magnetisation of some domains is illustrated by white arrows, the magnetic contrast in the domains appeared more like low angle walls than magnetisation ripple. When the reverse field was increased further (Fig. 8.6(e)) the magnetisation rotation was found to progress together with notable growth of some domains.

When a field of  $(-44 \pm 2)$  Oe was applied to the sample in the hard-axis-like direction, a time dependent process was triggered (Figs. 8.6(f)-(h)). The long domains were broken up and successively annihilated until the sample was almost uniformly magnetised with ripple-like contrast present and small areas surrounded by remaining  $360^\circ$  walls. The time scale for the changes was  $\geq 15$  seconds.



**Figure 8.6**

*Fresnel sequences of magnetisation reversal of sample 3 ('dirtiest' sample, base pressure  $0.9 \times 10^{-6}$  Torr). White arrows indicate magnetisation direction.*

*(a)-(h) Hard-axis-like transition; (i)-(p) easy-axis-like transition.*

These observations tie in quite well with the hysteresis loop for the hard axis in Fig. 8.3(c). The magnetic moment at remanence was notably reduced in the magnetising experiment as the sample was no longer single domain but instead split up in fine domains. Further gradual reduction of the magnetic moment of the sample under the influence of increasing reverse fields in the hysteresis loop also agreed well with the observed micromagnetic behaviour (magnetisation rotation and some degree of wall movement) as did the field range necessary to  $\approx$ saturate the sample (i.e. 40-50 Oe). There was however no indication for the time dependent behaviour of the magnetisation distribution, which was observed in the TEM experiment at  $(-44 \pm 2)$  Oe to be deduced from the MOKE loop. Furthermore it was difficult to determine the coercive field value exactly from the Fresnel images. It appears to be  $\approx 30$  Oe from the Fresnel experiment instead of 20 Oe determined by the MOKE loop.

Extracts of the reversal process of the sample with the field in the orthogonal direction (easy-axis-like direction) are shown in Figs. 8.6(i)-(p). Most notable is that time dependent variations of the magnetic microstructure were observed at three reverse field values (Figs. 8.6(k)-(o)).

When the field was reduced to  $(44 \pm 2)$  Oe after the maximum possible field was applied to the sample, magnetic dispersion was present and the clear directionality of the magnetisation ripple again indicated that the mean direction of magnetisation (illustrated by white arrow) was parallel to the field direction. At remanence (Fig. 8.6(j)) the ripple-like contrast was increased compared to that in Fig. 8.6(i). The mean direction of magnetisation was still pointing along the saturation field direction. Field reversal led first to further increase of dispersion followed by the development of low angle walls. At higher fields rotation of the magnetisation in adjacent domains was indicated by an increase in wall contrast. However, significant reversal of magnetisation did not occur until a field of  $(-30 \pm 2)$  Oe. At this field value a time dependent evolution (time scale  $\geq 15$  seconds) of the magnetic microstructure was observed and two stages are shown in Figs. 8.6(k) and (l). A large domain was generated in the field of view with the walls running almost perpendicularly to the walls developed at lower fields. At a slightly increased reverse field a second time dependent variation (duration  $\geq 10$  seconds) of the magnetic microstructure was observed resulting in growth of the previously generated domains. Areas with this previous domain configuration still present are clearly visible in the image of the final state of this process (top left and bottom right corners of

Fig. 8.6(m)). It should be noted that the new domain walls (A and B) were again very irregular but that the degree of dispersion within the reversed region was quite similar to that observed over the whole field of view at remanence. Hence the mean direction of magnetisation could again be deduced and is indicated by a white arrow. Figs. 8.6(n) and (o) show stages of the third and last time dependent process (time scale  $\geq 10$  seconds) with further reduction of the areas with the highly complex 'older' domain configuration. In the last image (Fig. 8.6(p) which was taken at a field of  $(-44 \pm 2)$  Oe the contrast observed was almost exclusively magnetic dispersion with the mean direction of magnetisation being nearly perfectly aligned with the applied field. Therefore the observed behaviour was consistent with the (squarish) low field MOKE loop of the easy axis magnetisation reversal in Fig. 8.3(c) and the coercive values from both experiments agree well (MOKE: 31 Oe, Fresnel: 30/33 Oe).

### Sample 2

Different stages of the magnetisation reversal processes in the hard-axis-like and easy-axis-like directions of the 'intermediate' sample 2 are shown in Fig. 8.7. As in the case of sample 3 (Fig. 8.6) magnetic dispersion was present after the applied field was reduced (Figs. 8.7(a), (i)) with the mean direction of magnetisation still being aligned with the applied field.

In the case of hard-axis-like reversal the dispersion contrast was increased at remanence and low angle walls became visible which were running  $\approx$ perpendicular to the original field direction (Fig. 8.7(b)).

For reverse fields the wall angle increased with increasing field and wall movement was also observed (Figs. 8.7(c)-(f)). The situation then changed at a field value of  $(-58 \pm 2)$  Oe when the wall contrast and therefore the wall angle decreased (Fig. 8.7(g)). This means that at this stage the magnetisation in adjacent domains started to align. The last image of this sequence (Fig. 8.7(h) shows the magnetic microstructure of the sample at the same field value as in the previous Fig. 8.7(g) but after a slightly higher field had been applied to the sample. The contrast of the remaining walls was further reduced and the overall micromagnetic configuration was highly erratic. It should be noted that the contrast in the images of Fig. 8.7 is generally lower compared to Fig. 8.6. As the imaging conditions and contrast limits were exactly the same, this is an indication that the degree of antiferromagnetic alignment was higher in sample 2 than in the dirtier sample 3.

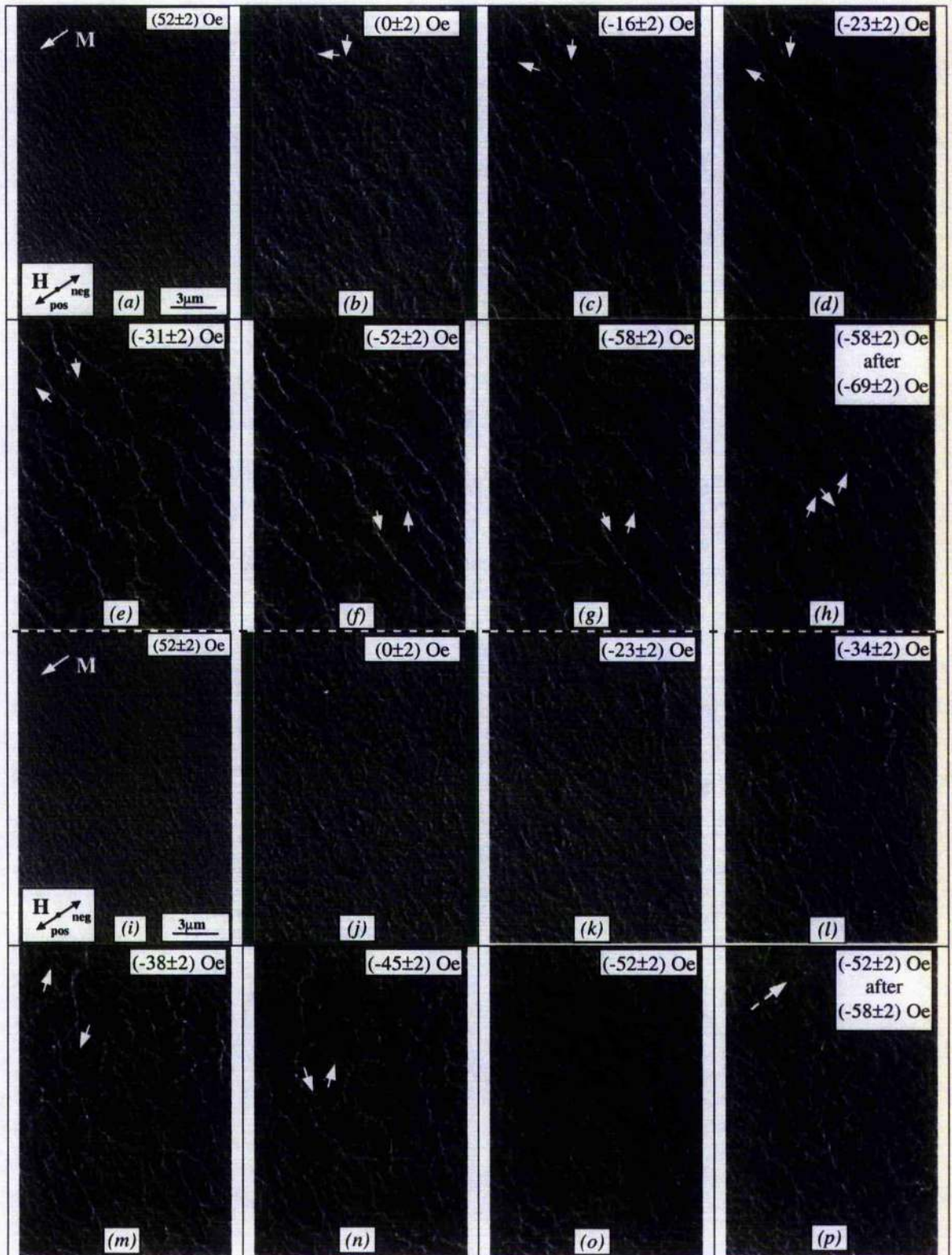


**Figure 8.7**

*Fresnel sequences of magnetisation reversal of sample 2 ('intermediate' sample, base pressure  $0.9 \times 10^{-6}$  Torr). White arrows indicate magnetisation direction.*

*(a)-(h) Hard-axis-like transition; (i)-(p) easy-axis-like transition.*

The reason for this assumption is that the overall Lorentz deflection of the electron beam after passing through the stack of exchange coupled layers is lower in the case of sample 2 and therefore results in reduced magnetic contrast (section 2.3.1).

The main characteristics of the corresponding hard axis hysteresis loop in Fig. 8.3(b) match again very well with the above described observations (i.e. reduced remanent moment, gradual change of magnetisation direction and wider hysteresis loop compared to sample 3). The determination of  $H_c$  from the Fresnel sequence is very uncertain due to the low dispersion contrast within the domains.  $H_c$  lies in the range  $-30/-50$  Oe in the Fresnel experiment and it was 35 Oe in the MOKE measurements.

Figs. 8.7(i)-(p) show a compilation of stages of the magnetic microstructure of sample 2 during easy-axis-like reversal (i.e. field direction orthogonal to the hard-axis-like direction). It should be noted that without prior determination of the hard-axis-like direction no observations were made neither in this direction nor close to it which were consistent with common easy axis reversal mechanisms. A look at the corresponding hysteresis loop in Fig. 8.3(b) explains this problem where the changes in magnetisation were also more gradual compared to Fig. 8.3(c).

When a field of  $(52 \pm 2)$  Oe was applied to the sample after application of the largest possible field magnetic dispersion was again visible with the mean direction of magnetisation being aligned with the field (Fig. 8.7(i)). At remanence (Fig. 8.7(j)) the degree of dispersion was increased and the dispersion was clearly less directional than in Figs. 8.7(i) and 8.7(b). When reverse fields were applied to the sample, the magnetic contrast was found to increase prior to the formation of highly irregular domain configurations (Figs. 8.7(k)-(n)). Increase of the reverse field to a value of  $(-52 \pm 2)$  Oe led to a notable reduction of wall contrast indicating further magnetisation rotation in adjacent domains leading to a higher degree of alignment of magnetisation (Fig. 8.7(o)). This evolution continued when a higher field of  $(-58 \pm 2)$  Oe was applied to the sample prior to subsequent reduction of the reverse field (Fig. 8.7(p)). The magnetic microstructure of the sample at this stage was still highly irregular however with an increased degree of directionality, which is indicated by the dashed arrow in Fig. 8.7(p). Therefore the micromagnetic behaviour of the sample in the Fresnel experiment agrees well with the corresponding hysteresis loop in Fig. 8.3(b) (i.e. gradual change of magnetisation) however the coercivity could only be determined in the range  $-40/-45$  Oe compared to 38 Oe in the MOKE measurement.

### Sample 1

Figure 8.8 shows an overview of Fresnel images taken during magnetising sequences with the cleanest sample 1. Figs. 8.8(a)-(h) show examples of the hard-axis-like reversal and the behaviour in the easy-axis-like direction is illustrated in Figs. 8.8(i)-(p). The most notable observation was further reduction of magnetic contrast compared with samples 2 and 3. This again corresponded well with the higher GMR of the sample and the expected higher degree of AF alignment. When the applied field was reduced in the hard-axis-like direction from the maximum possible value to  $(44\pm 2)$  Oe magnetic dispersion was visible with clear directionality and the mean direction of magnetisation could easily be deduced (Fig. 8.8(a)). At remanence low angle walls running  $\approx$ perpendicular to the original field direction were again visible despite being quite faint (Fig. 8.8(b)). The contrast of the walls increased and fine structure became visible when reverse fields were applied (Figs. 8.8(c) and (d)). Wall movement and further magnetisation rotation were apparent at later stages of the magnetisation reversal process (Figs. 8.8(e)-(h)). Despite the sample being almost uniformly magnetised parallel to the applied field at  $(-54\pm 2)$  Oe a considerable number of  $360^\circ$  walls were still present (Fig. 8.8(h)). This observed magnetisation reversal behaviour again tied in nicely with the measured hard axis hysteresis loop of the sample (Fig. 8.3(a)). Reduction of the magnetic moment at remanence was corroborated as was the successive gradual further reduction of the magnetisation dispersion under the influence of reverse fields. The  $H_c$  values also agree reasonably: The coercivity was 27 Oe in the MOKE loop and it was  $\approx 23$  Oe in the Fresnel series.

A compilation of Fresnel images of the reversal process of sample 1 in the direction orthogonal to the hard-axis-like direction is given in Figs. 8.8(i)-(p). Whilst termed the easy-axis-like direction the observed reversal behaviour indicated that this direction might slightly be off the 'real' easy-axis-like direction as a notable degree of magnetisation rotation was present in Figs. 8.8(i)-(k).

Fig. 8.8(i) displays the magnetic microstructure after reduction of the applied field from the maximum possible value to  $(44\pm 2)$  Oe where magnetic dispersion with clear directionality was visible and the associated mean direction of magnetisation is indicated by the white arrow. Reduction of the field to  $(0\pm 2)$  Oe led to an increase of magnetic contrast and some degree of magnetisation rotation (Fig. 8.8(j)). Faint low angle walls were present at  $(-23\pm 2)$  Oe with the walls clearly showing directionality and further rotation of the mean direction of magnetisation (Fig. 8.8(k)).

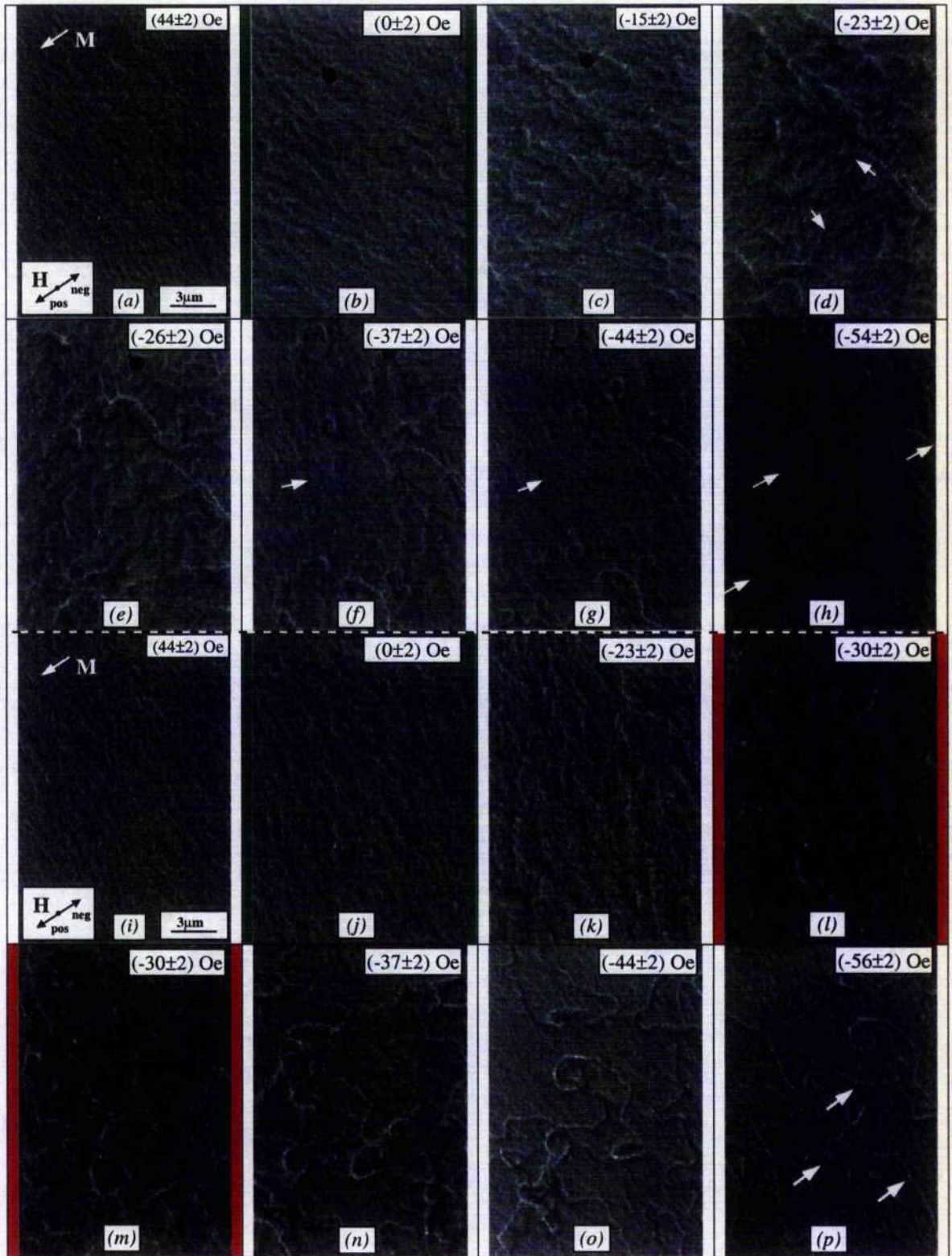


**Figure 8.8**

*Fresnel sequences of magnetisation reversal of sample 1 ('cleanest' sample, base pressure  $0.9 \times 10^{-6}$  Torr). White arrows indicate magnetisation direction.*

*(a)-(h) Hard-axis-like transition; (i)-(p) easy-axis-like transition.*

Under the influence of a higher reverse field directionality was no longer existent and the angle of the walls increased considerably. Furthermore there was a time dependent behaviour observed for  $(-30 \pm 2)$  Oe (Figs. 8.8(l), (m), duration  $\geq 20$  seconds) with wall movement and annihilation progressing without any change in the applied field. When the reverse field was increased further magnetisation rotation was observed within adjacent domains together with wall movement and annihilation (Figs. 8.8(n)-(p)). However at  $(-56 \pm 2)$  Oe there were still a considerable number of  $360^\circ$  walls present whilst the sample was almost uniformly magnetised parallel to the applied field (Fig. 8.8(p)). Despite the earlier mentioned uncertainty in the orientation of the sample (i.e. probably slightly off the easy-axis-like direction) there were no obvious contradictions between the observed behaviour in the Fresnel images and the easy axis hysteresis loop of Fig. 8.3(a). The coercivities agreed quite well with  $H_c(\text{MOKE}) \approx 27$  Oe and  $H_c(\text{Fresnel}) \approx 30$  Oe which might be mainly due to the almost isotropic behaviour of this sample in the MOKE experiment.

Summarising the Fresnel investigations it can be said that the low field reversal mechanisms revealed some anisotropy in all three samples as borne out by the low field MOKE. In all three cases the easy axis was defined by the growth field direction in the sputter chamber. However the degree of anisotropy seemed to be related to the quality of the AF coupling with good AF samples showing a more isotropic response to the applied field. In the Fresnel experiments it was not possible to find an obvious easy axis with a notably sharp switch of magnetisation in samples 1 and 2. The explanation of the existence of a pronounced anisotropy for a sample with a large remanent moment is unclear at this stage. It was possible to identify the switching behaviour observed in the TEM with the coercive fields measured from the low field MOKE in Figure 8.3. The highest degree of uncertainty resulted for sample 2 as there was no sharp switch of magnetisation or time dependent behaviour observed in the easy-axis-like direction. Furthermore the determination of  $180^\circ$  walls from the fine structure within domains generated in the hard-axis-like reversal was generally not very precise.

Another interesting feature of these experiments was that samples 2 and 3 seemed more similar in the low field MOKE, whilst in the Fresnel sequences samples 1 and 2 were more alike. It should be noted however that the samples all exhibit a continuous rise in GMR, AF alignment and isotropy of reversal with falling base pressure during

deposition. Sample 2 simply appeared more like 1 or 3 depending on the measurement technique used.

The differences in magnetic contrast for the different samples were consistent with their GMR values as good AF alignment resulted in high GMR and low magnetic contrast. Perfect AF alignment in alternate layers would result in negligible overall Lorentz-deflection of the electron beam while passing through the layer stack. Therefore the high contrast of sample 3 was in agreement with the low GMR of this sample ( $\approx 7\%$ ) whereas the much lower contrast of sample 1 was consistent with better antiferromagnetic alignment and therefore higher GMR ( $\approx 44\%$ ).

A very important result of the Fresnel investigations was that all films looked homogeneous in terms of magnetic contrast over the entire field of view ( $100 \times 100 \mu\text{m}^2$ ) during all stages of magnetisation reversal. This means that no indication was found for alternate regions with AF and FM coupling. Except for the change of overall magnetic contrast from one multilayer sample to another, there was no indication of the variation of exchange coupling in the different films and there is no option in Fresnel mode to get further or even quantitative information about the magnetic coupling in the three considered film systems. Much better suited from this point of view are LAD experiments which are discussed in the next section.

### 8.5.3.2 LOW ANGLE DIFFRACTION

#### **Preliminary considerations:**

Whilst the principles of low angle diffraction (LAD) were introduced in section 2.3.2 an overview is given in this section of the correlation between different exchange coupling models and the expected LAD patterns for easy- and hard-axis-like reversal prior to the presentation of recorded LAD patterns. The magnetising experiments were again carried out in the modified Philips CM20 FEG microscope.

Fig. 8.9 shows an overview of schematics for antiferromagnetic (AF, Fig. 8.9(a)), ferromagnetic (FM, Fig. 8.9(b)) and biquadratic (BQ, Fig. 8.9(c)) exchange coupling of two magnetic layers. Whilst in the case of AF coupling the resulting net induction is zero as both moments cancel out, there is a finite net resultant of induction in both other cases which is illustrated by red arrows in Figs. 8.9(b), (c). It should be noted that BQ coupling

does not mean an exact coupling angle of  $90^\circ$ , but the entire range between perfect AF ( $180^\circ$ ) and FM ( $0^\circ$ ) coupling.

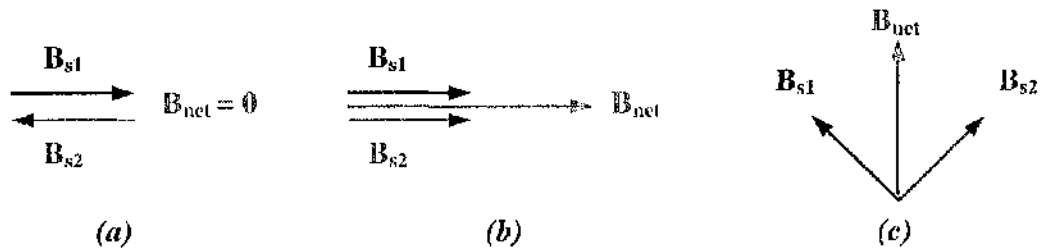


**Figure 8.9**

*Different kinds of exchange coupling of two successive Co-layers in Co/Cu multilayer systems. (a) Antiferromagnetic (AF), (b) ferromagnetic (FM), (c) biquadratic (BQ).*

It is this net resultant and its variation during magnetisation reversal processes which gives rise to changes of the Lorentz deflection  $\beta_L$  and this is ‘imaged’ in LAD. Tables 8.1 (‘easy axis’) and 8.2 (‘hard axis’) show overviews of models of the alignment of the magnetic induction in two successive cobalt-layers for different coupling mechanisms (AF, FM, BQ) at positive saturation, at remanence and at negative saturation together with the corresponding LAD patterns. The starting condition for each considered bilayer system is saturation in positive x-direction. The resulting LAD pattern is a focused spot which is deflected according to the Lorentz force.

In the case of easy-axis-like reversal AF coupled layers will ‘relax’ in their preferred AF state. The corresponding LAD image is a focused spot with zero deflection (Table 8.1(b)). When the sample is saturated in negative x-direction the electron beam is deflected in negative y-direction (solid circle, Table 8.1(c)). The situation for a FM coupled bilayer system is illustrated next. At remanence the magnetic moment of the sample has not changed compared to the saturated state. Therefore the expected LAD patterns are identical (Table 8.1(d), (e)). When the sample is saturated in negative x-direction the beam is deflected in negative y-direction (solid circle, Table 8.1(f)). BQ coupling which can be regarded as an intermediate state between AF and FM coupling is expected to result in a reduced net induction at remanence as the saturation inductions in two successive layers both possess reduced components of induction in positive x-direction (Table 8.1(h)). The net induction is therefore reduced compared to the FM case (Table 8.1(e)) and consequently the Lorentz deflection is also smaller.

'e.a.'	Saturation (pos)		Remanence		Saturation (neg)	
	alignment	→ LAD	alignment	→ LAD	alignment	→ LAD
AF	(a) 		(b) 		(c) 	
FM	(d) 		(e) 		(f) 	
BQ	(g) 		(h) 		(i) 	

**Table 8.1**

Overview of alignment of magnetic induction in bilayer systems with corresponding LAD patterns for different kinds of coupling (antiferromagnetic, ferromagnetic, biquadratic) in different external fields in easy axis.

▲▲ Saturation induction in single magnetic layers, ↑ net resultant of magnetic induction, ◦ corresponding LAD patterns (spots), × position for zero deflection, ◌ former spot location.

'h.a.'	Saturation (pos)		Remanence		Saturation (neg)	
	alignment	→ LAD	alignment	→ LAD	alignment	→ LAD
AF	(a) 		(b) 		(c) 	
FM	(d) 		(e) 		(f) 	
BQ	(g) 		(h) 		(i) 	

**Table 8.2**

As table 8.2 but for field applied in hard axis of AF, FM and BQ coupled samples.

In its saturated state the magnetic alignment in the sample and the corresponding LAD pattern are identical with the AF and FM cases (solid circles, Table 8.1(c), (f), (i)).

As far as the transition states of the magnetisation reversal of the considered bilayer systems are concerned it is not at all clear how the antiparallel alignment at remanence in the AF layers will form (i.e. gradual or sudden switch). The loci of the spots in positive saturation and at remanence are illustrated by open circles in the LAD pattern for negative saturation (Table 8.1(c)). Whether the intermediate states will all lie on a straight line or whether there will be some kind of spatial dispersion needs to be investigated.

The situation is much more comprehensible in the FM case. At the coercive field value there is a sharp switch of magnetisation expected which results in a 'jump' of the LAD spot from  $\beta_{L(sat)}$  to  $-\beta_{L(sat)}$ . Both positions are illustrated in the LAD schematic for negative saturation (Table 8.1(f)).

The expected transition states in the case of easy axis reversal of a BQ coupled bilayer system are also quite straight forward: After a notable reduction of the net resultant of induction due to biquadratic alignment of the saturation inductions in successive layers,  $\beta_L$  is reduced accordingly. Therefore the width of the anticipated 'jump' is also expected to be reduced compared to the FM coupling case. The loci of the most prominent LAD spots (saturation and prior to and after 'jump') are also illustrated in the LAD schematic for negative saturation of the BQ coupled system (open circles, Table 8.1(i)).

The expected situations for hard axis reversal for the three differently coupled bilayer systems are illustrated in Table 8.2. The starting condition is again saturation in positive x-direction and therefore the second column of Table 8.2 is identical with the second column in Table 8.1. When the field is reduced, however, different reversal mechanisms are expected compared to the easy axis processes with the main difference being a more gradual reversal of magnetisation (i.e. no sudden 'jumps').

In the case of AF coupled bilayers a gradual repulsion of the saturation inductions in the two layers is expected when the applied field is reduced. The corresponding reduction of the net induction results in a successive reduction of  $\beta_L$  down to zero deflection at remanence (Table 8.2(b)). When reverse fields are applied the magnetic moments in the different layers are thought to gradually align up again until parallel alignment is reached in saturation. The expected observation in a LAD experiment is therefore a gradual transition from  $\beta_{L(sat)}$  to  $-\beta_{L(sat)}$ . In the LAD schematic for negative saturation in the AF

case the loci of the spot at positive saturation and remanence are illustrated too (open circles, Table 8.2(c)).

The situation for hard axis reversal of FM coupled layers is also shown in Table 8.2. When the saturation field is reduced it is expected that domains are generated in order to minimise the magnetic moment of the sample. The FM alignment of the magnetic moments in successive layers within the domains however is maintained. As there are two equivalent possibilities of orientation of the net resultant within the domains, two simultaneous spots are expected in the corresponding LAD pattern. This is illustrated for the remanent state with the assumption of  $180^\circ$  walls in such a sample (Table 8.2(e)). When reverse fields are applied to the bilayer the two spots will successively migrate towards the locus of the spot for negative saturation which is illustrated by the solid circle in the corresponding schematic (Table 8.2(f)).

BQ coupling is expected to lead to a similar LAD pattern at remanence as a FM coupled sample. Compared to the case of the FM coupled layer system the distance between the two spots is reduced for BQ coupling as the net resultant of induction in adjacent domains is lower due to the non-parallel alignment of the magnetic moment in the successive layers (Table 8.2(h)). With increasing reverse fields the magnetic moments in adjacent layers are again aligned up and the resulting locus of the considered LAD spot of the saturated sample is illustrated in the schematic of the negative saturation LAD pattern (solid circle, Table 8.2(i)).

With the assumption that BQ coupling is the most realistic coupling mechanism a more detailed description of the expected LAD patterns during magnetisation reversal experiments is given next. Fig. 8.10 illustrates the changes in alignment of the saturation induction of two successive magnetic layers for magnetisation reversal in easy axis together with the corresponding LAD patterns. It should be noted that the bilayer film is presumed to be single domain throughout the entire easy axis magnetising cycle.

When the applied field is reduced the alignment of the magnetic induction in two successive layers (black and blue arrows) changes from parallel to almost antiparallel as the angle between the saturation induction of the two considered layers gradually increases. The situation at remanence and prior to the sudden switch of magnetisation are expected to be very similar.

At the coercive field value the magnetisation of the sample reverses in a sudden 'jump' which can also be detected in the LAD images. Successive increase of the applied field gradually leads to parallel alignment of the magnetic induction in the bilayer system

with the LAD spot migrating away from the image centre. It should be noted that only half the 'jump-width' is equivalent to the net resultant of induction.

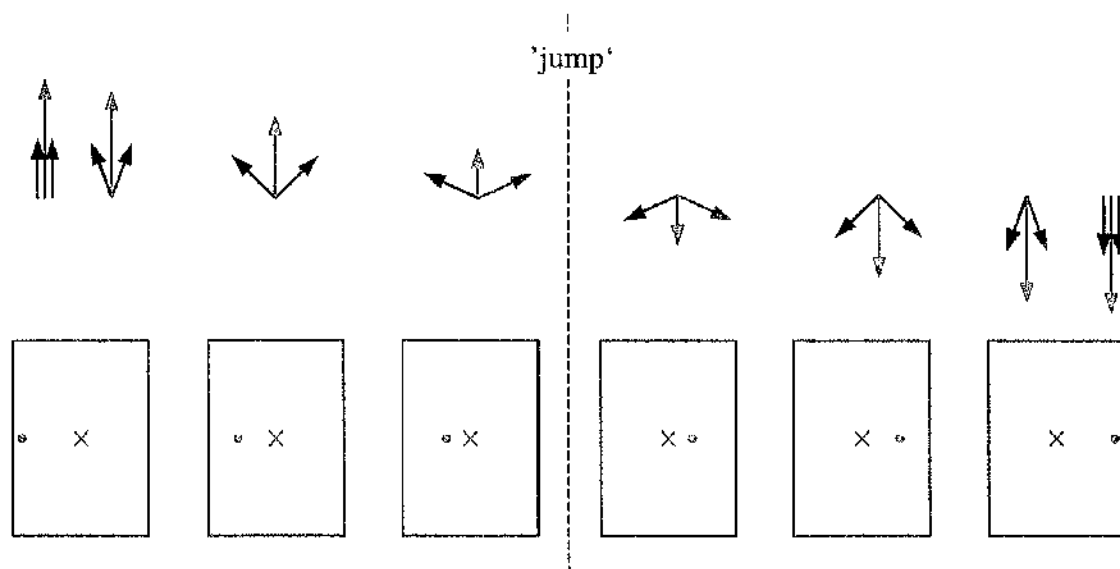


**Figure 8.10**

*Correlation of the alignment of magnetic induction in a bilayer system (arrow diagrams) with the resulting LAD patterns (bottom row) for magnetisation reversal in easy axis.*

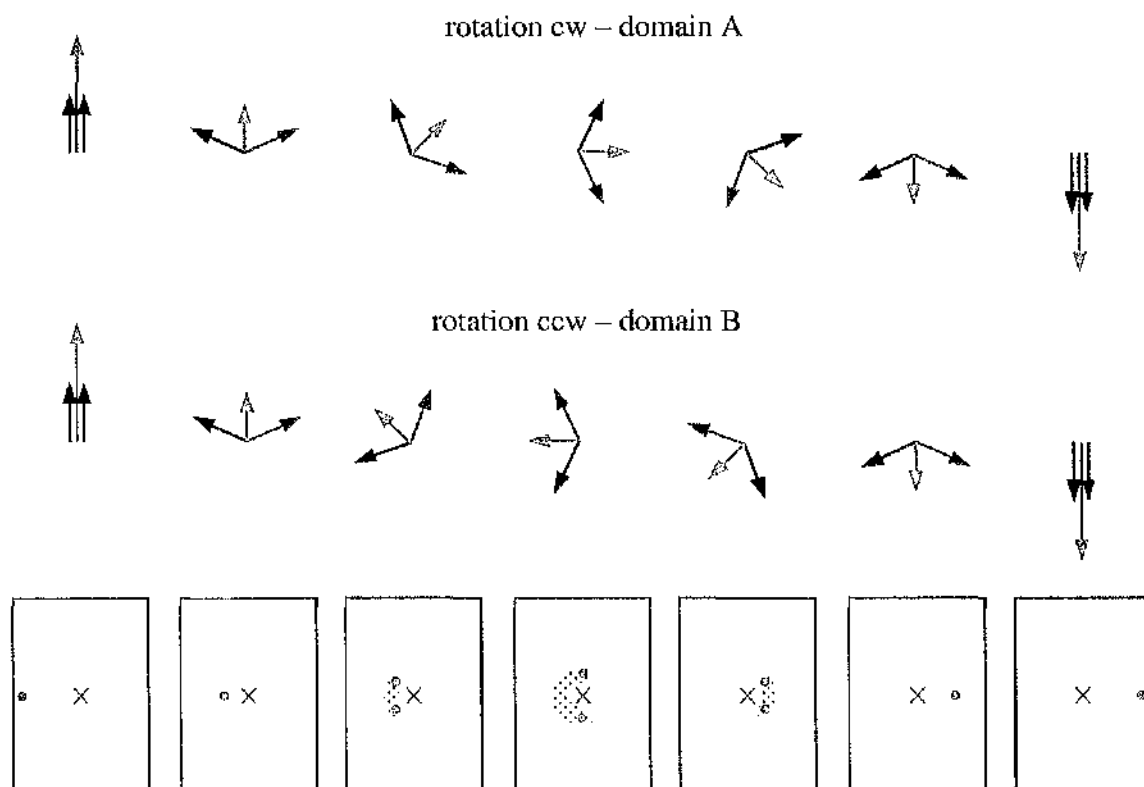
▲▲ Saturation induction in single magnetic layers, ↑ net resultant of magnetic induction, o corresponding LAD patterns (spots), x position for zero deflection.

Figure 8.11 illustrates the expected reversal processes in the hard axis of a BQ coupled bilayer system. In the case of hard axis reversal the formation of domains generally ought to be expected.

When the applied field is reduced the angle of the magnetic moments in the two layers opens up gradually. The resulting LAD pattern is a spot which migrates towards the centre of the image frame. Then domains are generated as the BQ coupled inductions and their net resultants rotate either clockwise (cw) or counterclockwise (ccw). This leads to the formation of two main spots in the LAD pattern which migrate along a circular locus as the net resultant of magnetic induction is constant. At remanence the overall magnetic moment is expected to cancel out as a result of the formation of  $180^\circ$  domains which leads to two major spots in the LAD pattern lying on opposite sides of the circular locus.

When a reverse field is applied the rotation of the net resultant of induction within adjacent domains is expected to continue until the magnetic moments are aligned up and

only one spot is imaged in the LAD pattern. Further increase of the applied field merely leads to migration of the spot away from the image centre as the saturation inductions in the two layers gradually align parallel to the external field and each other.



**Figure 8.11**

*Correlation of the alignment of magnetic induction in different areas (i.e. domains) of a bilayer system with the resulting LAD patterns for magnetisation reversal in hard axis. The two directions of rotation occur in different magnetic domains of the sample.*

↑↑ Saturation induction in single magnetic layers, ↑ net resultant of magnetic induction, • corresponding LAD patterns (spots), × position for zero deflection.

It should be noted that the previous considerations of the magnetic coupling of bilayers are also applicable to multilayer samples as these can be regarded as being made up from a stack of bilayer systems. For further evaluation and especially in order to relate the LAD patterns with the magnetic coupling within the investigated Co/Cu multilayers only some more elaboration is necessary. The way to proceed is as follows:

If the thickness  $t_{mm}$  of the magnetic material is known it is possible to quantify the net induction  $B_{net}$  simply by correlating it with the Lorentz deflection  $\beta_L$ :

$$\beta_L = \frac{e \cdot \lambda \cdot B_{net} \cdot t_{mm}}{h} \quad (8.1)$$

( $\beta_L$  can be determined from the LAD images,  $e$ : elementary charge,  $\lambda$ : wavelength of the electrons – here:  $\lambda(200kV) = 2.5 \cdot 10^{-12} m$ ,  $h$ : Planck's constant).

The final step is to determine the magnetic coupling within a multilayer system by working out the coupling angle  $2\theta$  between the magnetic induction of successive layers. Figure 8.12 illustrates the relation between the half angle  $\theta$  (between the saturation induction in a single layer and the net resultant of induction) and the coupling angle  $2\theta$ .

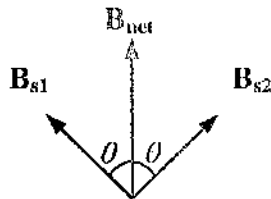


**Figure 8.12**

*Illustration of coupling angle  $2\theta$  in a multilayer system.*

With

$$B_{net} = B_s \cdot \cos\theta \quad (8.2)$$

it is then possible to calculate the coupling angle of a multilayer system when the saturation induction of the magnetic material is known.

### Experiments:

As mentioned previously the LAD experiments were carried out in the modified Philips CM20 FEG microscope. The camera length was 170mm for all presented LAD images. Hard- and easy-axis-like directions were determined as described in section 8.5.3.1. For easier orientation the LAD patterns of the remanent state of the samples are again highlighted by a green frame in all LAD sequences and images taken during time dependent processes are marked by red frames. It should be noted that it is generally not advisable to compare the absolute position of LAD spots in successive images as some degree of beam drift with time cannot be ruled out. The exposure time in all experiments was 0.1s and the images were taken in quick succession in order to minimise the drift

effects. Figures 8.13, 8.14 and 8.15 show overviews of LAD sequences of the three samples of magnetisation reversal in easy-axis-like direction.

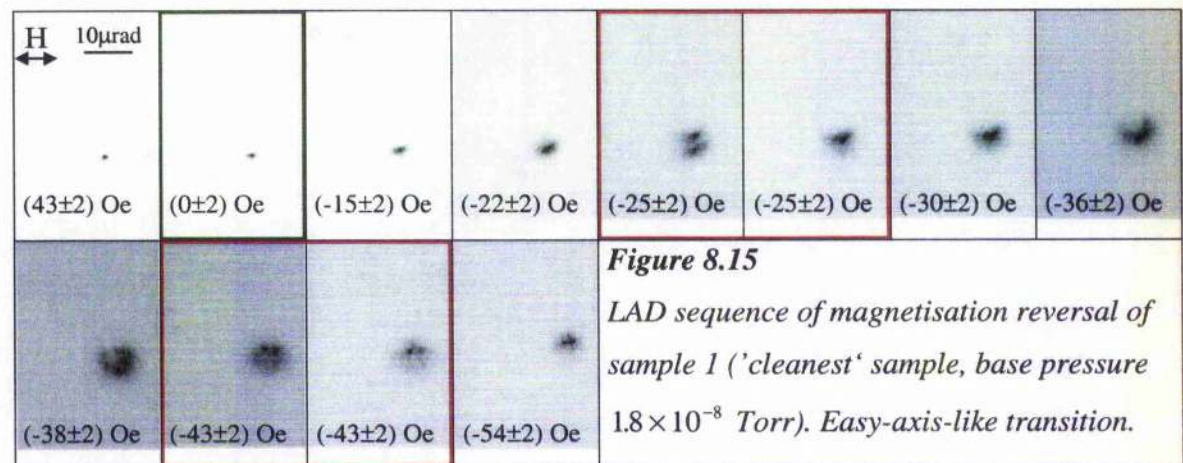
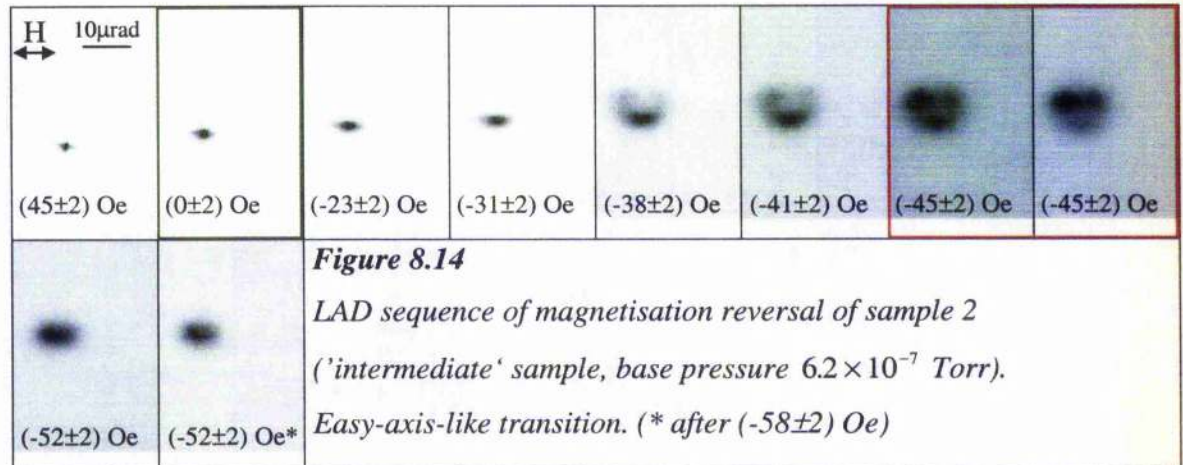
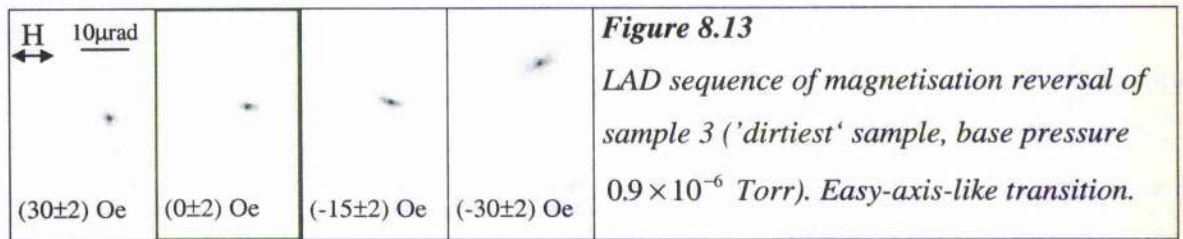


Figure 8.13 shows a sequence of LAD images taken during a magnetising experiment with the 'dirtiest' sample 3. The field was applied in easy-axis-like direction. The LAD sequence in Fig. 8.13 covers the field range between  $\approx 30$  and  $\approx -30$  Oe. The two main characteristics in the LAD images of this sequence are (i) the highly focused spot during the entire experiment and (ii) the sudden jump of the LAD spot at a field value of  $(-30 \pm 2)$  Oe. The highly focused spot indicates that there was only little magnetic

dispersion present in the sample and the sudden jump (too quick in the LAD experiment to capture it on one image despite the short exposure time of 0.1s) was the result of a sharp switch of magnetisation. Both findings are consistent with common easy axis reversal of a simple ferromagnetic film. They indicate further that the orientation of the sample during the LAD experiment was almost certainly even closer to the easy-axis-like direction than during the Fresnel experiment. The reason for this assumption is twofold: Firstly the magnetic dispersion was negligible during the entire LAD experiment and secondly the magnetisation reversal was even quicker in the LAD sequence (time scale  $<0.1\text{s}$ ) than in the Fresnel series (time scale  $\geq 15\text{s}$ , Figs. 8.6(k), (l)). The coercive field value however agreed very well ( $\approx 30\text{ Oe}$ ) for both TEM experiments. The coercive field and the overall behaviour of the sample (i.e. sharp switch of magnetisation and notable remanent moment) were also in good agreement with the corresponding MOKE loop (Fig. 8.3(c),  $H_c=31\text{ Oe}$ ).

Figure 8.14 gives an overview of the magnetisation reversal behaviour of sample 2 in its easy-axis-like direction. At remanence the spot was already notably more spread out than in the previous image where a field of  $(45 \pm 2)\text{ Oe}$  was applied to the sample. The spread increased when reverse fields were applied. A surprising evolution of the LAD pattern was observed for  $(-38 \pm 2)\text{ Oe}$  when the spot developed in a semicircular shape. At a higher reverse field of  $(-45 \pm 2)\text{ Oe}$  a time dependent variation of the LAD pattern occurred (red frame): The formerly most pronounced area on the circular locus migrated towards two intense spots on the opposite side of the circle. Under the influence of higher reverse fields most electrons were then focused in a smaller area which corroborates a higher degree of alignment of magnetisation in the sample compared to the previous state. Whilst these observations do not have much in common with usual easy axis reversal they are in good agreement with the observations in the Fresnel experiment and also with the MOKE measurements (Figs. 8.7(i)-(p), 8.3(b)): In neither Fresnel nor LAD experiment was a sharp switch of magnetisation determined in easy-axis-like direction for this sample. The coercive field value of  $38\text{ Oe}$  from the MOKE experiments is also in reasonable agreement with the observations in the TEM experiments. In the Fresnel experiments  $180^\circ$  walls were observed for  $\approx -40/-45\text{ Oe}$  and it was the same field range in the LAD experiments when the formation of the circular locus occurred. The highly complex domain configuration which was observed in the Fresnel image for  $-45\text{ Oe}$  (Fig. 8.7(n)) was also consistent with the formation of a wide spread LAD locus as observed for this field value. The increasing degree of alignment of magnetisation which was deduced from

the Fresnel images for increasing reverse field values (Figs. 8.7(o), (p)) was also corroborated in the corresponding LAD images.

The magnetisation reversal behaviour of the 'cleanest' sample 1 in its easy-axis-like direction is shown in Fig. 8.15. Compared to sample 2 the spot was much more focused at remanence and up to a reverse field of  $(-15 \pm 2)$  Oe indicating a higher degree of alignment of magnetisation at these stages in sample 1. A time dependent process was observed at  $(-25 \pm 2)$  Oe when a jump occurred. At higher reverse fields a similar behaviour was detected as discussed in the previous paragraph for sample 2: The spot developed in a circular locus prior to the formation of a more localised spot at higher fields  $(-30 \pm 2)$  to  $(-38 \pm 2)$  Oe). Comparison with the Fresnel sequence (Figs. 8.8(i)-(p)) and the associated MOKE loop shows that the coercive field value agreed reasonably for all three measurements especially considering the fact that the MOKE loop (Fig. 8.3(a)) was not very sharp: It was 27 Oe according to the MOKE experiment  $\approx 30$  Oe due to the time dependent process in the Fresnel experiment (no 'switch' observed there) and the jump in the LAD sequence occurred at  $\approx 25$  Oe. The domain configuration was again highly complex in the Fresnel images of Figs. 8.8(l)-(n) which were recorded for similar field values as the LAD images with the clear spread of the spot and development circular locus in Fig. 8.15. The considerable number of remaining  $360^\circ$  walls in the low field Fresnel experiment can of course not be deduced from the LAD pattern.

As discussed earlier (eqns. (8.1) and (8.2)) the 'jump-width' of the spot in the easy-axis-like magnetisation reversal process can be used to determine the corresponding coupling angle of a multilayer system. Figure 8.16 illustrates the determination of this 'jump-width' from the first detected time dependent process in each of the samples. It should be noted that in the case of sample 3 a superposition of the LAD images taken at  $(-15 \pm 2)$  Oe and  $(-30 \pm 2)$  Oe had to be used (Figs. 8.16(a), (b)) despite the earlier mentioned drift of the electron beam. However as these images were recorded one after another drift is not expected to perturb the result markedly. A cross grating with a repeat distance of  $a_x = (1/2160)$  mm was used for calibration purposes (the corresponding LAD pattern is shown later in Fig. 8.20(d)).  $\beta_L$  could therefore be deduced from the LAD images of the multilayer samples and with eqns. (8.1) and (8.2) it was possible to calculate the net induction  $B_{net}$  and the angle  $\theta$  between  $B_{net}$  and  $B_{s1}$  (Fig. 8.12), as the saturation induction  $B_s$  and the total thickness  $t_{nm}$  of the magnetic material were known. The thicknesses of the single layers of Co were known from other investigations

(Table 8.3, Marrows et al, 2000) as was the saturation induction of the layered Co,  $B_s \approx 1.16\text{T}$  which is generally found to be markedly reduced in multilayer systems compared to the bulk value (bulk value for fcc Co:  $B_s \approx 1.7\text{T}$ ).

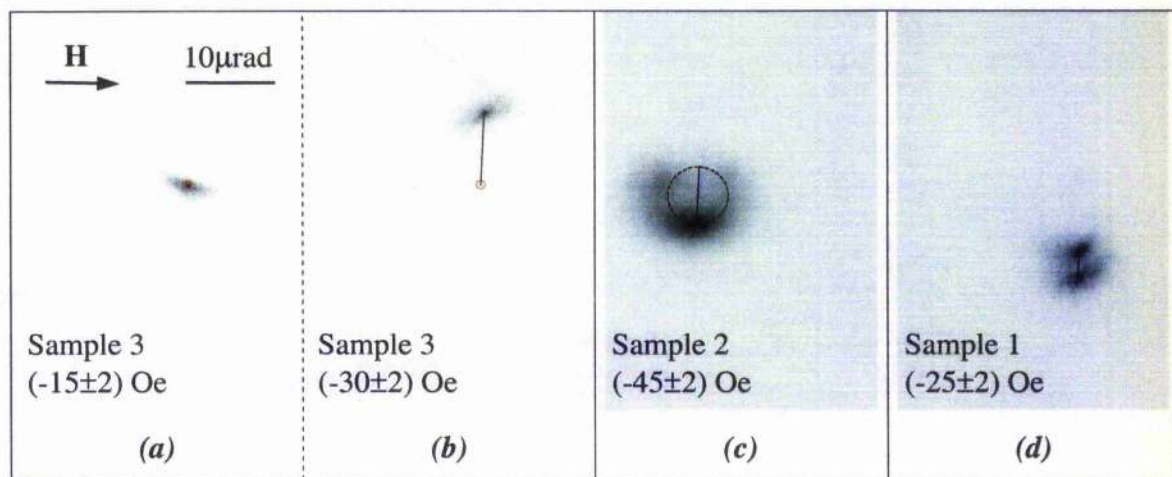


**Figure 8.16**

*Determination of 'jump-width' from easy-axis-like LAD patterns of samples 1, 2, 3.*

*Approximate field direction indicated in (a).*

sample	layer thickness of cobalt $t_{Co}$	⇒ total thickness of magnetic material $t_{mm}$
1	8.1 Å	20.25 nm
2	7.2 Å	18 nm
3	8.4 Å	21 nm

**Table 8.3**

*Layer thickness of Co in samples 1, 2, 3 with resulting total thickness of magnetic material  $t_{mm}$ .*

By means of eqns. (8.1) and (8.2) the corresponding net resultant of induction  $B_{net}$  and the angle  $\theta$  were worked out and the values are given in Table 8.4. As mentioned previously only half the 'jump-width' corresponds to  $B_{net}$ . It should be noted that the trend of the jump width suggested that the sample with best GMR effect displayed the shortest jump distance and that the distance between the positions for start and completion of a time dependent process increased with decreasing GMR. This corroborates at first glance the

expected better AF alignment for good GMR samples. However a closer look at the corresponding  $\theta$ -values does not support this assumption as the  $B_{net}$  and  $\theta$  values for the 2<sup>nd</sup> and 3<sup>rd</sup> sample are not only similar but identical. The reason for this is that the increase of  $B_{net}$  from sample 2 to 3 was also due to the higher thickness of magnetic material in sample 3 compared to sample 2.

sample	$\frac{1}{2}$ 'jump-width' $\beta_L$	$\Rightarrow$ $B_{net}$	$\Rightarrow$ $\theta$
1	1.9 $\mu$ rad	0.16 T	82°
2	3.6 $\mu$ rad	0.33 T	73°
3	4.2 $\mu$ rad	0.33 T	73°

**Table 8.4**

*Overview of  $B_{net}$  and  $\theta$  as introduced in Fig. 8.12 resulting from the magnetisation reversal experiment in the easy-axis-like direction.*

LAD sequences were also recorded of the three samples during magnetising experiments in the hard-axis-like direction and overviews of these observations are given in Figs. 8.17, 8.18 and 8.19.

As expected the highest variations of  $\beta_L$  were found for sample 3 and this is the reason why the findings for this sample are again discussed first. Fig. 8.17 shows an overview of some LAD images of sample 3 while applying a magnetic field in its hard-axis-like direction. It should be noted that the LAD spot was generally much bigger than in the easy-axis-like experiment (Fig. 8.13) which was an indication for a higher degree of magnetic dispersion in the sample during the experiment in the hard-axis-like direction. This was consistent with the expected behaviour for hard-axis-like reversal and it was also in good agreement with the observations in the Fresnel experiment (Figs. 8.6(a)-(h)). When a reverse field was applied the spot spread out considerably in an arc-like shape. At a later stage ( $(-40 \pm 2)$  Oe) a time dependent process was triggered where migration of two major spots over an ellipsoidal locus was observed (red frame). When a slightly higher field was applied the area covered by the LAD spot was much smaller and therefore the magnetisation within the sample in better alignment with the external field.

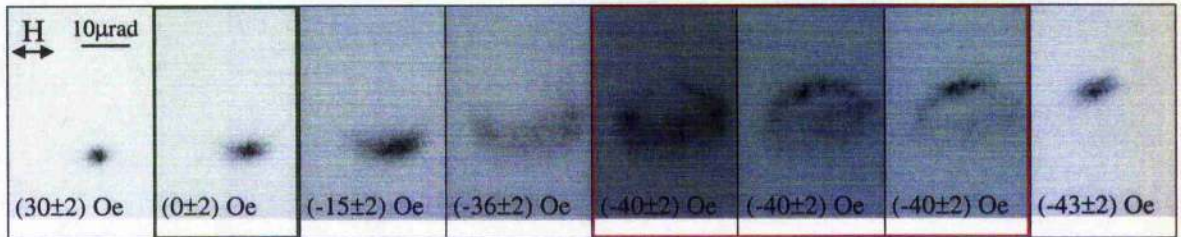


**Figure 8.17**

LAD sequence of magnetisation reversal of sample 3 ('dirtiest' sample, base pressure  $0.9 \times 10^{-6}$  Torr). Hard-axis-like transition.

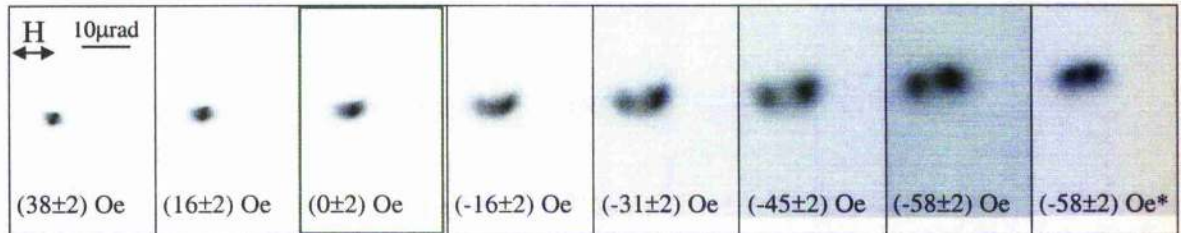


**Figure 8.18**

LAD sequence of magnetisation reversal of sample 2 ('intermediate' sample, base pressure  $6.2 \times 10^{-7}$  Torr). Hard-axis-like transition. (\* after  $(-69 \pm 2)$  Oe)

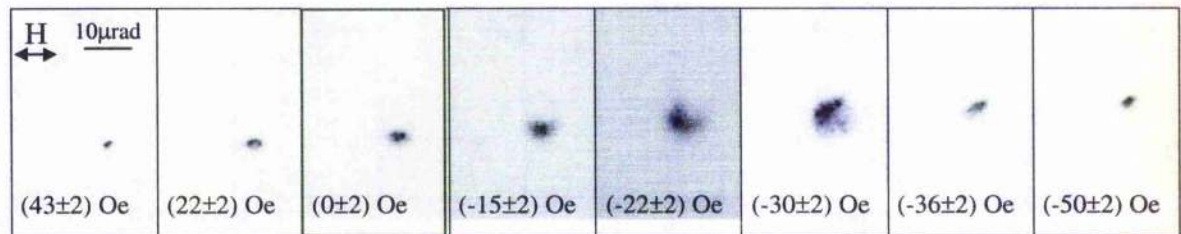


**Figure 8.19**

LAD sequence of magnetisation reversal of sample 1 ('cleanest' sample, base pressure  $1.8 \times 10^{-8}$  Torr). Hard-axis-like transition.

The most surprising characteristic in this LAD sequence (Fig. 8.17) was the development of an ellipsoidal locus as such a trajectory was not anticipated. Another important finding was that there was only one major spot present at remanence. This means that no  $180^\circ$  walls existed at remanence with the result of non-zero overall magnetisation.  $180^\circ$  walls must have been present, however, in the sample when the first image of the time dependent sequence was recorded ( $(-40 \pm 2)$  Oe) as it was at this stage where two opposing major spots were visible within the ellipsoidal locus. Therefore a non-zero magnetic moment at remanence which was also deduced from the Fresnel images was

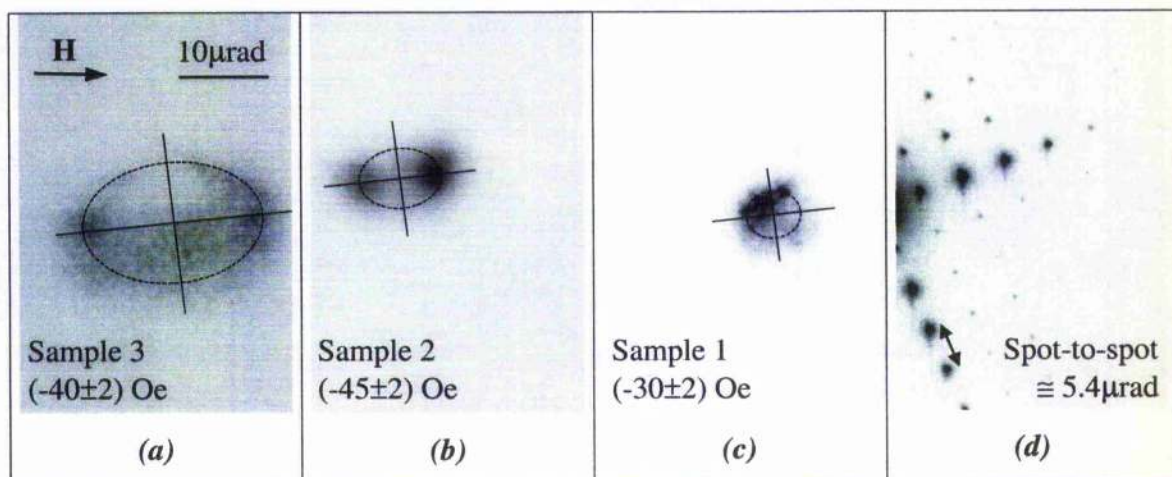
corroborated in the LAD experiment as was a time dependent process for field values in the range  $\approx -40/-44$  Oe. The coercive field value in the hard-axis-like direction according to the TEM experiments was considerably higher than deduced from the MOKE experiment. Whilst it was only 20 Oe in the MOKE loop (Fig. 8.3(c)) it was in the range 30-40 Oe in the TEM experiments.

Figure 8.18 shows a compilation of LAD images of sample 2 taken during a magnetising experiment in the hard-axis-like direction. The spot at remanence was again more spread out than the corresponding spot in the easy-axis-like direction (Fig. 8.14) therefore indicating a higher degree of magnetic dispersion in the sample. Whilst two major spots within an arc-shaped locus were already visible for a reverse field of  $(-31 \pm 2)$  Oe it took an even higher reverse field for the formation of  $\approx 180^\circ$  walls  $(-45 \pm 2)$  Oe). Further increase of the reverse field lead then to migration of the two spots towards each other on an arc-shaped trajectory. As in the case of sample 3 the coercive field values which were determined from the TEM experiments (Fresnel: between 30 and 50 Oe; LAD:  $\approx 45$  Oe) were higher than measured in the MOKE experiment (35 Oe). The non-zero magnetisation at remanence was found in all three experiments and the expected higher degree of dispersion compared to the easy-axis-like reversal was corroborated in both TEM experiments.

The observations for the hard-axis-like reversal of sample 1 are summarised in the LAD sequence in Fig. 8.19. The main findings agree well with the characteristic results in the two previous illustrations. The LAD spot at remanence is more spread out in the hard-axis-like direction than in the easy-axis-like direction (Fig. 8.15) and the generation of an arc-shaped locus was observed under the influence of reverse fields  $(-22 \pm 2)$  Oe) prior to the migration towards a single spot  $(-50 \pm 2)$  Oe). The reason that no pair of opposing spots was generated between  $(-22 \pm 2)$  and  $(-30 \pm 2)$  Oe is almost certainly due to slight misalignment of the sample off the exact hard-axis-like direction. Comparison of the hard-axis-like in-situ magnetising experiments in the TEM (Figs. 8.8(a)-(h) and 8.19) showed that in both cases the net magnetisation of the sample at remanence was not zero which was in agreement with the MOKE result (Fig. 8.3(a)). Good agreement was further found for coercive field values:  $H_c$  was 27 Oe in the MOKE loop and between  $\approx 23$  and  $\approx 30$  Oe in the TEM sequences.

Figure 8.20 illustrates the determination of the long and short axes of the ellipsoidal and almost circular loci of the three samples. The procedure to deduce the corresponding

values for  $\beta_L$ ,  $B_{net}$  and  $\theta$  is the same as described earlier (eqns. (8.1), (8.2)) and the results are summarised in a table 8.5.



**Figure 8.20**

Determination of  $\beta_L$  from hard-axis-like LAD patterns of samples 1, 2, 3. Approximate field direction indicated in (a), LAD pattern of cross grating as reference in (d).

sample	$\frac{1}{2}$ max. deflect.	$\Rightarrow$	$\Rightarrow$	$\frac{1}{2}$ min. deflect.	$\Rightarrow$	$\Rightarrow$	Ratio of ellipse axes
	$\beta_{L(max)}$	$B_{net(max)}$	$\theta_{min}$	$\beta_{L(min)}$	$B_{net(min)}$	$\theta_{max}$	
1	3.2 $\mu$ rad	0.26 T	77°	2.9 $\mu$ rad	0.24 T	78°	1.1
2	5 $\mu$ rad	0.46 T	67°	3.8 $\mu$ rad	0.35 T	72°	1.3
3	11.1 $\mu$ rad	0.87 T	41°	7.6 $\mu$ rad	0.6 T	59°	1.5

**Table 8.5**

Overview of  $B_{net}$  and  $\theta$  as introduced in Fig. 8.12 resulting from the magnetisation reversal experiment in the hard-axis-like direction.

Compared to the evaluation of the easy-axis-like reversal there was considerably more variation of  $B_{net}$  and therefore  $\theta$  resulting from the evaluation of the hard-axis-like reversal, especially in the case of the long axes. The values for the coupling angles  $2\theta$  are compared with the so-called equilibrium angles  $\theta_0$ , which describe the most favourable coupling angles in the samples. These equilibrium angles were determined by C. Marrows by the procedure outlined in Marrows et al, 2000 and they are given in table 8.6.

sample	min. coupling angle $2\theta_{\min}$	max. coupling angle $2\theta_{\max}$	equilibrium angle $\theta_0$
1	154°	156°	156°
2	134°	144°	100°
3	82°	118°	60°

**Table 8.6**

*Comparison of minimal  $2\theta_{\min}$  and maximal coupling angles  $2\theta_{\max}$  determined from LAD images with the coupling angle  $\theta_0$  worked out by C. Marrows and published in Marrows et al, 2000.*

Whilst there was extremely good agreement for the values of sample 1 there was considerable deviation for the other two samples. It should be noted though that the tendency of the minimal coupling angles agrees quite well with the equilibrium angles: The angle in the sample with the best GMR effect (sample 1) was in both cases found to be close to  $180^\circ$  (i.e. AF coupling) whilst the sample with the worst GMR effect (sample 3) had in both cases an angle  $<90^\circ$  and could therefore be regarded more as FM coupled than AM coupled. Sample 2, which had an intermediate GMR was also found to possess an intermediate coupling angle. Therefore biquadratic coupling was verified and quantified by means of two different evaluation methods.

Figure 8.21 illustrates the alignment of the magnetic inductions in two successive Co-layers at different positions in the considered LAD images. The approximate locations of the spots for parallel alignment in the case of saturated samples and nearly parallel alignment are given as well.

There was remarkable variation of the coupling angle deduced from the ellipsoidal locus of the LAD spot of sample 3 (Fig. 8.21(a)) whilst much less variation was derived in the case of sample 2 (Fig. 8.21(b)) and it was found that the exchange coupling was  $\approx$ constant in the case of sample 1 due to the circular locus of the LAD pattern (Fig. 8.21(c)). This means that there was in all samples a mixture of different micromagnetic states present at this one considered field value. It should be noted that this ties in well with the findings of the Fresnel experiments where multi-domain states were clearly observed in the hard-axis-like reversal processes. A main result of the LAD

experiments was therefore that with decreasing GMR some kind of additional anisotropy gave rise to a deterioration of the exchange coupling with a tendency to FM coupling.

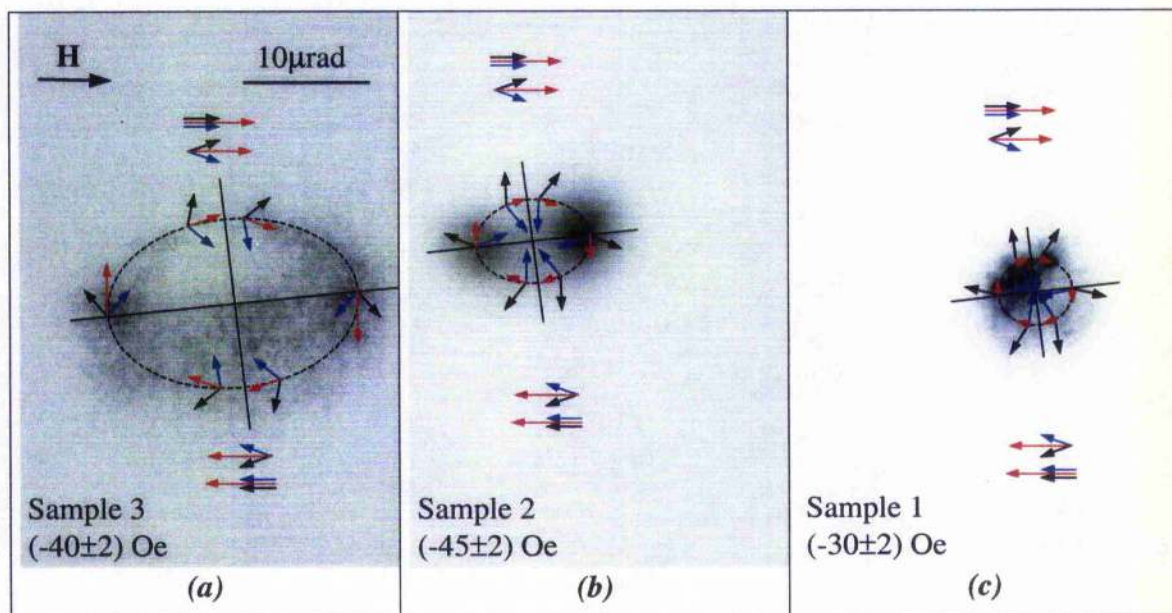


**Figure 8.21**

*Schematics of alignment of magnetic induction in two successive Co-layers for different positions in LAD images. Images from sequences in hard-axis-like reversal. Approximate field direction indicated in (a).*

## 8.6 SUMMARY

The effects of gas-damage on the GMR-performance and coupling mechanism of Co/Cu multilayers were investigated on a set of three samples. All samples were sputtered in a single run with different amounts of gas admitted into the chamber during the growth of the non-magnetic spacer layers.

Three techniques have been applied to determine the magnetic anisotropy and coercivity of the samples: Low field MOKE loops showed a certain degree of anisotropy for all three samples and this was corroborated by both applied Lorentz microscopy modes (Fresnel imaging and LAD). As far as the overall hysteresis behaviour is concerned good agreement was found for all three investigation methods despite considerable deviations between the MOKE and TEM values for the hard-axis-like directions of samples 2 (intermediate) and 3 (dirtiest). The  $H_c$  values are given for all samples and investigation methods in table 8.7.

sample	axis	$H_c$ in MOKE	$H_c$ in Fresnel	$H_c$ in LAD
1	easy-axis-like	27 Oe	30 Oe	25 Oe
	hard-axis-like	27 Oe	23 Oe	<30 Oe
2	easy-axis-like	38 Oe	40/45 Oe	40/45 Oe
	hard-axis-like	35 Oe	30/50 Oe	45 Oe
3	easy-axis-like	31 Oe	30/33 Oe	30 Oe
	hard-axis-like	20 Oe	$\approx$ 30 Oe	40 Oe

**Table 8.7**

*Comparison of the coercive field values of samples 1, 2, 3 for the easy- and hard-axis-like directions;  $H_c$  was determined in (i) MOKE-, (ii) Fresnel- and (iii) LAD-experiments.*

Samples with high GMR were characterised by low contrast in the Fresnel images, a corresponding low Lorentz deflection angle  $\beta_L$  in the LAD experiments and a very isotropic behaviour. Samples with low GMR on the other hand were showing less isotropy and stronger contrast in the Fresnel images and also higher values for  $\beta_L$ .

A novel experimental method to determine the coupling angles was presented. Comparison with the results of an alternative investigation including simulations showed excellent agreement in the case of the cleanest sample 1 (table 8.6). Despite the deviations of the values for the coupling angles of the other two samples the trend of variation (i.e. angle  $>90^\circ$  for samples with good GMR respectively  $<90^\circ$  for bad GMR) was as expected for biquadratic coupling. Therefore biquadratic coupling was not only verified but quantified for all investigated samples.

**CHAPTER 9:****SUMMARY, CONCLUSIONS AND FUTURE WORK**

In this work different modes of Lorentz microscopy have been used to determine information with high spatial resolution about the magnetic microstructure of two groups of magnetic thin film samples with reduced dimensions. One group comprised small magnetic elements with artificially textured edges and the other comprised continuous Co/Cu multilayer films. For some of the small magnetic elements micromagnetic simulations were carried out using commercially available software to aid interpretation of results and to evaluate the utility of the software when applied to a model system.

**9.1 SMALL MAGNETIC ELEMENTS**

The small magnetic elements (patterned thin film elements of permalloy) were fabricated and investigated with the aim of determining the effects of structuring their edges in an attempt to assess the influence of non-perfect (i.e. not entirely straight) edges as well as to evaluate the properties of the elements with deliberately modified edges. Hence so-called standard elements without deliberate edge structure were studied and compared with the behaviour of elements with structured edges. All elements were acicular with their length being in the micron range and they had pointed ends. Two different widths and lengths as well as two different tip ratios ( $t=l_{tip}/w_{tip}$ ) were investigated. The investigated edge structures were periodic repeats of triangles and rectangles and the period and height of the structure features were varied systematically.

The results are briefly summarised with respect to future work on small magnetic elements of permalloy with a film thickness in the range  $\approx 20\text{-}30\text{nm}$ :

Standard elements

## ◆ Coercivity

The coercivity of the elements was found to depend on the element width and the tip ratio:  $H_c$  decreases with increase of element width and increases for higher tip ratios (Fig. 5.10). It should be noted that elements with  $t=0.5$  were found to have a markedly lower coercivity than elements with  $t_1=1$  or  $t_2=2$ . This is due to the fact that the generation of end domains was associated with the kink in the tip region (see below and Figs. 4.8, 5.5-5.9). These end domains were the first domains, which developed during magnetisation reversal experiments. It should be noted that it is not expected that tip ratios with  $t>2.5$  will

lead to a further substantial increase of coercivity of standard elements. This is because the kink at the inner corners of the tip, which is responsible for the development of domain walls, is already fairly blunt (Fig. 4.9).

◆ Magnetisation reversal

All standard elements were found to reverse very rapidly (in an instant). This is described by the term 'switch' of magnetisation. While a certain degree of rotation was observed prior to switching, the actual reversal occurred too rapidly to infer any details about the ongoing changes.

◆ Micromagnetic state

At remanence

The standard elements with  $t_1$  and  $t_2$  were found to be single domain at remanence (Figs. 4.8, 5.5-5.9) while the elements with  $t=0.5$  supported end domains. It should also be noted that the elements with  $t=0.5$  possessed flux closure domain configurations in the ac-demagnetised state of the samples as the pointedness of the elements was not strong enough to outweigh the high magnetostatic energy of a single domain state.

Prior to switching

All elements were found to develop multi-domain states prior to switching. End domains were generated at the inner corners of the element tips (kink). When higher reverse fields were applied the contrast of the walls was observed to increase, indicating magnetisation rotation. In the case of the elements with the blunter tips  $t_1$  the magnetisation was found to switch at well defined field values without the generation of additional domains being observed. In the case of the elements with  $t_2$ , however, the end domains were found to develop in concertina domain configurations, which extended over the entire element prior to the rapid switch of magnetisation also at well defined reproducible field values (Figs. 4.8, 5.5-5.9).

Elements with structured edges

◆ Coercivity

The coercivity of the elements was again found to depend on the element width and the tip ratio. Whilst  $H_c$  was again increasing with decreasing element width and increasing

tip ratio (Figs. 4.12, 4.13, 5.17, 5.18, 5.23, 5.24, 6.8, 6.9, 6.13, 6.14), the overall geometry of the elements was also observed to distinctly influence  $H_c$ . With respect to the edge structure as well as variation of overall element width (Fig. 9.1) different trends of switching field values have been observed.

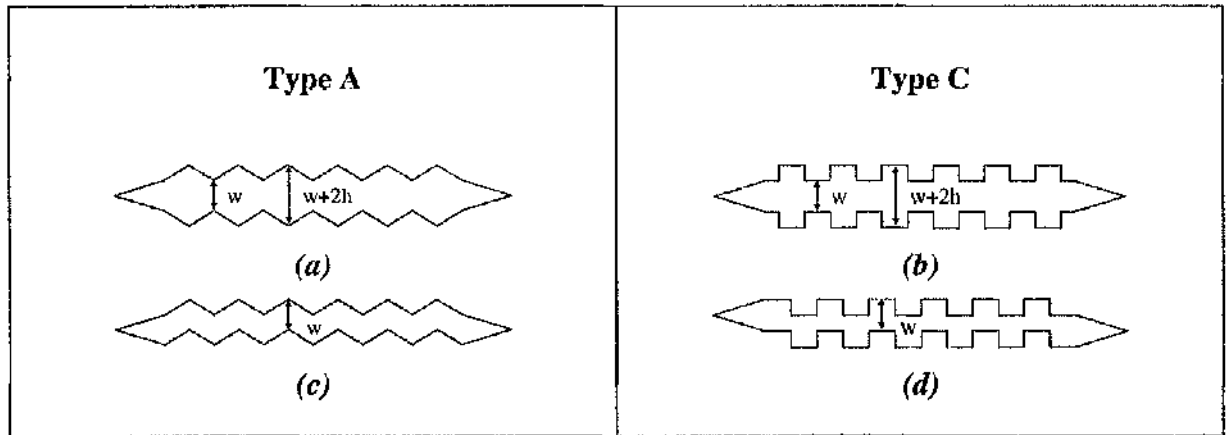


**Figure 9.1**

*Schematic of elements with structured edges with and without variation of the overall width of the elements.*

*(a), (b). Elements with variation of element width between  $w$  and  $w+2h$  ( $3^{\text{rd}}$  pattern ( $t_2$ )).*

*(c), (d) Elements with nominally constant element width ( $5^{\text{th}}$  pattern ( $t_2$ ))*

- Elements with variation of width

Most elements with structured edges were found to reverse at fields between the  $H_c$  values of the standard elements with the corresponding minimum and maximum width (Figs. 5.17, 5.18, 5.23, 5.24), however, the element tip was found to also play an important role in the trend of coercivity.

Whilst there was commonly an increase of coercivity observed for small periods of both structure types A and C, this increase was more pronounced for elements with blunter tips with  $t_1$  (Figs. 5.17, 5.23). In the case of the wider elements ( $w_2$ ) this increase of  $H_c$  for small periods even outweighed the frequently observed decrease of  $H_c$  for elements with structured edges compared to the magnetically harder standard elements.

For elements with the sharper tips  $t_2$ , however, the variation of  $H_c$  which depended on the structure parameters was much less pronounced. Furthermore it was observed that the

coercivity of elements with structured edges and  $t_2$  was generally much closer to lower limit coercivity of the standard elements (Figs. 5.18, 5.24).

- Elements with nominally constant width

The main difference between elements discussed in the previous paragraph and these here was that the elements with structured edges but nominally constant width (Figs. 9.1(c), (d)) were generally harder to switch (Figs. 6.8, 6.9, 6.13, 6.14) than their counterparts (Figs. 9.1(a), (b), 5.17, 5.18, 5.23, 5.24). This is not only due to the nominal constancy of the element width but also a result of the stronger pinning of the created domain walls (see following sections 'Magnetisation reversal' and 'Micromagnetic states'). Most surprising was that the majority of the elements with structured edges but nominally constant width had similar or even higher coercive field values than the standard elements.

It should be noted that with increase of structure height and period differences in the quality of pattern transfer depending on structure type were observed. In the case of structure type A with the highest investigated structure height  $h_3$  pattern transfer deteriorated markedly for small investigated periods due to proximity writing effects (Figs. 3.5, 5.3, 6.3). This led generally to less comparable results in the magnetisation reversal behaviour.

- ◆ Magnetisation reversal

Most elements were found to reverse very rapidly. This is again described by the term switch of magnetisation. Some elements, however, reversed in stages: These were most notably the elements of nominally constant width with structure type A with  $h_3$  and the small investigated periods ( $p=0.2\mu\text{m}$  and  $0.1\mu\text{m}$ ). In the case of edge structure type C it was observed that after magnetisation reversal occurred in the main body of the elements with  $0.2\mu\text{m}\leq p\leq 0.33\mu\text{m}$ , the magnetisation was not always reversed in the entire element (Figs. 5.22(b) and (c)) - regardless to the overall width of the elements.

- ◆ Micromagnetic states

As they are a very clear means to summarise the observed micromagnetic states of the elements, the tables from chapters 5 and 6 are again presented here (Tables 9.1-9.4).

Elements with Variation of Width - Structure Type A, $w_1, t_2$				
period	state	$h_1=50\text{nm}$	$h_2=100\text{nm}$	$h_3=250\text{nm}$
2.0 $\mu\text{m}$	R	single domain	(Fig. 5.11) single domain	quasi single domain
	PS	concertina	concertina*	concertina*
0.5 $\mu\text{m}$	R	single domain	(Figs. 5.12, 5.13) quasi single domain	parallelogram domains
	PS	parallelogram domains	parallelogram domains	parallelogram domains
0.33 $\mu\text{m}$	R	quasi single domain	quasi single domain	parallelogram domains
	PS	parallelogram domains	parallelogram domains	parallelogram domains
0.2 $\mu\text{m}$	R	quasi single domain	(Figs. 5.14, 5.16(a), (b)) quasi single domain	parallelogram domains
	PS	parallelogram domains	parallelogram domains	walls move and merge
0.1 $\mu\text{m}$	R	single domain	(Figs. 5.15, 5.16(c), (d)) single domain	low angle walls
	PS	concertina	concertina	concertina

Table 9.1

Micromagnetic states of elements with  $w_1$  and structure type A of 3<sup>rd</sup> pattern ( $t_2=2$ ).

Elements with Variation of Width - Structure Type C, $w_1, t_2$				
period	state	$h_1=50\text{nm}$	$h_2=100\text{nm}$	$h_3=250\text{nm}$
2.0 $\mu\text{m}$	R	quasi single domain	(Figs. 5.19, 5.20(a), (b)) quasi single domain	multi-domain (centre)
	PS	concertina*	concertina*	multi-domain (centre)
0.67 $\mu\text{m}$	R	quasi single domain	(Figs. 5.20(c), (d)) multi-domain	double y-configurations
	PS	multi-domain	multi-domain	double y-configurations
0.33 $\mu\text{m}$	R	quasi single domain	(Fig. 5.21) double y-configurations	double y-configurations
	PS	double y-configurations	double y-configurations	double y-configurations
0.25 $\mu\text{m}$	R	quasi single domain	double y-configurations	double y-configurations
	PS	double y-configurations	double y-configurations	double y-configurations
0.2 $\mu\text{m}$	R	double y-configurations	(Fig. 5.22) double y-configurations	double y-configurations
	PS	double y-configurations	double y-configurations	double y-configurations

Table 9.2

Micromagnetic states of elements with  $w_1$  and structure type C of 3<sup>rd</sup> pattern ( $t_2=2$ ).

Elements with Nominally Constant Width - Structure Type A, $w_1, t_2$				
period	state	$h_1=50\text{nm}$	$h_2=100\text{nm}$	$h_3=250\text{nm}$
2.0 $\mu\text{m}$	R	single domain	single domain	low angle wall at centre
	PS	concertina	concertina	walls at centre and ends
0.5 $\mu\text{m}$	R	parallelogram domains	parallelogram domains	parallelogram domains
	PS	parallelogram domains	parallelogram domains	parallelogram domains
0.33 $\mu\text{m}$			(Figs. 6.5, 6.6)	
	R	parallelogram domains	parallelogram domains	parallelogram domains
	PS	parallelogram domains	parallelogram domains	parallelogram domains
0.2 $\mu\text{m}$			(Figs. 6.7(a), (b))	
	R	parallelogram domains	parallelogram domains	parallelogram domains
	PS	parallelogram domains	parallelogram domains	walls move and merge
0.1 $\mu\text{m}$			(Figs. 6.7(c), (d))	
	R	single domain	single domain	quasi single domain
	PS	concertina	concertina	multi domain

Table 9.3

Micromagnetic states of elements with  $w_1$  and structure type A of 5<sup>th</sup> pattern ( $t_2=2$ ).

Elements with Nominally Constant Width - Structure Type C, $w_1, t_2$				
period	state	$h_1=50\text{nm}$	$h_2=100\text{nm}$	$h_3=250\text{nm}$ ('fishbone')
2.0 $\mu\text{m}$				Figs. 6.3(f), 6.4(f)
	R	quasi single domain	quasi single domain	closure domains
	PS	concertina*	concertina*	closure domains
0.67 $\mu\text{m}$			(Figs. 6.10, 6.12(a), (b))	
	R	quasi single domain	multi-domain	--
	PS	multi-domain	y-configurations	--
0.33 $\mu\text{m}$			(Figs. 6.11, 6.12(c), (d))	
	R	y-configurations	y-configurations	--
	PS	y-configurations	y-configurations	--
0.25 $\mu\text{m}$	R	y-configurations	y-configurations	--
	PS	y-configurations	y-configurations	--
0.2 $\mu\text{m}$	R	y-configurations	y-configurations	--
	PS	y-configurations	y-configurations	--

Table 9.4

Micromagnetic states of elements with  $w_1$  and structure type C of 5<sup>th</sup> pattern ( $t_2=2$ ).

R means 'remanent state' and PS stands for 'prior to switching'. For detailed description of the used terminology see appropriate text sections of tables 5.3, 5.4, 6.1 and 6.2. It should be noted that neither the tip ratio nor the element width was found to markedly influence the magnetic microstructure of the elements with structured edges. Therefore the tables are also valid for most of the elements with the blunter tips as well as the wider elements.

An important result was the observation of characteristic domains depending on the structure type. In the case of structure type A 'parallelogram' domains were frequently observed whereas the characteristic domain configurations of the elements with edge structure type C were 'y-configurations' (Figs. 5.4, 6.4). It should be noted though that there are apparently crucial values of the period. In the case of edge structure type A the characteristic parallelogram domains were no longer observed for  $p=0.1\mu\text{m}$  and  $p=2.0\mu\text{m}$ . Elements with edge structure type C only displayed y-configurations for periods with  $0.2\mu\text{m}\leq p\leq 0.67\mu\text{m}$ .

Another striking observation was the 'channelling' of magnetisation through the serpentine like elements with nominally constant element width (Fig. 6.4). The reason for that was that due to the parallel alignment of the magnetisation to the nearest edge the shape of the elements practically defined a path, which the magnetisation followed.

The shape of the investigated serpentine like elements was also found to result in a firm pinning of domain walls especially in the case of edge structure type A. This is apparently the reason for the higher coercivity of these elements compared to standard elements: As magnetisation reversal progresses, solely rotation of magnetisation within adjacent parallelogram domains was progressing over wide field ranges before the walls finally 'gave way' and the switch of magnetisation occurred. Neither the characteristic parallelogram domains nor a further increase in coercivity was however observed for elements with the smallest investigated period  $p=0.1\mu\text{m}$  and the elements with  $p=2.0\mu\text{m}$  were also not found to develop parallelogram domains. This is also suggestive for crucial parameters governing the micromagnetics of thin film samples.

### **Future work – Small magnetic elements**

As discussed previously, it was found in the course of this work that structuring the edges led to changes in the magnetic microstructure compared to so-called standard elements with nominally straight edges. An important result of the magnetising experiments was that all investigated elements, inclusive the standard elements, were

multi-domain prior to magnetisation reversal and that high densities of modified Néel walls (up to 1wall/100nm) were reproducibly generated depending on the period of elements with structured edges. As domain walls in ferromagnetic metals are known to be a source of resistance and this contribution was already identified on cobalt and nickel films (Allen et al, 1997), (Levy et al, 1997) such high wall densities might be exploited for GMR applications.

Most elements with structured edges were magnetically softer than standard elements of comparable dimensions. The effects were however much less pronounced for wider elements and elements with sharper tips. In the course of this work it was not possible to also investigate non-periodic edge structures (examples illustrated in Fig. 9.2).

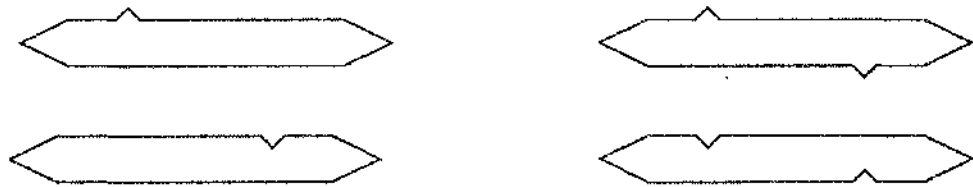


**Figure 9.2**

*Examples of small magnetic elements with non-periodic edge structure.*

This would however be important in order to assess the influence of random defects due to non-perfect pattern transfer e.g. for patterned storage media as well as field sensors and MRAM elements. It might therefore be useful to study such elements in a future project especially as observations were made in this work which suggest that there are critical values for edge structure period and height: Below a certain length scale, the magnetisation seems not to follow the nearest edge section. Further and more detailed investigation is however necessary in order to verify and quantify this.

In terms of ongoing research in the fields of MRAM and patterned storage media it might also prove fruitful to scale the dimensions of the small magnetic elements further down as the influence of non-perfect or deliberately structured edges might give rise to changes in the micromagnetic characteristics. Thus, elements might no longer be single domain at remanence as the variation of edge direction might give rise to the nucleation of unwanted walls whereas subtle variation of the edge geometry might result in a desirable reduction of unacceptably high coercivity.

## 9.2 MICROMAGNETIC SIMULATIONS

Simulations were carried out in the course of this thesis using a commercially available software package (LLG Micromagnetics Simulator™). The aims were to determine the agreement of experimental observations of the small magnetic elements with corresponding simulation results and to also work out the magnetisation reversal mechanisms. The latter was of particular importance as the magnetisation reversal occurred too quickly ('rapid switch') in the experiments to obtain any insight in the ongoing processes.

The equilibrium states of the simulations agreed very well with the experimental observations and are summarised by presenting tables 7.1-7.4 again (tables 9.5-9.8). For more detailed discussion and explanation of the applied terminology see the corresponding text sections in chapter 7. It should be noted that broad agreement was found between experimental observations and simulation results as far as characteristic domain configurations and crucial values were concerned (i.e. no parallelogram domains were found in the experiments as well as the simulations for elements with structure type A and  $p=0.1\mu\text{m}$ ). Questions arose, however, as far as details of the calculated reversal mechanisms were concerned (i.e. high number of Bloch-line-like features and (too?) many walls being generated as well as puzzling wall dynamics during magnetisation reversal; see Figs. 7.4, 7.5, 7.8 and corresponding text sections). It was suggested that these problems might be due to the chosen cell size in the simulations, which lay at the upper limit suggested in the LLG manual for permalloy.

### Future work - Simulations

In order to work out whether the formerly mentioned discrepancies are indeed a result of a too coarse grid it might be worthwhile to carry out further simulations. It should, however, be noted that a decrease of cell size leads to a pronounced increase in calculation time. To counteract this it might prove useful to also scale down the dimensions of the simulated element. Furthermore one could change the temperature in the simulations which was 0 K for all simulations carried out for this work to room temperature. If the details were in agreement with experimental data, especially in the case of the standard elements, then this would be a clear indication of progress! It should be noted, that altering

Elements with Variation of Width -Structure Type A ( $h_2$ ), $w_1$ , $t_2$					
period	2.0 $\mu$ m	0.5 $\mu$ m	0.33 $\mu$ m	0.2 $\mu$ m	0.1 $\mu$ m
<b>state: R</b>	single domain $t_1, t_2(0), t_f(0)$	quasi single domain $t_1, t_2(0), t_f(0)$	quasi single domain $t_1, t_2(0), t_f(0)$	quasi single domain $t_1, t_2(0), t_f(0)$	stripe domains <del><math>t_1, t_2(0), t_f(0)</math></del>
<b>state: PS</b>	concertina* $t_1, t_2(0), t_f(0)$	parallelogram domains $t_1, t_2(0), t_f(0)$	parallelogram domains $t_1, t_2(0), t_f(0)$	parallelogram domains $t_1, t_2(0), t_f(0)$	stripe domains <del><math>t_1, t_2(0), t_f(0)</math></del>
<b>S</b>	propagation of reversed area(s) $t_1, t_2(0), t_f(0)$				

Table 9.5

Micromagnetic states of elements with  $w_1$  and structure type A of 3<sup>rd</sup> pattern ( $t_2$ ) for simulated hysteresis loops with vertical field  $H_v=940$  Oe.

State R: Remanent state, State PS: Prior to switching, S: Switching.

$t_1$ : Simulation for element with  $t_1$  and  $H_v=700$  Oe;  $t_{1,2}(0)$ : Simulation with  $H_v=0$  Oe.

In case of different results for  $t_1, t_2(0), t_f(0)$ :  ~~$t_1, t_2(0), t_f(0)$~~ .

Elements with Variation of Width -Structure Type C ( $h_2$ ), $w_1$ , $t_2$					
period	2.0 $\mu$ m	0.67 $\mu$ m	0.33 $\mu$ m	0.25 $\mu$ m	0.2 $\mu$ m
<b>state: R</b>	quasi single domain $t_1, t_2(0), t_f(0)$	quasi single domain $t_1, t_2(0), t_f(0)$	double y-configurations <del><math>t_1, t_2(0), t_f(0)</math></del>	double y-, v-configurations <del><math>t_1, t_2(0), t_f(0)</math></del>	double v-configurations $t_1, t_2(0), t_f(0)$
<b>state: PS</b>	concertina* $t_1, t_2(0), t_f(0)$	multi-domain $t_1, t_2(0), t_f(0)$	double y-configurations $t_1, t_2(0), t_f(0)$	double y-configurations $t_1, t_2(0), t_f(0)$	double y-configurations $t_1, t_2(0), t_f(0)$
<b>S</b>	propagation of reversed area(s) $t_1, t_2(0), t_f(0)$	propagation of reversed area(s) $t_1, t_2(0), t_f(0)$	propagation of reversed area(s) $t_1, t_2(0), t_f(0)$	propagation of reversed area(s) $t_1, t_2(0), t_f(0)$	propagation of reversed area(s) $t_1, t_2(0), t_f(0)$

Table 9.6

Micromagnetic states of elements with  $w_1$  and structure type C of 3<sup>rd</sup> pattern ( $t_2$ ) for simulated hysteresis loops with vertical field  $H_v=940$  Oe.

State R: Remanent state, State PS: Prior to switching, S: Switching.

$t_1$ : Simulation for element with  $t_1$  and  $H_v=700$  Oe;  $t_{1,2}(0)$ : Simulation with  $H_v=0$  Oe.

In case of different results for  $t_1, t_2(0), t_f(0)$ :  ~~$t_1, t_2(0), t_f(0)$~~ .

Elements with Nominally Constant Width -Structure Type A ( $h_2$ ), $w_1, t_2$					
period	2.0 $\mu\text{m}$	0.5 $\mu\text{m}$	0.33 $\mu\text{m}$	0.2 $\mu\text{m}$	0.1 $\mu\text{m}$
state: R	single domain	parallelogram domains	parallelogram domains	parallelogram domains	$\approx$ concertina
	$t_1, t_2(0), t_1(0)$				
state: PS	concertina	parallelogram domains	parallelogram domains	parallelogram domains	$\approx$ concertina
	$t_1, t_2(0), t_1(0)$				
S	propagation of reversed area(s)				
	$t_1, t_2(0), t_1(0)$				

Table 9.7

Micromagnetic states of elements with  $w_1$  and structure type A of 5<sup>th</sup> pattern ( $t_2$ ) for simulated hysteresis loops with vertical field  $H_v=940$  Oe.

State R: Remanent state, State PS: Prior to switching, S: Switching.

$t_1$ : Simulation for element with  $t_1$  and  $H_v=700$  Oe;  $t_{1,2}(0)$ : Simulation with  $H_v=0$  Oe.

In case of different results for  $t_1, t_2(0), t_1(0)$ :  ~~$t_1, t_2(0), t_1(0)$~~ .

Elements with Nominally Constant Width -Structure Type C ( $h_2$ ), $w_1, t_2$					
period	2.0 $\mu\text{m}$	0.67 $\mu\text{m}$	0.33 $\mu\text{m}$	0.25 $\mu\text{m}$	0.2 $\mu\text{m}$
state: R	quasi single domain	multi-domain	y-configurations	y-configurations	y-configurations
	$t_1, t_2(0), t_1(0)$				
state: PS	concertina*	y-configurations	y-configurations	y-configurations	y-configurations
	$t_1, t_2(0), t_1(0)$				
S	propagation of reversed area(s)				
	$t_1, t_2(0), t_1(0)$				

Table 9.8

Micromagnetic states of elements with  $w_1$  and structure type C of 5<sup>th</sup> pattern ( $t_2$ ) for simulated hysteresis loops with vertical field  $H_v=940$  Oe.

State R: Remanent state, State PS: Prior to switching, S: Switching.

$t_1$ : Simulation for element with  $t_1$  and  $H_v=700$  Oe;  $t_{1,2}(0)$ : Simulation with  $H_v=0$  Oe.

In case of different results for  $t_1, t_2(0), t_1(0)$ :  ~~$t_1, t_2(0), t_1(0)$~~ .

the edges of standard elements in a way as described in the work of Gadbois et al (1995) was tried in the course of this work but did not result in notable changes of the coercivity.

To assure good comparability of simulation and experiment it is recommended to also carry out another series of experiments with smaller elements (as already suggested in the section 'Future work – Small magnetic elements'). It might be necessary to do this in two separate projects (i.e. two theses). With the ongoing research in magnetic microstructures this could prove very rewarding as Lorentz microscopy with its high spatial resolution offers the possibility to check the reliability of simulation results which then, when verified can be used to guide experiments and fabrication.

An important result of the simulations was that in the case of small magnetic elements the vertical field which was present at the samples during the magnetising experiments in the Philips CM20 FEG microscope can not be neglected, as it will almost certainly alter the reversal characteristics. As a result of the reduced dimensions of the elements the demagnetising factor out of the sample plane is no longer  $=1$  but slightly smaller than 1. Therefore the magnetisation of the elements will no longer be confined in the sample plane under the influence of a vertical field component but can easily be tilted a few degrees out of the sample plane (see sections 1.3.3, 1.5 and 7.4.1.1). With vertical components of magnetisation already present, it is much easier to generate Bloch-line-like features, which are expected to form during magnetisation reversal (Fig. 7.5). For future work it might be useful to run the simulations with variable vertical field (as present at the sample due to the varying tilt angles in the microscope) instead of keeping the vertical field component constant throughout the calculations.

### 9.3 Co/Cu MULTILAYERS

In this thesis a novel method was introduced to determine and to quantify the magnetic coupling behaviour of Co/Cu multilayer samples with different degrees of gas-damage. Biquadratic coupling was verified and quantified for low field reversal processes for all samples. An important result was that the coupling was consistent throughout the film instead of alternating regions with antiferromagnetic and ferromagnetic coupling for films with low GMR. It should be noted though that changes in coupling strength through the layer stack can not be ruled out as the interface/interlayer roughness might vary from bottom to top of the layer system. Actually this is quite likely and ties in with the large areas, which are illuminated in the LAD patterns and therefore correspond with different coupling angles (Fig. 8.21).

However, a tendency of increasing AF alignment (coupling angle  $>90^\circ$ ) for samples with appreciable GMR was already corroborated as well as the tendency of more FM alignment (coupling angle  $<90^\circ$ ) in the case of samples with low GMR (Table 8.6).

#### Future work – GMR-samples

To determine the magnitude of the above mentioned possible changes in coupling strength through the layer stack it might prove useful to investigate not only series of samples with different degrees of gas-damage but of different numbers of layers (i.e. 7, 11, 15, 19 and 25 Co/Cu layers).

The introduced method could in the future be applied to different kinds of continuous and patterned multilayers which exhibit GMR (Co/Cr, Fe/Cr), spin valves (Gillies et al, 1995) and TMR structures (Moodera et al, 1995) and then be compared to simulation results. Thus, the simulations could be adjusted to yield more realistic results and to work out crucial parameters in more detail.

## CONVERSION BETWEEN CGS AND SI UNITS

Quantity	Symbol	CGS	Conversion factor	SI
magnetic induction	$B$	$G$	$10^{-4}$	$T$
field strength	$H$	$Oe$	$\frac{10^3}{4\pi}$	$\frac{A}{m}$
volume magnetisation	$4\pi M$	$G$ or $Oe$	$10^{-4}$	$T$
magnetic moment per unit volume	$M$	$\frac{emu}{cm^3}$	$10^3$	$\frac{A}{m}$
demagnetisation factor	$N$	--	$\frac{1}{4\pi}$	--
anisotropy constant	$K$	$\frac{erg}{cm^3}$	$10^{-1}$	$\frac{J}{m^3}$
exchange constant	$A$	$\frac{erg}{cm}$	$10^{-5}$	$\frac{J}{m}$

## SYMBOLS AND ACRONYMS

<b>A</b>		<i>CMR</i>	colossal magnetoresistance
$\alpha$	damping parameter in Landau-Lifshitz-Gilbert equation	<i>CPP</i>	current perpendicular to plane
$\vec{\alpha}, \alpha$	direction cosine between $\vec{M}_s$ and $\vec{M}$	<i>CVD</i>	chemical vapour deposition
$\alpha_{1,2,3}$	change of edge direction for different tip ratios	<b>D</b>	
$\alpha_a$	angular aperture	<i>DPC</i>	differential phase contrast
$a$	lattice constant	<b>E</b>	
$a_x$	lattice constant of cross grating (1/2160)mm	$\epsilon$	tilting angle
$A$	exchange coupling constant	$e$	elementary charge
<i>AF</i>	antiferromagnetic	$E$	polarisation of light
<i>ALD</i>	Aldrich photoresist	$E_{ex}$	exchange energy
<i>AMR</i>	anisotropic magnetoresistance	$E_F$	Fermi energy
<b>B</b>		$E_h$	external magnetostatic field energy; Zeeman energy
$\vec{\beta}, \beta$	direction cosine between $\vec{M}_s$ and $\vec{M}$	$E_{inter}$	interaction energy
$\beta_L$	Lorentz deflection	$E_K$	magnetocrystalline anisotropy energy
$\beta_{L(sat)}$	Lorentz deflection of a saturated sample	$E_{Ks}$	surface magnetocrystalline anisotropy energy
$\vec{B}$	magnetic induction	$E_r$	magnetostrictive energy
$B_{net}$	net induction	$E_s$	magnetostatic self-energy
$B_s$	saturation induction	$E_{tot}$	total system energy
<i>BQ</i>	biquadratic	$E_w$	wall energy
<b>C</b>		<i>ELV</i>	Elvacite photoresist
$c$	speed of light in vacuum	<b>F</b>	
$C_c$	chromatic aberration coefficient	$f$	focal length
$C_s$	spherical aberration coefficient	$\pm \Delta f$	defocus
<i>CCD</i>	charge coupled device	$\vec{F}$	force
		$\vec{F}_L$	Lorentz force
		<i>FEG</i>	field emission gun
		<i>FFT</i>	fast Fourier transform
		<i>FM</i>	ferromagnetic

*FWHM* full width at half maximum

## G

$\gamma$  gyromagnetic ratio  
 $\vec{\gamma}, \gamma$  direction cosine between  $\vec{M}_r$  and  $\vec{M}$   
 $\gamma_e$  gyromagnetic ratio of a free electron  
 $g$  Landé  $g$ -factor; spectroscopic splitting factor  
*GMR* giant magnetoresistance

## H

$h$  Planck's constant  
 $h$  height of edge structure  
 $h_1$  height of edge structure = 50nm  
 $h_2$  height of edge structure = 100nm  
 $h_3$  height of edge structure = 250nm  
 $\vec{H}$  external magnetic field  
 $H_c$  coercive field  
 $\vec{H}_d$  demagnetising field  
 $\vec{H}_{eff}$  effective field  
 $H_{in}$  in-plane field value  
 $\vec{H}_m$  internal molecular field  
 $H_{obj}$  objective lens field  
 $H_{sat}$  magnetic field value necessary to saturate sample  
 $H_{switch}$  switching field value  
 $H_{vert}$  vertical field value  
 $H_{x,y,z}$  magnetic field value in certain direction

## I

*IPA* isopropyl alcohol

## J

$\vec{J}$  current density  
 $J(r_{ij})$  exchange integral for two interacting particles  
 $J$  exchange interaction constant

## K

$\vec{k}$  wave vector  
 $k_\alpha$  maximal spatial frequency in electron probe  
 $k_i$  largest spatial frequency falling on inner detector segments (MDPC)  
 $K_1, K_2$  anisotropy constants  
 $K_c$  cubic anisotropy constant  
 $K_m$  magnetostrictive anisotropy constant  
 $K_s$  surface anisotropy constant  
 $K_u$  uniaxial anisotropy constant

## L

$\lambda$  electron wavelength; for 200kV electrons =  $2.5 \cdot 10^{-12}$  m  
 $l$  length (of base rectangle)  
 $l_1$  length (of base rectangle) = 2.0 $\mu$ m  
 $l_2$  length (of base rectangle) = 4.0 $\mu$ m  
 $l_{tip}$  length of tip  
*LAD* low angle diffraction  
*LLG* LLG Micromagnetics Simulator™; solves Landau-Lifshitz-Gilbert equation

## M

$\mu$  absorption coefficient  
 $\mu_0$  permeability of vacuum  
 $m_e$  rest mass of electron

$\vec{M}$	magnetisation	<b>R</b>	
$M_R$	remanent moment	$\rho$	electrical resistance
$M_S$	saturation magnetisation	$\rho_{sat}$	electrical resistance at saturation magnetisation
$M_{x,y,z}$	magnetisation in certain direction	$\vec{r}$	spatial vector
$\vec{M}(\vec{r})$	magnetisation at a certain point	$r_{ij}$	distance between two interacting particles
<i>MBE</i>	molecular beam epitaxy	$r_{min}$	radius of disc of least confusion
<i>MDPC</i>	modified differential phase contrast	$R$	remanent state
<i>MFM</i>	magnetic force microscope	$R, r$	resistance
<i>MIBK</i>	methyl isobutyl ketone	$R_F$	Faraday amplitude
<i>MO</i>	magneto-optical	$R_K$	Kerr amplitude
<i>MOKE</i>	magneto-optical Kerr effect	$R_N$	regularly reflected electric field amplitude
<i>MRAM</i>	magnetic random access memory	<i>RO</i>	reverse osmosis
	<b>N</b>		
$n(E)$	density of states	<b>S</b>	
$\vec{n}$	normal surface vector	$\sigma_{wall}$	domain wall energy per unit area
$N$	demagnetising tensor	$\vec{s}$	spin
$N_{x,y,z}$	demagnetising factors	$S$	surface
		$S$	switching (mechanism)
		<i>STEM</i>	scanning transmission electron microscope
	<b>O</b>		
$\omega$	angular frequency	<b>T</b>	
		$\theta_0$	angle of incidence
		$2\theta$	coupling angle in a multilayer system
		$\theta_0$	equilibrium angle in a multilayer system
		$t$	time
		$t$	tip ratio = $l_{tip}/w_{tip}$
		$t_1$	tip ratio = 1
		$t_2$	tip ratio = 2
	<b>P</b>		
$\phi$	phase shift		
$\Phi$	magnetic flux		
$\Psi_{in}$	wave function of incident electron		
$\Psi_{out}$	exit wave function of electron		
$p$	period of edge structure		
<i>PEEM</i>	photoemission electron microscope		
<i>PMMA</i>	polymethylmethacrylate		
<i>PS</i>	prior to switching		
	<b>Q</b>		
$q(x,y)$	transmission function		

$l_{mm}$	thickness of magnetic material		
$t_s$	sample thickness	$\bar{v}$	velocity
$T$	temperature	$v_L$	Lorentz motion
$T_C$	Curie temperature	$V$	volume
<i>Type A</i>	edge structure type A, isosceles triangles		
<i>Type B</i>	edge structure type B, right angled triangles		
<i>Type C</i>	edge structure type C, rectangles		
<i>TEM</i>	transmission electron microscope		
<i>TMR</i>	tunnel magnetoresistance	<i>WAM</i>	WaveMaker
	<b>U</b>		
$U$	potential, voltage		
<i>UHV</i>	ultra high vacuum		
<i>USSL</i>	ultra small structures lab		
<i>UV</i>	ultra violet		
			<b>W</b>
		$w$	width (of base rectangle)
		$w_1$	width (of base rectangle) = 250nm
		$w_2$	width (of base rectangle) = 500nm
		$w_{tip}$	maximum width of tip of double pointed elements
			<b>X</b>
		<i>XTEM</i>	cross-sectional transmission electron microscopy
			<b>Y</b>
			<b>Z</b>

## REFERENCES

## CHAPTER 1

- ◆ Baibich MN, Broto JM, Fert A, Nguyen Van Dau F, Petroff F, Etienne P, Creuzet G, Friederich A, Chazelas J, *Phys. Lett.* **61**, p2472 (1988)
- ◆ Becker R, *Z. Physik* **62**, p253 (1930)
- ◆ Bitter F, *Phys. Rev.* **38**, p1903 (1931)
- ◆ Chikazumi S, *Physics of Magnetism*, John Wiley & Sons Inc., New York, London, Sydney (1964)
- ◆ Cowburn RP, *J. Phys. D: Appl. Phys.* **33**, pR1 (2000)
- ◆ Feldtkeller E, Thomas H, *Phys. Kondens. Materie* **4**, p8 (1965)
- ◆ Fuller HM, Hale ME, *J. Appl. Phys.* **31**, p238 (1960)
- ◆ Gillies MF, Chapman JN, Kools JCS, *J. Appl. Phys.* **78**, p5554 (1995)
- ◆ Gomez RD, Luu TV, Pak AO, Kirk KJ, Chapman JN, *J. Appl. Phys.* **85**, p6163 (1999)
- ◆ Grünberg P, Barnas J, Saurenbach F, Fuß JA, Wolf A, Vohl M, *J. Magn. Magn. Mat.* **93**, p58 (1991)
- ◆ Heisenberg W, *Z. Physik* **49**, p619 (1928)
- ◆ Heyderman LJ, Chapman JN, Parkin SSP, *J. Magn. Magn. Mat.* **138**, p344 (1994)
- ◆ Hoffmann H, *IEEE Trans. Mag.* **4**, p32 (1968)
- ◆ Huber Jr EE, Smith DO, Goodenough JB, *J. Appl. Phys.* **29**, p294 (1958)
- ◆ Hubert A, Schäfer R, *Magnetic Domains*, Springer-Verlag Berlin Heidelberg New York (1998)
- ◆ Jiles D, *Introduction to Magnetism and Magnetic Materials*, Chapman and Hall (1991)
- ◆ Kirk KJ, Chapman JN, *J. Magn. Soc. Japan* **21**, p1005 (1997a)
- ◆ Kirk KJ, Chapman JN, Wilkinson CDW, *Appl. Phys. Lett.* **71**, p539 (1997b)
- ◆ Landau LD, Lifshitz E, *Phys. Z. Sowjetunion* **8**, p153 (1935)
- ◆ Lifshitz E, *J. Phys. USSR* **8**, p337 (1944)
- ◆ Marrows C, Wisser N, Hickey BJ, Hase TPA, Tanner BK, *J. Phys. Condens. Matter* **11**, p81 (1999)
- ◆ McVitie S, Chapman JN, *IEEE Trans. Mag.* **24**, p1778 (1988)

- ◆ Middelhoek S, *J. Appl. Phys.* **34**, p1054 (1963)
- ◆ Néel L, *Cahiers de Phys.* **25**, p21 (1944)
- ◆ Parkin SSP, More N, Roche KP, *Phys. Rev. Lett.* **64**, p2304 (1990)
- ◆ Prutton M, *Thin Ferromagnetic Films*, Butterworth&Co (1964)
- ◆ Ramirez AP, *J. Phys. Condens. Matter* **9**, p8171 (1997)
- ◆ Scheinfein MR, Price E, *LLG Micromagnetics Simulator - User Manual* (1998)
- ◆ Smits J, *Physics World* **11**, p48 (1992)
- ◆ Thomson W, *Proc. Roy. Soc.* **8**, p546 (1851)
- ◆ Weiss P, *J. Phys.* **6**, p661 (1907)

## CHAPTER 2

- ◆ Aharanov Y, Bohm D, *Phys. Rev.* **115**, p485 (1959)
- ◆ Bitter F, *Phys. Rev.* **38**, p1903 (1931)
- ◆ Chapman JN, Morrison GR, *J. Magn. Magn. Mater.* **35**, p254 (1983)
- ◆ Chapman JN, *J. Phys. D; Appl. Phys.* **17**, p623 (1984)
- ◆ Chapman JN, MacFadyen IR, McVitie S, *IEEE Trans. Magn.* **26**, p1506 (1990)
- ◆ Chapman JN, McVitie S, Hefferman SJ, *J. Appl. Phys.* **69**, p6078 (1991)
- ◆ Chapman JN, Plößl R, Donnet DM, *Ultramicroscopy* **47**, p331 (1992)
- ◆ Chapman JN, Johnston AB, Heyderman LJ, McVitie S, Nicholson WAP, Bormans B, *IEEE Trans. Magn.* **30**, p4479 (1994)
- ◆ Chikazumi S, *Physics of Magnetism*, John Wiley & Sons Inc., New York, London, Sydney (1964)
- ◆ Cowley JM, *Appl. Phys. Lett.* **15**, p58 (1969)
- ◆ Cowley JM, *Diffraction Physics*, North-Holland Publishing Company (1981)
- ◆ Dahlberg ED, Proksch R, *J. Magn. Magn. Mater.* **200**, p720 (1999)
- ◆ Dekkers NH, de Lang H, *Optik* **41**, p452 (1974)
- ◆ Hale ME, Fuller HW, Rubinstein H, *J. Appl. Phys.* **30** p789 (1959)
- ◆ Hefferman SJ, Chapman JN, McVitie S, *J. Magn. Magn. Mat.* **95**, p76 (1991)
- ◆ Heumann M, Uhlig T, Zweck J, to be published
- ◆ Hubert A, Schäfer R, *Magnetic Domains*, Springer-Verlag Berlin Heidelberg New York (1998)

- ◆ Kortright JB, Awschalom DD, Stöhr J, Bader SD, Idzerda YU, Parkin SSP, Schuller IK, Siegmann HC, *J. Magn. Magn. Mater.* **207**, p7 (1999)
- ◆ Martin Y, Wickramasinghe HK, *Appl. Phys. Lett.* **50**, p1455 (1987)
- ◆ Rave W, Hubert A, *IEEE Trans. Mag.* **26**, p2813 (1990).
- ◆ Reimer L, *Transmission Electron Microscopy*, Springer-Verlag Berlin Heidelberg New York (1997)
- ◆ Rose H, *Ultramicroscopy* **2**, p251 (1977)
- ◆ Rührig M, Bartsch W, Vieth M, Hubert A, *IEEE Trans. Mag.* **26**, p2807 (1990)
- ◆ Swiech W, Fecher GH, Ziethen C, Schmidt O, Schönhense G, Grzelakowski K, Schneider CM, Frömter R, Oepen HP, Kirschner J, *J. of Electron Spectroscopy* **84**, p171 (1997)
- ◆ Tsuno K, Taoka T, *J. Appl. Phys.* **22**, p1047 (1983)
- ◆ Tsuno K, Inoue M, *Optik* **76**, p363 (1984)
- ◆ Uhlig T, Heumann M, Zweck J, to be published

### CHAPTER 3

- ◆ Akhter MA, Mapps DJ, Ma Tan YQ, Petford-Long A, Doole R, *J. Appl. Phys.* **81**, p4122 (1998)
- ◆ Chapman JN, McVitie S, Hefferman SJ, *J. Appl. Phys.* **69**, p6078 (1991)
- ◆ Cowburn RP, *J. Phys. D: Appl. Phys.* **33**, pR1 (2000)
- ◆ de Boeck J, Borghs G, *Physics World* **12**(4), p27 (1999)
- ◆ Gadbois J, Zhu J-G, *IEEE Trans. Mag* **31**, p3802 (1995)
- ◆ Gundlach AM, University of Edinburgh, Dept. of Electronics and Electrical Engineering, priv. communication (1999)
- ◆ Hefferman SJ, Chapman JN, McVitie S, *J. Magn. Magn. Mat.* **95**, p76 (1991)
- ◆ Hubert A, Schäfer R, *Magnetic Domains*, Springer-Verlag Berlin Heidelberg New York (1998)
- ◆ IBM Research Storage; <http://www.almaden.ibm.com/sst>
- ◆ Jiles D, *Introduction to Magnetism and Magnetic Materials*, Chapman and Hall (1991)
- ◆ Khamsehpour B, Wilkinson CDW, Chapman JN, Johnston AB, *J. Vac. Sci. Technol. B.*, **14**, p3361 (1996)

- ◆ Kirk KJ, Chapman JN, *J. Magn. Soc. Japan* **21**, p1005 (1997a)
- ◆ Kirk KJ, Chapman JN, Wilkinson CDW, *Appl. Phys. Lett.* **71**, p539 (1997b)
- ◆ Kirk KJ, Chapman JN, Wilkinson CDW, *J. Appl. Phys.* **85**, p5237 (1999)
- ◆ Mackie WS, PhD Thesis, University of Glasgow (1984)
- ◆ Mallinson JC, *Magneto-Resistive Heads*, Academic Press (1996)
- ◆ McVitie S, Chapman JN, *IEEE Trans. Mag.* **24**, p1778 (1988)
- ◆ McVitie S, Chapman JN, *Microscopy and Microanalysis* **3**, p146 (1997)
- ◆ Read-Rite Corporation; <http://www.readrite.com/html/tech.html>
- ◆ Reimer L, *Transmission Electron Microscopy*, Springer-Verlag Berlin Heidelberg New York (1997)
- ◆ Rührig M, Khamsehpour B, Kirk KJ, Chapman JN, Aitchison P, McVitie S, Wilkinson CDW, *IEEE Trans. Mag.* **32**, p4452 (1996)
- ◆ Schneider M, University of Regensburg, private communication (2000)
- ◆ Swiech W, Fecher GH, Ziethen C, Schmidt O, Schönhense G, Grzelakowski K, Schneider CM, Frömter R, Oepen HP, Kirschner J, *J. of Electron Spectroscopy and Related Phenomena* **84**, p171 (1998)
- ◆ Thoms S, Electron beam lithography course, University of Glasgow (1996)
- ◆ Tondra M, Daughton JM, Wang D, Beech RS, Fink A, Taylor JA, *J. Appl. Phys.* **83**, p6688 (1998)
- ◆ Ziethen C, Schmidt O, Fecher GH, Schneider CM, Schönhense G, Frömter R, Seider M, Grzelakowski K, Merkel M, Funnemann D, Swiech W, Gundlach H, Kirschner J, *J. of Electron Spectroscopy and Related Phenomena* **88**, p983 (1998)

#### CHAPTERS 4, 5, 6

- ◆ Arrott AS, Heinrich B, Aharoni A, *IEEE Trans. Mag.* **15**, p1228 (1979)
- ◆ Chapman JN, *J. Phys. D: Appl. Phys.* **17**, p623 (1984)
- ◆ Chikazumi S, *Physics of Magnetism*, John Wiley & Sons Inc., New York, London, Sydney (1964)
- ◆ Gadbois J, Zhu J-G, *IEEE Trans. Mag.* **31**, p3802 (1995)
- ◆ Hefferman SJ, Chapman JN, McVitie S, *J. Magn. Magn. Mat.* **95**, p76 (1991)
- ◆ Hubert A, Schäfer R, *Magnetic Domains*, Springer-Verlag Berlin Heidelberg New York (1998)
- ◆ Kirk K J, Chapman JN, Wilkinson CDW, *Appl. Phys. Lett.* **71**, p539 (1997)

- ◆ Kirk K J, Chapman JN, Wilkinson CDW, *J. Appl. Phys.* **85**, p5237 (1999)
- ◆ McVitie S, Chapman JN, *IEEE Trans. Mag.* **24**, p1778 (1988)
- ◆ McVitie S, Chapman JN, *Microscopy and Microanalysis* **3**, p146 (1997)
- ◆ Reimer L, *Transmission Electron Microscopy*, Springer-Verlag Berlin Heidelberg New York (1997)
- ◆ Rührig M, Khamsehpor B, Kirk KJ, Chapman JN, Aitchison P, McVitie S, Wilkinson CDW, *IEEE Trans. Mag.* **32**, p4452 (1996)
- ◆ Scheinfein M, Arizona State University, private communication (1998)
- ◆ Tsuno K, Inoue M, *Optik* **76**, p363 (1984)
- ◆ van den Berg HAM, Vatvani DK, *J. Appl. Phys.* **52**, p6830 (1981)

## CHAPTER 7

- ◆ Gadbois J, Zhu J-G, *IEEE Trans. Mag.* **31**, p3802 (1995)
- ◆ Hubert A, Schäfer R, *Magnetic Domains*, Springer-Verlag Berlin Heidelberg New York (1998)
- ◆ McVitie S, Chapman JN, *Microsc. Microanal.* **3**, p146 (1997)
- ◆ Scheinfein MR, Unguris J, Blue JL, Coakley KJ, Pierce DT, Celotta RJ, Ryan PJ, *Phys. Rev. B* **43**, p3395 (1991 a)
- ◆ Scheinfein MR, Blue JL, *J. Appl. Phys.* **69**, p7740 (1991 b)
- ◆ Scheinfein MR, Price E, *LLG Micromagnetics Simulator - User Manual* (1998)
- ◆ Scheinfein MR, private communication (2000)
- ◆ Victora RH, *Phys. Rev. Lett.* **58**, p1788 (1987)

## CHAPTER 8

- ◆ Baibich MN, Broto JM, Fert A, Nguyen Van Dau F, Petroff F, Etienne P, Creuzet G, Friederich A, Chazelas J, *Phys. Lett.* **61**, p2472 (1988)
- ◆ Chapman JN, *J. Appl. Phys.* **17**, p623 (1984)
- ◆ Cohen MS, Huber EE, Weiss GP, Smith DO, *J. Appl. Phys.* **31**, p291S (1960)
- ◆ Daresbury Laboratory - Station 2.3 Homepage;  
<http://www.dl.ac.uk/srs/XRD/2.3.dir/> (2000)

- ◆ Demokritov SO, *J. Phys. D: Appl. Phys.* **31**, pp925-941 (1998)
- ◆ Dieny B, *J. Magn. Magn. Mat.* **136**, p335 (1994)
- ◆ Duden T, Bauer E, *Phys. Rev. B* **59**, p474 (1999)
- ◆ Egelhoff WF, Chen PJ, Powell CJ, Stiles MD, McMichael RD, Judy JH, Takano K, Berkowitz AE, *J. Appl. Phys.* **82**, p6142 (1997)
- ◆ Endo Y, Kitakami O, Shimada Y, *Phys. Rev. B* **59**, p4279 (1999)
- ◆ Fuller HM, Hale ME, *J. Appl. Phys.* **31**, p238 (1960)
- ◆ Grünberg P, Barnas J, Saurenbach F, Fuß JA, Wolf A, Vohl M, *J. Magn. Magn. Mat.* **93**, p58 (1991)
- ◆ Grünberg P, Schreiber R, Pang Y, Brodsky MB, Sowers H, *Phys. Rev. Lett.* **57**, p2442 (1986)
- ◆ Heinrich B, Bland JAC, *Ultrathin Magnetic Structures 2*, various contributions to chapter 2, (Springer, Berlin, 1994)
- ◆ Heinrich B, Cochran JF, Monchesky T, Urban R, *Phys. Rev. B* **59**, p14520 (1999)
- ◆ Hoffmann H, *IEEE Trans. Mag.* **4**, p32 (1968)
- ◆ Hubert A, Schäfer R, *Magnetic Domains*, Springer-Verlag Berlin Heidelberg New York (1998)
- ◆ Kagawa K, Kano H, Okabe A, Suzuki A, Hayashi K, *J. Appl. Phys.* **75**, p6540 (1994)
- ◆ Khamsehpour B, Wilkinson CDW, Chapman JN, Johnston AB, *J. Vac. Sci. Technol. B* **14**, p3361 (1996)
- ◆ Kuo CC, Lin M-T, Huang HL, *J. Appl. Phys.* **85**, p4430 (1999)
- ◆ Marrows CH, Hickey BJ, Malinowska M, Mény C, *IEEE Trans. Mag.* **33**, p3673 (1997)
- ◆ Marrows CH, Hickey BJ, *Phys. Rev. B* **59**, p463 (1999 a)
- ◆ Marrows CH, Hickey BJ, Herrmann M, McVitie S, Chapman JN, *J. Magn. Magn. Mat.* **198-199**, p408 (1999 b)
- ◆ Marrows CH, Hickey BJ, Herrmann M, McVitie S, Chapman JN, Ormston M, Petford-Long AK, Hase TPA, Tanner BK, *Phys. Rev. B* **61**, p4131 (2000)
- ◆ Meissner CR, *Trans. 7<sup>th</sup> Nat. Vac. Symp.*, Pergamon Press, London, AVS p196 (1960)
- ◆ Rezende SM, Chcsman C, Lucena MA, de Moura MC, Azevedo A, de Aguiar FM, Parkin SSP, *J. Appl. Phys.* **85**, p5892 (1999)

- ◆ Rupp G, van den Berg HAM, *IEEE Trans. Mag.* **29**, p3102 (1993)
- ◆ Slonczewsky JC, *Magnetism vol. 1*, Academic: New York (eds. Rado GT, Suhl HD) (1963)
- ◆ Yanagihara H, Pettit K, Salamon MB, Kita E, Parkin SSP, *J. Appl. Phys.* **81**, p5197 (1999)
- ◆ Yoshizaki F, Kingetsu T, *Thin Solid Films* **239**, p229 (1994)
- ◆ Yu CC, Petford-Long AK, *J. Appl. Phys.* **85**, p5753 (1999)

## CHAPTER 9

- ◆ Allen W, Gregg JF, Ounadjela K, Viret M, Hehn M, Thompson SM, Coey JMD, *J. Magn. Magn. Mat.* **165**, p121 (1997)
- ◆ Gadbois J, Zhu J-G, *IEEE Trans. Mag.* **31**, p3802 (1995)
- ◆ Gillies MF, Chapman JN, Kools JCS, *J. Appl. Phys.* **78**, p5554 (1995)
- ◆ Levy PM, Zhang S, *Phys. Rev. Lett.* **79**, p5110 (1997)
- ◆ Moodera JS, Kinder LR, Wong TM, Meservey R, *Phys. Rev. Lett.* **74**, p3273 (1995)